DISSERTATION | DOCTORAL THESIS

Titel | Title

Large-scale magnetic fields in protoplanetary disks

verfasst von | submitted by

Daniel Steiner Bakk.rer.nat. MSc

angestrebter akademischer Grad | in partial fulfilment of the requirements for the degree of

Doktor der Naturwissenschaften (Dr.rer.nat.)

Wien | Vienna, 2025

Studienkennzahl lt. Studienblatt | Degree programme code as it appears on the student record sheet:	UA 796 605 413
Dissertationsgebiet lt. Studienblatt | Field of study as it appears on the student record sheet:	Astronomie
Betreut von | Supervisor:	Univ.-Prof. Dipl.-Phys. Dr. Manuel Güdel

This work is dedicated to Ernst Dorfi.[1]

[1]Credit: I would like to express my gratitude to Ernst Dorfi's wife for providing me with this image of Ernst Dorfi and granting me permission to use it.

Abstract

The study of protoplanetary disks surrounding young stars can provide insights into the formation of our own solar system. Young stars possess very strong magnetic fields, thereby interacting with their surrounding disk and therefore strongly influencing the accreting behavior of such disks. In the first part of this thesis, we study the long-term behavior of disks in the case of a stellar magnetic dipole field interacting with the disk. We use an implicit time integration scheme called TAPIR (The Adaptive Implicit RHD Code) to be able to simulate the innermost disk regions over the whole disk lifetime. The disk is self-consistently simulated and magnetically truncated at the inner disk boundary. Long-term simulations have shown that the inner disk should indeed be simulated hydrodynamically, as magnetic torques and pressure gradients are important for the evolution of the inner disk. Additionally, our studies show that the strength of the stellar magnetic dipole field can influence both the appearance and frequency of episodic accretion events.

Not only the stellar field, but also large-scale magnetic fields threading the disk, play an important role in the evolution of protoplanetary disks. The topology of large-scale magnetic fields is crucial for launching both magnetocentrifugally and magneto-thermally accelerated winds from the disk. In the second part of this thesis, we have therefore expanded TAPIR by adding a description of the large-scale magnetic fields and non-ideal MHD diffusion effects. Our analysis reveals that a stellar field dominates the large-scale field in the inner disk region, while in the outer disk the large-scale field dominates. Furthermore, a parameter study has shown that stellar parameters, such as the rotation period, the magnetic field strength, and the X-ray flux, can influence the topology of the large-scale magnetic field throughout in the disk.

Future work will also include magnetically induced winds, allowing us to self-consistently simulate the coupled system of star, disk, and disk winds over the whole disk lifetime. This will enable better modeling of the star-disk connection and allow us to study how magnetic field parameters influence the lifetime of protoplanetary disks.

Contents

List of Tables

List of Figures

Part I

Introduction and Scientific Background

Chapter 1

Introduction

The question of humanity's origin has been a fascinating topic ever since scientists have started to explore and study nature. One crucial piece in solving this puzzle is the question of how our solar system, or more generally how any planetary system was formed.

It is commonly believed that a protostellar disk is formed when an over-dense region in a molecular cloud becomes gravitationally unstable and collapses. The abundance of initial angular momentum with respect to the center of mass causes the collapsing cloud to rotate, which leads the in-falling mass to organize itself into a flattened, rotating envelope. The mass bound in the central object (the so-called *protostar*) is in this early stage comparable to the mass in the flattened envelope. Because it is commonly believed that most of this envelope falls onto the star, such a structure is called *protostellar disk*.[1] Eventually, at a later stage, most of the envelope accretes onto the protostar, whereas the remaining disk material organizes itself as a (quasi-)Keplerian disk (Terebey et al., 1984). The star and disk become separate, since the envelope which embedded the protostar has been fully accreted. In addition, planets form during this stage; hence, those more evolved star-disk systems are often named *protoplanetary disks* (PPDs) (see e.g., Armitage, 2011).

Several equally important competing physical processes occur simultaneously and on similar timescales. This fact makes it necessary not only to investigate disk physics isolated from each other but instead to try to get a global picture of PPDs by considering as many physical properties as possible. Moreover, they are not conserved systems, as PPDs are irradiated by the central star, undergo radiative cooling, and are threaded by large-scale magnetic fields. Those fields are causing the disk to lose angular momentum via magnetically coupled gas outflows. To get a better understanding of such magnetically induced outflows, it is necessary to also consider the global topology of the corresponding large-scale magnetic fields. The scientific goals of this thesis revolve around the coupling of a stellar magnetic field, the PPD, and a large-scale field, and are outlined in Sect. 2.

Observations (see Sect. 1.1) have shown that accretion of disk material onto the protostar, as well as accretion-powered stellar winds, are very likely. Additionally, there are also observations indicating outflows from the disk surface (disk winds). Accretion is accompanied

[1] The nomenclature *protostellar disk* is in no way universal, but will be adopted throughout this thesis.

by angular momentum transport, whether by internal stresses or by external torques. One such class of external sources are primordial magnetic fields, which thread the disk vertically and extract angular momentum by torques from magnetically induced winds. Blandford and Payne (1982) first investigated the possibility of a magnetocentrifugally driven wind (MCW) from the disk surface. This idea has since then been extensively tested and improved both theoretically (see e.g., Ferreira et al., 2006; Ogilvie, 1997) and numerically (see e.g., Bai and Stone, 2013; Bai and Xue-Ning, 2014; Bai et al., 2015; Guilet and Ogilvie, 2012,1; Lesur, 2021; Leung and Ogilvie, 2019).

Understanding the implications of the observations mentioned above necessitates the development of physical models, which are then tested by conducting numerical simulations. This thesis centers around two publications, which investigate the influence of a stellar dipole field on the long-term evolution of a PPD (see Paper I) and the poloidal large-scale field topology in a PPD (see Paper II). Both papers use the 1+1D simulation package *TAPIR* (The Adaptive Implicit RHD Code, see Ragossnig et al., 2020, and Paper I for a detailed description). In Paper II a description of the ionization fraction, resistivities and a poloidal large-scale magnetic field model were added to TAPIR. The numerical implementation of these new features is described in Sect. 5.2.

1.1 Observational context

The focus of this thesis is the development of models and simulations to investigate the influence of large-scale magnetic fields on disk. However, ultimately, every model has to be verified against observations. Therefore, it is important to understand the observational evidence that scientists have gathered to date and how these observations constrain theoretical models. The relative lifetime of disks, compared to the main-sequence lifetime of a star, is very short (10^{-3} to 10^{-4}); consequently, observations of disks are relatively rare. Moreover, two well-known star-forming regions, Taurus (see e.g., Torres et al., 2012) and Orion (see e.g., Kounkel et al., 2017) have distances of approximately 140 pc and 400 pc, respectively. Due to their small size of a few 100 au, the resolution of their structure poses a challenge. The *Atacama Large Millimeter/Submillimeter Array* (ALMA) has the spatial resolution required to resolve disk structures in the millimeter range and has, since its commissioning in 2013, provided a much better understanding of the dusty structures in PPDs. Additionally, optical observations of dust-scattered light with e.g., the *Spectro-Polarimetric High-contrast Exoplanet REsearch (VLT-SPHERE)* instrument of the *Very Large Telescope (VLT)* provide important information about the disk structure (see e.g., Stasevic et al., 2023). However, the inner region ($\lesssim 1$ au) of disks remains very challenging to observe due to 2 factors: (i) the high spatial resolution needed, and (ii) dust sublimation due to high temperatures in the inner disk. With the advent of optical and IR interferometry it now becomes feasible to also observe the innermost disk region (for a review of observations of the inner disk, see Dullemond and Monnier, 2010).

Young stellar objects (YSOs) can be categorized into various evolutionary stages throughout their lifetime. All disks discussed in this thesis are assumed to be characterized as *Class II* objects. Therefore, a brief overview over the classification of such young star-disk systems is given in Sect. 1.1.1. The stellar magnetic field is now commonly accepted to play a significant role for the very inner disk dynamics and in truncating the disk at a certain radius. The corresponding observational evidence is briefly outlined in Sect. 1.1.3. Lastly, since an essential part of this thesis investigates large-scale magnetic disk fields, important observations on this aspect of PPDs are reviewed in Sect. 1.1.4.

1.1.1 Classifications of star-disk systems

The classification of YSOs is based on the observations of the *spectral energy distribution (SED)* of the star-disk system. The basic idea is that a forming star in earlier stages is surrounded by a prominent disk. As a consequence, light is not only originating from the star but also from the dust in the disk, which dominantly emits in the infrared (IR) frequency range.

A natural choice of classification is therefore to find a measure for the IR excess α_{IR} in the SED compared to a (isolated) main-sequence star, which was defined by Lada and Wilking (1984) to be the slope of the SED in the IR-range between $2.2\,\mu\mathrm{m}$ and $10\,\mu\mathrm{m}$,

$$\alpha_{\mathrm{IR}} = \frac{\mathrm{d}\,\log(\nu\,F_\nu)}{\mathrm{d}\,\log(\nu)} = \frac{\mathrm{d}\,\log(\lambda\,F_\lambda)}{\mathrm{d}\,\log(\lambda)}\,, \tag{1.1}$$

where ν, λ, F_ν and F_λ denote frequency, wavelength, frequency-dependent, and wavelength-dependent spectral radiation flux density, respectively. At the earliest evolutionary stage a YSO is still fully embedded in an envelope, as material from the collapsing molecular cloud core continues to fall towards the star. A star-disk system in this stage is classified as *Class 0* and the definition depicted in Eq. (1.1) is not applicable. This is because the envelope fully obscures the central object. Consequently, almost no emission of light in the optical or near-IR is detectable (see Fig. 1.1). Due to ongoing accretion of material from the envelope the protostar continues to grow more massive, which leads to an increase in angular momentum. This angular momentum is then partially lost by collimated, bipolar stellar winds. Those winds start to blow off the envelope in the vicinity of the protostar's rotational axis.

At the same time the envelope is falling onto the disk. This allows, together with the effects of material blown away by winds, to distinguish contributions from the star gradually more, as this process continues. As a result, an increasing fraction of the stellar radiation is not

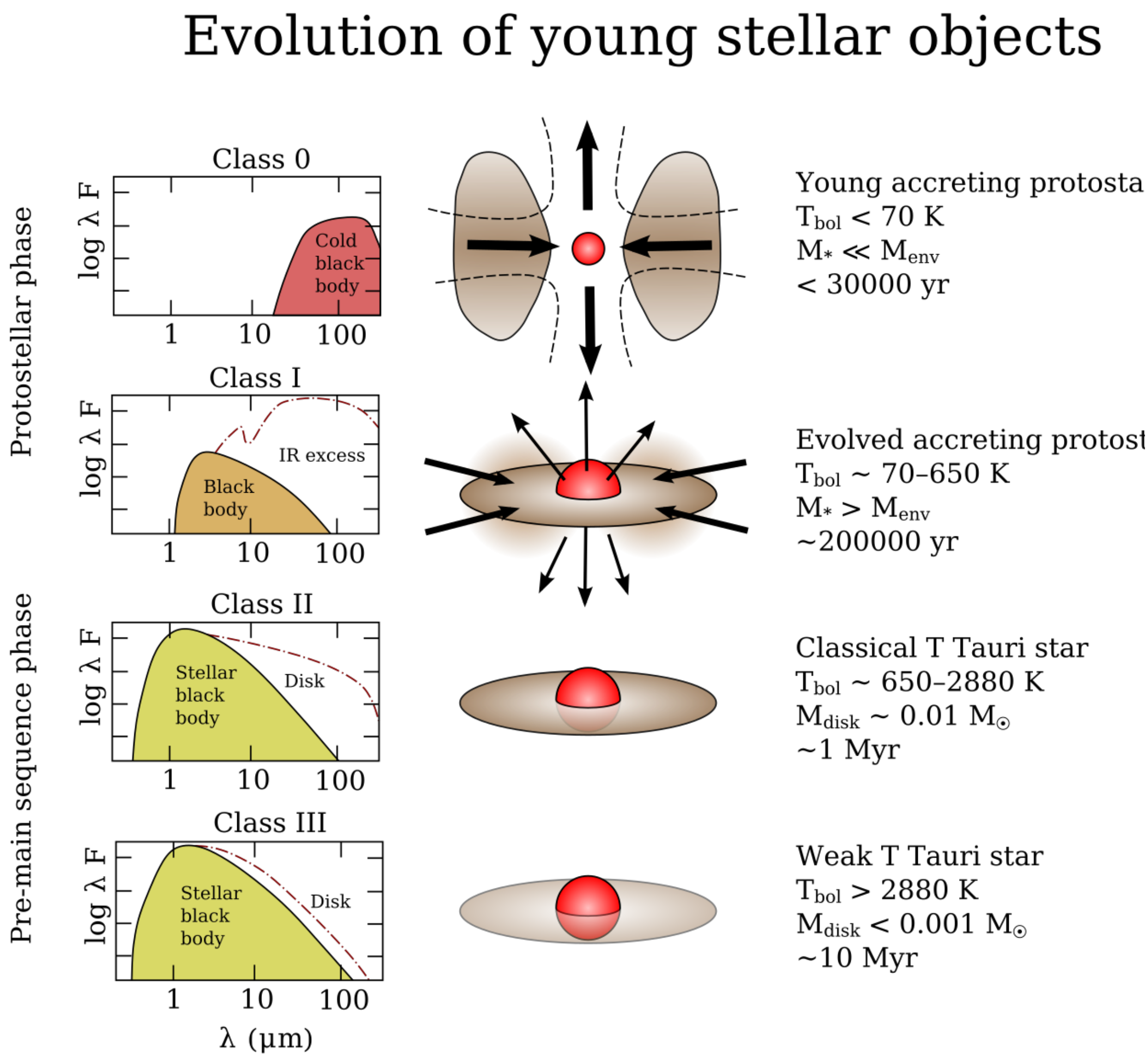

Figure 1.1: Different stages of a star-disk lifetime. Credit: *"Young stellar objects evolutionary stages: spectrum (left column), view (middle column), parameters (right column)"* (https://commons.wikimedia.org/wiki/File:Evolution_of_young_stellar_objects.svg) created by "User:Vallastro" (https://commons.wikimedia.org/wiki/User:Vallastro) and licensed under CC BY-SA-4.0 (https://creativecommons.org/licenses/by-sa/4.0/deed.en).

reddened by the disk anymore, which yields a SED with a positive slope of α_{IR} (cf. Tab. 1.1). The resulting SED consists of two contributions: (i) the star at shorter wavelengths and (ii) a dominant contribution of the disk at the near- and mid-IR. PPDs showing these characteristics are classified as *Class I*.

Angular momentum conservation leads to the core rotating faster as it further collapses. This leads to an increasingly flattened envelope, which reveals more and more light from the star. Therefore, the star's contribution to the SED becomes more prominent and α_{IR} becomes flatter. Greene et al. (1994) proposed therefore an additional refinement in classification of YSOs and introduced *flat spectrum sources*, which are defined by $-0.3 < \alpha_{\mathrm{IR}} < 0.3$.

Eventually the majority of the cloud core has been accreted onto the star-disk system, and

Class 0	α_{IR} cannot be defined
Class I	$\alpha_{\mathrm{IR}} > 0.3$
FS (flat spectrum)	$-0.3 < \alpha_{\mathrm{IR}} < 0.3$
Class II	$-1.6 < \alpha_{\mathrm{IR}} < -0.3$
Class III	$\alpha_{\mathrm{IR}} < -1.6$

Table 1.1: Classification of YSOs following the definition of Williams and Cieza (2011).

the envelope surrounding the YSO has been either fully accreted or ejected by stellar outflows. The disk at this stage is clearly distinguishable from the star and flat. Additionally, protostar and disk are connected through a strong stellar magnetic field and planet formation continues during this stage. Disk winds may occur and are caused by magnetocentrifugal acceleration or photoevaporation. This evolutionary stage is referred to as *Class II*.

Those outflows and accretion onto the central object ultimately lead to the dissipation of the disk. This reveals a SED similar to a blackbody with a typical negative slope in the IR, with $\alpha_{\mathrm{IR}} < -1.6$. Star-disk systems with those characteristics are referred to as *Class III*.

As mentioned earlier, Eq. (1.1) fails to characterize Class 0 YSOs, because no light is emitted in the near and mid-IR. Therefore, Myers and Ladd (1993) proposed an alternative classification of YSOs, which is based on the bolometric temperature T_{bol}. This is the typical temperature corresponding to a blackbody with the same mean frequency $\overline{\nu}$ as the observed SED. The mean frequency $\overline{\nu}$ is an average weighted with the spectral radiation flux density F_ν of the SED (see Ladd et al., 1991):

$$\overline{\nu} = \frac{\int_0^\infty \nu\, F_\nu\, d\nu}{\int_0^\infty F_\nu\, d\nu}\,, \tag{1.2}$$

which is then used to define T_{bol} (see e.g., Myers and Ladd, 1993),

$$T_{\mathrm{bol}} = \frac{\zeta(4)}{4\,\zeta(5)}\,\frac{h\,\overline{\nu}}{k}\,. \tag{1.3}$$

There ζ, h and k denote the Riemann zeta function, the Planck constant, and the Boltzmann constant, respectively. Based on Eq. (1.3), Chen et al. (1995) proposed that the YSO classes originally defined via the infrared excess α_{IR} can be reproduced by selecting appropriate threshold values for T_{bol} for each class, as shown in Tab. 1.2.

Class 0	$T_{\rm bol} < 70$ K
Class I	$70\,\mathrm{K} \leq T_{\rm bol} \leq 650$ K
Class II	$650\,\mathrm{K} < T_{\rm bol} < 2800$ K

Table 1.2: Classification of YSOs following the definition of Chen et al. (1995).

1.1.2 Observational constraints of protoplanetary disk properties

This section follows the reviews of Armitage (2020) and Andrews (2020).

PPDs are observed across different wavelengths and are also spectroscopically analyzed. Three main groups of observational indicators are used to gain different insights into the internal disk structure,

- scattered light,
- continuum emission, and
- spectral line emissions.

Typical pictures of these tracers are shown in Fig. 1.2. In the following the origin of these

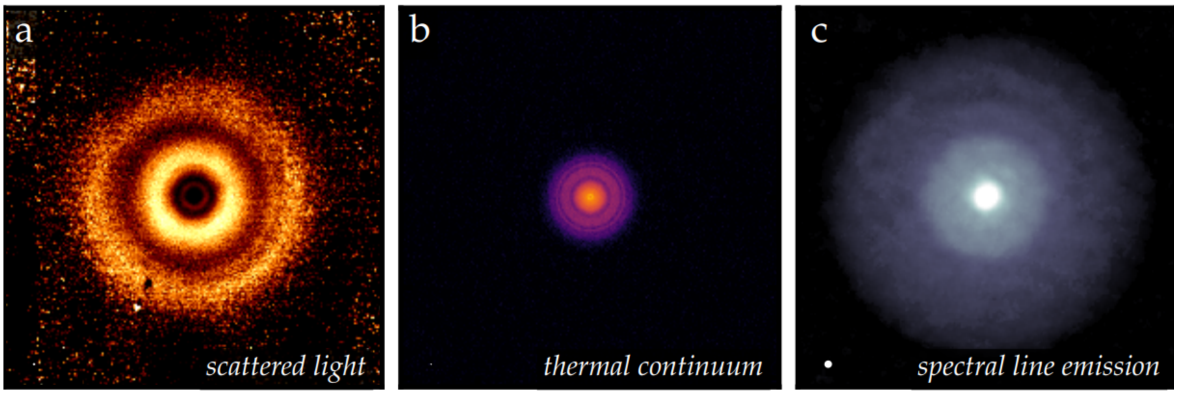

Figure 1.2: All three panels cover a diameter of 500 au of the disk of TW Hya. (a) The scattered light is emitted from dust at a wavelength of $\lambda = 1.6\,\mu m$. (b) Thermal continuum emission of small solids at $\lambda = 0.9$ mm. (c) The molecular CO J=3-2 line emission, which is used as an indicator for molecular gas. The respective resolutions (beam sizes) are depicted in the lower left of each panel as a white-filled ellipse (only well visible in panel (c)). Credit: Reproduced with permission of Annual Reviews, Inc. and authors, from Andrews (2020); Permission conveyed through Copyright Clearance Center, Inc.

different tracers is briefly outlined.

Scattered Light: PPDs mostly consist of gas and only a very small fraction ($\sim 1\%$) are solid materials. These solids eventually aggregate to small dust grains (see e.g., Williams and Cieza, 2011). They form over a large radial range within a PPD and settle preferably towards the disk midplane. However, some grains are mixed up in the disk atmosphere due to turbulence or as a result of fragmentation due to the collision of two particles. These atmospheric dust grains are irradiated by the central star and reflect a fraction of this light in the optical and near-IR spectrum.

Key properties of dust grains like its absorption opacity, albedo, and mean scattering angle strongly depend on the size distribution and porosity of dust grains (see e.g., Birnstiel et al., 2018). Therefore, observations in multiple frequency ranges are able to place constraints on the grain size and distribution of dust in the atmosphere. Additionally, scattered light is observable in the optical, hence, earth-bound telescopes with advanced image correction methods can be used to achieve a very high resolution. However, optical observations make it impossible to investigate the inner disk regions (< 10 au) due to the high contrast difference between central star and disk. Scattered emissions are typically very faint and therefore pose a challenge on the sensitivity of telescopes (see e.g., Fukagawa et al., 2010). Additionally, it is rather difficult to obtain information about the vertical settling of dust grains, since characteristic disk aspect ratios are $z/r \lesssim 0.1$ au, thus requiring very high resolution observations or disks observed at large inclination angles.

Continuum emission: The thermal continuum emitted from PPDs typically originates from dust within the disk and covers the wavelength range from micrometers (μm) to centimeters (cm). Below a temperature of approximately 1500 K the opacity is dominated by dust. As a result, continuum radiation originating from dust with temperatures below 1500 K is optically thick for a wide range of wavelengths. Both optically thin and thick radiation are useful to determine various key disk properties.

PPDs are optically thick ($\tau_\nu \gg 1$) over their full radial extent for wavelengths in the near- and mid-IR, with an optical depth (see Armitage, 2020). The radiation flux density F_ν is obtained from solving the radiation transfer equation in the optical thick limit. Assuming a prescribed radial dust temperature profile of $T_\mathrm{d} \propto r^{-q}$, one then finds a proportionality $\nu F_\nu \propto \nu^{4-2/q}$. Therefore, by measuring the optically thick SED, it is possible to put constraints on the radial profile of the dust disk temperature T_d.

In the optically thin limit ($\lambda \approx$ 1mm) the Planck-averaged dust temperature $\overline{T_\mathrm{d}}$ of the disk can be used to obtain the expression $F_\nu \propto B_\nu(\overline{T_\mathrm{d}})\,\kappa_\nu\,M_\mathrm{disk}/D$, where D, B_ν and κ_ν are the distance to the disk, Planck function and dust opacity, respectively. Therefore, the continuum emission from the optical thin IR continuum emission can be used to calculate the disk mass M_disk. Additionally, when observing wavelengths where the Rayleigh-Jeans approximation to the Planck function is applicable ($B_\nu \propto \nu^2$), the frequency dependency of κ_ν can be constrained for an assumed power law $\kappa_\nu \propto \nu^\beta$, which yields $\nu F_\nu \propto \nu^{\beta+3}$. The inferred constraints for the dust disk mass and dust frequency dependency from observing the continuum emission of PPDs make it a very powerful tool to gather information about disks, nevertheless there are still uncertainties which should be remembered. First, only dust in a certain size range is observable in the near- and mid-IR, which poses the risk of underestimating the mass of dust in a disk, since larger grains (which hold most of the mass) cannot be seen. Additionally, the use of power laws for $T_{\rm d}$ and disk column density Σ oversimplifies complex physical processes in disks and can therefore only provide a coarse estimate of the actual disk structure.

Spectral line emissions: Unfortunately, the most abundant molecule in disks ($\rm H_2$) does not have any strong vibrational nor rotational emission lines due to its homonuclear nature. Therefore, disks essentially appear dark when probed for $\rm H_2$ emissions. However, the molecule HD can be used as an alternative by assuming that the abundance of the molecule HD relative to $\rm H_2$ is known: the *Herschel space observatory* detected emission lines from the J=1→0 rotational transition (see e.g., Bergin et al., 2013), which allow making estimates of the gas mass in disks.

Although HD measurements represent a rich source of scientific research concerning disk masses, the amount of observations is limited due to Herschel's decommissioning in 2013. With the advent of ALMA, emission lines can now be analyzed with a very high resolution. This enables to utilize Doppler broadening of lines to determine the velocities of the corresponding molecules (cf. Fig. 1.3). However, the rare abundance of molecules with rotational transitions (e.g., HD, CO) results in faint lines and therefore poses a sensitivity problem, even for the large effective telescope diameter size of ALMA.

in summary, the dust disk mass is determined predominantly by using continuum emission from dust in the disk, whereas the gas disk mass is constrained by observing lines emitted from tracer molecules like HD. The total disk mass is also sometimes inferred by using only either gas or dust disk mass and the assumption of a constant dust-to-gas ratio (typically ~ 0.01, see e.g., Mohanty et al., 2018). In addition to the determination of the disk mass $M_{\rm disk}$ it is also important to constrain the disk size $R_{\rm disk}$ and the radial profiles of surface density $\Sigma(r)$ and gas temperature $T_{\rm gas}$.

Size measurements: For the determination of the disk size, continuum emissions and observations of scattered light are used. Since there exists no unique definition of where a disk "ends", empirical methods are used to truncate the disk at a reasonable radius. For example, in a large survey of about 200 disks, the disk size was defined as the radius where the disk encompasses a certain threshold value of the millimeter-continuum emission $L_{\rm mm}$, e.g., for the mentioned survey the threshold luminosity is $0.9\,L_{\rm mm}$ (see Andrews et al., 2018;

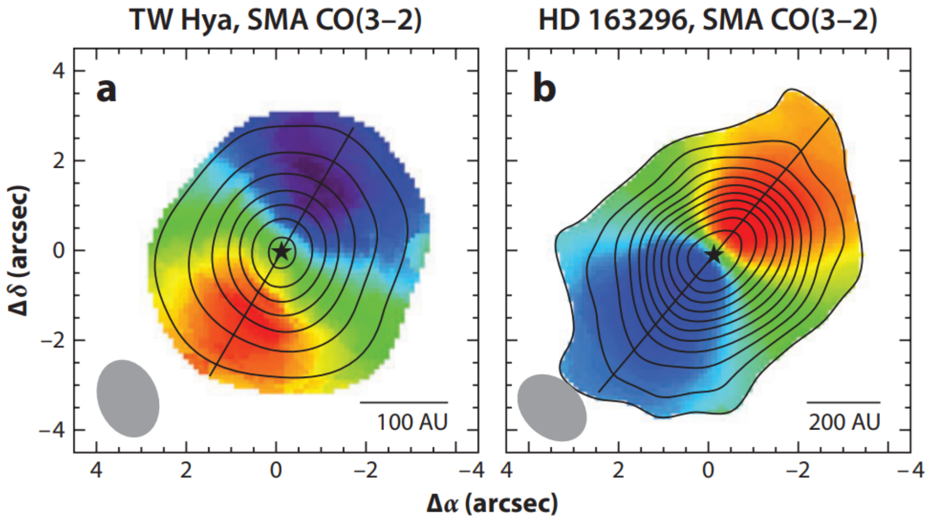

Figure 1.3: Line emissions (CO J=3⟶2 transition) for (a) TW Hydra and (b) HD 163296. The contours mark regions of equal emission intensity, whereas the color-coding depicts different measured velocities. Credit: Reproduced with permission of Annual Reviews, Inc. and authors, from Williams and Cieza (2011); Permission conveyed through Copyright Clearance Center, Inc.

Hendler et al., 2020; Tripathi et al., 2017). The disk size determined this way seems to be physically correct, since the expected scaling between L_{mm} and R_{disk} can be also seen in distance-corrected observations (cf. panel (a) of Fig. 1.4).

Disk sizes derived from continuum emission are systematically larger than those determined by CO line emission spectra (cf. panel (b) of Fig. 1.4). The reasons could be (i) different abundances of CO and disk gas, (ii) a discrepancy between the optical depths of CO and thermal continuum emission, and (iii) the inward migration of dust due to gas drag, which would also result in smaller dust disks in comparison to gas disks.

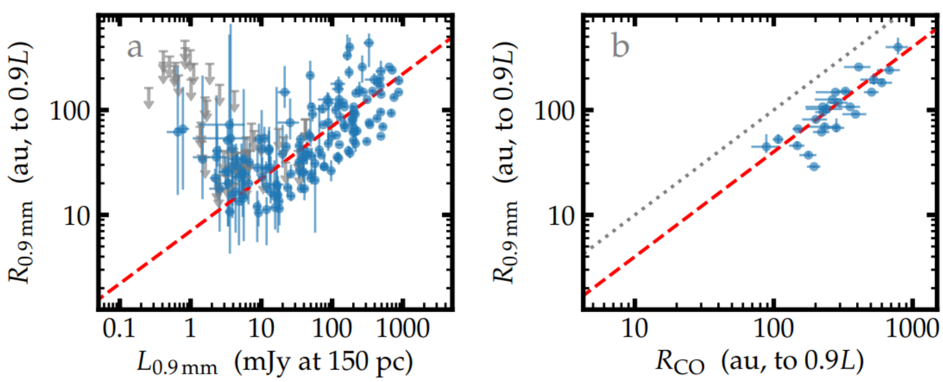

Figure 1.4: Disk sizes determined with 2 methods. (a) Size determined with the use of continuum emission. The red dashed line denotes the best fit with $R_{0.9\ \mathrm{mm}} \propto L^{0.5}_{0.9\,\mathrm{mm}}$. (b) Size measurements based on the CO-line emission. The dotted gray line marks $R_{\mathrm{CO}} = R_{0.9\,\mathrm{mm}}$, whereas the red dashed line describes the relation $R_{\mathrm{CO}} \approx 2.5\, R_{0.9\,\mathrm{mm}}$. Credit: Reproduced with permission of Annual Reviews, Inc. and authors, from Andrews (2020); Permission conveyed through Copyright Clearance Center, Inc.

Surface density measurements: Continuum emissions in the far IR spectrum (millimeter range) can be used to estimate the dust surface density Σ_d. Such observations can only observe the outer regions of PPDs ($\gtrsim$ 20 au) due to limited spatial resolution of the currently available telescopes (see e.g., Tazzari et al., 2017). The inner disk surface density is inferred by using a power-law function, $\Sigma_\mathrm{d}(r) \propto r^{-q}$, which is then fitted with outer disk data and extrapolated towards smaller radii (cf. Fig. 1.5). The gas surface density Σ can be estimated by observing spectral lines, which trace the gas density sufficiently well (as mentioned earlier, currently mostly CO, see e.g., Williams and McPartland, 2016; Zhang et al., 2019). Measurements of Σ pose some challenges, particularly because of the "shielding" of CO line emissions for high Σ_d: in this case the continuum emissions from dust becomes optically thick and no line emissions from deeper disk layers can be observed.

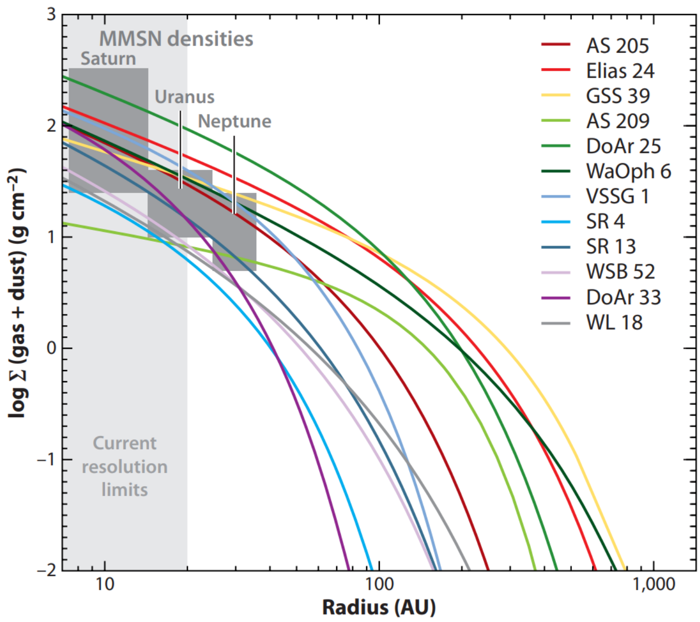

Figure 1.5: Various radial surface density profiles based on observations of disks at λ = $880\,\mu\mathrm{m}$. The grey rectangles mark the minimum mass solar nebular (MMSN) densities for the depicted planets. Credit: Reproduced with permission of Annual Reviews, Inc. and authors, from Williams and Cieza (2011); Permission conveyed through Copyright Clearance Center, Inc.

Gas temperature measurements: Light emitted from the YSO in the center of the disk is absorbed by dust grains in the upper disk atmosphere (disk photosphere), which then re-emit a fraction of that energy in the IR. Part of that dust emission is directed towards deeper disk layers and hence warms gas within the disk. Since stellar irradiation is strongest in the inner disk regions, the gas temperature T_gas at the disk surface is expected to be higher closer to the star. However, secondary heating sources, such as viscous accretion (see e.g., D'Alessio et al., 1998) or radioactive heating (see e.g., Cleeves et al., 2013), can significantly alter the disk's temperature structure, especially in the vertical direction.

Observational constraints on T_{gas} are achieved by observing the SED in the IR spectrum and then compare it with synthetic SEDs obtained from radiative transfer models. These include a prescribed $\Sigma(r)$ and opacity distribution and calculate the disk's temperature distribution in radial and vertical direction. Alternatively, the high resolution of ALMA allows for the spatial resolution of line emissions from different species, each of which become optically thick at different vertical disk heights. This allows for probing different disk layers and radii for their temperature distribution $T(r, z)$ (see e.g., Dullemond et al., 2020).

1.1.3 Observations of the stellar magnetic field

YSOs in their early stages are believed to transport most of the energy produced due to hydrogen fusion convectively, increasing the probability that efficient dynamos are generating strong magnetic fields in young stars (see e.g., Mestel, 1965). Direct observational evidence had to wait until the emergence of high-quality spectro-polarimetry measurements of e.g. Donati et al. (2010), which showed a magnetic field strength of the T Tauri star *V2247 Oph* of a few kG. Furthermore, analysis of the polarization of emission lines revealed a concentration of the magnetic field at mid-latitudes of the star *Proxima Cen*, indicating that this region may be an accretion funnel connecting to the star (cf. Fig. 1.6). Since 2018 there is also

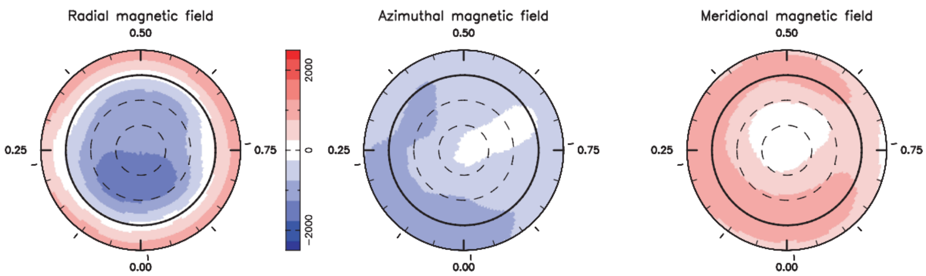

Figure 1.6: From the left to right are the radial, azimuthal and meridional components of the field of Proxima Cen. Credit: Reproduced with permission of first author, from Klein et al. (2021).

a new spectro-polarimeter (*SPIRou*, see Donati et al., 2020), which operates in the near-IR and is dedicated to observe magnetic fields. One of its main objectives is to investigate how magnetic fields influence star- and planet formation, with a focus on still-accreting Classical T Tauri stars (CTTS) in their late Class I and Class II stage. This instrument has a very high sensitivity and is expected to provide significantly more accurate magnetic field measurements of protostars (see e.g., Donati et al., 2025). The magnetic field strengths of the observed objects range between ~ 100 mG and a few kG (see e.g., Johnstone et al., 2014; Zaire et al., 2024).

1.1.4 Observations of large-scale magnetic fields in disks

Observations of large-scale magnetic fields in PPDs have been conducted using the following methods:

Polarization measurements of continuum dust emission: Spinning dust grains align their short axis with the magnetic field lines give long enough time (Lazarian and Hoang, 2007). This effect can in theory be used to measure the polarization of the emitted dust continuum radiation and further allow the magnetic field topology of the large-scale field to be inferred (see e.g., Bertrang et al., 2017). However, the detection of such features is challenging in the case of PPDs, because until recently the quality of linear polarization observations was reduced by scattering emissions from dust aligned by other mechanisms than the magnetic field (see Kataoka et al., 2019). One example is the *helical grain mechanism*, stating that dust grains tend to align normal to the gas flow in a differentially rotating subsonic flow.

ALMA has been extensively used to probe the large-scale field topology of disks by using dust continuum emissions at different wavelengths (see e.g., Harrison et al., 2019; Segura-Cox et al., 2015; Stephens et al., 2014). They found that the inferred field topology changes for different ALMA wavelength bands, which is definitely not expected from magnetically aligned dust grains. These results suggest that the dominant dust alignment mechanisms are not due to magnetic fields, but are instead caused by mechanical or radiative alignment mechanisms. Moreover, the continuum emission of dust can be scattered at other dust grains (dust self-scattering), also leading to polarized dust continuum emission (see e.g., Kataoka et al., 2015). This mechanism, however, needs an anisotropic light emission source (in the case of dust self-scattering the emission of dust itself), which can occur in PPDs with lopsided dust concentrations.

Zeeman effect observations: The Zeeman effect has been used extensively in astronomy to study the magnetic fields in gas clouds and protostellar cores; however, direct measurements of the large-scale field in disks have so far unsuccessful. Attempts using ALMA to detect large-scale fields in AS 2029 (see Harrison et al., 2021, see also Fig. 1.7) and TW Hya (Vlemmings et al., 2019) have so far only resulted in upper limits on the toroidal field strength of the large-scale field. The reason for this is that their method is based on the detection of circular polarized dust emission, which has very high requirements on instrumental sensitivity (see Lankhaar and Teague, 2023). Additionally, circular polarization is caused by magnetic fields in the line of sight of observations, which in the case of weakly inclined disks mainly captures the weaker vertical and radial disk field components and not the up to 10 times stronger toroidal field. Furthermore, the toroidal field component changes sign at the disk midplane (due to the vertical field getting wound-up in the disk, see e.g., Mazzei et al., 2020), leading to a near cancellation of the circular polarization for inclined disks (see Lankhaar and Teague, 2023).

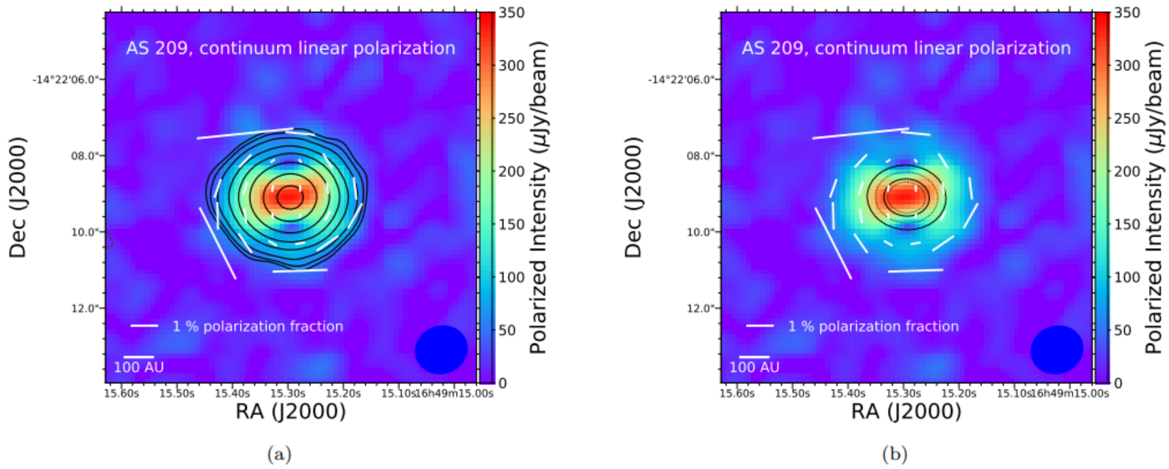

Figure 1.7: Results from Zeeman observations of AS 209. The white lines mark the toroidal field orientation and strength of the disk in both panels. The black contours denote the total intensity in (a) and the location of ring structures in (b). Credit: Reproduced with permission of authors, from Harrison et al. (2021); © AAS. Reproduced with permission.

An alternative approach has been proposed by Lankhaar and Teague (2023), who use linearly polarized light to detect Zeeman splitting. Although this approach poses even higher demands on both instrumental sensitivity and resolution, it has the advantage of being sensitive to the magnetic field component projected on the plane of the sky. This means that even in weakly inclined disks the toroidal field component could be detected directly.

Goldreich-Kylafis observations: The Goldreich-Kylafis effect (Goldreich and Kylafis, 1981) describes that light can be linearly polarized to some degree (a few percent) in a moderately optically thin ($\tau \sim 1$) gas. This occurs because light-emitting molecules in a moderately optically thin ($\tau \sim 1$) gas experience Zeeman splitting of the rotational excitation levels into magnetic sublevels. Line transitions between those sublevels emit either linearly polarized light perpendicular or parallel to the magnetic field component on the plane of the sky. This effect depends on the anisotropy of the velocity of those molecules: the more uniform the velocity of those atoms/molecules, the stronger the polarization (Ching et al., 2016, see e.g.,). Hence, this effect allows observing the large-scale disk magnetic field components either parallel or perpendicular with respect to the plane of the sky.

Despite all the efforts on observing large-scale magnetic fields in PPDs more observations are needed to get a more concise picture of large-scale fields in PPDs. Additionally, methods like linear polarization Zeeman observations require an even higher sensitivity and finer

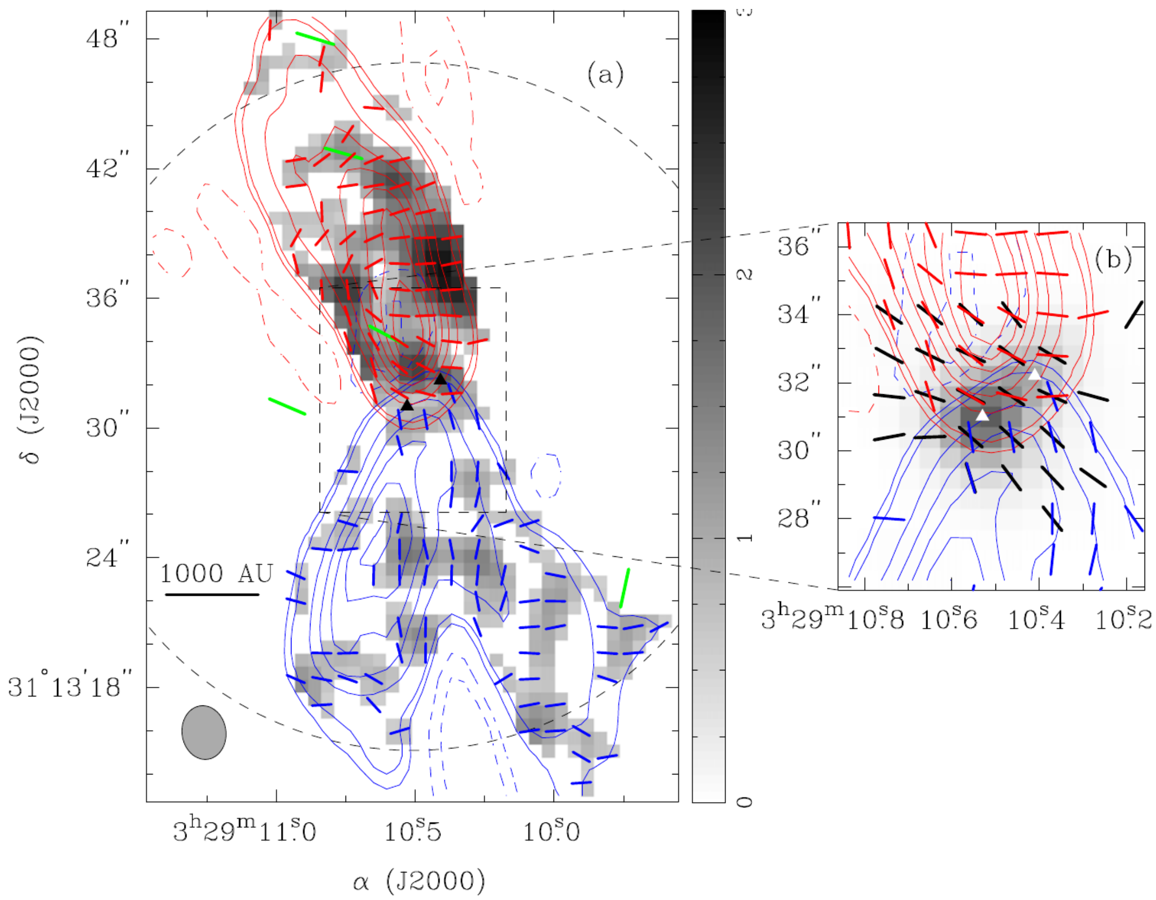

Figure 1.8: Goldreich-Kylafis observations of IRAS 4A are shown in panels (a) and (b). The contours denote various emission strengths of the CO J=3-2 and J=2-1 lines, whereas the blue and red colour-coding states if the corresponding emission lines are blue- or red-shifted. Additionally, the blue, thick lines represent the inferred magnetic field component. The black lines in (b) show the magnetic field orientation as it would be inferred by dust continuum polarization observations. Credit: Reproduced with permission of authors, from Ching et al. (2016); © AAS. Reproduced with permission.

resolution from upcoming instruments to finally achieve direct large-scale field detections in PPDs.

1.2 Protoplanetary disks and magnetic fields

Both stellar and large-scale disk fields are believed to significantly influence the evolution of PPDs (see e.g., Gressel et al., 2015; Guilet and Ogilvie, 2014; Lesur et al., 2022). The inner disk is truncated at the radius where the stellar magnetic field is strong enough to divert the near-Keplerian flow of an accretion disk into magnetic funnels before accreting onto the star. This process is dependent on the density ρ, the mass transport rate $\dot{M}$ and the stellar magnetic field strength $B_\star$. Equally, the large-scale magnetic field topology strongly depends on the disk dynamics together with the radial and vertical disk structure. A model describing both star-disk interaction and large-scale magnetic fields therefore requires a description of the radial and vertical disk structure as well as the dynamic disk evolution (see Sect. 1.2.1 and Sect. 1.2.2).

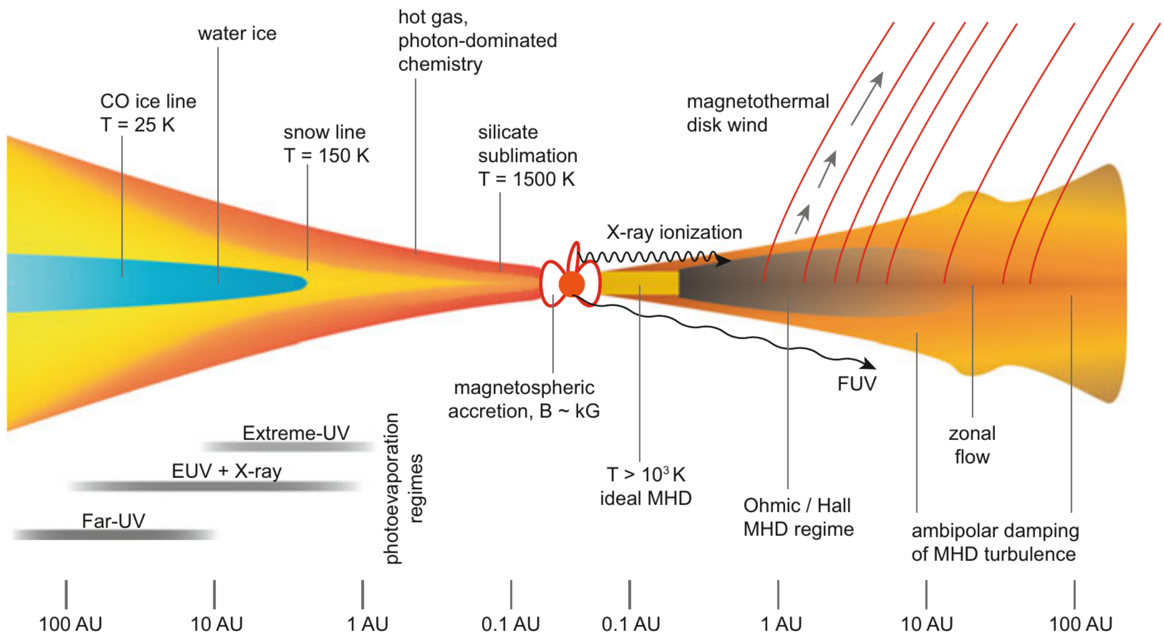

Figure 1.9: Depiction of structure of a PPD with respect to vertical thermal and ionization structure. Additionally, an illustration of both stellar magnetic field and large-scale field and its associated physical processes is shown. Finally, the dominant ionization process for each radial range is indicated by grey bars. Credit: Reproduced with permission from Springer Nature and author, from Armitage (2018); Permission conveyed through Copyright Clearance Center, Inc.

A detailed study of star-disk interaction (see innermost parts close to the star in Fig. 1.9) requires 3D-MHD models to properly describe the complex funnel flows occurring at the star-disk interface (see also paragraph "Magnetic disk truncation" of Sect. 1.2.3). The disadvantage of such complex simulations is the short time covered compared to the disk lifetime (see e.g., Romanova and Kurosawa, 2014). A detailed review of such models, or an in-depth explanation of the intricate physical and numerical details, is beyond the scope of this thesis. Instead, we focus on the determination of the position of the inner rim and the influence of a stellar field on the inner disk dynamics suitable for long-term disk evolution simulations (see Sect. 1.2.3).

Similarly, detailed MHD simulations of large-scale magnetic fields either only cover a very limited fraction of the disk lifetime ($t \sim 1000\,\Omega_{\rm in}^{-1}$, see e.g., Lesur, 2021; Sarafidou et al., 2025, $\Omega_{\rm in}$ denotes Keplerian velocity at the innermost simulated radius) or are constrained to local shearing-box models (see e.g., Bae et al., 2013; Bai and Stone, 2017). The fundamental processes determining the large-scale field topology are discussed in Sect. 1.2.4.

1.2.1 Vertical disk structure

The vertical structure of PPDs is important both for modeling the magnetic star-disk connection and for studying the large-scale magnetic field topology. Most important in this context are the vertical density structure $\rho(z)$, the temperature profile $T_{\text{gas}}(z)$ and the vertical ionization fraction profile $x_{\text{e}}(z)$.

Density Class II PPDs are assumed to be in hydrostatic equilibrium in the vertical direction to a very good approximation (no self-gravity, dominantly supported by thermal pressure). This means that the disk gas in vertical direction is hydrostatically stratified in both directions and therefore takes the expected form of a Gaussian profile $\rho(z) \propto \exp\left(-z^2/H_{\text{p}}^2\right)$, with the pressure scale height H_{p} describing the vertical extent of the disk (see e.g., Armitage et al., 2019). Deviations from this profile are occurring in either Class I disks (see Fig. 1.1), where the protostellar envelope is still accreting onto the disk, or in the presence of strong large-scale magnetic fields of comparable thermal and magnetic pressure (corresponding to a plasma-beta $\beta \sim 1$). In the latter case, magnetic compression leads to a much shallower Gaussian density profile in the disk surface layer, resulting in a more extended disk in vertical direction.

Temperature The central star irradiates the surrounding disk, heating the upper layers of a PPD. At the same time the disk also cools radiatively, which in the case of a purely passive disk (i.e., a disk without any other heating mechanism) would lead to an equilibrium between heating and cooling. Stellar irradiation can only penetrate the surface layers of a PPD, where the specific penetration depth is described by the optical depth τ_ν [2]. The optical depth depends on the opacity κ_ν, which in turn is dominated by the vertical distribution of dust in the disk. Additionally, complex thermochemical processes determine the abundance of certain molecules and atoms, further influencing κ_ν. This brief and incomprehensive outline of the processes involved in determining κ_ν and τ_ν demonstrates the complex models needed to adequately model the vertical thermal disk structure (see Fig. 1.10).

Over most of their radial extent protoplanetary disks are optically thick with respect to stellar irradiation ($\tau \gg 1$, see e.g., Armitage et al., 2019). In the case of high τ radiation cannot penetrate into the disk directly and is transported vertically through diffusion. The disk surface is irradiated by the central star at a certain incident angle (see Fig. 1.11) with a certain radiation flux F_{irr}, depending on the distance to the star r, the stellar radius $R_\star$ and the stellar luminosity $L_\star$. The radiation flux F_{irr} is then transported inwards by diffusion, heating up the gas within the disk. The heating rate per unit surface Γ determines how fast the gas in

[2] The subscript ν denotes the dependency of a quantity on the frequency and is commonly adapted in the scientific field of radiation transfer.

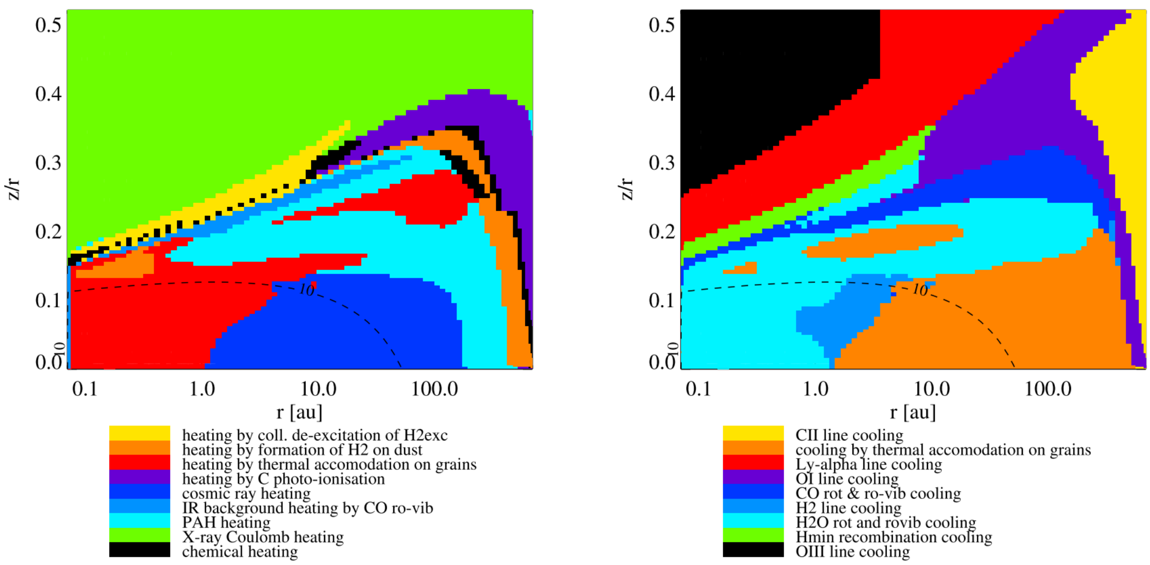

Figure 1.10: Illustration of the dominant heating and cooling sources in a PPD, which illustrates quite nicely the complexity of a detailed thermo-chemical model of the vertical disk. Credit: Reproduced with permission of first author, from Rab et al. (2016); Licensed under CC BY-4.0 (`https://creativecommons.org/licenses/by/4.0/deed.en`)

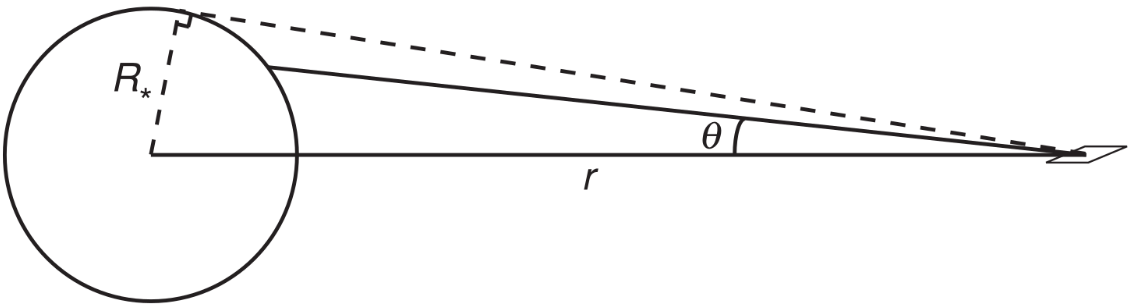

Figure 1.11: Depiction of the incident angle θ, at which a unit surface area is irradiated from a star with radius $R_\star$ at the distance r. Credit: Reproduced with permission of first author and Cambridge University Press through PLSclear from Armitage (2020).

the disk interior heats up and requires a description of the vertical radiation transport. At the same time energy is also transported from the disk interior outwards towards the disk surface and is radiated away. This requires a model of the vertical radiation transport and is denoted as the cooling rate per unit surface area Λ. In the case of an optically thick disk, the radiation flux in vertical direction $F(z)$ can be written as (see Dong et al., 2016),

$$\frac{dF(z)}{dz} = \rho(z)\, S(z) \;, \tag{1.4}$$

where S denotes the *source function*, which in our case depicts a yet unspecified, non-radiative heating rate per unit mass within the disk. In the case of a constant S (i.e., a constant heating rate at every height z) and assuming isotropic emission at the disk surface, we obtain the following description for Γ and Λ (see Dong et al., 2016),

$$\Gamma = \frac{4\,\tau_{\mathrm{P}}\,F_{\mathrm{irr}}/\sigma}{1 + 2\,\tau_{\mathrm{P}} + 3/2\,\tau_{\mathrm{R}}\,\tau_{\mathrm{P}}}\,, \tag{1.5}$$

$$\Lambda = \frac{4\,\tau_{\mathrm{P}}\,T^4_{\mathrm{gas},0}}{1 + 2\,\tau_{\mathrm{P}} + 3/2\,\tau_{\mathrm{R}}\,\tau_{\mathrm{P}}}\,, \tag{1.6}$$

$$\tau_{\mathrm{R}} = \frac{1}{2}\,\Sigma\,\kappa_{\mathrm{R}}\,, \tag{1.7}$$

$$\tau_{\mathrm{P}} = \frac{1}{2}\,\Sigma\,\kappa_{\mathrm{P}}\,, \tag{1.8}$$

where σ, $T_{\mathrm{gas},0}$, κ_{R} and κ_{P} denote the Stefan-Boltzmann constant, the gas temperature at the disk midplane, the *Rosseland mean opacity* and the *Planck mean opacity* (see e.g., Mihalas and Mihalas, 1984). Note that κ_{R} and κ_{P} encapsulate all the aforementioned complexity with respect to thermochemical modelling and are used in both Paper I and Paper II by adapting pre-compiled opacity tables (see Ferguson et al., 2005).

Viscously accreting PPDs are not only heated by stellar irradiation but also through viscous dissipation. Consequently, the source function S corresponds to the viscous energy dissipation rate per unit mass, which is dependent on the viscous properties and the dynamical evolution of the disk (see Sect. 1.2.2).

Ionization Magnetic fields only "feel" charged particles; therefore the ionization degree x_{e} in PPDs is an important quantity for describing magnetic field coupling to the gas. PPDs are either ionized thermally or non-thermally, where the latter includes ionization by cosmic rays (CR), far-ultraviolet radiation (FUV), X-ray radiation (XR), or radioactive decay of isotopes within the disk (see e.g., Armitage, 2020; Delage et al., 2022). Disk gas is not staying ionized indefinitely but is subject to recombination, either radiatively or because dust grains are sweeping up free electrons on their surfaces. Hence, ionization sources and their respective ionization rates are counterbalanced by recombination rates associated to these recombination mechanisms.

Thermal ionization dominantly happens in the very inner disk regions ($r \leq 1$ au) and is described by the *Saha equation*, enabling us to calculate the number densities of ions and electrons, n_{i} and n_{e}, respectively, for a gas with the total number density n in thermal equilibrium (see e.g., Armitage, 2020; Delage et al., 2022; Dudorov and Khaibrakhmanov, 2014),

$$\frac{n_{\mathrm{i}}\,n_{\mathrm{e}}}{n} = \frac{2\,U_{\mathrm{i}}}{U}\left(\frac{2\,\pi\,m_{\mathrm{e}}\,k_{\mathrm{B}}\,T_{\mathrm{gas}}}{h^2}\right)^{3/2}\exp\left\{-\frac{\chi}{k_{\mathrm{B}}\,T_{\mathrm{gas}}}\right\}. \tag{1.9}$$

The parameters U and χ denote the partition function and the ionization potential, respectively. The subscripts i and e specify the corresponding quantity for ions and electrons, respectively. Finally, the physical constants h and k_B depict the Planck constant and the Boltzmann constant, respectively. The Saha equation holds true separately for every atom species, which adds complexity when describing the thermal ionization profile in a disk in detail. This is because the abundances of all species in the disk gas would need to be known. Alkali metals have the lowest ionization potential χ and are therefore the first group of atoms to become ionized in the case of rising gas temperature (see e.g., Armitage, 2020). We can therefore make the simplification of using a mean ionization potential $\bar{\chi}$ and a mean relative abundance $\overline{n_\mathrm{i}/n}$, comprised of the most abundant alkali metals, to calculate the thermal ionization fraction (see e.g., Delage et al., 2022; Dudorov and Khaibrakhmanov, 2014, see also Paper II where we use Potassium as the only species with a fixed relative abundance of $n_\mathrm{i}/n = 10^{-7}$). Gas is dominantly thermally ionized close to the disk midplane (apart from the innermost region, where the disk is completely ionized). The explanation for this is that viscous heating is most effective in regions of high gas density, consequently leading to a larger effective viscous α (see e.g., Jankovic et al., 2021).

The surface layers of a disk are ionized by X-rays and FUV radiation originating from the central star. Most young stars in the center of PPDs can be classified as CTTS (see e.g., Williams and Cieza, 2011, see also Fig. 1.1), which show a highly elevated X-ray and FUV luminosity compared to main-sequence stars in the range between $10^{29} - 10^{31}\,\mathrm{erg\,s^{-1}}$ and therefore qualify as an effective non-thermal ionization source (see e.g., Feigelson and Montmerle, 1999). The most energetic part of the X-ray emission ($\sim 5 - 10$ keV) mostly

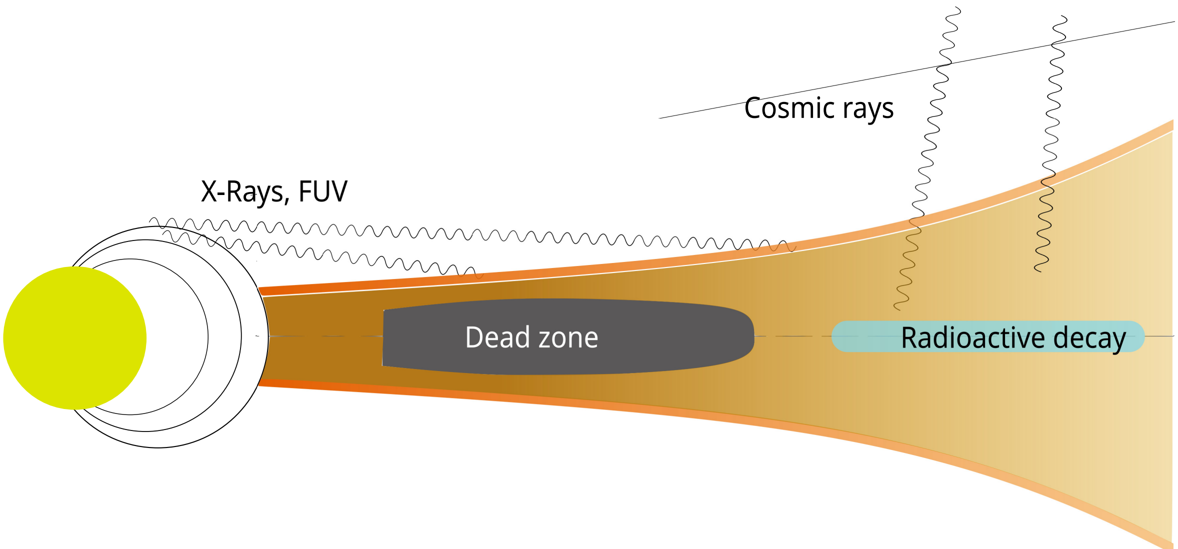

Figure 1.12: Illustration of various non-thermal ionization sources. Stellar X-rays and FUV radiation cannot penetrate deep into the disk interior, in contrast to cosmic rays, which are able to penetrate much deeper. In the disk interior radioactive decay provides a base level of ionization, regardless of other ionization sources.

originates from the magnetized corona of T Tauri stars and can penetrate into the disk down to a surface density of the order of $\sim 10\,\mathrm{g\,cm^{-2}}$ (see e.g., Armitage, 2020). Over most of the radial extent of a typical PPD this means that X-ray only penetrate into a thin surface layer (see Fig. 1.12).

CRs penetrate much deeper into the disk ($\sim 10^2\,\mathrm{g\,cm^{-2}}$, managing to even reach the midplane in the outer disk. At smaller disk radii, PPDs are typically dense enough to deny CRs to reach the deeper disk layers, effectively preventing non-thermal ionization. Such very weakly ionized regions are denoted as *dead zones* (DZ, see e.g., Umebayashi and Nakano, 1981, see also Fig. 1.12). The importance of CRs in ionizing PPDs is not undisputed. These doubts arise from the large uncertainties in modeling the CR ionization rate, caused by an incomplete picture of the influence of stellar winds. These outflows are able to completely shield CRs from entering the disk (see e.g., Cleeves et al., 2013).

Finally, radioactive decay is mostly dominated by the decay of $^{26}\mathrm{Al}$, which has a half-life of ~ 0.7 Myrs and therefore is shorter than the usual lifetime of a disk (a few Myrs). Consequently, the ionization rate from radioactive decay significantly reduces over the lifetime of a disk (see e.g., Armitage, 2020).

As mentioned above, recombination either occurs when ions capture an electron and radiate away the excess energy (radiative recombination, see Spitzer, 1978), or when electrons stick to the surfaces of dust grains (dust recombination, see e.g., Vorobyov et al., 2020). Radiative recombination requires at least one electron per ion and therefore is, in the case of singly ionized atoms, proportional to x_e^2, whereas dust recombination linearly scales with the number of free electrons ($\propto x_\mathrm{e}$). These dependencies lead to the following balance between the ionization rate (thermal + non-thermal) ξ and the recombination rates:

$$(1 - x)\,\xi = \alpha_\mathrm{r}\, x_\mathrm{e}^2\, n + \alpha_\mathrm{d}\, x_\mathrm{e}\, n\ , \tag{1.10}$$

where α_r and α_d are the radiative and dust recombination rates, respectively (see e.g., Vorobyov et al., 2020, in this form used in Paper II).

The ionization fraction obtained from Eq. (1.10) should be considered as a crude estimate of x_e. A detailed model requires a chemical model of many molecular species: In a realistic disk dissociative recombination occurs, where an ionized molecule is dissociated into at least two other neutral molecules by capturing an electron. Dissociative recombination is often neglected, since dust recombination occurs very fast, whereas radiative recombination happens significantly slower. Therefore, dust and radiative recombination provide a lower and upper limit to x_e, respectively. Nevertheless, dissociative recombination has a timescale shorter than radiative recombination, and is therefore able to alter the available electron fraction (see e.g., Armitage, 2020; Dudorov and Khaibrakhmanov, 2014).

1.2.2 Disk evolution and angular momentum transport

PPDs are dynamic structures and therefore cannot be fully described by defining their structure only (see Sect. 1.2.1). In fact, disks are rotationally supported accretion disks, in which angular momentum is redistributed radially or is lost, leading to disk gas slowly drifting radially inwards. The mechanisms causing this angular momentum loss are among the fundamental problems in describing the long-term evolution of disks.

Molecular viscosity inherent to the disk gas is not able to explain mass transport rates expected by observations (see e.g., Balbus and Hawley, 1998). This caused the search for alternative physical processes capable of angular momentum transport. Some mechanisms have been found, which mostly depend on the development of turbulence in the disk gas. Alternatively, also large-scale magnetic fields can transport angular momentum away from the disk. Interestingly, many of the found mechanisms are confined to specific disk regions, both radially and vertically, and are dependent on gas properties such as density, temperature, strength of a magnetic field, and the ionization degree (see e.g., Armitage, 2020).

Regardless of the specific angular momentum mechanism, a dimensionless α-viscosity parameter (also called Shakura-Sunyaev α, see Shakura and Sunyaev, 1973) can be defined, which is used to describe the effective viscosity ν,

$$\nu = \alpha \, c_\mathrm{s} \, H_\mathrm{p} \, , \tag{1.11}$$

where c_s denotes the speed of sound. Subsequently, we want to review some angular momentum loss mechanisms present in PPDs during its evolution.

Gravitational instabilities (GI) During the early evolution of PPDs, the gas envelope of the enclosing cloud is still falling onto the disk (see Fig. 1.1), resulting in a more massive disk (compared to later Stage I/II disks). Hence, parts of these disks can become gravitationally unstable, resulting in the formation of vortices in the outer disk (see e.g., Vorobyov, 2010; Vorobyov and Basu, 2007).

The *Toomre criteria* (Toomre, 1964) is a condition describing if an astronomical object can become gravitationally unstable. In the case of PPDs it reads as,

$$Q = \frac{\Omega \, c_\mathrm{s}}{\pi \, G \, \Sigma} < Q_\mathrm{crit} \tag{1.12}$$

where Q, G and c_s denote the Toomre parameter, the gravitational constant, and the speed of sound, respectively. Q_crit is the critical Toomre parameter below which a portion of a PPD becomes gravitationally unstable and whose value is typically taken to be slightly above unity (see e.g., Vorobyov and Basu, 2007).

High Σ and low Ω facilitate the development of GI, which is also verified in global simulations of massive disks (see e.g., Dong et al., 2018; Vorobyov and Basu, 2007; Vorobyov and Pavlyuchenkov, 2017). In those simulations most vortices develop in the outer disk and then migrate inwards over time. These vortices are mostly localized in the disk and are non-axisymmetric. However, various authors have developed formulations of $\alpha_{\rm GI}$, expressing the effective viscosity (analogously to the Shakura-Sunyaev-α) (see e.g., Lin and Pringle, 1987; Schib et al., 2021). $\alpha_{\rm GI}$ lies in the range between $\sim 10^{-3}$ and 10^{-1}, depending on the used formulation for $\alpha_{\rm GI}$ and the exact value of $Q_{\rm crit}$.

Magnetorotational instability (MRI) MRI can develop in a differentially rotating disk with a magnetic field present. The mathematical, detailed description is complex and beyond the scope of this work (see Balbus and Hawley, 1991). However, the basic idea is that an instability develops, which can be viewed as a spring connecting faster rotating, slightly ionized gas in an inner disk ring, to slower rotating gas further outwards via a magnetic field. This results in the gas further inwards braking and therefore transferring angular momentum to the gas in the outer, slower rotating ring. The gas in the outer ring accelerates, which is equivalent to radial outward-directed angular momentum transport. The effectiveness of MRI depends on various factors, such as the ionization degree and the magnetic field strength and can range between 10^{-3} and 10^{-1} (see e.g., Bai and Xue-Ning, 2014; Delage et al., 2022; Lubow et al., 1994; Mohanty et al., 2018; Vorobyov et al., 2020).

The dependency of MRI on the ionization degree has raised some concerns lately about its effectiveness throughout the disk. Stratified shearing-box simulations show that MRI is largely subdued in disk regions where non-ideal MHD effects occur (i.e., ambipolar diffusion and Hall effect; non-ideal MHD effects are briefly reviewed below in Sect. 1.2.4). Hence, the regions most likely to develop MRI are the thermally ionized innermost disk regions and the disk surface layer, which has a higher ionization degree due to non-thermal ionization mechanisms (see e.g., Delage et al., 2022; Mohanty et al., 2018; Vorobyov et al., 2020). Interestingly, stratified 3D-MHD shearing-box simulations show that MRI can also develop in disk regions with strong ambipolar diffusion, but with reduced efficiency (see e.g., Bai and Stone, 2011).

Thermo-hydrodynamical instabilities GI predominantly occurs in massive disks early-on during disk evolution (Stage 0/I), whereas MRI is mostly active in the surface layers of disks and in the innermost, thermally ionized disk of Class II systems. However, MRI is not efficient in large parts of the disk, which motivated the search for alternative angular momentum redistribution mechanisms in disks. As a result, three, as of then unnoticed, hydrodynamical instabilities have gained growing attention: (i) The *Vertical Shear Instability*

(VSI), (ii) the *Convective Overstability (COS)* and (iii) the *Zombie Vortex Instability (ZVI)* (see the review of Lesur et al. (2022)). To determine where in the disk these instabilities are most likely to occur, the gas cooling timescale $\tau_{\rm cool}$ is used: For the VSI $\tau_{\rm cool}$ has to be much shorter than the dynamical timescale $1/\Omega(r)$, whereas for the COS to develop it suffices that $\tau_{\rm cool} \approx 1/\Omega(r)$. Finally, the ZVI develops when the condition $\tau_{\rm cool} \gg 1/\Omega(r)$ is met. Typical Shakura-Sunyaev α parameters for VSI, COS, and ZVI are of the order of $\sim 10^{-4}$, $\sim 10^{-3}$ and $\sim 10^{-5} - 10^{-4}$, respectively (see e.g., Barranco and Marcus, 2005; Lesur et al., 2022).

Torques from magnetically induced winds The aforementioned mechanisms (MRI, GI) result in radially outwards directed angular momentum transport. By contrast, outflows from a disk can also extract angular momentum (in addition to the obvious removal of mass), when connected to a large-scale field threading the disk (see e.g., Bai and Stone, 2013; Blandford and Payne, 1982; Guilet and Ogilvie, 2014; Lesur, 2021; Lubow et al., 1994). There are two basic physical mechanisms able to drive such an outflow:

- *Magnetocentrifugally driven wind (MCW)*: The upper layer of a PPD is sufficiently well ionized due to non-thermal ionization processes. If a large-scale field is present, it therefore couples to the gas at the disk surface to enforce corotation with the disk at $\Omega(r)$. In the case of outward-bent magnetic field lines, gas flowing along the magnetic field is magnetocentrifugally accelerated (assuming a rigidly rotating field, see Fig. 1.13). The minimum inclination angle i for cold gas to overcome the gravitational barrier without any heating is 30° (see e.g., Blandford and Payne, 1982; Lubow et al., 1994; Spruit, 1996). The gas accelerated to supersonic speeds along the magnetic field lines until it reaches the Alfvénic surface, where the gas reaches super-Alfvénic speed. Above that surface the rigidity of the magnetic field cannot be assumed any further and the field lines wind up by the inertia of the outflowing gas. This means that beyond the Alfvénic surface no more angular momentum can be transported by a MCW (see e.g., Spruit, 1996). Mass-loading along the field lines leads to the development of a toroidal field component B_φ, which produces a torque acting on the disk, braking the gas and removing angular momentum from the disk. The magnetic torque $T_{\rm m}$ is calculated as follows (see e.g., Armitage, 2020),

$$T_{\rm m} = \frac{B_{\rm z}\, B_\varphi^{\rm s}}{2\,\pi}\, r \,, \tag{1.13}$$

  where $B_{\rm z}$ is the vertical field component and the superscript "*s*" denotes the corresponding quantity at the disk surface. An important factor in determining the possibility and strength of MCWs is the magnetic field topology of the large-scale field (i.e., the inclination angle i and the magnetic field strength), which is discussed in Sect. 1.2.4 and which is also the central topic of Paper II.

- *Magneto-thermal winds:* Outflows from the disk can also be driven by photoevaporation (Ercolano and Pascucci, 2017; Owen, 2016, see e.g.,). In this case, high-energy radiation from the star leads to photo-electric heating of the disk surface layers to the point where thermal pressure suffices to allow gas to become gravitationally unbound. Photoevaporative winds are not transporting angular momentum away from the disk, as long as there are no large-scale fields involved. However, in the presence of a large-scale field, the evaporated gas couples to the magnetic field and therefore leads to angular momentum loss. In the case of neither magnetocentrifugal acceleration nor photoevaporation succeeding to launch an outflow on their own, it is possible that the combination of both effects leads to enough acceleration to launch a wind (see e.g., Bai et al., 2016; Spruit, 1996). In this scenario a large-scale field is present with an insufficiently inclined field to launch an outflow on its own. However, thermal pressure due to heating of the upper disk layers is lifting material to the point where the gas is magnetocentrifugally accelerated. The key parameter for magneto-thermally driven winds is the large-scale magnetic field topology (i.e., the inclination and strength of the field lines at the disk surface; see Sect. 1.2.4).

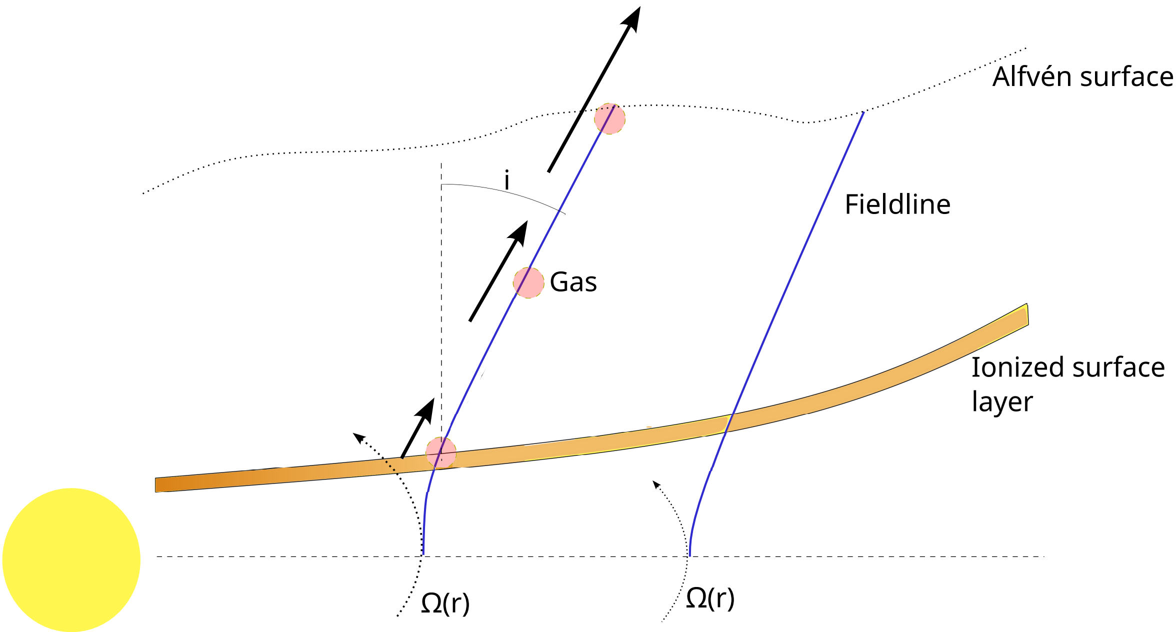

Figure 1.13: Illustration of the principle of magnetocentrifugal acceleration. A gas package (red circle) couples to a magnetic field line with an inclination angle i with respect to the midplane normal. The field lines (blue lines) are rotating rigidly with the gas with $\Omega(r)$. Rigidity of the field lines is assumed up to the Alfvén surface. The gas is lifted up along the field line and further accelerates.

There is an ongoing effort to answer where in PPDs magneto-thermal and magnetocentrifugal winds are launched, how strong those outflows are, and in which way MCWs affect the long-term evolution of PPDs (see e.g., Bai and Stone, 2017; Lesur, 2021). No conclusive answer has been found yet; two of the main challenges are: (i) a global long-term disk evolution simulation of both disk and large-scale field is numerically very challenging, especially in the inner disk region (see Sect. 5.2), and (ii) the determination of the large-scale field topology is dependent on the vertical and radial disk structure (see Sect. 1.2.1). Moreover, MCWs also significantly alter the dynamical evolution of disks, resulting in changes to the field topology. Hence, the disk and the large-scale magnetic field depend non-linearly on each other (see e.g., Campbell and G., 1999; Cui and Bai, 2021; Lubow et al., 1994; Suzuki et al., 2016).

1.2.3 The influence of a stellar magnetic field on the inner disk

The innermost disk region ($r < 0.1$ au) is an important region for several reasons: (i) the accretion onto the star is determined in this region, often dominated by a strong stellar magnetic field (see e.g., Romanova and Kurosawa, 2014); (ii) stellar irradiation leads to high temperatures in the inner disk, which may triggers episodic accretion (see e.g., Bell and Lin, 1994; Zhu et al., 2009, see also Paper I); (iii) the radial density profile of PPDs is strongly dependent on the mass transport rate $\dot{M}$ in the innermost disk region (see e.g., Vorobyov et al., 2019). For these reasons the study of the inner disk has gained large interest, both from an observational and a modeling perspective (see e.g., Hartmann et al., 2016).

Generally, gas is transported by some angular momentum transport mechanism (see Sect. 1.2.2) into the innermost disk region. There the accretion flow is redirected at a certain radius into magnetic funnels along stellar magnetic field lines. The typical magnetic field strength of a CTTS lies in the range between ~ 0.1 kG and $\sim$ 2kG (see e.g., Donati et al., 2018; Johnstone et al., 2014), which is sufficiently strong to disrupt the disk at a few stellar radii, defining the so-called *magnetic truncation radius* r_{t}.

r_{t} determines how far inwards the disk can extend, which is important, because the closer the disk is to the star, the more it is heated up. High temperatures can trigger instabilities such as the so-called *thermal instability (TI)*, or the onset of MRI in deeper disk layers. As a result, episodic accretion events occur, during which the accretion rate and luminosity of the star-disk system are significantly enhanced for short periods in time (see e.g., Bell and Lin, 1994; Vorobyov and Pavlyuchenkov, 2017; Vorobyov et al., 2019; Zhu et al., 2009). Thus, we subsequently also revisit the mechanisms leading to TI or to the onset of MRI in deeper disk layers.

Magnetic disk truncation Disk gas transported increasingly closes towards the star is eventually disrupted and redirected into magnetic funnels at a certain radius. An appropriate model describing this inner disk truncation requires a description of the stellar magnetic field structure of a T Tauri star. Typically, the magnetic field is approximated as dipolar field, threading the innermost disk region (see e.g., Donati et al., 2007). Note that the assumption of a dipolar field is an over-simplification in many cases (see e.g., Gregory et al., 2008); however, the dipole component of a stellar magnetic field dominates at increasingly larger distances from the star, therefore the essentials of magnetic truncation can be reproduced with a dipole (also used to model the stellar field in Paper I and Paper II). The disk gas can effectively be redirected to follow magnetic field lines, if the ram pressure P_{ram} of the gas accreting inwards is comparable to the magnetic pressure P_{m} of the stellar field. Assuming a dipolar stellar field, the truncation radius r_{t} reads as (see e.g., Hartmann et al., 2016),

$$r_{\mathrm{t}} = \xi \left(\frac{B_\star^4 \, R_\star^{12}}{2 \, G \, M_\star \, \dot{M}^2} \right)^{1/7} , \tag{1.14}$$

where G, $M_\star$, $B_\star$, and $R_\star$ denote the gravitational constant, stellar mass, stellar surface magnetic field strength, and the stellar radius, respectively. The factor ξ parametrizes the complexity of magnetospheric accretion, which in reality is a highly dynamic and complex process. Detailed 3D-MHD models of e.g., Romanova and Kurosawa (2014); Romanova et al. (2011); Zhu et al. (2024) show that magnetospheric accretion is a non-axisymmetric process (see Fig. 1.14). Magnetic reconnection and magnetospheric ejections and outflows can add further complexity (see Fig. 1.14) and are all accounted for by the factor ξ in the simple model described by Eq. (1.14).

Detailed simulations of magnetospheric accretion are not feasible in long-term evolution models for PPDs due to the enormous computation cost of such simulations. Hence, we compare the simple model for r_{t}, as described in Eq. (1.14), to 3D-MHD simulation of the star-disk connection (see e.g., Romanova and Kurosawa, 2014) for verifying its validity. Bessolaz et al. (2008) compare analytical estimates for r_{t} against axisymmetric 2D-MHD simulations. They show that the truncation radius in their simulations is very close to the point where the magnetic plasma $\beta \approx 1$, which is approximately at the point where magnetic funnels are anchored in the innermost disk. Bessolaz et al. (2008) concluded that with $\beta \approx 1$, the factor ξ in Eq. (1.14) can be estimated as $\xi \approx \mathcal{M}_{\mathrm{s}}^{2/7}$, where $\mathcal{M}_{\mathrm{s}}$ denotes the Mach number of the accretion flow at the disk midplane. This relates to a value of ξ between 0.5 and 0.8.

Episodic accretion Photometric observations of T Tauri stars have revealed that almost all CTTS exhibit variable light curves (see e.g., Herbst et al., 1994). These changes in luminosity can be caused by unrelated mechanisms, such as time-dependent accretion, extinction, or less luminous features on the surface of those stars (analogously to sunspots). We want to focus on the mechanisms, which are caused by variations of the accretion rate, as these are the most relevant in the context of this thesis. Subsequently, we want to summarize the three most

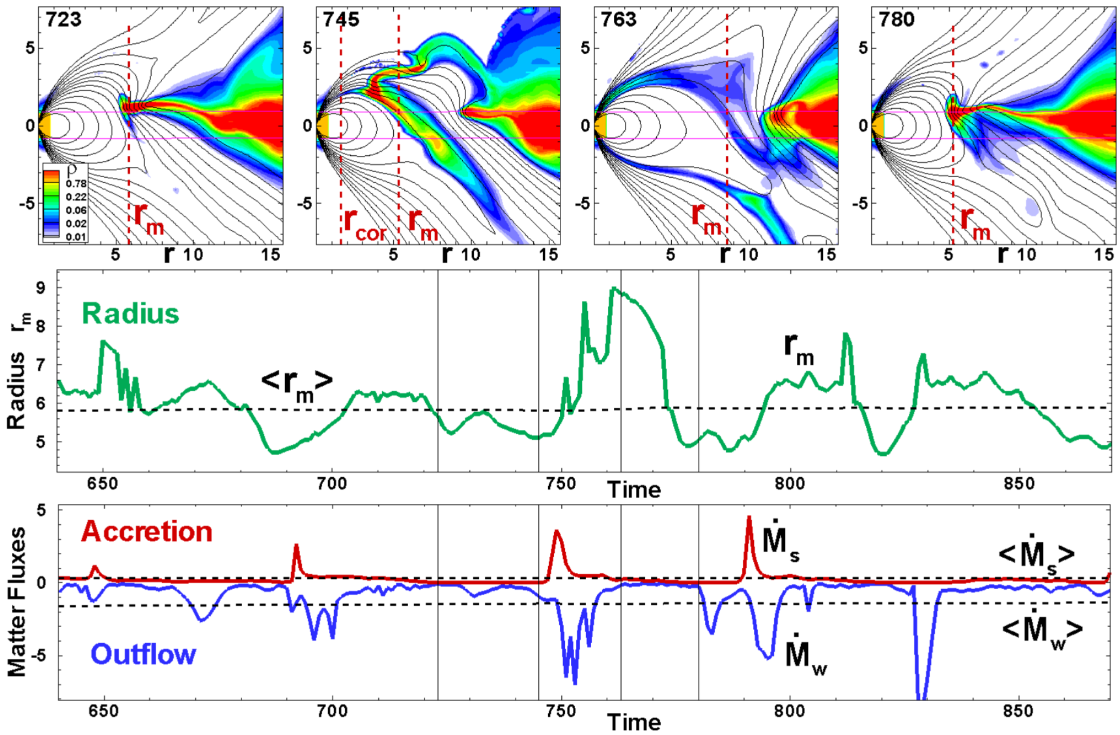

Figure 1.14: Magnetospheric accretion onto a T Tauri star with a strong magnetic field. The number in the upper four panels denotes the time in rotation cycles, whereas r_{m} and r_{cor} denote the magnetospheric truncation radius (denoted as r_{t} in main text) and the corotation radius, respectively. The middle panel shows that r_{t} also varies with time, and the lower panel reveals that not only material is accreted but also outflows can occur (also see second and third chart in upper row). Credit: Reprinted from Romanova et al. (2018), with permission from Elsevier; Permission conveyed through Copyright Clearance Center, Inc.

common sources of such variations in luminosity:

- *Irregular short-lived variations:* These variations are probably caused by time-dependent magnetospheric accretion due to unstable accretion along magnetic funnels and occur on short timescales (see e.g., Romanova and Kurosawa, 2014, see also Fig. 1.14). They originate either from Rayleigh-Taylor instabilities or from newly forming (or disappearing) accretion funnels (see e.g., Blinova et al., 2016; Kurosawa and Romanova, 2013). The frequency of these variations ranges from $\sim 1\,\mathrm{day}^{-1}$ to $\sim 0.3\,\mathrm{day}^{-1}$ (see Hartmann et al., 2016).

- *EXor outbursts:* These outbursts are named after EX Lup, the first observed star-disk system showing this type of episodic accretion (Herbig, 1977). They are characterized by an increase of the accretion rate by a factor of $\sim 10-100$ over a typical period of a few months (see e.g., Aspin et al., 2010). This relatively short timescale indicates that EXor outbursts likely originate in the innermost disk. Additionally, Banzatti et al. (2015) argue that their observations of EXor outbursts can be explained by an increased surface density in the innermost disk. One possible explanation is that, during the quiescent phase, accretion is reduced due to r_t being located outside the corotation radius r_{cor} (see D'Angelo and Spruit, 2010). As a result, material outside r_{cor} getting accelerated by the stellar dipole (assuming a rigidly rotating stellar dipole), which in turn counteracts viscous accretion. This leads to a slow buildup of material close to the corotation radius until the increasing gas pressure gradient pushes r_t inside r_{cor}. As soon as this happens, material inside r_{cor} is decelerated and material begins to fall towards the star, resulting in an outburst.

- *FU Ori outbursts:* FU Ori outbursts are characterized by a large and sudden increase in luminosity of many magnitudes. Outbursts typically last between 10 and 100 years, whereas the quiescent phase between two outbursts is significantly longer (10^3 – 10^4 years, see e.g., the review of Audard et al., 2014). The reason for those outbursts is a significant and sharp increase in the accretion rate up to $\dot{M} \sim 10^{-5}\,\mathrm{M_\odot\,yr^{-1}}$, in contrast to $\dot{M}$ of $\sim 10^{-8} - 10^{-7}\,\mathrm{M_\odot\,yr^{-1}}$ in the quiescent phase (see e.g., Audard et al., 2014; Hartmann et al., 2016). The increase in $\dot{M}$ is caused by either TI, or a combination of TI and MRI activation in deeper disk layers, depending on the mass and accretion rate in the disk.
  TI develops when hydrogen is ionized, which happens at a temperature $T \approx 5000$ K (see e.g., Zhu et al., 2009), leading to a sudden increase in opacity. As a result, the disk heats up even further, resulting in a runaway of heating and ionization. An ionization front develops, which propagates radially outwards and ionizes more gas along its path (see e.g., Bell and Lin, 1994; Zhu et al., 2009). The ionized and very hot gas has a large Shakura-Sunyaev-α of $\sim 0.1 - 1$ and therefore causes the ionized gas to rapidly accrete onto the star, essentially emptying the inner disk during this phase. A decreasing surface density in the outer disk eventually leads to an offset of the ionization front, allowing colder gas from the outer disk to be transported inwards again. Material flows into the inner disk until the gas becomes hot enough to trigger TI again, hence resulting in the start of a new cycle.

The problem TI has in the context of PPDs is the requirement of very high temperatures of ~ 5000 K to operate. Such high temperatures are only possible in the inner disk region of massive Class 0/I (maybe very early Class II) disks with an envelope still accreting onto the disk (see e.g., Kadam et al., 2020). However, observations of CTTS with relatively low-mass disks in their (late) Class II stage have also shown light curves indicating FU Ori-like outbursts (see e.g., the observations of *HBC 722*, see Kóspál et al., 2016).

The layered-accretion model of Gammie (1996) is able to come to the rescue in resolving this issue. They propose that MRI cannot be sustained everywhere, i.e., only layers sufficiently well ionized are MRI-active. As a consequence, MRI is only active in the innermost disk region with sufficiently high temperatures and in the surface layers of the outer disk (see paragraph on ionization of Sect. 1.2.1). As a result, a DZ with a strongly decreased viscous $\alpha \approx 10^{-5} - 10^{-4}$ forms within the disk and which is centered around the midplane. Gas from the outer disk layers is transported inwards either by MRI or GI, until it reaches the DZ. There the disk gas accumulates, resulting in an increase of Σ and T until thermal ionization causes MRI to operate also in deeper disk layers. As a result, α increases abruptly and leads to a largely increased accretion rate $\dot{M}$. During this violent accretion phase a lot of accretion energy is released in the form of radiation (accretion luminosity). This results in further heating and can cause TI to be triggered on top of the onset of MRI in deeper disk layers, leading to even stronger outbursts (see e.g., Zhu et al., 2010, see also Paper I, where MRI instability causes episodic accretion).

1.2.4 Large-scale magnetic fields

Magnetic fields probably play a fundamental role in describing the evolution of PPDs. On small scales, these fields may allow for the development of MRI under certain conditions (see Balbus and Hawley, 1991, see also paragraph 'Magnetorotational instability' in Sect. 1.2.2). Large-scale fields, however, thread the disk over its full extent and can extract angular momentum via magnetocentrifugally or magneto-thermally driven outflows (see paragraph 'Torques from magnetically induced winds' in Sect. 1.2.2). In this section we focus on the key aspects of a model describing large-scale fields and their evolution over the lifetime of a PPD. First, we briefly distinguish between two different theories regarding the origin of large-scale fields:

- *Self-excited dynamo:* In the presence of an arbitrarily weak seed magnetic field, the disk may generate and maintain a large-scale magnetic field within itself via amplification of the seed field by a dynamo process (see e.g., Pudritz, 1981; Stepinski and Levy, 1991). Such a dynamo-powered field is theoretically strong enough to support the launching of a magnetically induced outflow; however, due to its closed field configuration it is almost impossible for an outflow to actually leave the disk (Konigl and Pudritz, 2000). It is worth noting that with modifications, such as the addition of weak external fields, an open large-scale field topology can be constructed, enabling magnetically induced outflows from a dynamo-generated disk field (see e.g., Moss and Shukurov, 2004).
- *External large-scale magnetic field:* In the case of an interstellar large-scale field threading an interstellar cloud, a collapsing cloud core drags the field inwards. This leads to an amplification of the large-scale field and to an open field configuration,

resembling an hour-glass shape (see e.g., Konigl and Pudritz, 2000). Core collapse simulations have revealed that the strength of the vertical large-scale field component saturates at about ~ 0.1 G for radii $r \lesssim 1-5$ au, which is due to the onset of AD above a certain density threshold of $n \sim 10^{11}\,\mathrm{cm}^{-3}$ (see e.g., Masson et al., 2016; Xu and Kunz, 2021, see also Fig. 1.15). As the disk evolves from Class 0/I to Class II, most of the during core collapse accumulated magnetic flux is lost once more due to non-ideal diffusion effects, stabilizing at a magnetic field strength of ~ 1 mG at a radius $r \sim 10$ au (Mauxion et al., 2024). This result is consistent with observed magnetic field strengths in late Class II disks (see Sect. 1.1.4).

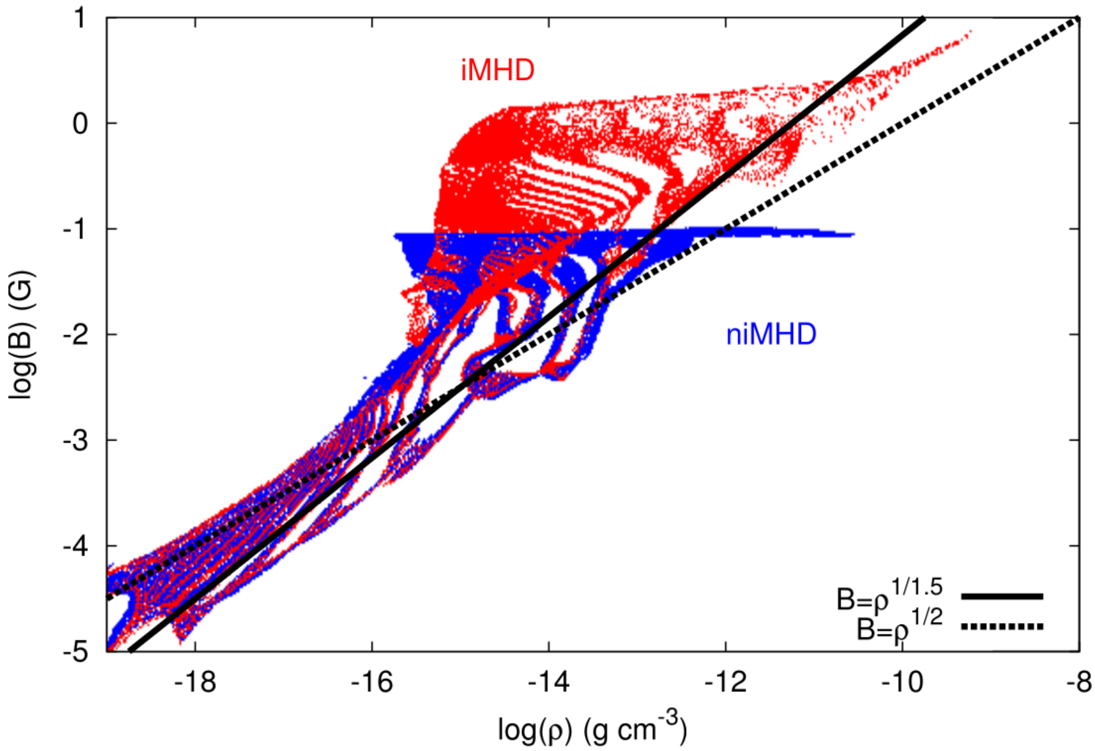

Figure 1.15: Core-collapse simulations of a core with a prescribed initial magnetization 200 years after the protostellar core has formed. The solid and dashed black line show power-law dependencies on the magnetic field on the density, $B \propto \rho^{2/3}$ and $B \propto \rho^{1/2}$, respectively. The red lines represent simulations in the ideal MHD limit, whereas the blue lines show the simulations including non-ideal effects. Credit: Reproduced with permission of first author, from Masson et al. (2016); Reproduced with permission © ESO.

We limit the subsequent review of large-scale magnetic fields to the scenario of an external large-scale magnetic field. This case is preferred by most authors as it leads to an open field configuration. This is due to magnetic advection and magnetic diffusion balancing each other for a certain field configuration, allowing the launch of magnetically induced outflows (see e.g., Konigl and Pudritz, 2000; Lubow et al., 1994). This way the obtained field configuration resembles the earlier mentioned shape of an hour-glass, and requires the radial field component to change sign in the midplane (see e.g., Dudorov and Khaibrakhmanov, 2014; Lubow et al., 1994). The ionization degree of the gas, x_e, is a key parameter in

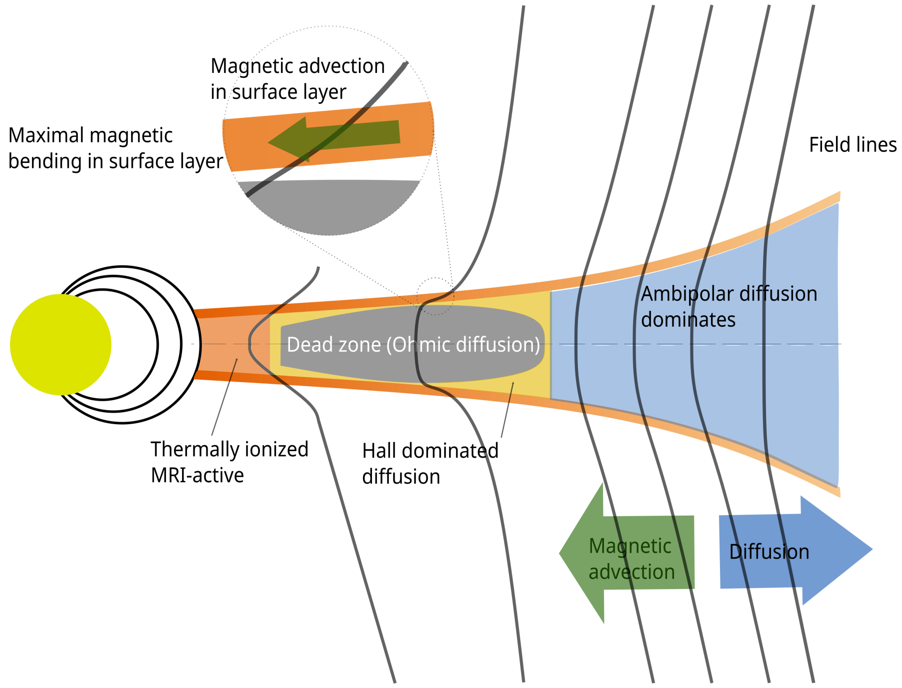

Figure 1.16: Schematic representation of the advection-diffusion mechanisms for the evolution of large-scale magnetic fields. In the innermost disk ($r < 0.1$ au) thermal ionization enables effective MRI and therefore bending occurs mainly in the midplane. In the radial region of the DZ magnetic advection predominantly happens in the surface layers, whereas in the outer disk MRI can operate again in a reduced state and magnetic field bending occurs again in the inner disk layers. Diffusion always counterbalances magnetic advection, which eventually leads to an equilibrium state for the large-scale field. For a better overview the dominant non-ideal diffusion processes are also shown.

describing magnetic diffusion. It typically depicts the fraction of free electrons with respect to neutral atoms (see e.g., Delage et al., 2022; Mohanty et al., 2018, see also Sect. 1.2.1). In addition to turbulent diffusion, three laminar, non-ideal MHD diffusion processes exist; (i) *Ohmic diffusion (OD)*, (ii) *ambipolar diffusion (AD)*, and (iii) the *Hall effect (HE)*. Magnetic diffusion quantifies how well a magnetic field can slip through the gas and are therefore important for the determination of the large-scale field topology. Turbulent diffusion as well as laminar, non-ideal MHD effects are briefly reviewed in the subsequent paragraph 'Non-ideal MHD diffusion processes'.

Magnetic flux transport is most effective in regions of low magnetic diffusion, which are located in disk regions of an elevated ionization degree (see e.g., Delage et al., 2022). This is the case for the disk surface layers (see e.g., Lesur, 2021, see also Fig. 1.16) as well as thermally ionized regions (in the innermost disk close to the midplane, see e.g., Dudorov and Khaibrakhmanov, 2014; Mohanty et al., 2018, see also Fig. 1.16 and Paper II). In regions of low magnetic diffusion magnetic flux can be transported radially inwards effectively, resulting in layered magnetic accretion over most of a disk's radial extent (see e.g., Delage et al., 2022; Lesur, 2021). By contrast, the DZ has a high diffusivity due to a very low x_e, leading to very inefficient magnetic flux transport.

The outer disk is dominated by AD (Bai and Stone, 2011; Delage et al., 2022; Dudorov and Khaibrakhmanov, 2014); however, simulations performed by Bai and Stone (2011) show that MRI still develops in an AD-dominated regime, even though at reduced efficiency (see the subsequent paragraph 'Non-ideal MHD diffusion processes').

Non-ideal MHD diffusion processes: Magnetic diffusion is caused by microphysical processes in the disk gas, which have their origin either in turbulence or in non-ideal coupling of gas and magnetic field. These differences in the origin allow for a broad categorization: turbulent diffusion and non-ideal, laminar MHD effects.

Turbulent diffusion, on a microscopic level, is the constant reconnection and reordering of chaotic and turbulent small-scale field distortions due to turbulent gas, resulting in macroscopic diffusion of the corresponding large-scale field (see e.g., Wardle, 2007). MRI has its origin also in turbulence, which strongly suggests a comparable magnitude between turbulent α-viscosity (see Magnetorotational Instability (MRI) of Sect. 1.2.2) and turbulent diffusion. The *Magnetic Prandtl number* $\mathcal{P}$ accounts for that by relating α and the turbulent resistivity η_t (see e.g., Guilet and Ogilvie, 2012, see also Lubow et al. (1994), but note that they have redefined $\mathcal{P}$ as its inverse). It reads as,

$$\mathcal{P} \equiv \frac{\nu}{\eta_t} = \frac{\alpha\, c_s\, H_p}{\eta_t}\,, \tag{1.15}$$

where ν and c_s are the kinematic viscosity and the speed of sound, respectively. ν and η_t are likely to be comparable in magnitude, yielding $\mathcal{P} \approx 1$ (see e.g., Guilet and Ogilvie, 2012; Lubow et al., 1994). η_t is rarely the dominant diffusion process (apart from the innermost disk region, where MRI is operating at maximum efficiency) and only plays a minor role in PPDs (see e.g., Dudorov and Khaibrakhmanov, 2014; Khaibrakhmanov, 2024).

The efficiency of all laminar, non-ideal diffusion processes depends on the relative abundances of neutral gas, ions, and electrons as well as on the magnetic field strength. Two microphysical processes are causing non-ideal laminar diffusion: the relative drift between (i) charged particles and neutrals, and (ii) ions and electrons. The *Hall parameter* β_j provides a measure of the magnetic coupling of a species j (either ion species or electron) in a gas with a certain density.

The value of β_j determines, if electric and/or magnetic forces suffice for a particle of species j to follow the magnetic field motion, or if collisions with neutrals lead to decoupling from the magnetic field. More specifically, $\beta_\mathrm{j} \gg 1$ means that charged particles of species j are well coupled to the magnetic field. By contrast, $\beta_\mathrm{j} \ll 1$ states that collisions with neutrals dominate the particle's trajectory and magnetic coupling cannot be maintained. β_j has the following dependencies (for an in-depth explanation see e.g., Wardle, 2007),

$$\beta_\mathrm{j} \propto B\,(\gamma_\mathrm{i}\,\rho)^{-1}\,m_\mathrm{j}^{-1}\ , \tag{1.16}$$

where B, m_j and $\gamma_\mathrm{i}\,\rho$ are the large-scale magnetic field strength, the atomic mass of species j, and the frequency of species j colliding with neutrals, respectively. Eq. (1.16) shows that $\beta_\mathrm{i} \ll \beta_\mathrm{e}$ due to $m_\mathrm{i} \gg m_\mathrm{e}$, with subscripts '$e$' and '$i$' denoting electrons and ions, respectively. The physical explanation behind this statement is that ions collide more often than electrons due to their difference in size. As a result, ions decouple much easier from the magnetic field than electrons.

OD is the relative drift of all charged particles with respect to the bulk of the gas without the need for a magnetic field exerting a force. The relative drift of charged particles is caused by an electric field, which exists in the case of finite conductivity σ and non-uniformly distributed charged particles. For OD to be efficient, both β_e and β_i have to be small, otherwise the charged particles would couple to a magnetic field to a certain degree.

Multiple-charged ions (classified by the charge number Z_j) couple stronger to an electric field. Moreover, a larger number density of charged particles n_j leads to higher conductivity. Combined, this leads to the following form of the Ohmic conductivity σ_O (see e.g., Mohanty et al., 2018; Wardle, 2007),

$$\sigma_\mathrm{O} = \frac{e\,c}{B}\sum_j n_\mathrm{j}\,|Z_\mathrm{j}|\,\beta_\mathrm{j}\ , \tag{1.17}$$

where e and c denote the electron charge and the speed of light, respectively. Note that σ_O is independent of the magnetic field strength (see B-dependency in Eq. (1.16)). Finally, OD η_O, is proportional to $1/\sigma_\mathrm{O}$ and reads as (see e.g., Wardle, 2007),

$$\eta_\mathrm{O} = \frac{c^2}{4\,\pi\,\sigma_\mathrm{O}}\ . \tag{1.18}$$

Assuming only single-charged ions and electrons ($Z_\mathrm{i} = |Z_\mathrm{e}| = 1$) and ignoring that also dust can act as a charge carrier, we can determine ambipolar diffusion η_A and the Hall effect η_H

as (see e.g., Wardle, 2007),

$$\eta_{\mathrm{A}} = \beta_{\mathrm{i}}\,\beta_{\mathrm{e}}\,\eta_{\mathrm{O}} \propto B^2\,\rho^{-2}\,, \tag{1.19}$$

$$\eta_{\mathrm{H}} = \beta_{\mathrm{e}}\,\eta_{\mathrm{O}} \propto B\,\rho^{-1}\,. \tag{1.20}$$

On a microscopic level AD is the separation of neutrals from all charged particles in the presence of a large-scale magnetic field. The field moves through the gas and sweeps up all charged particles, while the neutrals are not influenced. This requires the gas density to be relatively low, otherwise collisions lead to the decoupling of ions/electrons from the magnetic field. Magnetic diffusion dominated by AD translates into $1 \ll \beta_{\mathrm{i}} \ll \beta_{\mathrm{e}}$ (see e.g., Wardle, 2007), meaning that AD is largest in the presence of a strong magnetic field and low gas density (see Eq. (1.19)).

As mentioned earlier, ions are significantly larger than electrons, leading to a much higher collision frequency of ions. If the disk is moderately dense, ions therefore decouple from a magnetic field, while electrons are still tied to the field. A magnetic field with a motion relative to the gas therefore leads to a separation of ions of species j and electrons. This explains HE microphysically, being the dominant magnetic diffusion process in the case of the Hall parameters for ions and electrons fulfilling the condition $\beta_{\mathrm{i}} \ll 1 \ll \beta_{\mathrm{e}}$ (see e.g., Wardle, 2007).

In PPDs, different non-ideal MHD diffusion processes are dominant at certain locations in the disk: OD dominates in regions of high density and a low ionization degree, such as the DZ (low β_{i} and β_{e}). In the outer, low-density disk, the magnetic field is still sufficiently strong to tie to charged particles, rendering AD to be the dominant diffusion process. Over a large extent of the disk (above and below the DZ, and in the radial zone between AD-dominated disk and DZ) the HE is the dominant non-ideal MHD effect. This emphasizes the importance of all three non-ideal MHD effects for describing magnetic diffuson everywhere in the disk (see e.g., Delage et al., 2022; Mohanty et al., 2018).

MHD simulations of Bai and Stone (2011) have found a strong correlation between the plasma beta β and the effectivity of MRI (expressed via the viscous-α) in AD-dominated disk regions,

$$\beta \approx \frac{1}{2\,\alpha}\,. \tag{1.21}$$

Additionally, a correlation exists between AD and the minimum β (equivalently maximum α with the help of Eq. (1.21)) viable for MRI to operate (see also Fig. 1.17):

$$\beta_{\mathrm{min}}(Am) = \left[\left(\frac{50}{Am^{1.2}}\right)^2 + \left(\frac{8}{Am^{0.3}} + 1\right)^2\right]^{1/2}\,. \tag{1.22}$$

$Am = v_A^2/(\eta_A\,\Omega)$ is the ambipolar Elsässer number, whereas $v_\mathbf{A}$ and Ω denote the Alfvén velocity and the angular velocity of the gas, respectively. Other global MHD simulations

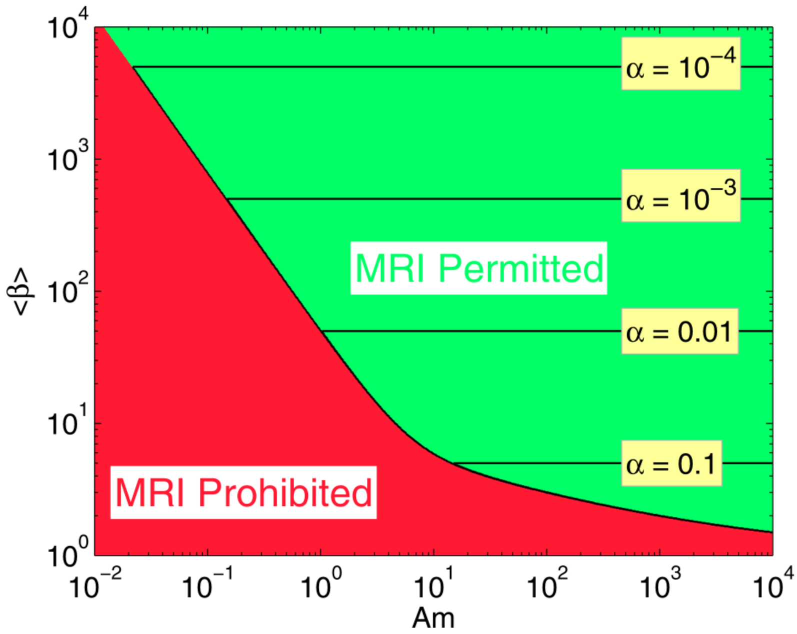

Figure 1.17: Correlation between β and the maximum viscous α, dependent on the effectivity of AD (expressed as the ambipolar Elsässer number Am). There are values of Am and β where MRI is completely suppressed by AD, whereas in other regions it is only reduced. Credit: Reproduced with permission of both authors, from Bai and Stone (2011); © AAS. Reproduced with permission.

have confirmed that AD indeed seems to dampen MRI in the outer disk (Gressel et al., 2015; Simon et al., 2013).

We want to emphasize that the HE is, in contrast to OD and AD, not a dissipative process. It modifies the large-scale field geometry in the case of a toroidal field component B_φ, while AD and OD lead to dissipation and heating of the gas (see e.g., Khaibrakhmanov, 2024; Leung and Ogilvie, 2019). This becomes very important in the case of a toroidal large-scale field component, which in real disks probably exist. This is due to recent observations and simulations strongly promoting the development of magnetically induced outflows (see Sect. 1.1.4). This leads to the development of a toroidal field component due to torques acting on the large-scale field (Bai and Stone, 2013; Bai and Stone, 2017; Ogilvie, 1997). Depending on the alignment between the radial and toroidal field components it is possible that the HE acts in the same direction as magnetic advection, while AD and OD always lead to an outward directed diffusion of the large-scale field (see e.g., Bai and Stone, 2017; Leung and Ogilvie, 2019).

Magnetocentrifugally accelerated winds (MCW): Magnetically-induced outflows modify the picture of an advection/diffusion-controlled large-scale field. As mentioned in the paragraph 'Torques from magnetically induced winds' of Sect. 1.2.2, MCWs heavily influence the disk structure and evolution by removing mass and angular momentum from the disk. Subsequently, we review the fundamental processes involved in launching a MCW, showing that the large-scale field topology is a key parameter for describing magnetically induced outflows (see e.g., Bai et al., 2015; Ogilvie, 1997; Spruit, 1996).

Outflows are preferably launched at a height above the disk, where the magnetic pressure equals the thermal pressure of the gas. This height is typically referred to as the *magnetic surface* $z_{\rm B}$ and is located at $\sim 3-5\,H_{\rm p}$ above the disk midplane (see e.g., Bai and Stone, 2013; Guilet and Ogilvie, 2012). Disk gas at this height is ionized sufficiently well for using ideal MHD, i.e., the gas couples almost perfectly to the magnetic field lines. Thereafter, we assume axisymmetric, steady-state MCWs, allowing a discussion of the basic physics.

Outflows moving along a magnetic field line have four conserved quantities (see e.g., Bai et al., 2015; Spruit, 1996):

$$k \equiv \frac{4\pi\rho\, u_{\rm p}}{B_{\rm p}} \qquad \text{(conservation of mass)}\,, \tag{1.23}$$

$$\omega \equiv \Omega - \frac{k\, B_\varphi}{4\pi\,\rho\, r} \qquad \text{(conservation of magnetic flux)}\,, \tag{1.24}$$

$$l \equiv \Omega\, r^2 - \frac{r\, B_\varphi}{k} \qquad \text{(conservation of angular momentum)}\,, \tag{1.25}$$

$$E = \frac{u_{\rm p}^2 + (u_\varphi - \omega\, r)^2}{2} + h + \phi_{\rm eff} \qquad \text{(conservation of energy)}\,, \tag{1.26}$$

where k is the mass flux density per unit of poloidal magnetic flux, and ω can be interpreted as the angular velocity of the field line. l denotes the specific angular momentum flux along a field line, and E refers to the Bernoulli integral, which is the sum of kinetic, thermal, gravitational, and centrifugal energy. In addition to these conserved quantities, Ω denotes the angular velocity of the gas at the field line foot point. Moreover, $u_{\rm p}$, h and $\phi_{\rm eff}$ describe the poloidal flow velocity along the field line, the specific enthalpy, and the effective potential (gravitation minus centrifugal acceleration), respectively.

$\phi_{\rm eff}$ is dependent on the inclination of the field lines (see Fig. 1.18), i.e., a strongly inclined field triggers a strong wind (large k, see Eq. (1.23)). This results in a massive, but slow wind (see e.g., Spruit, 1996), whereas MCWs cannot be launched at all in the case of an almost vertical field. In the intermediate case, however, a MCW cannot be launched solely by magnetocentrifugal acceleration. With the help of gas being elevated to higher z by thermal pressure, however, it may overcomes the potential barrier (a magneto-thermal wind, see 'Torques from magnetically induced winds' in Sect. 1.2.2).

The two most critical quantities of a MCW are the transport rates of mass and angular momentum. A rigorous mathematical solution of the wind flow requires the wind to pass

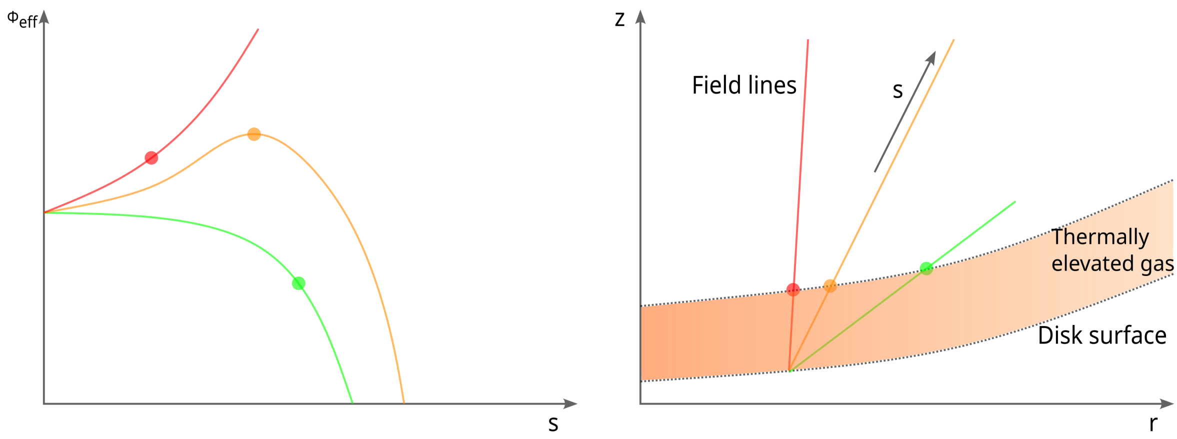

Figure 1.18: Illustration of the magnetocentrifugal effective potential in three cases. *Left panel:* The effective potential $\phi_{\rm eff}$ of three different field lines along the field line (s denotes the distance following the field line). The red curve shows a very steep field line (no thermal heating is sufficient to overcome the gravitational barrier), whereas the green line shows $\phi_{\rm eff}$ for a strongly inclined field line. The orange line depicts the case of a field line at an intermediate angle, which requires initial thermal heating to overcome the initial bump in $\phi_{\rm eff}$. *Right panel*: The depiction of the three field lines, in the r-z plane of a disk. Disk gas can be elevated due to increased thermal pressure, which is also indicated by the orange area. The three dots in both panels mark the position at the disk surface in the case of disk gas with high temperatures. Credit: Own illustration, but inspired by Spruit (1996).

through three critical points. These are the *slow magnetosonic point*, the *fast magnetosonic point* and the *Alfvén point*; they denote the position on a field line, where the flow velocity $u_{\rm p}$ surpasses the slow (fast) magnetosonic speeds $u_{\rm s(f),p}$ as well as the Alfvén velocity $v_{\rm A}$, respectively (see e.g., Bai et al., 2015). An outflow becoming gravitationally unbound requires a large Alfvén speed. This justifies the simplification of the slow magnetosonic speed being very close to the sonic speed (i.e., $v_{\rm s,p} \approx c_{\rm s}$, see Spruit, 1996). With this approximation we can write (see e.g., Ogilvie and Livio, 2001; Spruit, 1996),

$$\dot{M}_{\rm wind} \approx \rho_0\, c_{\rm s,0}\, \exp\left\{-\frac{\phi_{\rm eff,c} - \phi_{\rm eff,0}}{c_{\rm s,c}}\right\}, \tag{1.27}$$

where the subscripts '0' and 'c' denote quantities at the disk surface and at the sonic point, respectively. Eq. (1.27) shows that the sonic point is a key parameter in controlling the strength of a MCW.

Determination of the angular momentum extraction requires the radial position $r_{\rm A}$ of the Alfvén point. Using Eq. (1.24) and Eq. (1.25), the conserved quantity l can be rewritten as,

$$\omega - \Omega = \frac{l - \omega\, r^2}{r^2\,(u_{\rm A,p}^2/u_{\rm p}^2 - 1)}, \tag{1.28}$$

where $u_{\mathrm{A,p}}$ is the Alfvén velocity associated to the poloidal large-scale field line. The Alfvén point is defined as the radius r_{A}, where $u_{\mathrm{A,p}} = u_{\mathrm{p}}$. For Eq. (1.28) not becoming singular at the Alfvén point, the following condition has to be fulfilled (see e.g., Bai et al., 2015),

$$l = \omega r_{\mathrm{A}}^2 , \tag{1.29}$$

$$\omega - \Omega = \frac{r_{\mathrm{A}}^2/r^2 - 1}{u_{\mathrm{A,p}}^2/u_{\mathrm{p}}^2 - 1} . \tag{1.30}$$

Eq. (1.30) states that field lines are rotating slower than the disk ($\omega < \Omega$) in the case of outward-bent field lines with $r_{\mathrm{A}} > r$. The larger r_{A}/r is, the slower the field rotates, which shows that the ratio $(r_{\mathrm{A}}/r)^2$ controls the amount of angular momentum extraction from the disk. This is because the slower rotating magnetic field brakes the disk due to the magnetic coupling between magnetic field and disk. The ratio $(r_{\mathrm{A}}/r)^2$ is therefore typically denoted as the lever arm λ. The actual position of r_{A} is dependent on the geometry of the large-scale field above the disk. Therefore, to determine the angular momentum loss of magnetically coupled outflows, the large-scale field topology must be known.

Chapter 2

Research questions and goals

Magnetically threaded disks have been studied extensively over the past decades. Magnetic fields act on every spatial scale in disks and therefore are a crucial factor in developing a comprehensive model describing the structure and evolution of PPDs. In the innermost region, stellar fields are threading the disk and heavily influence the structure and evolution in this disk region. But also the rest of the disk is threaded by large- and small-scale magnetic fields. Small-scale fields are important for the development of MRI and therefore provide an effective angular momentum transport mechanism in some disk regions, whereas large-scale fields can remove mass and angular momentum from the disk through outflows coupling to the field.

This thesis has an overarching science topic: Which implications can large-scale magnetic fields have on disk evolution? In this context we also treat stellar fields as a large-scale field component, after all it also acts on spatial scales larger than the scale height of PPDs (at least in the inner disk). A single scientists' lifetime will most probably not suffice to provide a satisfactory answer to all science questions related to this topic. Hence, we will focus on two aspects in this thesis: (i) How does a stellar magnetic field influence the long-term behavior of protoplanetary disks? (ii) How does the large-scale poloidal field in Class II protoplanetary disks look like? Subsequently I will elaborate in which ways these research questions can contribute to a better understanding of PPDs and how this work fits into the plethora of already existing work on magnetically threaded disks.

One of the most crucial regions of PPDs is the inner disk, as many physical processes take place close to the star, determining the disk's structure and long-term evolution (see Sect. 1.2.1 and Sect. 1.2.2). However, self-consistent, hydrodynamical long-term evolution simulations of PPDs (even in 1D models) have so far not been conducted due to severe time step limitations in the inner disk, imposed by the Courant-Friedrichs-Levy (CFL) condition (see Courant et al., 1928, also see Sect. 5.2 for a more detailed analysis of the numerical challenges). Long-term evolution models, including the innermost disk region, do exist; however, all of these models use a diffusion-approximation model describing the evolution of the surface density Σ. Such simple models are unable to take crucial features, such as pressure gradients or magnetic torques caused by a stellar dipole, into account (see e.g., Armitage et al., 2001; Bell and Lin, 1994). Moreover, an important task of every simulation of a boundary-value problem (which every hydrodynamical simulation is) is the proper treatment of computational domain boundaries. For a PPD around a magnetized T Tauri star the magnetic truncation radius marks the position of the inner boundary (see Sect. 1.2.3). Any change in the accretion rate or stellar magnetic field will modify the position of the inner disk boundary. With that said, in Paper I we provide further insights into how a stellar dipole can modify the long-term behavior of PPDs. Vorobyov et al. (2019) further argues that the processes in the inner disk dominate the long-term evolution of the whole disk. Although more advanced 2D and 3D MHD models exist, all of them either are unable to perform simulations over significant fraction of a disk's lifetime, or they spare out the innermost disk region. The models presented in this thesis provide the missing link between simulations of the inner disk and more sophisticated multidimensional simulations of the outer disk.

The second part of this thesis studies in more detail the large-scale field topology of Class II PPDs. Recent global wind simulations (see e.g., Cui and Bai, 2021; Gressel et al., 2015; Lesur, 2021; Suzuki et al., 2016) show that magnetically induced outflows can explain the radial mass transport rates of PPDs, despite the disk not being MRI-active in most regions (see e.g., Lesur et al., 2022, see also Sect. 1.2.4). Magnetocentrifugally accelerated winds require the existence of an outward-bent, large-scale magnetic field anchored in the disk. Such fields evolve together with the disk through magnetic flux transport due to magnetic advection and diffusion (see Sect. 1.2.4). However, there is no conclusive answer available yet how such a field evolves, i.e., where and under which conditions in PPDs magnetic flux is transported inwards or outwards (see e.g., Lesur et al., 2022). Long-term evolution models of large-scale fields in a non-ideal, laminar Class II disk do not exist yet and are very challenging to develop. The work done in Paper II is the first of its kind and provides a better understanding of the initial conditions favorable for a disk driving MCWs. We also incorporate the inner disk boundary model of Paper I. This allows us to investigate the influence of a stellar dipole on the evolution of a large-scale disk field in the inner disk.

Finally, the numerical capabilities of our simulation framework TAPIR in mind (see Ragossnig et al., 2020), we will also use the studies conducted in Paper I and Paper II as a starting point to perform time-dependent simulations of PPDs including MCWs in the future. This allows us to study wind-driven accretion over the whole disk lifetime. It therefore embeds the work presented in this thesis in a wider field of global MHD and wind-driving disk simulations, with a distinct focus on long-term evolution and the inclusion of the inner disk region.

Part II

Numerical Method

Chapter 3

Brief review of TAPIR

The numerical code used in both publications presented in this thesis (Paper I and Paper II) is called *TAPIR* (The Adaptive Implicit RHD Code, for an in-depth review see Ragossnig et al., 2020). This chapter does not repeat every aspect of TAPIR. Instead, it highlights selected features relevant for understanding the two main extensions developed in this thesis: (i) a time-dependent inner boundary (see Ch. 4), and (ii) the inclusion of a large-scale magnetic field (see Ch. 5). Unlike conventional adaptive grid algorithms, which add and remove points based on local resolution requirements, TAPIR employs a *grid equation*. This equation is solved alongside the physical system and determines the position of each grid point according to the resolution requirements of the solution. Sect. 3.1 reviews the basic concept of this grid equation. Sect. 3.2 then introduces the discretization framework of TAPIR, which is essential for implementing the induction equation governing the evolution of large-scale magnetic disk fields.

The partial differential equations (PDEs) describing PPDs constitute a boundary value problem. Consequently, appropriate boundary conditions are a key component of any hydrodynamic simulation. Sect. 3.3 therefore reviews the boundary conditions implemented in TAPIR, excluding the newly developed, variable inner boundary, which is addressed separately in Ch. 4. Finally, Sect. 3.4 provides a brief overview of the solving strategy and time-integration scheme used in TAPIR.

3.1 Grid equation

The basic idea is that grid points can move within the physical domain, reacting to the requirements of the solution $\mathbf{X}$. This may result in a higher grid point density in regions of increased importance. The slope of the radial profile of an as yet arbitrary physical quantity provides the metric for the determination of the required grid point density (see Fig. 3.1).

The grid equation should fulfill the following requirements: (i) the grid points have to be distributed monotonically at all times, i.e., $r_{\mathrm{i}+1} > r_{\mathrm{i}}$, and (ii) the grid variations have to be smooth both in space and time. As a result, grid points cannot move indefinitely fast and grid point density variations have to be smooth between neighboring grid cells (see LeVeque

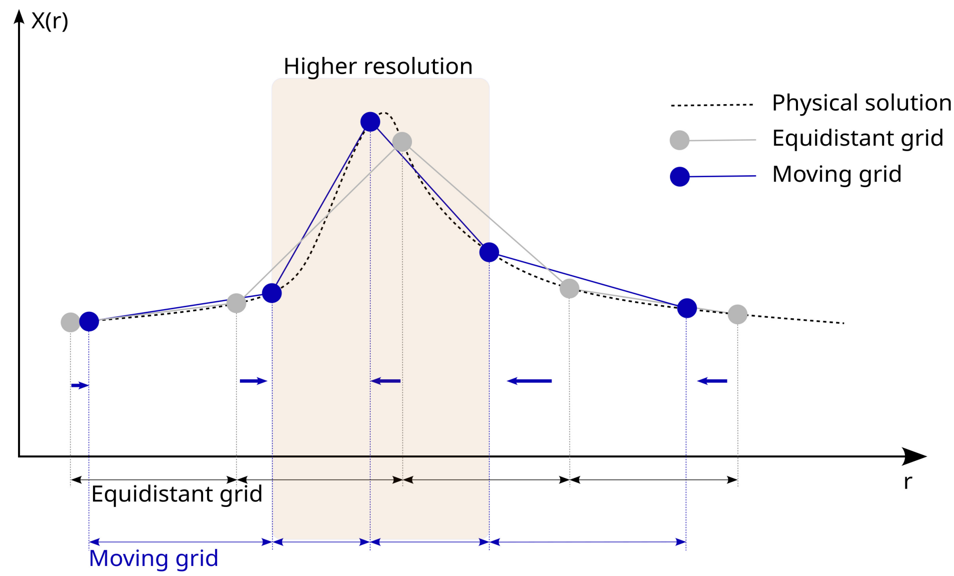

Figure 3.1: Illustration of a moving grid governed by a grid equation. The dashed black line corresponds to an unknown solution to a physical problem. The light-gray dots and lines denote an initially equidistant grid and the corresponding solution, respectively. The grid equation redistributes the grid points such that the arc-length of the physical solution is constant (blue dots and lines). A solution obtained this way better resolves steep gradients of the physical solution $\mathbf{X}(r)$.

et al., 1997). The grid point concentration $n_{\rm i}$ is defined as,

$$n_{\rm i} = \frac{\chi_{\rm i}}{r_{\rm i+1} - r_{\rm i}} \,, \tag{3.1}$$

where $\chi_{\rm i}$ denotes a local scale of the grid and determines its structure in the absence of any physical structure (e.g. $\chi_{\rm i}$ =<length of computational domain> defines an equidistant grid everywhere). The grid should be able to react to any physical quantity necessary, which means that we have to generalize the idea of a projected arc-length $\mathcal{R}$ to more than one physical quantity $x_{\rm m}$ ($m \in [1, M]$ and M is the number of variables we want the grid reacting to). The generalized projected arc-length $\mathcal{R}_{\rm i}$ at the i-th grid point $r_{\rm i}$ is then given by (see LeVeque et al., 1997),

$$\mathcal{R}_{\rm i} \propto \sqrt{1 + \sum_{m=1}^{M} \left(\frac{dx_{\rm m}}{dr_{\rm i}} \right)^2} \,. \tag{3.2}$$

Finally we can connect $R_{\rm i}$ to $n_{\rm i}$ by simply requiring these two quantities to be proportional,

$$n_{\rm i} \propto \mathcal{R}_{\rm i} \,, \tag{3.3}$$

which satisfies the condition of a monotonically distributed grid. The maximum grid point concentration variation between neighboring grid cells is restricted via the spatial smoothing parameter α_g,

$$\frac{\alpha_\mathrm{g}}{\alpha_\mathrm{g}+1} \leq \frac{n_\mathrm{i}}{n_\mathrm{i+1}} \leq \frac{\alpha_\mathrm{g}+1}{\alpha_\mathrm{g}} \ . \tag{3.4}$$

Eq. (3.4) can be rewritten as a localized description of the temporally smoothed grid point concentration $\hat{n}_\mathrm{i}$ (see LeVeque et al., 1997),

$$\hat{n}_\mathrm{i} = n_\mathrm{i} - \alpha_\mathrm{g}(\alpha_\mathrm{g}+1)(n_\mathrm{i-1} - 2\,n_\mathrm{i} + n_\mathrm{i+1}) \propto \mathcal{R}_\mathrm{i} \ . \tag{3.5}$$

Finally, temporal smoothing is implemented analogously by restricting the maximum change of n_i between two timesteps,

$$\tilde{n}_\mathrm{i}^{(\mathrm{new})} = \hat{n}_\mathrm{i}^{(\mathrm{new})} + \frac{\tau_\mathrm{g}}{\Delta t}\left(\hat{n}_\mathrm{i}^{(\mathrm{new})} - \hat{n}_\mathrm{i}^{(\mathrm{old})}\right) \propto \mathcal{R}_\mathrm{i} \ . \tag{3.6}$$

Here, τ_g denotes the temporal smoothing time and Δt the timestep between the two times $t^{(\mathrm{old})}$ and $t^{(\mathrm{new})}$[1]. In the case of PPDs, two physically motivated choices for τ_g are either: (i) the dynamic timescale t_dyn, or (ii) the viscous timescale t_visc. These choices reflect that PPDs evolve on a viscous timescale, whereas short-term perturbations often occur on a dynamical timescale. For the work presented in Paper I and Paper II, t_visc has been used to temporally smooth the grid variations,

$$\tau_\mathrm{g} = t_\mathrm{visc} \ . \tag{3.7}$$

The temporally and spatially smoothed grid point concentration $\tilde{n}_\mathrm{i}$ is then used to formulate the grid equation by eliminating the proportionality factor between n_i and $\mathcal{R}_\mathrm{i}$ (omitting the superscript (new) for a clearer representation)

$$\frac{\tilde{n}_\mathrm{i}}{\mathcal{R}_\mathrm{i}} = \frac{\tilde{n}_\mathrm{i-1}}{\mathcal{R}_\mathrm{i-1}} \ . \tag{3.8}$$

The grid equation is solved together with the physical equations. This way the grid points can move through the computational domain, thereby reducing the risk of introducing perturbations as a consequence of the insertion or removal of grid points. The relative importance of different quantities for calculating the grid point concentration is determined by weights (omitted in this brief review, as it is not essential for a basic understanding of the grid equation). However, these weights have to be calibrated when executing a simulation that uses the grid equation. Otherwise, the grid may experience an 'over- or underreaction' in response to changes. These likely cause numerical instabilities or yield a coarse grid resolution in specific locations (see LeVeque et al., 1997). Inappropriate quantities or suboptimally chosen

[1] The superscripts (old) and (new) denote quantities at the old and new time, respectively.

weights may also lead to grid points being redistributed into regions of no particular scientific interest.

3.2 Discretization

The numerical solution of a set of ordinary or partial differential equations (PDEs) can only be obtained at discrete points described by a numerical grid. This makes it necessary to discretize the physical equations. In TAPIR, the numerical grid is organized as a so-called *staggered mesh*, in which scalar-valued quantities, such as the surface density Σ and the inner energy e are discretized on a scalar grid. Radial components of vector-like quantities (e.g. the radial velocity u_r) are then discretized analogously on the vectorial grid. The two grids are shifted radially by half the distance between two grid points (see LeVeque et al., 1997; Ragossnig et al., 2020, see also Fig. 3.2). The discretization of u_φ represents

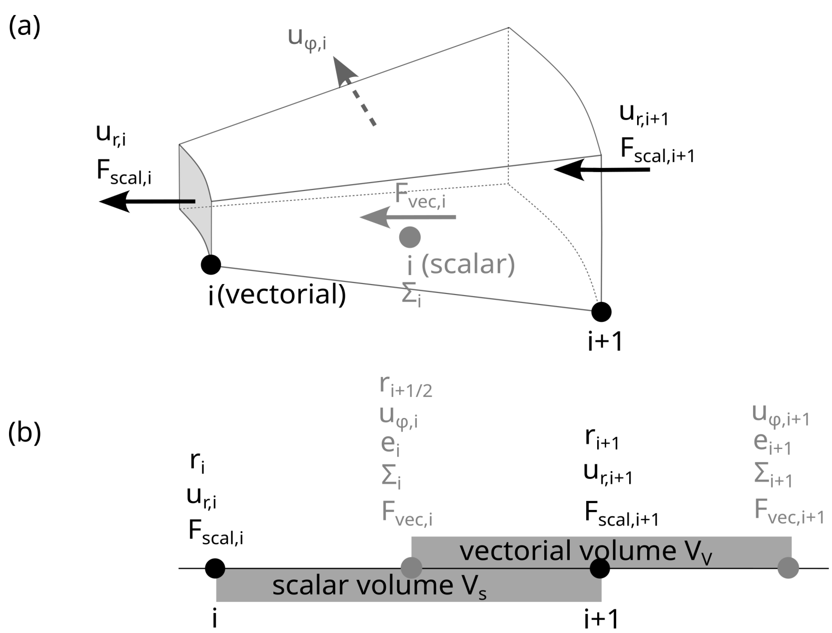

Figure 3.2: Illustration of the localization of various quantities on the numerical grid. In both panels, black and gray dots/text refer to the discretization with respect to the vectorial grid and scalar grid, respectively. (a) A wedge of a protoplanetary disk between two grid points i and i+1. The angular direction is only hinted at but not discretized, since it is not necessary for the intended explanations. The localization of some primary variables and the fluxes of scalar quantities $F_{\mathbf{scal,i}}$ and vector quantities $F_{\mathbf{vec,i}}$, are shown. u_φ is a vector-like quantity and is localized at the center of the cell interfaces in angular direction. (b) Projection of the wedge of panel (a) onto a 1D grid in radial direction. Note that u_φ is also localized at the scalar grid due to its projection from the cell interface center in angular direction to the 1D grid. The corresponding scalar and vectorial cell volumes, V_s and V_v, respectively, are also shown.

an exception to this rule in the 1+1D TAPIR implementation: A multidimensional grid in cylindrical coordinates corresponds to grid cells shaped in the form of wedges (see panel (a) of Fig. 3.2). u_φ is a vector-like quantity that is oriented in angular direction. Therefore, it is localized on the vectorial grid in angular direction. The projection of the two-dimensional wedge onto a 1D radial grid translates into u_φ being localized at the center of the grid cell, which corresponds to the scalar grid (see panel (b) of Fig. 3.2). The grid equation is used to determine the positions r_i on the vectorial grid. As a consequence, physical quantities localized on the scalar grid $r_{\mathrm{i}+1/2}$ have to be calculated as a mean between two vectorial grid points.

TAPIR uses a finite-volume method for discretizing the system of equations. Consequently, it is necessary to define the volumes of the grid cells corresponding to scalar and vector quantities, V_s and V_v, respectively. V_s and V_v are defined such that the scalar and vector variables are located at the center of the respective volumes (see Fig. 3.2).

Localized dependencies: It is imperative to consider not only the localization of variables and fluxes on the grid, but also the interaction between various quantities at different grid points. TAPIR uses an implicit integration scheme, making it necessary to invert a Jacobian $\mathbf{J}$ that describes all possible dependencies between various variables at different positions (see Sect. 3.4). In the case of a narrow matrix bandwidth of $\mathbf{J}$ (i.e., if only the main diagonal and few diagonals left and right of it are non-zero), the inverse of $\mathbf{J}$ can be determined very efficiently (see LeVeque et al., 1997). Therefore, the discretization of a differential equation at a grid position r_i is required to depend solely on variables from the next two adjacent grid points in both directions (a so-called *5-point stencil*, see Fig. 3.3). TAPIR uses a finite-

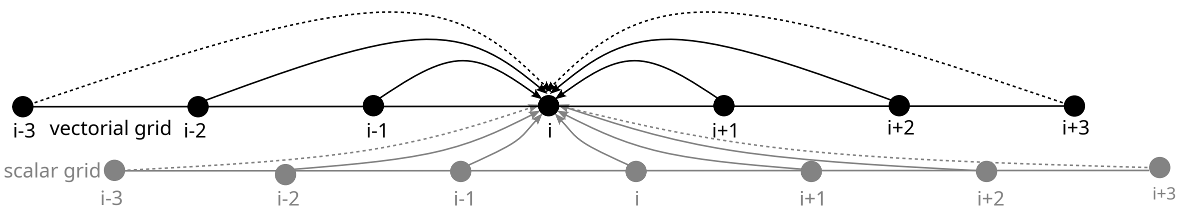

Figure 3.3: Illustration of the staggered grid and the 5-point/7-point stencil. The solid arrows show the dependencies of a 5-point stencil if it is discretized at the vectorial grid, i.e. the dependency of a variable on other variables at other grid points. The dashed arrows mark the additional dependencies, if a 7-point stencil is used instead (important in Ch. 5).

volume discretization method, making it necessary to integrate all physical equations over its grid cell volume V. In a 1+1D cylindrical geometry suitable for protoplanetary disks, this essentially entails calculating the integral radially and in angular direction over an annulus between two grid points (in vertical direction the physical quantities are averaged). This results in a two-dimensional "volume", both for the scalar and vectorial cells (see Fig. 3.2),

$$V_{\mathrm{s,i}} = \pi\,(r_{\mathrm{i+1}}^2 - r_{\mathrm{i}}^2) \qquad \text{(scalar volume)}\,, \tag{3.9}$$

$$V_{\mathrm{v,i}} = \frac{1}{2}\,\pi\,(r_{\mathrm{i+1}}^2 - r_{\mathrm{i-1}}^2) \qquad \text{(vectorial volume)}\,. \tag{3.10}$$

Discretization at boundaries: The use of a 5-point stencil requires, for every grid point, that the next two adjacent grid points in both radial directions exist. At the inner and outer boundaries this is not applicable, Therefore, TAPIR introduces so-called *ghost cells* at the innermost and outermost two scalar and vectorial grid cells are so-called *ghost cells*. These ghost cells have a vanishing volume (see Fig. 3.4)

$$r_1 = r_2 = r_3 \Longleftrightarrow V_{\mathrm{s,1}} = V_{\mathrm{s,2}} = V_{\mathrm{v,1}} = V_{\mathrm{v,2}} = 0 \qquad \text{(inner boundary)}\,, \tag{3.11}$$

$$r_{\mathrm{N-2}} = r_{\mathrm{N-1}} = r_{\mathrm{N}} \Longleftrightarrow V_{\mathrm{s,N-2}} = V_{\mathrm{s,N-1}} = V_{\mathrm{v,N-1}} = V_{\mathrm{v,N}} = 0 \qquad \text{(outer boundary)}\,. \tag{3.12}$$

Note that the vectorial volumes at $i = 3$ and $i = N - 2$ have a non-vanishing volume and are therefore not ghost cells, despite their partial overlap with the scalar ghost-cells (see Fig. 3.4). From a numerical point of view those two cells are indistinguishable from any other grid cell. The physical equations are discretized within the computational domain at all grid points,

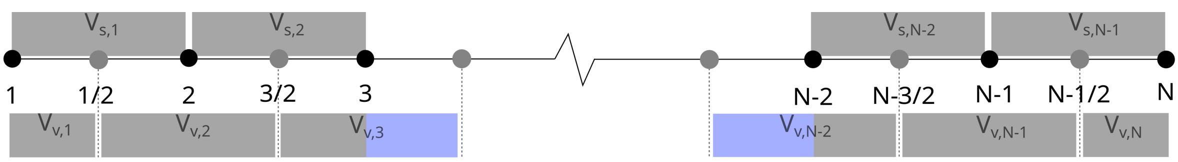

Figure 3.4: Illustration of the staggered grid at the grid boundaries. Black and gray dots correspond to the vectorial and scalar grid, respectively. Cells with zero volume are shows as gray areas (ghost cells), whereas blue areas mark a non-zero volume. The vectorial volumes $V_{\mathrm{v,3}}$ and $V_{\mathrm{v,N-2}}$ are non-zero, although they are partly located in the ghost-cell region.

except for the ghost cells (in the interval $i \in [3, N - 2]$). This allows the use of a 5-point stencil for all physically relevant grid points. The boundary conditions are applied separately at the innermost and outermost two grid cells (see Sect. 3.3).

Volume integration with moving grid: As discussed in Sect. 3.1, the grid is adaptive and able of repositioning grid points. As a consequence, the grid cell sizes are variable too, with a time-dependent volume $V(t)$. Additionally, the grid cell boundaries are moving, which has to be taken in consideration when defining fluxes over a moving boundary. The so-called *Reynolds transport theorem* (see e.g., Mihalas and Winkler, 1986) is used for this purpose, and, applied to our adaptive grid, reads as,

$$\frac{d}{dt}\left(\int_{V(t)} f \, dV\right) = \int_{V(t)} \frac{\partial f}{\partial t} dV + \int_{\partial V} f \, \mathbf{u}_{\text{grid}} \cdot d\mathbf{S} \,, \tag{3.13}$$

where f denotes an arbitrary scalar quantity. $\mathbf{u}_{\text{grid}}$ and $d\mathbf{S}$ represent the velocity of the grid point and the radially outward-directed unit normal vector corresponding to the volume surface element ∂V, respectively. A typical hydrodynamic equation, describing advection of some quantity f with source and sink terms, A_{source} and A_{sink}, respectively, reads as,

$$\frac{\partial f}{\partial t} + \nabla \cdot (\mathbf{u} \, f) - A_{\text{source}} + A_{\text{sink}} = 0 \,. \tag{3.14}$$

Integrating over the cell volume, applying the Gauss theorem and the Reynolds transport theorem yields the following volume-integrated form, while respecting a moving grid,

$$\frac{d}{dt}\left(\int_{V(t)} f \, dV\right) + \int_{\partial V} f \, (\mathbf{u} - \mathbf{u}_{\text{grid}}) \cdot d\mathbf{S} - \int_{V(t)} (A_{\text{source}} + A_{\text{sink}}) \, dV = 0 \,. \tag{3.15}$$

First, the discretized equations of continuity, inner energy, as well as the equation of motion in radial and angular directions, are volume-integrated according to Eq. (3.15). Afterward, the integrated equations are vertically averaged and discretized, either on the scalar or the vectorial grid (see Fig. 3.2). The full set of discretized equations is not listed in this text, but can be studied in Ragossnig et al. (2020).

3.3 Boundary conditions

The system of PDEs, describing the structure and evolution of PDEs, is formulated as a boundary value problem. This means that the solution itself is uniquely determined by the conditions applied at the computational domain boundaries. *Dirichlet boundary conditions* are defined as equations, which set the value of a variable x (e.g., Σ or e) to a certain, predetermined value at the respective boundary they are applied at. Generally, they are formulated in the following way,

$$x_1 = x_2 = x_3 = x_{\text{bound,in}} \,, \tag{3.16}$$

$$x_{\text{N}-2} = x_{\text{N}-1} = x_{\text{N}} = x_{\text{bound,out}} \,, \tag{3.17}$$

where $x_{\text{bound,in}}$ and $x_{\text{bound,out}}$ denote the boundary value at the inner and outer boundary, respectively.

Note that, as a consequence of the presence of ghost cells at the computational boundaries, Dirichlet boundary values are applied Simultaneously to the innermost and outermost three grid points (for a 5-point stencil; four grid points in the case of a 7-point stencil, see Sect. 3.2).

Similarly, *Neumann boundary conditions* are equations that describe the gradient of a quantity at a specific boundary. In TAPIR, they are implemented in the following way,

$$\left.\frac{\partial x}{\partial r}\right|_{\mathrm{r=r_3}} = 0 \Rightarrow \begin{cases} x_4 - x_3 = 0 \\ x_1 = x_2 = x_3 \end{cases} , \tag{3.18}$$

$$\left.\frac{\partial x}{\partial r}\right|_{\mathrm{r=r_{N-2}}} = 0 \Rightarrow \begin{cases} x_{\mathrm{N-3}} - x_{\mathrm{N-2}} = 0 \\ x_{\mathrm{N}} = x_{\mathrm{N-1}} = x_{\mathrm{N-2}} \end{cases} . \tag{3.19}$$

In TAPIR, Dirichlet boundary conditions are applied for the grid equation at the inner and outer boundaries,

$$r_1 = r_2 = r_3 = r_{\mathrm{in}} \ , \tag{3.20}$$

$$r_{\mathrm{N-2}} = r_{\mathrm{N-1}} = r_{\mathrm{N}} = r_{\mathrm{out}} \ , \tag{3.21}$$

which confine the computational domain between the inner radius r_{in} and the outer radius r_{out}. Moreover, the grid point concentrations, denoted by $\tilde{n}_{\mathrm{i}}$ (see Eq. (3.6) in Sect. 3.1) are constant at $i = 4$ and $i = N - 3$. This prevents the formation of a gap in the grid in proximity to the computational boundaries r_{in} and r_{out} (see LeVeque et al., 1997),

$$\tilde{n}_3 = \tilde{n}_4 \ , \tag{3.22}$$

$$\tilde{n}_{\mathrm{N-4}} = \tilde{n}_{\mathrm{N-3}} \ . \tag{3.23}$$

3.4 Solving strategy

Common to all time-evolution codes is the requirement of a time integration scheme. This typically involves finding a solution $\mathbf{X}^{(\mathrm{new})}$ at a specific time $t^{(\mathrm{new})}$ (subsequently referred to as the new time) by using the solution $\mathbf{X}^{(\mathrm{old})}$, defined at a previous time, $t^{(\mathrm{old})} < t^{(\mathrm{new})}$ (analogously named old time). The solution vector $\mathbf{X}$ contains all primary variables of the system of partial differential equations (PDEs) at each grid point. In the context of 1+1D disk simulations in cylindrical coordinates, $\mathbf{X}$ reads as,

$$X_{\mathrm{i}} = (x_{1,\mathrm{i}}, ..., x_{\mathrm{M,i}}) = (\Sigma_{\mathrm{i}},\ e_{\mathrm{i}},\ u_{\mathrm{r,i}},\ u_{\varphi,\mathrm{i}},\ r_{\mathrm{i}}) \ , \tag{3.24}$$

$$\mathbf{X} = (X_1, ..., X_{\mathrm{N}})^{\mathbf{T}} \quad , \tag{3.25}$$

where the subscript “i” indicates the value of the corresponding variables at the grid position r_{i}. The symbol $x_{\mathrm{m,i}}$ denotes the primary variable at the “i-th“ grid point (where, in the case of a 5-point stencil, $m \in [1, M]$, and $M = 5$). The solution vector $\mathbf{X}$ has the dimension $M \cdot N$, with N denoting the number of grid points. Note that TAPIR is currently limited to 1+1D hydrodynamic simulations of a thin disk, resulting in $u_\mathrm{z} = 0$. The variable r_i in the solution vector is added as a consequence of the grid equation being solved together with the physical equations (see Sect. 3.1).

The discretization process of the system of PDEs yields an algebraic system of equations, which is usually non-linear (for details see LeVeque et al., 1997; Ragossnig et al., 2020) This system can be rearranged such that all terms are on the left-hand side and the right-hand side equals zero:

$$\mathcal{G}(\mathbf{X}) = 0 \Longleftrightarrow \mathcal{G}_\mathrm{m}(X_\mathrm{i}) = 0\,, \tag{3.26}$$

where we have introduced $\mathcal{G}$, representing the non-linear, implicit system of $N \cdot M$ equations. The index notation of $\mathcal{G}_\mathrm{m}(X_\mathrm{i})$ denotes the equation of the "m-th" primary variable at the "i-th" grid point. We note that $\mathcal{G}$ is dependent on both the solution at the old and the new time. This is because the discretized equations typically contain a time derivative describing the temporal evolution of a quantity from the old to the new time (see Ragossnig et al., 2020). Eq. (3.26) is valid for any solution of the system at any given time. No explicit solution exists, therefore an iterative approach, the so-called *Newton-Raphson method*, is used to solve the system of equations (see LeVeque et al., 1997).

Subsequently, the Newton-Raphson iteration, as it is implemented in TAPIR, is briefly reviewed. We start by using the first-order Taylor approximation of $\mathcal{G}(\mathbf{X}^{(i)})$,

$$\mathcal{G}(\mathbf{X}^{(i+1)}) = \mathcal{G}(\mathbf{X}^{(i)}) + \frac{\partial \mathcal{G}(\mathbf{X}^{(i)})}{\partial \mathbf{X}} \left(\mathbf{X}^{(i+1)} - \mathbf{X}^{(i)}\right) = 0\,, \tag{3.27}$$

where $\mathbf{J} \equiv \partial \mathcal{G}(\mathbf{X}^{(i)})/\partial \mathbf{X}$ denotes the Jacobian with dimension $N \cdot M \times N \cdot M$. The symbols $\mathbf{X}^{(i)}$ and $\mathbf{X}^{(i+1)}$ represent the "i-th" and the subsequent "i+1-th" iteration steps, respectively, of the Newton-Raphson method toward the desired solution at the new time. $\mathbf{X}^{(\mathrm{new})}$. The iteration is initiated by using the old solution as the starting point, i.e, $\mathbf{X}^{(i=1)} = \mathbf{X}^{(\mathrm{old})}$. Subsequently, we can invert Eq. (3.27) and, under the assumption that $\mathbf{X}^{(i+1)}$ is already a solution (i.e., $\mathcal{G}(\mathbf{X}^{(i+1)}) = 0$), arrive at the following expression,

$$\mathbf{X}^{(i+1)} = \mathbf{X}^{(i)} - \mathbf{J}^{-1}\,\mathcal{G}(\mathbf{X}^{(i)})\,. \tag{3.28}$$

The approximate solution $\mathbf{X}^{(i+1)}$ is then reinserted in Eq. (3.27) and a new iteration is started. As soon as $\mathbf{X}^{(i+1)} - \mathbf{X}^{(i)}$ is lower than a specific threshold, the iteration is halted and a solution at the new time, $\mathbf{X}^{(\mathrm{new})}$, is found.

The most time-consuming task is the inversion of $\mathbf{J}$. Due to the requirement of localized dependencies for any variable x_{i} (e.g., ρ_{i}, or e_{i}; see also Sect. 3.2 regarding localized dependencies), the Jacobian has non-zero entries only in a narrow band around the main diagonal. The general structure of the Jacobian is then a block-pentadiagonal matrix with $N \times N$ blocks,

$$
\mathbf{J} = \begin{pmatrix}
\mathcal{A}_{1,1} & \mathcal{A}_{1,2} & \mathcal{A}_{1,3} & 0 & & & \cdots & & \\
\mathcal{A}_{2,1} & \mathcal{A}_{2,2} & \mathcal{A}_{2,3} & \mathcal{A}_{2,4} & 0 & & & \cdots & \\
\mathcal{A}_{3,1} & \mathcal{A}_{3,2} & \mathcal{A}_{3,3} & \mathcal{A}_{3,4} & \mathcal{A}_{3,5} & 0 & & \cdots & \\
 & \ddots & \ddots & \ddots & \ddots & \ddots & & & \\
\cdots & 0 & \mathcal{A}_{\mathrm{i,i-2}} & \mathcal{A}_{\mathrm{i,i-1}} & \mathcal{A}_{\mathrm{ii}} & \mathcal{A}_{\mathrm{i,i+1}} & \mathcal{A}_{\mathrm{i,i+2}} & 0 & \cdots \\
 & & & \ddots & \ddots & \ddots & \ddots & \ddots & \\
 & \cdots & & 0 & \mathcal{A}_{\mathrm{N-4,N-2}} & \mathcal{A}_{\mathrm{N-3,N-2}} & \mathcal{A}_{\mathrm{N-2,N-2}} & \mathcal{A}_{\mathrm{N-1,N-2}} & \mathcal{A}_{\mathrm{N,N-2}} \\
 & & \cdots & & 0 & \mathcal{A}_{\mathrm{N-2,N-1}} & \mathcal{A}_{\mathrm{N-1,N-1}} & \mathcal{A}_{\mathrm{N,N-1}} & \mathcal{A}_{\mathrm{N+1,N-1}} \\
 & & & \cdots & & 0 & \mathcal{A}_{\mathrm{N-2,N}} & \mathcal{A}_{\mathrm{N-1,N}} & \mathcal{A}_{\mathrm{N,N}}
\end{pmatrix}, \tag{3.29}
$$

where $\mathcal{A}_{\mathrm{i,j}}$ are again $M \times M$-matrices (using $x_{\mathrm{m,i}}$ as defined in Eq. (3.24))

$$
\mathcal{A}_{\mathrm{i,j}} = \frac{\partial \mathcal{G}_{\mathrm{m}}(X_{\mathrm{i}})}{\partial x_{\mathrm{m,j}}} = \begin{pmatrix}
\frac{\partial \mathcal{G}_{1}(X_{\mathrm{i}})}{\partial x_{1,\mathrm{j}}} & \cdots & \frac{\partial \mathcal{G}_{1}(X_{\mathrm{i}})}{\partial x_{\mathrm{M,j}}} \\
\vdots & \ddots & \vdots \\
\frac{\partial \mathcal{G}_{\mathrm{M}}(X_{\mathrm{i}})}{\partial x_{\mathrm{M,j}}} & \cdots & \frac{\partial \mathcal{G}_{\mathrm{M}}(X_{\mathrm{i}})}{\partial x_{\mathrm{M,j}}}
\end{pmatrix}. \tag{3.30}
$$

The block-pentadiagonal matrix can be readily inverted by using a LU-decomposition and subsequent back-substitution (see LeVeque et al., 1997), which allows us to calculate the next iteration of the solution vector $\mathbf{X}^{(i+1)}$(see Eq. (3.28)).

3.5 Adaptive timestep

Recall that $\mathcal{G}(\mathbf{X})$ contains time derivatives, which after discretization, contain the timestep Δt. As a consequence, the solution $\mathbf{X}^{(\mathbf{new})}$, found with the Newton-Raphson method, depends on the choice of Δt. If the value for Δt is chosen too large, the iteration process will not converge toward a new solution and is therefore limiting the maximum achievable timestep (see LeVeque et al., 1997). Note that the Courant-Friedrichs-Levy (CFL) condition does not apply for implicit integration methods.

Subsequently, we briefly review the corresponding adaptive timestep algorithm. A combination of two different criteria, Eq. (3.31) and Eq. (3.33), are used to determine the value of Δt for the following iteration: (i) the magnitude of the increment/decrement of Δt is controlled by the number of iterations $n_{\rm it}$ needed for obtaining a new solution, and (ii) the relative maximum variation $\mathrm{Res_m}$ of the primary variable $x_{\rm m,i}$ at any grid point between two consecutive solutions. The following algorithm is currently implemented in TAPIR using $n_{\rm it}$ (see also Eq. A.1 in App. A of Paper II; reproduced here for a complete overview of both criteria used for the adaptive timestep control):

$$\Delta t^{\rm (new)}_{\rm cond1} = \begin{cases} 1.5\,\Delta t^{\rm (old)} & \text{if} \quad n_{\rm it} = 1 \\ 1.2\,\Delta t^{\rm (old)} & \text{if} \quad n_{\rm it} = 2 \\ 1.0\,\Delta t^{\rm (old)} & \text{if} \quad n_{\rm it} = 3 \\ 0.8\,\Delta t^{\rm (old)} & \text{if} \quad n_{\rm it} = 4 \\ 0.5\,\Delta t^{\rm (old)} & \text{otherwise} \end{cases} , \tag{3.31}$$

where the maximum relative change $\mathrm{Res_m}$ of a variable $x_{\rm m}$ is defined as follows,

$$\mathrm{Res_m} = \max_i \mathrm{Res_{m,i}} = \frac{|x^{\rm (new)}_{\rm m,i} - x^{\rm (old)}_{\rm m,i}|}{|x^{\rm (new)}_{\rm m,i}| + \eta_{\rm m,i}} , \tag{3.32}$$

where $\mathrm{Res_{m,i}}$ denotes the relative maximum variation of $x_{\rm m,i}$ at the "i-th" grid point. The symbol $\eta_{\rm m,i}$ denotes a small numerical value to exclude zero in the denominator of Eq. (3.32).

$$\Delta t^{\rm (new)}_{\rm cond2} = \begin{cases} 1.5\,\Delta t^{\rm (old)} & \text{if} \quad \mathrm{Res_m} < 0.2\,\mathrm{Res_{m,max}} \\ 1.2\,\Delta t^{\rm (old)} & \text{if} \quad \mathrm{Res_m} < 0.3\,\mathrm{Res_{m,max}} \\ 1.1\,\Delta t^{\rm (old)} & \text{if} \quad \mathrm{Res_m} < 0.4\,\mathrm{Res_{m,max}} \\ 1.0\,\Delta t^{\rm (old)} & \text{if} \quad \mathrm{Res_m} < 0.5\,\mathrm{Res_{m,max}} \\ 0.9\,\Delta t^{\rm (old)} & \text{if} \quad \mathrm{Res_m} < 0.6\,\mathrm{Res_{m,max}} \\ 0.8\,\Delta t^{\rm (old)} & \text{if} \quad \mathrm{Res_m} < 0.7\,\mathrm{Res_{m,max}} \\ 0.5\,\Delta t^{\rm (old)} & \text{otherwise} \end{cases} . \tag{3.33}$$

The value of $\mathrm{Res_{m,max}}$ denotes the maximum allowed variation of $x_{\rm m}$ at any grid point and is an input parameter in TAPIR. The new timestep $\Delta t^{\rm (new)}$ is then determined by taking the minimum for Δt as obtained by the two conditions,

$$\Delta t^{\rm (new)} = \min\left(\Delta t^{\rm (new)}_{\rm cond1}, \Delta t^{\rm (new)}_{\rm cond2}\right) . \tag{3.34}$$

Note that in Paper II we have adapted Eq. (3.31) as the sole criteria used for adaptive timestep control. This is because condition Eq. (3.33) is replaced in Paper II by an upper limit imposed on the timestep. This is due to the presence of explicit terms in the induction equation, caused by the inclusion of large-scale magnetic fields (see Eq. (5.40) in Sect. 5.2).

None of the two criteria, Eq. (3.31) and Eq. (3.33), pose an upper limit on Δt. As a result, the timestep is increased indefinitely in the absence of variations in any variable, thereby strongly indicating that a solution has truly reached a stationary state (we use this fact in Paper II for the construction of stationary disk and large-scale field solutions).

Chapter 4

Implementation of the time-dependent inner boundary in TAPIR

In Sect. 1.2.3 we have outlined the truncation of the disk at some radius r_{t} by a stellar magnetic field (see Eq. (1.14)). In principle, implementing magnetic truncation in TAPIR as a Dirichlet boundary at some radius would simply require setting the inner radius r_{in} equal to r_{t},

$$r_{\mathrm{t}} = r_{\mathrm{in}} = r_3 \; . \tag{4.1}$$

However, including a dynamic, time-dependent inner boundary in TAPIR turned out to be challenging. In the subsequent paragraphs the reasons for these challenges, as well as the solutions to the encountered problems toward a working implementation, are discussed.

Problem: (Too) fast variation of the magnetic truncation radius: The magnetic truncation radius r_{t} is dependent on the accretion rate $\dot{M}$ at the innermost grid point $i = 3$ (see Eq. (1.14)). In the case of quiescent PPDs with minimal variation in $\dot{M}$ over time, r_{t} only moves very moderately between two timesteps. The grid can adapt accordingly in time, consistent with temporal smoothing.

However, a sudden increase in $\dot{M}$ during a FU Ori-like episodic accretion event poses a challenge to the adaptive grid: A radially inward-bound ionization front (see e.g., Bell and Lin, 1994, Paper I) causes a sudden increase in the mass transport rate $\dot{M}$ over many orders of magnitude as soon as the front reaches the inner disk boundary. This results in r_{t} getting pushed fast toward the star over a timescale that may be significantly shorter than t_{visc}, depending on the strength of the outburst. The grid point concentration $\tilde{n}_{\mathrm{i}}$ is determined by the radial gradient of hydrodynamic quantities, such as Σ, e and u_{φ} (see Eq. (3.6)). However, these quantities change on the viscous timescale. Consequently, in the case of the innermost grid point r_{in} moving too quickly, $\tilde{n}_{\mathrm{i}}$ decouples from the rest of the grid.

This leads to a gap between r_{in} and the adjacent grid points, resulting in the issue that small-scale disk features cannot be resolved anymore. Moreover, the simulation is generally very sensitive to variation of the inner boundary. From a mathematical viewpoint, the system of equations is a boundary value problem. This means that the solution of the entire disk depends on the values at the boundary. Inadequate resolution at the inner boundary results in a poor representation of the solution at the inner boundary. Consequently, the Newton-Raphson method may have difficulties in converging toward a solution, leading to an increased number of iteration steps needed, and further to a reduction of the timestep (for an overview over the adaptive timestep control implemented in TAPIR, see Sect. 3.5). This process continues until the simulation stops due to reaching a minimum allowed timestep.

Solution: We have mitigated this issue by limiting the maximum velocity of the innermost grid point, ensuring that the inner boundary cannot decouple from the rest of the grid. The corresponding adaptation of the Dirichlet boundary condition governing the movement of the inner boundary, reads as,

$$r_{\rm in}^{\rm (new)} = \begin{cases} r_{\rm in}^{\rm (old)} + \frac{\Delta t}{\tau_{\rm g}}\left(r_{\rm t}^{\rm (new)} - r_{\rm in}^{\rm (old)}\right) & \forall\, \Delta t < \tau_{\rm g} \\ r_{\rm t} & \forall \Delta t \geq \tau_{\rm g} \end{cases} , \tag{4.2}$$

where $\tau_{\rm g}$, as mentioned earlier, is typically of the order of $t_{\rm visc}$. Eq. (4.2) ensures that for timesteps Δt smaller than the temporal smoothing time, the innermost grid point can only move as far as the rest of the grid can adapt within Δt. In the case of larger timesteps, temporal smoothing is not the limiting factor and the inner boundary is equivalent to $r_{\rm t}$. The smoothing implemented in Eq. (4.2) still allows for a sufficiently fast movement of $r_{\rm in}$ during the onset of an episodic accretion event. This is because occurs on a timescale of the order of years (see e.g., Kóspál et al., 2016), whereas the viscous timescale at ~ 0.04 au is of the order of days (see appendix of Paper I for a comparison of the relevant timescales).

Problem: Inner boundary conditions during initial model construction: The choice of physically relevant boundary conditions is challenging for both explicit and implicit methods. However, extra care must be taken into formulating boundary conditions of implicit methods. The background is that implicit methods involve solving the system of equations at every timestep, which also includes boundary conditions (see Sect. 3.4). In TAPIR, the inner boundary conditions (IBC) for Σ and $u_{\rm r}$ are defined as follows:

$$\left.\frac{\partial \Sigma}{\partial r}\right|_{r=r_{\rm in}} = 0 \qquad \Longrightarrow \qquad \Sigma_2 = \Sigma_3 \,, \tag{4.3}$$

$$\left.\frac{\partial u_{\rm r}}{\partial r}\right|_{r=r_{\rm in}} = 0 \qquad \Longrightarrow \qquad u_{\rm r,2} = u_{\rm r,3} \,. \tag{4.4}$$

The inner boundary condition for e is chosen such that it ensures that the gas temperature at the disk midplane $T_{\rm gas,0}$ remains constant across the inner boundary. This Neumann boundary condition is fully described by viscous heating and stellar irradiation, i.e., advection of inner energy is not considered over the inner boundary,

$$\left.\frac{\partial T_{\mathrm{gas},0}}{\partial r}\right|_{r=r_{\mathrm{in}}} = 0 \qquad \Longrightarrow \qquad T_{\mathrm{gas},0,2} = T_{\mathrm{gas},0,3} \ , \tag{4.5}$$

where $T_{\mathrm{gas},0,\mathrm{i}}$ denotes the midplane gas temperature at the i-th grid point.

In the absence of a stellar magnetic field, a Dirichlet boundary condition enforcing Keplerian rotation, u_{K}, at the inner boundary constant suffices, i.e.$u_{\varphi,3} = u_{\mathrm{K}}$. However, if magnetic torques from the stellar magnetic field are braking the disk, the rotational velocity at the inner boundary is also best described by a zero-gradient Neumann boundary condition,

$$\left.\frac{\partial u_{\varphi}}{\partial r}\right|_{r=r_{\mathrm{in}}} = 0 \qquad \Longrightarrow \qquad u_{\varphi,2} = u_{\varphi,3} \ . \tag{4.6}$$

Implicit methods require an initial model at the time $t = 0$, which already is a solution of the problem, for the Newton-Raphson iteration to work (see Ragossnig et al., 2020, Paper I, see also Sect. 3.4). This is achieved by initially assuming a Keplerian disk without any accretion, which is then evolved in time. As the simulation progresses, the inner boundary transitions from an arbitrary initial position to its final position determined by r_{t}.

The initial position at the start of the simulation is chosen deliberately to be outside the corotation radius r_{cor} (radius where the stellar magnetic field corotates with the disk), or equivalently, $r_{\mathrm{t}} > r_{\mathrm{cor}}$. This way, the influence of a stellar magnetic field gradually increases, as the simulation progresses. This is because the inner boundary slowly moves toward the magnetic truncation radius, which, for typical mass transport rates, is typically inside r_{cor}.

Eventually, this leads to $r_{\mathrm{t}} \sim r_{\mathrm{cor}}$ at some time, which may cause $u_{\varphi} \gtrsim u_{\mathrm{K}}$ for sufficiently strong stellar magnetic fields due to the magnetic propeller effect. The IBCs are formulated as open outflow-conditions (apart from Eq. (4.5)) and, strictly speaking from a mathematical perspective, the equations including the IBCs do not form a well-posed problem. As a consequence, the Newton-Raphson iteration does not find a unique solution determined by the boundary conditions. Instead, it converges toward a random choice from a family of similar solutions. In the special situation of $u_{\varphi} \gtrsim u_{\mathrm{K}}$, a very small change in u_{φ} could lead to randomly changing sign in u_{r} between two subsequent times, caused by the ambiguous nature of the solution. This may result in numerical instabilities at the inner boundary, leading to inaccurate simulation results.

Solution: To ensure a stable simulation, we limit the maximum allowed variation of u_{φ} at the inner boundary. This significantly reduces the probability of u_{φ} switching sign due to the aforementioned ambiguous solution. Additionally, the value of u_{φ} is held constant for an entire iteration cycle, and is updated only if a new solution is found, just before the start of a new iteration cycle (see Fig. 4.1). The reason for this is that a Dirichlet boundary condition is mimicked, by holding the value constant during an iteration cycle, resulting in a significantly *less* less ambiguous solution. The inner boundary condition for u_φ is implemented as follows,

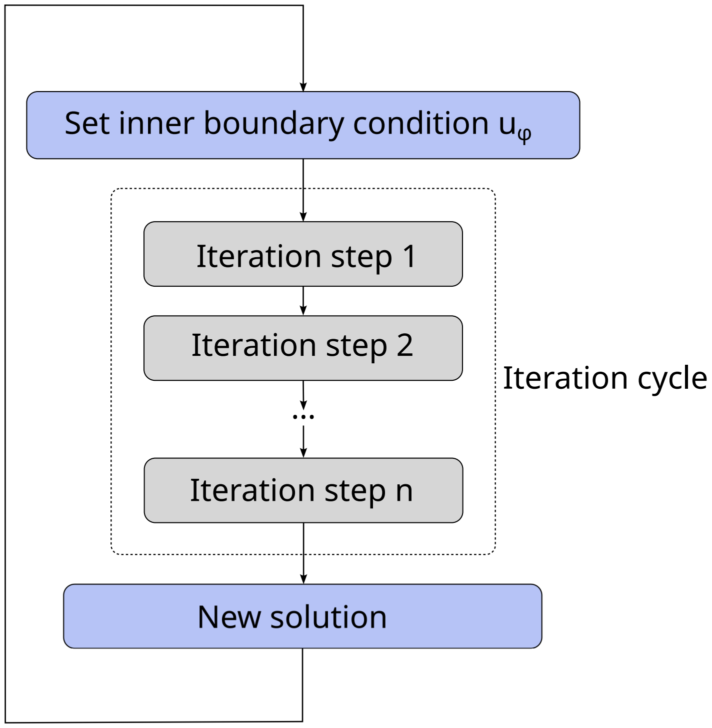

Figure 4.1: Iteration loop towards finding a new solution in TAPIR. The IBC for u_φ is updated at the beginning of an iteration cycle but not for every step.

$$u_{\varphi,2}^{(\mathrm{new})} = u_{\varphi,2}^{(\mathrm{old})} + \frac{\Delta t}{\zeta\, t_{\mathrm{visc}}} \left(u_{\varphi,3}^{(\mathrm{new})} - u_{\varphi,2}^{(\mathrm{old})} \right) , \tag{4.7}$$

where ζ is a parameter governing the variation timescale of u_φ at the inner boundary. Based on our experience with simulations of episodic accretion events, optimal results have been achieved for values of ζ between 10^3 and 10^4. This means that the inner boundary condition for u_φ is varied on a timescale $\sim 10^3$ to $\sim 10^4$ times longer than t_{visc}. This results in a very slow migration of u_φ toward its final value, which is not physically motivated but poses no problem during the construction of an initial model.

Note that during an actual simulation run, the inner disk rim is typically located inside the corotation radius, i.e., $r_{\mathrm{in}} < r_{\mathrm{cor}}$. As mentioned earlier, in this case the ill-posed boundary conditions do not affect the quality of the obtained simulation results. As a consequence, we only apply this very slowly changing IBC for u_φ during the construction of an initial model.

Chapter 5

Implementation of large-scale magnetic fields in TAPIR

The implementation of large-scale magnetic fields in TAPIR requires including the induction equation as a new equation in TAPIR. Large-scale magnetic fields evolve in time and are controlled by the balance between magnetic advection and diffusion. Especially magnetic diffusion demands including non-ideal, laminar, magnetic resistivities, which in turn makes it necessary to also provide a model descrbing the ionization degree within the disk. In the context of 1+1D implicit MHD simulations, both the inclusion of large-scale fields and the magnetic diffusion model pose significant challenges for the following reasons:

- *Non-local magnetic field effects:* Forces caused by large-scale magnetic fields are non-local, which poses a problem for inverting the Jacobian **J** during a Newton-Raphson iteration cycle (see Sect. 3.4). However, efficient and fast inversion of **J** requires a narrow bandwidth of non-zero matrix entries.

- *Vertical structure of disk important for large-scale magnetic fields:* The 1+1D implementation in TAPIR only solves the equations radially whereas the vertical structure is assumed to be hydrostatic. However, large-scale magnetic fields are sensitive to the velocity- and ionization degree profiles also in vertical direction.

- *Analytic descriptions for vertical velocity- and ionization degree profiles:* The construction of the Jacobian **J** requires calculating the derivatives of every variable at every grid point with respect to all variables located at adjacent grid points (5-point or 7-point stencil, see Sect. 3.2). As a result the description of both ionization degree and vertical velocity profiles have to be included as analytic, differentiable functions.

Subsequently, the implementation of the induction equation in TAPIR is shown in Sect. 5.1, whereas the numerical challenges related to the non-local influence of large-scale magnetic fields are discussed in Sect. 5.2.

5.1 New equations in TAPIR

The induction equation reads as,

$$\frac{\partial \mathbf{B}}{\partial t} = \nabla \times (\mathbf{u} \times \mathbf{B} - \eta \nabla \times \mathbf{B}) \ , \tag{5.1}$$

where $\mathbf{B}$, $\mathbf{u}$, and η denote the magnetic field vector, the gas velocity, and the magnetic diffusion (equivalently also named magnetic resistivity), respectively. Assuming an axisymmetric $\mathbf{B}$ and cylindrical coordinates, we can split the magnetic field into a poloidal field $\mathbf{B}_\mathrm{p} = (B_\mathrm{r}, 0, B_\mathrm{z})^\mathrm{T}$ and a toroidal field component B_φ. The poloidal field $\mathbf{B}_\mathrm{p}$, by introducing the magnetic flux function ψ, can be represented in the following way,

$$B_\mathrm{r} = -\frac{1}{r}\frac{\partial \psi}{\partial z} \ , \tag{5.2}$$

$$B_\mathrm{z} = \frac{1}{r}\frac{\partial \psi}{\partial r} \ . \tag{5.3}$$

This allows us to rewrite $\mathbf{B}$ in the following form (see e.g., Guilet and Ogilvie, 2012),

$$\mathbf{B} = -\frac{1}{r}\mathbf{e}_\varphi \times \nabla\psi + B_\varphi \, \mathbf{e}_\varphi \ . \tag{5.4}$$

Finally, using Eq. (5.4), the induction equation Eq. (5.1) can be formulated as an advection/diffusion equation for ψ,

$$\frac{\partial \psi}{\partial t} + \mathbf{u} \cdot \nabla\psi - \eta \, r^2 \, \nabla \cdot \left(\frac{1}{r^2}\nabla\psi\right) = 0 \ . \tag{5.5}$$

Formulating Eq. (5.5) in conservative form enables discretization analogously to the other equations governing hydrodynamic disk evolution (continuity equation, momentum equations, inner energy equation, for a detailed description of the discretization see Ragossnig et al., 2020). Particularly advection is implemented in TAPIR using the *van Leer advection function* (see van Leer, 1974), whcih requires the formulation of the corresponding equation in conservative form. By differentiating Eq. (5.5) with respect to $1/r \, \partial/\partial r$, and by using Eq. (5.3) and Eq. (5.2), we can formulate the advection / diffusion equation for B_z in conservative form (for an axisymmetric thin disk, i.e., $u_\mathrm{z} = 0$). In cylindrical coordinates (r, φ, z) it reads as,

$$\frac{\partial B_\mathrm{z}}{\partial t} + \frac{1}{r}\frac{\partial}{\partial r}(r \, u_\mathrm{r} \, B_\mathrm{z}) - \frac{1}{r}\frac{\partial}{\partial r}\left(\eta \, r \, \frac{\partial B_\mathrm{z}}{\partial r} - \eta \, r \, \frac{\partial B_\mathrm{r}}{\partial z}\right) = 0 \ . \tag{5.6}$$

The first and second term describe how B_z is evolving in time, if B_z is advected with the velocity u_r. The third term corresponds to magnetic diffusion and consists of two parts:

(i) diffusion effects scaling with the radial gradient of B_z, and (ii) the dependency on the vertical disk structure of B_r. Especially this last term expresses the dependency of the vertical magnetic field on the vertical disk structure. Eq. (5.6) can be rewritten in the following way (see e.g., Guilet and Ogilvie, 2012, see also Paper II),

$$\frac{\partial B_z}{\partial t} + \frac{1}{r}\frac{\partial}{\partial r}\left(r\, u_\psi\, B_z\right) = 0\,, \tag{5.7}$$

$$u_\psi \equiv u_r + \frac{\eta}{B_z}\left(\frac{\partial B_r}{\partial z} - \frac{\partial B_z}{\partial r}\right)\,, \tag{5.8}$$

where u_ψ denotes the magnetic flux transport velocity, showing its dependency on magnetic advection and magnetic diffusion.

Vertical averaging of induction equation: The issue with Equs. (5.6) - (5.7) in the context of 1+1D radial hydrodynamic simulations is the vertical dependency of B_r. Consequently, the implementation of a vertical averaging mechanism is important for covering the essentials of magnetic flux transport in disks. Magnetic fields are coupled to the disk gas more effectively in regions of high conductivity σ, or equivalently in regions of low magnetic resistivity $\eta \propto 1/\sigma$. As a result, magnetic advection is expected to be dominant in regions of high σ and serves as the basic idea of conductivity-weighted vertical averaging (see e.g., Guilet and Ogilvie, 2012; Ogilvie, 1997, see also Paper II),

$$\frac{1}{\bar{\bar{\eta}}(r)} = \frac{1}{z}\int_0^z \frac{1}{\eta(r,z')}\,dz'\,, \tag{5.9}$$

$$\bar{\bar{u}}_r(r) = \frac{\bar{\bar{\eta}}}{z}\int_0^z \frac{u_r(r,z')}{\eta(r,z')}\,dz'\,, \tag{5.10}$$

where $\bar{\bar{u}}_r$ and $\bar{\bar{\eta}}$ depict the conductivity-weighted vertically averaged values of the radial advection velocity, and the resistivity, respectively. The vertical average is calculated up to a height that is yet to be determined, referred to as $z_{\rm upper}$. Guilet and Ogilvie (2014) argue that a reasonable choice for $z_{\rm upper}$ is the magnetic surface $z_{\rm B}$ (the height above and below the disk midplane where the magnetic pressure equals the thermal pressure), i.e., $z_{\rm upper} = z_{\rm B}$. This differs from the density-weighted averages typically employed for hydrodynamic quantities such as Σ and e (also used in TAPIR, see e.g., Ragossnig et al., 2020). The reason for this is that the magnetic field cannot be safely averaged between the limits $(-\infty, \infty)$, since for any height $z > z_{\rm B}$ the magnetic field dominates the gas dynamics. The obvious result from averaging this way would be that the vertically averaged magnetic advection velocity $\bar{\bar{u}}_r$ equals the advection velocity in the magnetically dominated disk corona. This result is problematic because the effects of magnetic diffusion inside the disk cannot be described in this way (see e.g., Guilet and Ogilvie, 2014). Moreover, weighting the average with ρ does not capture the dominant quantity driving magnetic advection: as explained earlier, regions with high conductivity $\sigma \propto 1/\eta$ dominantly drive magnetic advection, justifying the use of a conductivity-weighted average (see e.g., Ogilvie and Livio, 2001).

Applying the conductivity-weighted average to Eq. (5.8) leads to an expression for u_ψ (see e.g., Ogilvie and Livio, 2001, see also Paper II),

$$u_\psi = \bar{\bar{u}}_\mathrm{r} + \frac{\bar{\bar{\eta}}}{B_\mathrm{z}} \left(\frac{B_\mathrm{r}(z = z_\mathrm{B}^-)}{z_\mathrm{B}} - z_\mathrm{B} \frac{\partial B_\mathrm{z}}{\partial r} \right) , \tag{5.11}$$

where z_B^- denotes the height that is infinitesimally close to the magnetic surface, yet still within the disk (analogously z_B^+ denotes the height just above the magnetic surface). This distinction is important because we use an analytic profile for B_r, which is connected at the magnetic surface to a force-free magnetic field in the disk exterior (for details see Guilet and Ogilvie, 2014, Paper II). We want to stress the point that the apparent elimination of the dependency of B_r on the vertical structure is deceiving because the vertical disk structure is now incorporated into the vertical averages $\bar{\bar{u}}_\mathrm{r}$ and $\bar{\bar{\eta}}$. Finally, after vertical averaging, we can write Eq. (5.6) as follows,

$$\frac{\partial B_\mathrm{z}}{\partial t} + \frac{1}{r}\frac{\partial}{\partial r}\left(r\, \bar{\bar{u}}_\mathrm{r}\, B_\mathrm{z}\right) - \frac{1}{r}\frac{\partial}{\partial r}\left[\bar{\bar{\eta}}\, r \left(\frac{\partial B_\mathrm{z}}{\partial r} - \frac{B_\mathrm{r}(z = z_\mathrm{B}^-)}{z_\mathrm{B}}\right)\right] = 0 \, . \tag{5.12}$$

Radial magnetic field component B_r^s: As discussed by Guilet and Ogilvie (2014); Ogilvie (1997) and in Paper II, the radial magnetic field component $B_\mathrm{r}(z = z_\mathrm{B}^-)$ in Eq. (5.12) is determined by the disk's vertical structure (i.e., the vertical velocity profile, and the vertical ionization profile, see Sect. 1.2.1). The resulting vertical profile of B_r is unique but for one unknown, which is determined by matching the profile to the external magnetic field at the disk surface, B_r^s. While the required vertical structure is readily provided by analytic expressions (see Paper II), the calculation of B_r^s requires some more explanation from a numerical point of view. If we assume that, (i) there is vacuum above and below the disk beyond the disk surface (i.e., beyond $|z| > z_\mathrm{B}$), and/or (ii) that there are no poloidal currents (equivalently no toroidal field component in the disk magnetosphere, i.e., $B_\varphi(|z| > z_\mathrm{B}) = 0$), then the poloidal large-scale magnetic field is solely determined by toroidal currents in the disk $j_\varphi(r, z)$ (see e.g., Guilet and Ogilvie, 2014; Lubow et al., 1994). This lets us write[1] (see also Paper II),

$$J_\varphi^\mathrm{s} = 2\, B_\mathrm{r}^\mathrm{s} \, , \tag{5.13}$$

where $J_\varphi^\mathrm{s}(r) = \int_0^{z_\mathrm{B}} j_\varphi(r, z')\, dz'$ denotes the surface current density up to the magnetic surface. The magnetic flux function ψ consists of contributions from currents at infinity ψ_∞, the stellar

[1] Note that J_φ^s corresponds to the vertically integrated current density and therefore has the unit $[\mathrm{A\,m^{-1}}]$, which can be readily converted to the magnetic field strength [G].

magnetic field $\psi_\star$, and from currents in the disk ψ_d, which are caused by J^s_φ. Hence, some operator $\mathcal{L}$ must exist that connects J^s_φ to ψ_d (see e.g., Guilet and Ogilvie, 2014; Lubow et al., 1994; Ogilvie, 1997, see also Paper II),

$$\psi_\mathrm{d} = \mathcal{L}\, J^\mathrm{s}_\varphi = 2\,\mathcal{L}\, B^\mathrm{s}_\mathrm{r} \,. \tag{5.14}$$

We are able to obtain B^s_r by applying the inverse operator $\mathcal{L}^{-1}$ to ψ_d,

$$B^\mathrm{s}_\mathrm{r} = \frac{1}{2}\,\mathcal{L}^{-1}\,\psi_\mathrm{d} \,. \tag{5.15}$$

The representation of $2\,\mathcal{L}$ as a linear operator L in the discretized system of equations[2] is discussed in Sect. 5.2, as are the numerical difficulties associated with the efficient inversion of L. In this section, the focus is on the determination of ψ_d. Integrating Eq. (5.3) radially gives,

$$\psi(r) = \psi_\infty + \psi_\star + \psi_\mathrm{d} = \int_0^r r'\, B_\mathrm{z}(r')\, dr' \,. \tag{5.16}$$

We can see that ψ is an integrated quantity, which has certain implications for the discretization of Eq. (5.12). $\psi_\mathrm{d}(r)$ represents the integrated magnetic flux enclosed in the disk at radius r, i.e., $\psi_\mathrm{d} = \psi_\mathrm{d}(B_\mathrm{z}(r \leq r))$. This violates our requirement of localized dependencies, which is important for an efficient inversion of the Jacobian $\mathbf{J}$ (see the requirement of a narrow bandwidth in $\mathbf{J}$ in paragraph 'Localized dependencies' of Sect. 3.2). Therefore, we have included a second new equation in TAPIR covering the integration of Eq. (5.16). This ensures that at every grid point r_i, the equation adds the contribution between $r_{\mathrm{i}-1}$ and r_i to the integral of $\psi_{\mathrm{i}-1}$, which then fulfills the requirement of local dependencies again.

Discretization: Subsequently, the discretization of the two newly added equations, Eq. (5.12) and Eq. (5.16), is briefly discussed. We use the same nomenclature as in Ragossnig et al. (2020) to represent temporal and spatial differences:

$$\delta[X] \triangleq X^{(new)} - X^{(\mathrm{old})} \qquad \text{(temporal difference)}\,, \tag{5.17}$$

$$\Delta(X_\mathrm{i}) \triangleq X_{\mathrm{i}+1} - X_\mathrm{i} \qquad \text{(spatial difference)}\,. \tag{5.18}$$

In order to discretize the terms covering magnetic advection in Eq. (5.12), it is necessary to calculate the fluxes of a quantity over the two cell interfaces at r_i and $r_{\mathrm{i}+1}$ (for the schematics of a cell on the scalar grid, see Sect. 3.2). The discretization has to take into account the

[2] Note that $\mathcal{L}$ corresponds to an operator describing the correlation between B^s_r and J^s_φ for the non-discretized axisymmetric current distribution, whereas L describes the relation between the magnetic field and discrete, axisymmetric current loops for the discretized equations.

movement of the cell interfaces due to the adaptive grid (see Eq. (3.13)),

$$\Delta\mathrm{VolM}_{\mathrm{s,i}} = 2\pi\, r_{\mathrm{i}}\, \bar{\bar{u}}_{\mathrm{r,i}}\, \delta t - \pi \left[\left(r_{\mathrm{i}}^{(\mathrm{new})} \right)^2 - \left((r_{\mathrm{i}}^{(\mathrm{old})} \right)^2 \right] , \tag{5.19}$$

$$\sum \tilde{X} \Delta\mathrm{VolM}_{\mathrm{s}} \triangleq \tilde{X}_{\mathrm{i+1}}\, \Delta\mathrm{VolM}_{\mathrm{s,i+1}} - \tilde{X}_{\mathrm{i}}\, \Delta\mathrm{VolM}_{\mathrm{s,i}} \qquad \text{(advection)} , \tag{5.20}$$

where the sum symbol denotes summation of a quantity over both cell boundaries. δt depicts the timestep (not to be confused with the notation ΔX used earlier, which represents a spatial difference) and $\tilde{X}$ describes the flux-limited quantity X according to the van Leer advection method (see e.g., Ragossnig et al., 2020; van Leer, 1974). Finally, $\mathrm{VolM}_{\mathrm{s,i}}$ describes the change in scalar volume (marked by the subscript "s"), denoting advection of an arbitrary quantity from one grid cell to an adjacent cell with the magnetic advection velocity $\bar{\bar{u}}_{\mathrm{r}}$. B_{z} is a vectorial component oriented in vertical direction. Consequently, analogously to the discretization process of u_{φ}, it is mapped onto the one-dimensional, radial grid (see Sect. 3.2). As a result, B_{z} is localized at the center of a vectorial cell, which is equivalent as if it would be discretized on the scalar grid (see Sect. 3.2).

Integration over the cell volume of a disk (in our case, the cell volume corresponds to a ring) and discretization result in the following final form,

$$\delta[B_{\mathrm{z,i}}] + \sum \tilde{B}_{\mathrm{z}}\, \Delta\mathrm{VolM}_{\mathrm{s}} + 2\pi\, \delta t\, \Delta \left(r_{\mathrm{i}}\, B_{\mathrm{z,i}}\, u_{\psi,\mathrm{i}} \right) = 0 . \tag{5.21}$$

Note that the last term of Eq. (5.21) is formally incorrect. It should read $\Delta \left(r_{\mathrm{i}}\, B_{\mathrm{z,i-1/2}}\, u_{\psi,\mathrm{i}} \right)$. This is because the scalar cell boundaries are at r_{i} and $r_{\mathrm{i+1}}$, whereas the value of B_{z} at those boundaries is $B_{\mathrm{z,i-1/2}} = 1/2(B_{\mathrm{z,i-1}} + B_{\mathrm{z,i}})$ and $B_{\mathrm{z,i+1/2}}$, respectively. However, we have encountered numerical instabilities in the case of a "proper" discretization, making it necessary to use the radially shifted discretization of the diffusion term in Eq. (5.21).

The discretization of Eq. (5.16) is rather straightforward, since this equation is not describing the evolution of ψ; rather, it is used to obtain a localized description of the dependency of ψ_{i} on the total magnetic flux enclosed within the disk up to a radius r_{i}. Consequently, neither advection nor temporal evolution terms are needed, and the discretized equation reads,

$$\psi_{\mathrm{i+1}} = \psi_{\mathrm{i}} + \frac{1}{2}\, B_{\mathrm{z,i}} (r_{\mathrm{i+1}}^2 - r_{\mathrm{i}}^2) , \tag{5.22}$$

where we have used that the discretized value of $B_{\mathrm{z,i}}$ is constant between r_{i} and $r_{\mathrm{i+1}}$.

7-point stencil: The discretized magnetic diffusion term in Eq. (5.21), in its fully expanded form, reads as,

$$2\pi\, \delta t\, \left(r_{\mathrm{i+1}}\, B_{\mathrm{z,i+1}}\, u_{\psi,\mathrm{i+1}} - r_{\mathrm{i}}\, B_{\mathrm{z,i}}\, u_{\psi,\mathrm{i}} \right) , \tag{5.23}$$

which reveals a dependency on $u_{\psi,\mathrm{i}+1}$. Moreover, $u_{\psi,\mathrm{i}+1}$ is dependent on $B_{\mathrm{r,i}+1}(z = z_{\mathrm{B}}^{-})$ (see Eq. (5.11)) and therefore also dependent on the external, force-free magnetic field $B_{\mathrm{r}}^{\mathrm{s}}$ (see Guilet and Ogilvie, 2012; Leung and Ogilvie, 2019, see also Paper II). As discussed further down in the text, $B_{\mathrm{r}}^{\mathrm{s}}$ is implemented in TAPIR with dependencies on ψ at the two adjacent cells in both directions, i.e., $B_{\mathrm{r,i}}^{\mathrm{s}} = f(\psi_{\mathrm{i}-2}, \psi_{\mathrm{i}-1}, \psi_{\mathrm{i}-1}, \psi_{\mathrm{i}-1}, \psi_{\mathrm{i}+2})$ (see paragraph "Inversion of operator L" in Sect. 5.2). Consequently, $B_{\mathrm{r,i}+1}^{\mathrm{s}}$ then has a dependency on $\psi_{\mathrm{i}+3}$, justifying the necessity of applying a 7-point stencil.

Boundary conditions for new equations: The IBCs for Eq. (5.21) and Eq. (5.22) are implemented as Neumann outflow boundary conditions (analogously to the hydrodynamic equations in TAPIR, see Ragossnig et al., 2020, see also Sect. 3.3),

$$\left.\frac{\partial B_{\mathrm{z}}}{\partial r}\right|_{r=r_{\mathrm{in}}} = \left.\frac{\partial \psi}{\partial r}\right|_{r=r_{\mathrm{in}}} = 0\ . \tag{5.24}$$

These conditions describe the advection of magnetic flux across the inner boundary, which prevents the build-up of magnetic flux at the inner boundary. As a result, the radial profiles of B_{z} and ψ do not show any numerical artifacts close to the inner disk boundary.

The outer boundary conditions (OBCs) are chosen in the following way,

$$\left.\frac{\partial B_{\mathrm{z}}}{\partial r}\right|_{r=r_{\mathrm{out}}} = 0\ , \tag{5.25}$$

$$\delta[\psi_{N-3}] + \delta t\, B_{\mathrm{z,N}-3}\, r_{\mathrm{i}}\, u_{\psi,\mathrm{i}} = 0\ . \tag{5.26}$$

The OBC for ψ describes how magnetic flux is transported radially inward or outward across the outer boundary. Consequently, depending on the sign of the magnetic transport velocity u_{ψ}, $\psi_{\mathrm{N}-3}$ is increased or decreased. Note that inflow corresponds to a negative sign of u_{ψ} whereas a positive u_{ψ} denotes outflow of the computational domain, according to the ratio of magnetic advection and magnetic diffusion.

5.2 Numerical challenges

The implementation of large-scale magnetic fields in TAPIR has presented certain challenges. The most fundamental problem is that magnetic fields act on long-range distances. In the context of implementing large-scale fields in TAPIR this means that the requirement of localized dependencies between primary variables cannot be guaranteed (for the discussion about localized dependencies, see Sect. 3.2). Another issue is that the calculation of the linear operator L (equivalent to the operator $\mathcal{L}$, but for discrete current loops) in Eq. (5.14) is time-consuming. In the subsequent paragraphs, these challenges and the solutions to address them, are discussed.

Calculation of operator L**:** The implementation of the operator $\mathcal{L}$ in Eq. (5.14) in the thin-disk limit is as follows (ψ_d is only considered at $z = 0$, see e.g., Guilet and Ogilvie, 2014; Ogilvie, 1997, see also Paper II),

$$\psi_\mathrm{d}(r) = \frac{2}{\pi} \int_{r_\mathrm{in}}^{r_\mathrm{out}} \frac{r\,r'}{r+r'} \left[\frac{(2-k^2)\,K(k) - 2\,E(k)}{k^2} \right] B^\mathrm{s}_\mathrm{r}(r')\,dr' \,, \tag{5.27}$$

$$k^2 \equiv \frac{4\,r\,r'}{(r+r')^2} \,, \tag{5.28}$$

where r_in, r_out, $K(k)$ and $E(k)$ denote the inner and outer disk radii, and the complete elliptic integrals of the first and second kind, respectively. Eq. (5.27) states that the magnetic flux ψ_d consists of the contributions of all current loops J^s_φ (or equivalently B^s_r, see Eq. (5.13)) present in the disk between r_in and r_out.

Following discretization, the integral in Eq. (5.27) is represented by a sum over the contributions of $B^\mathrm{s}_\mathrm{r,j}$ at all other grid points r_j to the magnetic flux at the "i-th" grid point $\psi_\mathrm{d,i}$ (see e.g., Guilet and Ogilvie, 2014),

$$\psi_\mathrm{d,i} = \sum_{j=4}^{N-3} L_\mathrm{ij}\, B^\mathrm{s}_\mathrm{r,j} \,, \tag{5.29}$$

$$L_\mathrm{ij} = \frac{2}{\pi} \int_{r_\mathrm{j-1/2}}^{r_\mathrm{j+1/2}} \frac{r_\mathrm{i}\,r'}{r_\mathrm{i}+r'} \left[\frac{(2-k^2)\,K(k) - 2\,E(k)}{k^2} \right] dr' \,. \tag{5.30}$$

Note that the sum in Eq. (5.29) ranges from 4 to $N-3$. This is due to the adaption of a 7-point stencil (three ghost cells at the inner and outer boundary, see Sect. 3.2). Numerical integration of L_ij at the vectorial "j-th" grid cell n the range $[r_\mathrm{j-1/2}, r_\mathrm{j+1/2}]$ proved to be challenging.

The operator $\mathcal{L}^{-1}$ in Eq. (5.14), representing the relation between an axisymmetric, purely toroidal, current density distribution $J^\mathrm{s}_\varphi(r)$ and an axisymmetric, poloidal magnetic field $\mathbf{B} = (B_\mathrm{r}, 0, B_\mathrm{z})$, represented by ψ_d, is *unique* (see e.g., Jackson, 1999). Consequently, the inverse of this relation, $\mathcal{L}^{-1}$, exists too. Therefore, following discretization, the numerical integration in Eq. (5.30) should be carried out as precisely as possible to ensure that L_ij is still invertible.

However, the magnetic field B at r_i, created by an infinitely thin current loop at r_j, scales with $B \propto 1/|r_\mathrm{i} - r_\mathrm{j}|$, which leads to a logarithmic singularity for the diagonal elements L_ii (see Guilet and Ogilvie, 2014). The integration of a function containing a logarithmic singularity yields a finite result. For this reason we have used the quadrature integration package *quadpack*, which is capable of dealing with singularities while maintaining sufficient integration speed and precision when integrating L_{ij} (method *qapg*, see Piessens et al., 1983).

Inversion of operator L: L_{ij} is a $(N-6)\times(N-6)$-matrix and is inverted using methods from the *LAPACK* library. The inversion process involves a LU-factorization, followed by a subsequent inversion (methods *DGETRF* and *DGETRI* of LAPACK, see Anderson et al., 1999). The resulting inverse L^{-1}_{ij} is used to determine $B^{\mathrm{s}}_{\mathrm{r}}$ in the following way (see also App. A of Paper II),

$$B^{\mathrm{s}}_{\mathrm{r,i}} = \sum_{\mathrm{j=i-2}}^{\mathrm{i+2}} L^{-1}_{\mathrm{ij}}\, \psi^{(\mathrm{new})}_{\mathrm{d,j}} + \sum_{\mathrm{j=4}}^{\mathrm{i-3}} L^{-1}_{\mathrm{ij}}\, \psi^{(\mathrm{old})}_{\mathrm{d,j}} + \sum_{\mathrm{j=i+3}}^{\mathrm{N-3}} L^{-1}_{\mathrm{ij}}\, \psi^{(\mathrm{old})}_{\mathrm{d,j}} \,, \tag{5.31}$$

where $\psi^{(\mathrm{old})}_{\mathrm{d,j}}$ and $\psi^{(\mathrm{new})}_{\mathrm{d,j}}$ represent the magnetic flux due to currents in the disk at the old and new times, respectively. The first term in Eq. (5.31) is the “implicit” part, denoted by a function f, of the form $B^{\mathrm{s}}_{\mathrm{r,i}} = f(\psi_{\mathrm{i-2}}, \psi_{\mathrm{i-1}}, \psi_{\mathrm{i-1}}, \psi_{\mathrm{i-1}}, \psi_{\mathrm{i+2}})$. Note that also the dependencies of $B^{\mathrm{s}}_{\mathrm{r,i-1}}$ and $B^{\mathrm{s}}_{\mathrm{r,i+1}}$ are needed (i.e., as part of $u_{\psi,\mathrm{i+1}}$ in Eq. (5.21)), which is why we cannot include the dependencies $\psi_{\mathrm{i-3}}$ and $\psi_{\mathrm{i+3}}$ in the implicit term due to the limitations of the 7-point stencil.

The operator L_{ij} is dependent only on the position of the grid points r_{i}. In the case of a rigid grid this means that the inverse L^{-1}_{ij} must be calculated only once. However, due to the inner disk position being time-dependent, a moving grid has to be used (apart from the fact that the grid in TAPIR is adaptive in general, see Sect. 3.1 and Ch. 4). As a result, it is necessary to calculate L^{-1}_{ij} for each iteration step. L_{ij} is a $(N-6)\times(N-6)$-matrix and its calculation and inversion is numerically expensive. To mitigate the numerical cost, we have implemented two different approaches in TAPIR:

1. *Skipping inversion for a couple of timesteps:* The idea is that the grid variations between two timesteps are typically very small, indicating that the inversion of L_{ij} can be omitted until the current grid configuration deviates noticeably from the grid positions used for the calculation of L^{-1}_{ij} (see App. A of Paper II).

2. *Partially rigid grid:* A partially rigid grid facilitates a more efficient calculation of L^{-1}_{ij}. Realizing a partially rigid grid in TAPIR involves changes to the grid equation (see Sect. 3.1) and implementing blockwise inversion of L_{ij}. The details of this approach are explained below.

The grid has been modified to stay adaptive in the inner disk region for all grid points $i < i_{\mathrm{fixed}}$:

$$\text{grid configuration} = \begin{cases} \text{adaptive grid} & \forall i \in [4, i_{\mathrm{fixed}}] \\ \text{fixed grid} & \forall i \in [i_{\mathrm{fixed}}, N-3] \end{cases} . \tag{5.32}$$

It is sufficient to hold the outer grid points constant and to use the grid equation only on the grid points between $[4, i_{\text{fixed}}]$ (see Sect. 3.1). The spatial and temporal smoothing built into the grid equation (see Eq. (3.8)) then allows the grid point concentration $\tilde{n}_{\text{i}_{\text{fixed}}}$ at $r_{\text{i}_{\text{fixed}}}$, to smoothly transition from the variable grid to the constant $\tilde{n}_{\text{i}}$ of the fixed grid. Therefore, the grid is fully described by the following set of equations,

$$\tilde{n}_4 = \tilde{n}_5 \qquad \text{(constant grid point concentration at } i = 4) \; , \tag{5.33}$$

$$\tilde{n}_{\text{i}_{\text{fixed}}-1} = \tilde{n}_{\text{i}_{\text{fixed}}} \qquad \text{(constant grid point concentration at grid point } i_{\text{fixed}}) \; , \tag{5.34}$$

$$\frac{\tilde{n}_{\text{i}}}{\mathcal{R}_{\text{i}}} = \frac{\tilde{n}_{\text{i}-1}}{\mathcal{R}_{\text{i}-1}} \qquad \text{(grid equation for } i \in [5, i_{\text{fixed}} - 1]) \; , \tag{5.35}$$

$$r_{\text{i}}^{(\text{new})} = r_{\text{i}}^{(\text{old})} \qquad \text{(constant grid for } i \in [i_{\text{fixed}}, N - 3]) \; , \tag{5.36}$$

A fixed grid between $r_{\text{i}_{\text{fixed}}}$ and r_{out} allows us to invert L_{ij} more efficiently by identifying different block matrices L_{var}, L_{mixed} and L_{const},

$$L_{\text{ij}} = \begin{pmatrix} L_{\text{var}} & L_{\text{mixed}}^{\text{T}} \\ L_{\text{mixed}} & L_{\text{const}} \end{pmatrix} , \tag{5.37}$$

where we have used that L_{ij} is symmetric (see Lubow et al., 1994). L_{const} represents the contributions from the constant grid and has the dimension $(N - 3 - i_{\text{fixed}}) \times (N - 3 - i_{\text{fixed}})$ matrix[3] (recall that N represents the number of grid points), whereas L_{var} represents contribution solely from the variable grid and is a $(i_{\text{fixed}} - 3) \times (i_{\text{fixed}} - 3)$ matrix. The non-quadratic matrix L_{mixed} denotes long-range contributions from both the fixed and the variable grid and has the rank $(N-3-i_{\text{fixed}}) \times (i_{\text{fixed}}-3)$. The matrix L_{const} remains constant over the whole simulation, thereby requiring to be calculated and inverted only once. The inversion can then be calculated as follows,

$$L_{\text{ij}}^{-1} = \begin{pmatrix} L_{\text{var}}^{-1} + L_{\text{var}}^{-1} \, L_{\text{mixed}}^{\text{T}} \, S^{-1} \, L_{\text{mixed}} \, L_{\text{var}}^{-1} & -L_{\text{var}}^{-1} \, L_{\text{mixed}}^{\text{T}} \, S^{-1} \\ -S^{-1} \, L_{\text{mixed}} \, L_{\text{var}}^{-1} & S^{-1} \end{pmatrix} , \tag{5.38}$$

$$S \equiv L_{\text{const}} - L_{\text{mixed}} \, L_{\text{var}}^{-1} \, L_{\text{mixed}}^{\text{T}} \, , \tag{5.39}$$

where we have introduced the matrix S. The only matrix inversions required are L_{var}^{-1} and S^{-1}, In the case of a relatively small variable grid region, the numerical cost of inverting L_{ij} is significantly reduced.

[3] Note that the innermost and outermost three grid cells are ghost cells. As a result, only the "real" grid is used for calculations of L_{ij}, explaining the range of $[4, N - 3]$, between which the grid is split into an adaptive and a fixed part.

Timestep limitations: The second and third terms in Eq. (5.31) use $\psi_{\rm d,j}^{\rm (old)}$ at the old time, and are therefore "explicit" terms. These explicit term do not result in additional entries in the Jacobian (see Sect. 3.4). These explicit terms enter the induction equation Eq. (5.21) as part of the diffusion term. Theoretically, this results in certain restrictions on the timestep due to the CFL condition. However, the electric current loops that predominantly contribute to the creation of the magnetic field at some radius $r_{\rm i}$ are those that are closest to the magnetic field line at $r_{\rm i}$. These adjacent current loops are therefore calculated implicitly.

Consequently, only subdominant terms are calculated explicitly, significantly reducing the risk of numerical instability due to the violation of the CFL condition. Nevertheless, we noticed numerical instability issues in the case of changes in $\psi_{\rm i}$, $B_{\rm z,i}$, or $r_{\rm i}$ between the old and new solution exceeding a certain threshold. For this reason a large series of simulations were conducted, revealing that restricting the timestep to the CFL limit in disk regions where the magnetic field is not stationary yet (i.e., $\partial/\partial t \mathbf{B} \neq 0$), leads to a stable simulation. The maximum allowed timestep according to the CFL, $\delta t_{\rm CFL}$, is given by (see Guilet and Ogilvie, 2014; Lubow et al., 1994),

$$\delta t_{\rm CFL} = \min_{\partial/\partial t \mathbf{B} \neq 0} \left(\frac{\Delta r}{\pi \left| u_\psi - \bar{\bar{u}}_{\rm r} \right|} \right) , \tag{5.40}$$

where $u_\psi - \bar{\bar{u}}_{\rm r}$ describes the diffusion velocity of the magnetic field. In comparison to the CFL condition of Guilet and Ogilvie (2014), we only have to consider diffusion for an estimate of the maximum stable timestep, since magnetic advection is calculated implicitly. Once the magnetic field has reached stationarity in a certain disk region, the simulations do not become unstable anymore in this region, even for timesteps exceeding the CFL limit, i.e., $\delta t \gg \delta t_{\rm CFL}$.

Part III

Publications

Chapter 6

Paper I - Impact of the inner boundary on disk evolution

Title: Time-dependent, long-term hydrodynamic simulations of the inner protoplanetary disk - I. The importance of stellar magnetic torques
Authors: **D. Steiner**, L. Gehrig, B. Ratschiner, F. Ragossnig, E. I. Vorobyov, M. Güdel, E. A. Dorfi
Year: 2021
Journal: Astronomy & Astrophysics 655, A110 (2021)
State of publication: Published
DOI: 10.1051/0004-6361/202140447

Personal Contribution: As first author, the majority of the writing has been done by me. All figures but one (Appendix, Fig. A.1) have been done by me. All simulations have been performed by me. Most of the work on the simulation code has been done by me. The co-authors have written or rewritten single paragraphs and have provided feedback on the final manuscript and in the form of scientific discussions.

This publication examines the impact of a magnetically truncated inner boundary on the long-term evolution of disks in the context of episodic accretion events. We have used an implicit time integration method to include the inner disk region in long-term hydrodynamical simulations of protoplanetary disks. The position of the disk's truncation radius depends on parameters such as the stellar magnetic field strength and the accretion rate in the innermost region. To study these dependencies we have performed a parameter study, in which we modified the stellar dipole strength. We can show that the modified disk dynamics due to a stellar dipole field can be sufficient to either facilitate or suppress the development of episodic accretion, dependent on the stellar magnetic field strength. We have also analyzed in detail the significance of a self-consistent hydrodynamical treatment of the inner disk in the context of axisymmetric 1+1D models.

A&A 655, A110 (2021)
https://doi.org/10.1051/0004-6361/202140447

Astronomy & Astrophysics

Time-dependent, long-term hydrodynamic simulations of the inner protoplanetary disk

I. The importance of stellar magnetic torques

D. Steiner[1], L. Gehrig[1], B. Ratschiner[1], F. Ragossnig[1], E. I. Vorobyov[1,2], M. Güdel[1], and E. A. Dorfi[1,†]

[1] Institute for Astronomy (IfA), University of Vienna, Türkenschanzstrasse 17, 1180 Vienna, Austria
e-mail: daniel.steiner@univie.ac.at
[2] Institute of Astronomy, Russian Academy of Sciences, 48 Pyatnitskaya St., Moscow 119017, Russia

Received 29 January 2021 / Accepted 8 May 2021

ABSTRACT

Aims. We conduct simulations of the inner regions of protoplanetary disks (PPDs) to investigate the effects of protostellar magnetic fields on their long-term evolution. We use an inner boundary model that incorporates the influence of a stellar magnetic field. The position of the inner disk is dependent on the mass accretion rate as well as the magnetic field strength. We use this model to study the response of a magnetically truncated inner disk to an episodic accretion event. Additionally, we vary the protostellar magnetic field strength and investigate the consequences of the magnetic field on the long-term behavior of PPDs.

Methods. We use the fully implicit 1+1D TAPIR code which solves the axisymmetric hydrodynamic equations self-consistently. Our model allows us to investigate disk dynamics close to the star and to conduct long-term evolution simulations simultaneously. We assume a hydrostatic vertical configuration described via an energy equation which accounts for the radiative transport in the vertical direction in the optically thick limit and the equation of state. Moreover, our model includes the radial radiation transport in the stationary diffusion limit and takes protostellar irradiation into account.

Results. We include stellar magnetic torques, the influence of a pressure gradient, and a variable inner disk radius in the TAPIR code to describe the innermost disk region in a more self-consistent manner. We can show that this approach alters the disk dynamics considerably compared to a simplified diffusive evolution equation, especially during outbursts. During a single outburst, the angular velocity deviates significantly from the Keplerian velocity because of the influence of stellar magnetic torques. The disk pressure gradient switches sign several times and the inner disk radius is pushed towards the star, approaching $<1.2\,R_\star$. Additionally, by varying the stellar magnetic field strength, we can demonstrate several previously unseen effects. The number, duration, and the accreted disk mass of an outburst as well as the disk mass at the end of the disk phase (after several million years) depend on the stellar field strength. Furthermore, we can define a range of stellar magnetic field strengths, in which outbursts are completely suppressed. The robustness of this result is confirmed by varying different disk parameters.

Conclusions. The influences of a prescribed stellar magnetic field, local pressure gradients, and a variable inner disk radius result in a more consistent description of the gas dynamics in the innermost regions of PPDs. Combining magnetic torques acting on the innermost disk regions with the long-term evolution of PPDs yields previously unseen results, whereby the whole disk structure is affected over its entire lifetime. Additionally, we want to emphasize that a combination of our 1+1D model with more sophisticated multi-dimensional codes could improve the understanding of PPDs even further.

Key words. accretion, accretion disks – stars: formation – stars: magnetic field – stars: protostars – protoplanetary disks

1. Introduction

During the collapse of a molecular cloud, a protostar and its surrounding protostellar disk are formed. Observations of such star–disk systems reveal that the luminosity of the central object varies with time (e.g. Herbig 1989; Contreras Peña et al. 2017). Some of those young variable stars can be classified as FU Orionis (FU Ori) objects, which show a rise in luminosity over several orders of magnitudes for a short period of time (e.g., Hartmann & Kenyon 1996; Audard et al. 2014). Spectroscopic observations by Zhu et al. (2007) and Eisner & Hillenbrand (2011) indicate that such high-luminosity phases (bursts) are associated with an increased accretion rate of disk material onto the protostar. The frequency of FU Ori-type eruptions in the solar neighborhood suggests that a protostellar accretion burst is not a single but a recurring phenomenon (Hartmann & Kenyon 1996). Moreover, numerical simulations indicate that an FU Ori-like star–disk system undergoes at least 10 to 20 such eruptive events (Hartmann & Kenyon 1996).

Thermal instability (TI) of the inner disk provides a possible explanation for the aforementioned eruptive episodic accretion events. Ionization of most of the hydrogen in the very inner parts of a disk ($10\,R_\odot \lesssim r \lesssim 0.1$ AU) leads to enhanced viscosity caused by runaway heating of the optically thick inner disk regions and therefore to an increased accretion rate (e.g., Bell & Lin 1994). Although their model is able to predict bursts, the explanation of the burst duration is unsatisfying because of the narrow radial region in which the disk can become sufficiently ionized and hence may become thermally unstable (Zhu et al. 2009a). To expand the potentially thermally unstable regions of a disk, a model with vertical layers of different viscosity has been proposed (e.g., Gammie 1996). A warm, irradiated

[†] Deceased.

surface layer is sufficiently ionized for the magneto-rotational instability (MRI) to efficiently operate, but also acts as a shield for the deeper disk layer close to the midplane. Hence, MRI cannot develop in the deep layer and the subsequent reduced viscosity leads to a pile-up of material from the outer disk (dead zone). Eventually, the gas temperature in the dead zone rises above a certain threshold, caused by enhanced viscous heating of the accumulated mass. The deep disk layer then becomes MRI unstable, which may be sufficient to trigger the TI in the dead zone, effectively broadening the radial region where the disk can become thermally unstable. Recent work (e.g., Armitage et al. 2001; Zhu et al. 2009a, 2010) assumed gravitational instabilities (GIs) to act as an effective mechanism to enhance the mass transport rate from the outer disk towards the inner regions. However, observations of low-luminosity accretion events –identified as FU Ori events (see e.g., Kóspál et al. 2016; Hillenbrand et al. 2018)– show that low-mass protostellar star–disk systems with masses lower than 0.01 $M_{\odot}$ can also undergo episodic accretion. Those systems are, contrary to FU Ori for example, not in the embedded (Class I) but in the late Class II phase (cf. Kóspál et al. 2016) and additionally have disks with masses $M_{\rm disk} \approx 0.01\,M_{\odot}$, which are too low for GI to contribute significantly (even in the outer disk) to the averaged mass transport rate.

As TI is likely to develop in the very inner disk parts, especially for low-mass disks, the position of the inner disk rim is a crucial parameter. Magneto-hydrodynamic (MHD) simulations in 3D show that protoplanetary disks are eventually disrupted by strong protostellar magnetic fields (e.g., Romanova et al. 2004; Bouvier et al. 2007; Romanova & Kurosawa 2014; Romanova & Owocki 2015). The accretion flow is then funneled along magnetic field lines onto the star. This is especially important in the case of episodic accretion, as then the inner disk rim is moving towards the star (e.g., Hartmann et al. 2016; Zhu et al. 2020) and consequently the inner disk dynamics is altered. To be able to consider the influence of stellar magnetic torques on the disk evolution and simultaneously calculate the radial position of the inner disk radius self-consistently, it is necessary to solve the full set of hydrodynamic equations.

The work of Bell & Lin (1994), Armitage et al. (2001) and Zhu et al. (2007, 2008, 2009a) for example is able to explain FU Ori-like outbursts by either purely thermally unstable inner disks or by including a layered viscosity model. Due to time-step limitations of explicit methods, especially in disk regions close to the star ($r \leq 0.5$ AU) (Appendix A), neither the influence of protostellar magnetic fields nor the effects of local steep pressure gradients could be reproduced. However, the findings of Bouvier et al. (2007) and Romanova & Kurosawa (2014), for example, indicate that the very inner regions of disks are crucial for understanding episodic accretion. Recent hydrodynamic models of MRI and thermal instability bursts (Bae et al. 2013; Kadam et al. 2020; Vorobyov et al. 2020) have strong limitations in modeling the innermost disk regions, therefore necessitating the development of numerical codes that can realistically treat the star–disk interface in global disk simulations. Combining the requirements of (i) self-consistent treatment of both the gas dynamics in the inner disk including the effects of a stellar magnetic field and the position of the inner disk radius, (ii) the inclusion of an energy equation to investigate the effects of TI-induced episodic accretion, and (iii) maintaining the ability to resolve the very inner disk parts of a few stellar radii and carry out long-term calculations up to a few million years, we choose to use an implicit 1+1D RHD code (TAPIR, see Stoekl & Dorfi 2014; Ragossnig et al. 2020) that enables us to meet all the requirements without being time-step-limited by the Courant-Friedrichs-Levy (CFL) condition (Appendix A). Until now, no comparable numerical code has combined the above requirements. We also compare our simulations to similar work (e.g., Zhu et al. 2010, 2020) and point out the differences due to a time-dependent and self-consistent treatment of the component $u_{\varphi}(r,t)$.

In Sect. 2 we briefly describe the physical equations and the layered viscosity model. Details of our method and the implementation of the boundary conditions used are explained in Sect. 3. The position of the inner disk edge as well as the importance of a consistent treatment of the inner disk region is outlined in Sect. 4. Our results are presented and discussed in Sect. 5 and are then summarized in Sect. 6.

2. Physical setup

Protoplanetary disks and their evolution in time can be described by adopting the equations of hydrodynamics using the turbulent viscosity prescription introduced by for example Shakura & Sunyaev (1973) or Balbus & Hawley (1991) and an energy equation. This set of equations is briefly presented in Sect. 2.1. Additionally, the stellar magnetic field (Sect. 2.2), a description of the energy equation (Sect. 2.3), the adapted viscosity model (Sect. 2.4), and the gas and dust opacities (Sect. 2.5) are presented.

2.1. Theoretical framework

The following equations describe the time evolution of a viscous accretion disk in the thin-disk limit (pressure scale-height $H_{\rm p} \ll$ radius r) around a protostar. The energy equation contains radial and vertical radiation transport in an approximated way (see Sect. 2.3) and incorporates irradiation from the central object. Because of the thin-disk approximation, the equations can be vertically integrated and read as,

$$\frac{\partial}{\partial t}\Sigma + \nabla\cdot(\Sigma\,\boldsymbol{u}) = 0, \tag{1}$$

$$\frac{\partial}{\partial t}(\Sigma\,\boldsymbol{u}) + \nabla\cdot(\Sigma\,\boldsymbol{u}:\boldsymbol{u}) - \frac{B_z\boldsymbol{B}}{2\pi} + \nabla P_{\rm gas} + \nabla\cdot Q + \Sigma\,\nabla\psi + H_{\rm p}\,\nabla\left(\frac{B_z^2}{4\pi}\right) = 0, \tag{2}$$

$$\frac{\partial}{\partial t}(\Sigma\,e) + \nabla\cdot(\Sigma\,\boldsymbol{u}\,e) + P_{\rm gas}\,\nabla\cdot\boldsymbol{u} + Q:\nabla\boldsymbol{u} - 4\pi\,\Sigma\,\kappa\,(J-S) + \dot{E}_{\rm rad} = 0, \tag{3}$$

where Σ, $P_{\rm gas}$, and $\boldsymbol{u}$ denote the gas column density, the vertically integrated gas pressure, and the gas velocity vector, respectively. Q represents the viscous pressure tensor and ψ marks the gravitational potential of the system (star and disk). In most of our calculations, we focus on late class II systems, in which the gravitational force from the protostar dominates. The protostellar magnetic field is presented by $\boldsymbol{B} = (B_{\rm r}, B_{\varphi}, B_z)^{\rm T}$ and is modeled via a prescribed field in polodial and torodial directions (see Sect. 2.2). The term $B_z\,\boldsymbol{B}/2\,\pi$ corresponds to magnetic stress exerted on the disk gas, whereas $\nabla(B_z^2/4\pi)$ describes the magnetic pressure force density. In Eq. (3), e denotes the specific internal energy density, J stands for the zeroth moment of the radiation field and S represents the source function. The $(J-S)$ in Eq. (3) is treated approximately as described in Sect. 2.3. To describe the internal structure of the ideal gas in radial and vertical directions, we utilize the ideal equation of state (EOS),

$$P_{\rm gas} = (\gamma - 1)\,e, \tag{4}$$

where γ denotes the adiabatic coefficient.

2.2. Stellar magnetic field

Livio & Pringle (1992) used an analytic approach to describe a stellar magnetic field which threads an accretion disk,

$$B_z(r) = B_\star \left(\frac{R_\star}{r}\right)^3, \tag{5}$$

$$B_\varphi^{\mathrm{I}}(r) \simeq B_z(r)\left(1 - \frac{\Omega(r)}{\Omega_\star}\right), \tag{6}$$

where B_z is the vertical magnetic field component and is assumed to have a positive sign. The stellar magnetic field is modeled in Eqs. (5) and (6) as a dipole field and a toroidal component B_φ^{I} due to the torque exerted on the threaded protoplanetary disk by the stellar magnetic field, respectively. However, Eq. (6) has the problem that $|B_\varphi| \gg |B_z|$ very close to the star. Therefore, various authors (e.g., Rappaport et al. 2004; Kluźniak & Rappaport 2007) use a slightly modified version of Eq. (6), which reads,

$$\alpha_{\mathrm{cor}} = \begin{cases} +1 & \text{if } r < r_{\mathrm{cor}} \\ -1 & \text{if } r > r_{\mathrm{cor}} \end{cases}, \tag{7}$$

$$B_\varphi^{\mathrm{II}}(r) \simeq -\alpha_{\mathrm{cor}}\, B_z(r)\left[1 - \left(\frac{\Omega_\star}{\Omega(r)}\right)^{\alpha_{\mathrm{cor}}}\right]. \tag{8}$$

The superscripts I and II are applied to differentiate between the two models for B_φ, whereas α_{cor} takes account of changing the field prescription to inside and outside the corotation radius. The model described by B_φ^{II} confers the advantage that $|B_\varphi| \approx |B_z|$ for radii not close to r_{cor}. This is also physically motivated, as larger $|B_\varphi|$ are not possible because a too tightly wound up toroidal field would lead to an opening up of the field configuration because of the increased magnetic energy (see e.g., Rappaport et al. 2004). Typical values for the protostellar magnetic field are of the order of several kG (see e.g., Bouvier et al. 2007; Kurosawa et al. 2008).

2.3. Energy equation

The energy equation Eq. (3) is described by Ragossnig et al. (2020) and accounts for viscous heating, radiative cooling, and radial diffusion of inner energy. Furthermore, a vertical radiation transport is included to also account for stellar irradiation on to the surface of the disk. In cylindrical coordinates, Eq. (3) reads,

$$Q = \frac{\mu}{2}\left[\nabla \boldsymbol{u} + (\nabla \boldsymbol{u})^{\mathrm{T}} - \frac{2}{3}(\nabla \cdot \boldsymbol{u})\,\mathbb{1}\right], \tag{9}$$

$$\epsilon_Q \equiv 2\,Q : \boldsymbol{\nabla u}, \tag{10}$$

$$\frac{\partial}{\partial t}(\Sigma\, e) + \frac{1}{r}\frac{\partial}{\partial r}(r\, u_{\mathrm{r}}\, \Sigma\, e) + P\frac{1}{r}\frac{\partial}{\partial r}(r\, u_{\mathrm{r}}) + \epsilon_Q + \dot{E}_{\mathrm{rad}} - 4\pi\,\frac{\sigma}{3\,r\,\pi}\frac{\partial}{\partial r}\left(\frac{r}{\kappa_{\mathrm{R}}\,\rho}\frac{\partial T_0^4}{\partial r}\right) = 0, \tag{11}$$

where the second and third terms in Eq. (11) represent advection due to accretion and work done by pressure, respectively. Here, ϵ_Q denotes the viscous energy dissipation (e.g., Tscharnuter & Winkler 1979). The last term in Eq. (11) describes radial radiative transport as a diffusion approximation in the Eddington limit (e.g., Ragossnig et al. 2020), whereas $\dot{E}_{\mathrm{rad}}$ depicts the net radiation heating or cooling rate per unit surface area of the protoplanetary disk. This latter can be obtained by solving the vertical, stationary radiation transfer equation in the optically thick limit ($\tau \to \infty$) assuming local thermal equilibrium and utilizing an Eddington factor $f_{\mathrm{edd}} = 1/3$,

$$\dot{E}_{\mathrm{rad}} = \frac{8\sigma}{3\tau}\left(T_0^4 - T_{\mathrm{surf}}^4\right). \tag{12}$$

$\dot{E}_{\mathrm{rad}}$ is a balance of protostellar irradiation $\dot{E}_{\mathrm{irr}}$, radiative cooling $\dot{E}_{\mathrm{cool}}$, and irradiation from the ambient medium $\dot{E}_{\mathrm{amb}}$,

$$\dot{E}_{\mathrm{rad}} + \dot{E}_{\mathrm{irr}} + \dot{E}_{\mathrm{amb}} - \dot{E}_{\mathrm{cool}} = 0, \tag{13}$$

$$\dot{E}_{\mathrm{irr}} = \frac{L_\star}{r^2\,\pi}\, f_{\mathrm{irr}}\, \max\left[\Delta\left(\frac{H_{\mathrm{p}} - H_\star}{r}\right), 0\right], \tag{14}$$

$$\dot{E}_{\mathrm{amb}} = 2\,\sigma T_{\mathrm{amb}}^4, \tag{15}$$

$$\dot{E}_{\mathrm{cool}} = 2\,\sigma T_{\mathrm{surf}}^4, \tag{16}$$

where $L_\star$ and $H_\star$ denote stellar luminosity and an effective stellar radius, respectively. Furthermore, black-body irradiation is assumed for the cooling term and the ambient radiation. The final form reads (Ragossnig et al. 2020),

$$\dot{E}_{\mathrm{rad}} = \sigma\frac{1}{1+\tau'}\left(T_0^4 - T_{\mathrm{amb}}^4\right) - \frac{L_\star}{r^2\,\pi}\, f_{\mathrm{irr}}\, \max\left[\Delta\left(\frac{H_{\mathrm{p}} - H_\star}{r}\right), 0\right], \tag{17}$$

$$\tau' \equiv \frac{3}{4}\tau, \tag{18}$$

where f_{irr} determines how much of the irradiation can be processed by the gas and which fraction gets reflected.

2.4. Viscosity model

The kinematic viscosity ν is defined as (Shakura & Sunyaev 1973)

$$\nu = \alpha\, c_{\mathrm{S}}\, H_{\mathrm{P}}, \tag{19}$$

where α is the viscous parameter, c_{S} the isothermal sound speed, and H_{p} the pressure scale height. We apply the thin-disk approximation (Armitage 2010) which allows a vertical integration of the physical disk quantities via the EOS,

$$P_{\mathrm{gas,0}} = \rho_0\, c_{\mathrm{S}}^2, \tag{20}$$

where $P_{\mathrm{gas,0}}$ is the midplane gas pressure. The vertically integrated dynamical viscosity μ is then written as

$$\mu = \alpha\, c_{\mathrm{S}}\, H_{\mathrm{P}}\, \Sigma. \tag{21}$$

For the viscosity parameter α we adopt the layered-viscosity model (Gammie 1996), which is a sum of contributions of vertically stratified disk layers,

$$\alpha = \alpha_{\mathrm{base}} + \alpha_{\mathrm{surf}} + \alpha_{\mathrm{deep}} + \alpha_{\mathrm{grav}}, \tag{22}$$

where α_{base} is a base value for the viscosity (e.g., within a deadzone) and α_{surf} is the MRI viscosity in the permanently active surface layer, which is ionized by cosmic rays and stellar irradiation for example. α_{deep} accounts for the viscosity in parts of the disk, where the temperature exceeds the threshold for thermal ionization (e.g., Zhu et al. 2009a). The parameter α_{grav} denotes GIs acting as effective viscosity.

The separation of the surface and deep layer is controlled by the local surface density. If the surface density at an arbitrary radius exceeds a value Σ_0, the disk develops a deep disk layer at that radius. To handle this, we introduce a density switch that is $s_\Sigma = 1$ if $\Sigma \geq \Sigma_0$ and $s_\Sigma = 0$ if $\Sigma \leq \Sigma_0$. Parts of the deep layer then become MRI active if the local gas temperature T_0 is higher than a constant temperature threshold $T_{\rm active}$ for thermal ionization. Hence, the viscosity parameter for the surface layer reads

$$\alpha_{\rm surf}(r) = \alpha_{\rm MRI}\left[s_\Sigma \frac{\Sigma_0}{\Sigma(r)} + (1 - s_\Sigma)\right], \tag{23}$$

where $\alpha_{\rm MRI}$ (e.g., Zhu et al. 2010; Hartmann & Bae 2018) is a constant value for MRI-active regions. We adopt $\Sigma_0 = 100\,{\rm g\,cm^{-2}}$ for all calculations in this work. Additionally, the viscosity parameter for the deep layer is temperature dependent, that is,

$$\alpha_{\rm deep}(r) = \alpha_{\rm MRI}\, s_\Sigma \left(1 - \frac{\Sigma_0}{\Sigma(r)}\right) s(T_0), \tag{24}$$

where $s(T_0)$ is a temperature switch,

$$s(T_0) = \frac{1}{2}\left[1 + \tanh\left(\frac{T_0 - T_{\rm active}}{T_{\rm width}}\right)\right], \tag{25}$$

which controls whether the deep layer is MRI-active or not (see e.g., Flock et al. 2016). For faster convergence of the Newton-Raphson iteration method (see Sect. 3), Eq. (25) is utilized to establish a smooth transition between active and inactive parts within the deep layer, where $T_{\rm width} = 10{-}50\,{\rm K}$ is a smoothing width for the temperature. This smooth transition creates a temperature zone below $T_{\rm active}$ in which viscosity is already increased and the disk becomes MRI unstable. This MRI active zone starts at $\approx T_{\rm active} - 2 \cdot T_{\rm width}$.

We define the viscosity parameter for gravitationally unstable regions as

$$\alpha_{\rm grav} = \alpha_{\rm GI}\, s_{\rm G}\left(\frac{Q^2_{\rm T,crit.}}{Q^2_{\rm T}} - 1\right), \tag{26}$$

where $\alpha_{\rm GI} = 0.01$ is a constant value for gravitationally unstable regions within the disk, and $Q_{\rm T}$ is the Toomre parameter (Toomre 1964). The critical value for the Toomre parameter at which GIs occur is set to $Q_{\rm T,crit} = 1.0$. The quantity $s_{\rm G}$ is a switch for the GI and is $s_{\rm G} = 1$ if the disk is unstable ($Q_{\rm T} < Q_{\rm T,crit.}$) and $s_{\rm G} = 0$ otherwise. In this paper we have chosen disks with masses low enough ($M_{\rm disk} < 0.1\,M_\star$) to not exceed the Toomre criterion, thus avoiding GIs within the disk.

2.5. Gas and dust opacities

For the gas opacity description $\kappa_{\rm R,gas}$ we use the Rosseland-mean opacity tables created by Ferguson et al. (2005), who compiled low-temperature opacity tables by employing opacity sampling methods with a considerably higher sampling resolution than the previous opacity tables provided by Alexander & Ferguson (1994). In this work we use opacities for solar abundance ($X = 0.7$, $Z = 0.02$) based on Caffau et al. (2011) in the temperature range from 500 K to 30 000 K.

Opacities below 500 K are dust-dominated, and therefore we use the dust opacity model introduced by Pollack et al. (1985) for very low temperatures. Dust grains are believed to consist of silicates, iron, troilite, organics, and ice (see e.g., Pollack et al. 1994; Henning & Stognienko 1996), which can have different metal abundances and shapes. Pollack et al. (1985) divided silicates into iron-poor, iron-rich, and normal species, which have

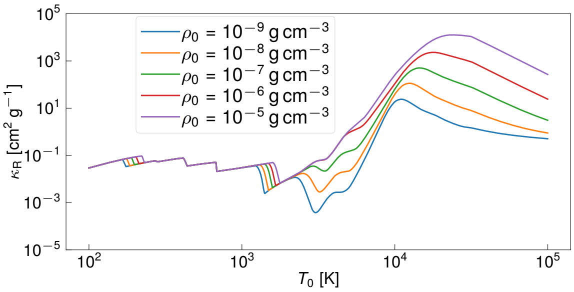

Fig. 1. Rosseland-mean opacities $\kappa_{\rm R}$ for various midplane gas densities ρ_0.

Fe/(Fe + Mg) ratios of 0.0, 0.4, and 0.3, respectively. These latter authors also considered different shapes as spherical and aggregate grains, as well as a distinction between homogeneous, composite, and porous dust grains. For our calculations, the dust-to-gas ratio $f_{\rm dust}$ is kept constant in the whole disk and in time, which is an oversimplification. However, we do not treat gas and dust separately in our simulations and cannot calculate a time-dependent and radially changing $f_{\rm dust}$. The total Rosseland-mean opacity $\kappa_{\rm R}$ for various midplane gas densities $\rho_0(r)$ is shown in Fig. 1 and can be calculated by combining gas and dust opacities,

$$\kappa_{\rm R} = \kappa_{\rm R,gas} + f_{\rm dust}\,\kappa_{\rm R,dust}. \tag{27}$$

3. Method description

The reasons for using a 1D implicit integration method in this work are briefly explained in Sect. 3.1 and the method is described in Sect. 3.2. Some vital details of our numerical method are briefly presented in Sect. 3.3, whereas the boundary conditions used in our simulation are presented in Sect. 3.4. An implicit numerical integration scheme needs an initial model to start the simulation with. The construction of such a model is briefly outlined in Sect. 3.5.

3.1. Justification of the 1D approach

In recent years, the advent of 2D and 3D models of protoplanetary disks (e.g., Zhu et al. 2009b, 2020; Vorobyov & Basu 2007; Vorobyov & Pavlyuchenkov 2017; Kadam et al. 2019) has lead to a detailed understanding of the complicated interactions of equally important physical processes abundant in such star–disk systems. Hence, the question must be asked, what new insights can be added by another 1D approach.

The study of magnetically truncated, self-consistently simulated protoplanetary disks cannot (at the time of writing) be combined with an investigation of the influence of magnetic fields on the long-term disk behavior. This is because of severe time-step limitations for simulations of the inner disk. An implicit integration scheme (see Sect. 3.2) is not limited to those restrictions (see Appendix A).

We understand that global protoplanetary disk simulations outside the very inner regions ($r > 0.5$ AU) should be at least 2D for studies of the gravitationally unstable phases of disk evolution (e.g., Vorobyov et al. 2019), and 3D for a detailed understanding of complex features such as turbulence for example (e.g., Flock et al. 2016). However, in the region within approximately 0.5 AU, those models are confined to coarse simplifications (e.g., to the viscous diffusion ansatz or an inner "smart" sink-cell approach) and cannot include important features such as the effects of torques caused by a protostellar magnetic field. Besides time-step limitations imposed by the CFL condition, multi-dimensional models are either confined to a limited, specific simulation region compared to the whole disk dimensions (e.g., Vorobyov et al. 2019) or tend to evolve towards a quasi-stationary state after several orbital periods of the inner disk (e.g., Romanova et al. 2004; Zhu et al. 2020). Both cases are not ideal for investigating the long-term effects over several million years in the innermost disk region. Additionally, the increased shearing forces towards smaller radii tend to smooth out instabilities in angular directions (see e.g., Lesur 2020) in the very inner disk.

Using an implicit numerical method allows consistent treatment of the inner disk by including the effects of a stellar magnetic field while simultaneously maintaining the ability to carry out long-term evolution studies. Additionally, the self-consistent treatment of large-scale magnetic fields during protoplanetary disk evolution as well as the interaction of the stellar magnetic field and the inner disk makes it necessary to solve the toroidal velocity component u_φ in a time-dependent manner in order to cover magnetic torques (see e.g., Lubow et al. 1994; Guilet & Ogilvie 2012, 2014). Disk winds are not included in our simulations but will be addressed separately in a follow-up paper. Apart from a more realistic handling of the radial gas flow, this further supports the choice of solving all hydrodynamic quantities for long-term evolution studies of protoplanetary accretion disks.

The hydrodynamic equations for protoplanetary disks are formulated as a boundary value problem. It is equally true for explicit and implicit methods that boundary conditions for the column density Σ, the gas velocity $\boldsymbol{u}$ and the internal energy e imposed on the disk at the inner and outer boundaries determine the radial structure and influence its evolution. An implicit time integration on the other hand will not converge towards a solution at a new time, if the boundary conditions are chosen such that no physical radial structure for Σ, $\boldsymbol{u}$, and e can be found for the equations involved. Therefore, an implicit method, despite being more difficult to set up, provides feedback with respect to the physical correctness of the boundary conditions used (see Dorfi & Drury 1987; Stoekl & Dorfi 2014, for further details).

Consequently, a 1D implicitly integrated simulation of the inner disk can indeed lead to a better understanding of important features and could for example be used as the inner boundary for more sophisticated 2D and 3D models by providing a physically more accurate description of the very inner regions (e.g., Crida et al. 2007).

3.2. Implicit integration scheme

A numerical method utilizing an implicit integration scheme (e.g., Dorfi & Drury 1987; Stoekl & Dorfi 2014) requires a substantial amount of additional work in development compared to explicit methods. This is because, for each iteration in time Δt, a Jacobian has to be constructed, which consists of the derivations of each variable at a certain grid point with respect to each variable at every grid point in the computational domain. This matrix must then be subsequently inverted as often as a multidimensional Newton-Raphson iterator needs to converge towards a new solution of the problem at a new time $t + \Delta t$. Another complication is the requirement of an initial model that already solves the discretized set of algebraic equations. The additional work for an implicit integration scheme has the advantage of not being time-step-limited by the Courant-Friedrichs-Levy (CFL) condition. This translates into a condition that information is not transported over more than one grid cell during a single time-step. This constraint effectively limits the time-step of every hydrodynamic disk simulation with an explicit time-integration scheme. Comparing the time-step of our implicit method to the constraint dictated by the CFl condition (see Appendix A), we can confirm that the simulation time would be increased by several orders of magnitude to achieve the same radial resolution (2000 radial points are used throughout the simulations in this paper) in the inner regions of the disk with an explicit method. Consequently, full-blown 3D MHD calculations are very time-consuming and can only be conducted for between a few hundred and a maximum of one thousand orbital periods (see e.g., Romanova & Kurosawa 2014; Zhu et al. 2020), which would result in an inner disk radius of $r_{\mathrm{in}} = 0.06\,\mathrm{AU}$ for a covered simulation time-period of $t_{\mathrm{total}} \leq 15$ years.

3.3. Numerical method details

The equations are formulated in one-dimension in the radial direction, are axisymmetric and conservative, and are integrated using a finite-volume method. Also, a van Leer advection scheme (van Leer 1977) is used at the cell boundaries. This ensures that the method is second order in space, while the same accuracy in time is achieved by using time-centered variables (for details see e.g., Dorfi 1998; Dorfi et al. 2006).

The equations are discretized by using a staggered mesh (see Ragossnig et al. 2020), where scalar entities as column density Σ and internal energy e are discretized on a scalar mesh while vector-like quantities as the gas velocity component u_{r} are discretized on the vector mesh, which is spatially displaced from the scalar mesh by half a grid cell. The velocity component u_φ is of vectorial nature, because for the degeneration of grid cell faces in the angular direction for a 1D radial treatment, u_φ has to be discretized at the scalar mesh. In addition to the numerical treatment of the physical equations, we use an adaptive numerical grid. We apply the grid point distribution introduced by Dorfi (1998), which avoids the need for coping with artificially introduced perturbations due to grid adaptations, because the mesh configuration is simultaneously solved with the equations. The specific details of our numerical method as well as the detailed discretizations performed for the physical set of equations presented in equations Eqs. (1)–(3) and the implementation of the grid equation can be studied in more detail in Ragossnig et al. (2020).

3.4. Numerical boundary conditions

Protoplanetary disk quantities such as surface density structure $\Sigma(r)$, disk mass M_{disk}, and accretion flow $\dot{M}(r)$ sensitively depend on the choice of the inner and outer boundary conditions imposed on the disk. At the inner boundary, magnetic torques caused by the stellar magnetic field brake the disk in the angular direction, and consequently the radial flow starts to accelerate towards the star. At a certain point, the magnetic field dominates the disk dynamics and the accretion transitions from a radial drift into an accretion stream along magnetic funnels. The simulation of this magnetically dominated region is intrinsically 3D and cannot be tackled by a 1D approach (see e.g., Bouvier et al. 2007; Romanova & Kurosawa 2014). Hartmann et al. (2016) argued that the disk approximation fails at the magnetic truncation radius r_{trunc} and is therefore chosen as our inner boundary r_{in} as defined in Eq. (47).

A self-consistent treatment of the inner boundary requires the angular velocity to adapt to the magnetic torque of the stellar magnetic field. This is best represented with a zero gradient condition,

$$\left.\frac{\partial u_\varphi}{\partial r}\right|_{r=r_{\rm in}} = 0, \tag{28}$$

$$\left.\frac{\partial u_{\rm r}}{\partial r}\right|_{r=r_{\rm in}} = 0. \tag{29}$$

The gas temperature structure at the inner boundary is chosen such that the sum of contributions of viscous heating and stellar irradiation determines the gas temperature at the inner boundary, which is mapped by employing a Van Neumann boundary condition for the midplane gas temperature T_0 at the inner boundary,

$$\left.\frac{\partial T_0}{\partial r}\right|_{r=r_{\rm in}} = 0. \tag{30}$$

At the inner boundary, the surface density $\Sigma_{\rm in}$ must be able to adapt to different mass transport rates $\dot{M}_{\rm in}$, for example during an episodic accretion event. Hence, we choose a Van Neumann boundary condition for $\Sigma_{\rm in}$,

$$\left.\boldsymbol{\frac{\partial \Sigma}{\partial r}}\right|_{\boldsymbol{r=r_{\rm in}}} \boldsymbol{= 0}. \tag{31}$$

At the outer boundary, a mass flux $\dot{M}_{\rm out}$ is assumed to act as an external mass reservoir for the disk.

$$\left.\frac{\partial \Sigma}{\partial r}\right|_{r=r_{\rm out}} = 0, \tag{32}$$

$$u_{\rm r}(r_{\rm out}) = \frac{\dot{M}_{\rm out}}{2\,\pi\, r_{\rm out}\, \Sigma(r_{\rm out})}. \tag{33}$$

The angular velocity u_φ is assumed to be Keplerian and a Van Neumann boundary condition is used for the internal energy e at the outer boundary condition, which results in

$$\left.\frac{\partial e}{\partial r}\right|_{r=r_{\rm out}} = 0, \tag{34}$$

$$u_\varphi(r_{\rm out}) = \Omega_{\rm K}(r_{\rm out})\, r_{\rm out}, \tag{35}$$

where $\Omega_{\rm K}(r_{\rm out})$ is the Keplerian velocity at the outer boundary. In this study, we focus on the star–disk interaction, and therefore an outer radius of 30 AU is chosen for all simulations.

3.5. Stationary initial model

An implicit numerical method requires an initial model to start with, which already solves the discretized equations along with the grid equation described by Dorfi (1998). Although, in principle, every solution to the set of equations can be used as a starting model, we aim to construct stationary solutions to start our simulations. Such solutions can be used for verification of the numerical method, because analytical results exist for the assumption of time-independence (see e.g., Armitage 2010).

We construct these stationary solutions in a two-stage process. At first, we choose a Keplerian disk with no radial velocity $u_{\rm r}$ (see Fig. 2). This disk is in local thermal equilibrium (LTE) in the vertical and radial directions. Second, we introduce a time-independent mass flow across the outer boundary $\dot{M}_{\rm out}$. Collectively, a certain outer mass flux, other boundary conditions, stellar parameters (mass $M_\star$, luminosity $L_\star$, magnetic field $B_\star$, rotation period P, and radius $R_\star$), and viscosity model parameters (cf. Sect. 2.4) fully determine the internal radial structure of the disk.

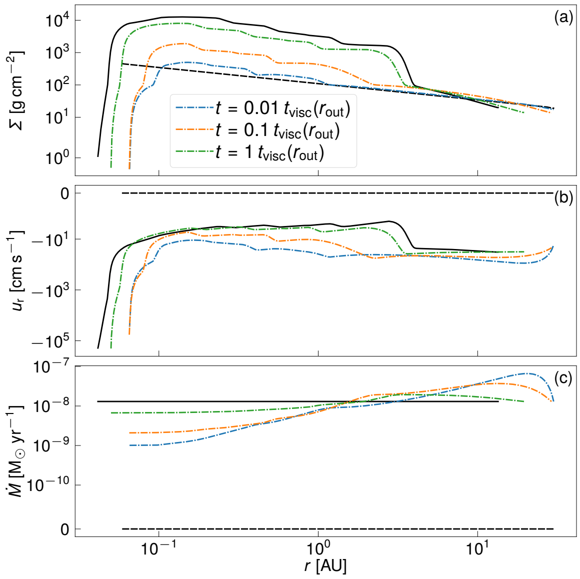

Fig. 2. Snapshots in time, which show the convergence towards a stationary initial model for (*a*) the surface density $\Sigma(r)$, (*b*) the radial velocity $u_{\rm r}(r)$, and (*c*) the mass transport rate $\dot{M}$. The black dashed line shows the initial Keplerian disk, and the black solid line denotes the final stationary model.

The transition from the starting model to the stationary model occurs on the viscous timescale $t_{\rm visc}$,

$$t_{\rm visc}(r) = \frac{r^2}{\nu(r)}. \tag{36}$$

In Fig. 2 this transition can be seen as mass is transported through the disk, fed by $\dot{M}_{\rm out}$. After $t \gtrapprox t_{\rm visc}(r_{\rm out})$, the disk becomes stationary and has adjusted to the boundary conditions and the mass transport rate of the stationary initial model $\dot{M}_{\rm init}$ is constant throughout the whole disk, and therefore $\dot{M}_{\rm init}$ is equal to $\dot{M}_{\rm out}$ (cf. panel c of Fig. 2). We also note that $r_{\rm in}$ adjusts accordingly for a changing value of $\dot{M}$ (cf. Fig. 2 and Sect. 4.3).

We want our simulations to trigger thermal instability and to develop an episodic accretion onto the protostar. During construction of the initial model, this behavior is undesired, and therefore outbursts have to be prevented. We achieve this by increasing the activation temperature $T_{\rm active}$ during the first stage to a value that the disk gas temperature T_0 does not surpass at any radius. As the model becomes stationary, the time-step can rise due to the implicit nature of the numerical method. Contrary to explicit numerical methods, time-steps can become larger than the viscous timescale $t_{\rm visc}$, because they are not restricted by the CFL condition. This effectively subdues the thermal instability, which develops on a much shorter thermal timescale. Therefore, after $\Delta t > t_{\rm visc}(r_{\rm out})$, the initial model construction enters the second stage, where we smoothly decrease $T_{\rm active}$ to the desired value and let the disk model become stationary. We note that this procedure is not physical but is utilized to generate a quasi-stationary initial model, which solves the equations of hydrodynamics.

4. The importance of the inner disk region

The limitations imposed on explicit numerical methods by the CFL condition (see Sect. 3.3) are mitigated in Bell & Lin (1994) and subsequent works (e.g., Armitage et al. 2001; Zhu et al. 2009a) by using a diffusion ansatz with a low spatial resolution (compared to our approach) for describing the radial disk evolution. In Sect. 4.1 the differences between a full hydrodynamic simulation and the diffusion ansatz are investigated. The importance of the pressure force is evaluated in Sect. 4.2 and the position of the inner disk boundary is discussed in Sect. 4.3.

4.1. Revisiting the diffusion equation

The radial evolution equation reads (e.g., Pringle 1981),

$$\frac{\partial \Sigma}{\partial t} = -\frac{1}{r}\frac{\partial}{\partial r}\left[\frac{1}{(r^2\,\Omega)'}\frac{\partial}{\partial r}(\nu\,\Sigma\,r^3\,\Omega')\right], \tag{37}$$

where $\Omega(r)$ corresponds to the angular velocity. In the derivation of Eq. (37), pressure gradients are not included in the angular momentum equation (e.g., Pringle 1981). If $\Omega(r) \propto \Omega_\mathrm{K}(r)$, with $\Omega_\mathrm{K}(r)$ depicting the Keplerian velocity, Eq. (37) becomes

$$\frac{\partial \Sigma}{\partial t} = \frac{3}{r}\frac{\partial}{\partial r}\left[\sqrt{r}\,\frac{\partial}{\partial r}(\nu\,\Sigma\,\sqrt{r})\right], \tag{38}$$

$$u_\mathrm{r} = -\frac{3}{\Sigma\,\sqrt{r}}\frac{\partial}{\partial r}(\nu\,\Sigma\,\sqrt{r}), \tag{39}$$

where the continuity equation Eq. (1) is used to obtain a formulation for the radial drift velocity u_r. Torques due to for example protostellar magnetic fields cannot be treated in a self-consistent way with Eq. (38), because this would involve braking (or acceleration) of the angular velocity component in a way in which $\Omega(r)$ is no longer proportional to $\Omega_\mathrm{K}(r)$. In order to see the impact of a perturbation in the angular velocity profile $\Omega(r)$, one can model the angular velocity as Keplerian with a small linear perturbation Ω_1,

$$\Omega(r) = \Omega_\mathrm{K}(r) + \Omega_1(r). \tag{40}$$

After linearization of Eq. (37) with respect to Ω_1, the following expression is obtained:

$$f_\mathrm{corr} = \frac{2\,(r^2\Omega_1)'}{r\,\Omega_\mathrm{K}} + \frac{2\,(\nu\,\Sigma\,r^3\Omega_1')'}{3\,(\nu\,\Sigma\,r^2\Omega_\mathrm{K})'}, \tag{41}$$

$$\frac{\partial \Sigma}{\partial t} = \frac{3}{r}\frac{\partial}{\partial r}\left[\sqrt{r}\,\frac{\partial}{\partial r}(\nu\,\Sigma\,\sqrt{r})\,(1 - f_\mathrm{corr})\right]. \tag{42}$$

$$u_\mathrm{r} = -\frac{3}{\Sigma\,\sqrt{r}}\frac{\partial}{\partial r}(\nu\,\Sigma\,\sqrt{r})(1 - f_\mathrm{corr}), \tag{43}$$

where a primed quantity A' denotes its radial derivative $\partial A/\partial r$. The first term of the correction factor f_corr depends on the radial gradient of Ω_1; hence a radially localized, sharp perturbation in $\Omega(r)$ can lead to a non-negligible effect. During the onset of an FU Ori-like outburst, an ionization front is propagating radially inwards and outwards through the disk (for a detailed discussion see Bell & Lin 1994). Along these waves, the disk is adapting itself to a changed disk temperature and viscosity. Various authors (e.g., Bell & Lin 1994; Armitage 2010; Zhu et al. 2009a) have shown that those waves occur in the column density $\Sigma(r)$, the internal energy profile $e(r)$, and in the radial mass transport rate $\dot{M}(r)$. However, the ionization front is also visible as a wave in the radial angular velocity profile $\Omega(r)$, which then modifies the accretion rate and subsequently the density profile. The second term in Eq. (41) takes into account that a modified relative angular velocity between two neighboring radial disk annuli also changes the shear that those disk rings are experiencing. f_corr can be interpreted as the deviation from the viscous contribution to the diffusion equation. In Eq. (43) a correction factor $f_\mathrm{corr} > 1$ leads to a radially localized, outward-bound mass flow, which is caused by redistribution of angular momentum in sharp angular velocity perturbations $\Omega_1(r)$.

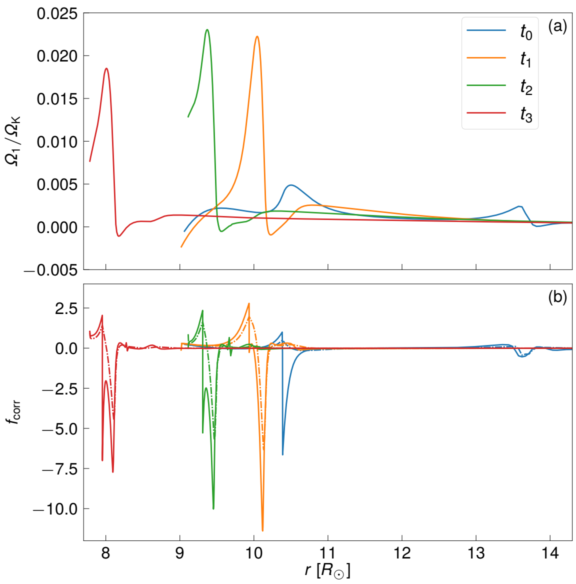

Fig. 3. *a*: Ω_1 waves for four different, arbitrarily chosen times t_0 to t_3 during the onset of a FU Ori-like outburst. *b*: correction factors as defined in Eq. (41) for the same times as in (*a*). The dashed-dotted lines correspond to the first term in Eq. (41), whereas the full lines show the total value of f_corr.

In Sect. 5.1 we provide a detailed description of the perturbations during the onset of a FU Ori-like outburst, whose influence on f_corr is shown in Fig. 3. An angular velocity perturbation Ω_1 induced by sharp peaks of MRI efficiency due to density waves causes a radially localized peak in $|f_\mathrm{corr}|$. Four snapshots are taken for four different times $t_0 < t_1 < t_2 < t_3$ immediately after the onset of TI and shows the inward-bound ionization front (cf. Sect. 5.1). The first term of Eq. (41) is plotted separately in Fig. 3 to show the direct influence of a nonKeplerian velocity u_φ compared to the additional influence of altered shear between two neighboring disk annuli. For a yet unpronounced perturbation at time t_0, the modified shear clearly dominates f_corr, but at later times t_1 to t_3 the direct influence of Ω_1 is also non-negligible. While the diffusion equation approach Eq. (38) appears to be well suited to describing the disk evolution in the absence of such waves, without solving the momentum equation in angular direction, there are, at least locally, substantial deviations to be expected.

The deviations in Fig. 3 represent a snapshot during time evolution at a certain time t, which can affect the short term behaviour of the disk. A more qualitative way to investigate how strongly a certain disk region is affected by f_corr over a longer period of time is shown in Fig. 4. During the duration of an outburst ($\Delta t_\mathrm{burst} \sim 20$ years) in our fiducial model, we have added

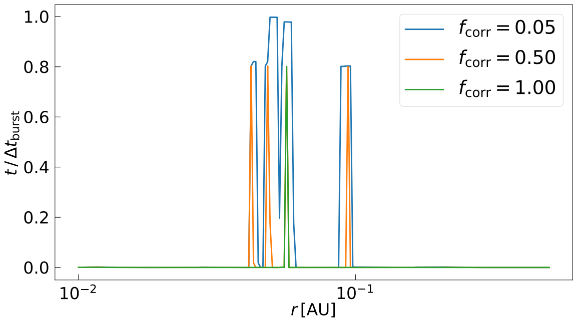

Fig. 4. Time relative to the burst duration in the fiducial model $\Delta t_{\rm burst}$, in which a region in the inner 0.5 AU exceeds a certain $f_{\rm corr}$ threshold (0.05, 0.5 and 1.0). The radial range is divided in 200 equally spaced logarithmic bins.

up the times in which the absolute value of $f_{\rm corr}$ is larger than a certain threshold (0.05, 0.5 and 1.0). In the innermost disk ($\lesssim$0.1 AU) $f_{\rm corr}$ can exceed 0.05 over 90% of $\Delta t_{\rm burst}$. Even values of $f_{\rm corr} = 0.50$ and $f_{\rm corr} = 1.00$ are exceeded during 80% of $\Delta t_{\rm burst}$ in some regions of the inner disk.

4.2. Importance of the pressure gradient

In a steady-state protoplanetary disk the gas rotation velocity u_φ (neglecting radial viscous forces, magnetic fields, and radial advection of momentum) is essentially given by

$$\frac{u_\varphi^2}{r} \approx \frac{G\,M_\star}{r^2} + \frac{1}{\rho}\frac{\mathrm{d}P}{\mathrm{d}r}. \tag{44}$$

Therefore, in order to have a subKeplerian steady-state accretion disk, the pressure gradient has to yield $\mathrm{d}P/\mathrm{d}r < 0$. For all radii but the very innermost parts ($r < 0.1$ AU), this condition is usually fulfilled. Furthermore, the pressure gradients are of minor order compared to the centrifugal forces, and at the inner boundary a zero-torque boundary condition is usually applied for such models in the absence of a stellar magnetic field. For example the IBC applied by Bell & Lin (1994),

$$\Sigma(r = r_{\rm in}) \approx 0, \tag{45}$$

models a disk extending to the stellar surface and therefore accounts for the transition of a protoplanetary disk to $u_{\rm r} = 0$. However, a magnetically braked inner disk has an increased accretion rate and therefore a lower column density Σ and diminished gas pressure $P_{\rm gas,0}$ close to the inner rim (see Fig. 5). Hence, in the very innermost regions ($r \lessapprox 0.2$ AU) the pressure gradient force $-\boldsymbol{\nabla} P$ (cf. Eq. (2)) helps the gravitational force to push material inwards, which leads to a super-Keplerian u_φ according to Eq. (44). This can also be seen in Fig. 3, where $\Omega_1 > 0$ (except for the declining slopes of the ionization fronts). The pressure gradient force also exceeds the viscous force contribution in the region of the ionization front (see Sect. 5.1). In the very inner regions, the diffusion equation ansatz of Eq. (38) is less suitable for describing the time evolution of the disk. This is especially true for thermally unstable disks (cf. Figs. 3 and 5), where due to localized perturbations of u_φ the deviations from the diffusion equation Eq. (38) are non-negligible (see Fig. 4).

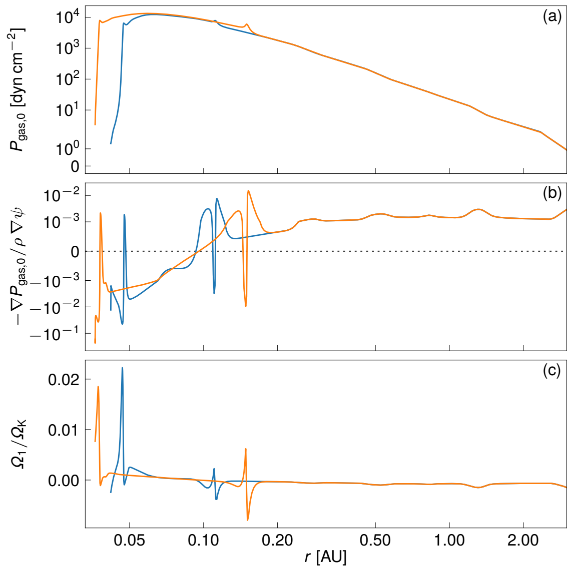

Fig. 5. *a*: midplane gas pressure $P_{\rm gas,0}$ between 0.04 AU and 2 AU for two different times during an FU Ori like outburst. *b*: midplane pressure gradient force $-\nabla P_{\rm gas,0}$ relative to the gravitational force is plotted. The radially localized changes in sign occur at the positions of the ionization fronts running inwards and outwards. The deviation from the Keplerian angular velocity is shown in (*c*).

4.3. The position of the inner disk boundary

The inner disk is coupled to the star via the stellar magnetic field, which means that, inside the corotation radius $r_{\rm cor}$, the angular momentum of the disk is transferred to the protostar, whereas outside of $r_{\rm cor}$ the disk is accelerated. This star–disk connection results in mutual transfer of angular momentum between the star and the inner disk (e.g., Matt et al. 2010). However, in the present study, the spin-up or spin-down of the star due to gain or loss of angular momentum is not considered, as our focus is on the influence of stellar magnetic torque on the inner disk. The inclusion of angular momentum transfer introduces a further complexity which makes it more difficult to separate the various influences altering the long-term evolution of a protoplanetary disk and has to be investigated in further studies.

The corotation radius is defined according to Kepler's third law,

$$r_{\rm cor} = \left(\frac{GM_\star P^2}{4\pi^2}\right)^{1/3}, \tag{46}$$

where P is the stellar rotational period. Following Herbst et al. (2001), we choose the stellar rotation period $P = 6$ days such that $r_{\rm cor} \approx 0.06$ AU for all simulations in this work. Magnetic torques tend to slow down the disk inside $r_{\rm cor}$ and the disk's toroidal velocity u_φ becomes subKeplerian. Consequently, the disk material inside $r_{\rm cor}$ starts to radially accelerate towards the star until it reaches the magnetic truncation radius $r_{\rm trunc}$. Inside $r_{\rm trunc}$, the magnetic pressure of the stellar dipole field exceeds the ram pressure $P_{\rm ram}$ of the infalling material, and therefore the disk gets disrupted and accretes along magnetic funnels onto the star. Consequently, $r_{\rm trunc}$ is a natural choice for the inner disk edge in the case of strong accretion, where $P_{\rm ram}$ exceeds the gas pressure $P_{\rm gas}$. Consequently, $r_{\rm in}$ is given as follows (for details

Table 1. Simulation run parameters.

Model	$M_\star$ [$M_\odot$]	$R_\star$ [$R_\odot$]	$B_\star$ [kG]	$r_{\rm cor}$ [AU]	$M_{\rm disk,init}$ [$M_\odot$]	$\dot{M}_{\rm init}$ [$M_\odot$ yr^{-1}]	$\alpha_{\rm MRI}$	$\alpha_{\rm MRI}/\alpha_{\rm base}$	$T_{\rm active}$ [K]
`fid`	1.0	1.5	2.0	0.0609	10^{-2}	1.3×10^{-8}	2.1×10^{-2}	50	1530
`1p5kG`	1.0	1.5	1.5	0.0609	10^{-2}	1.3×10^{-8}	2.1×10^{-2}	50	1530
`3p0kG`	1.0	1.5	3.0	0.0609	10^{-2}	1.3×10^{-8}	2.1×10^{-2}	50	1530
`4p0kG`	1.0	1.5	4.0	0.0609	10^{-2}	1.3×10^{-8}	2.1×10^{-2}	50	1530
`5p0kG`	1.0	1.5	5.0	0.0609	10^{-2}	1.3×10^{-8}	2.1×10^{-2}	50	1530

cf. Hartmann et al. 2016):

$$r_{\rm in}(P_{\rm gas} < P_{\rm ram}) \approx 18\,\xi\,R_\odot \left(\frac{B_\star}{10^3\,{\rm G}}\right)^{4/7} \left(\frac{R_*}{2\,R_\odot}\right)^{12/7} \left(\frac{M_\star}{0.5\,M_\odot}\right)^{-1/7} \times \left(\frac{\dot{M}_\star}{10^{-8}\,M_\odot/{\rm yr}}\right)^{-2/7}, \quad (47)$$

where $B_\star$, $R_\star$, and $M_\star$ are the stellar magnetic field at the stellar surface, the protostellar radius, and its mass, respectively, and ξ is a correction factor that accounts for the rather complicated details of disk–star interactions and is usually set to $\xi < 1$ according to Hartmann et al. (2016). In this work, we choose $\xi = 0.65$. Further, $\dot{M}_\star$ denotes the accretion flow over the inner boundary onto the star and is in general time-dependent. As the inner radius $r_{\rm in}$ is dependent on the accretion rate $\dot{M}_\star$, it is likely to move inwards during increased accretion, for example during a FU Ori-like burst. The magnetic field cannot withstand the high accretion rate during an outburst event, and therefore the stellar magnetosphere gets squashed closer to the star. The movement of the inner boundary according to the time-dependent mass accretion rate $\dot{M}_\star(t)$ for our fiducial model (see Table 1 and Sect. 5.1) during an outburst is shown in Fig. 6. During an outburst, $r_{\rm in}$ is pushed towards the stellar radius $R_\star$ (cf. Eq. (47)). We want to emphasize that our method is able (from a numerical point of view) to cover the case of $r_{\rm in} \sim R_\star$ in combination with long-term simulations.

In regions where the ram pressure $P_{\rm ram}$ exceeds the gas pressure $P_{\rm gas}$, Eq. (47) describes the movement of $r_{\rm in}$ well. If $P_{\rm gas}$ is larger than $P_{\rm ram}$, the protostellar magnetic field is able to disrupt the disk as soon as the magnetic pressure $P_{\rm mag} = B_z^2/(8\,\pi)$ becomes comparable to $P_{\rm gas}$, which for a dipole field approximation occurs at

$$r_{\rm in}(P_{\rm gas} > P_{\rm ram}) = \frac{{B_\star}^{1/3} R_\star}{{P_{\rm gas}}^{1/6}\,(8\pi)^{1/6}}. \quad (48)$$

In this work, we find two scenarios in thermally unstable disks where the gas pressure $P_{\rm gas}$ exceeds the accretion ram pressure $P_{\rm ram}$. The first is after an outburst, when the accretion rate decreases until the disk evolves towards the next burst (cf. Sect. 5). The second is towards the end of a disk's lifetime when the accretion rate decreases, which yields a lower ram pressure $P_{\rm ram}$ (see Sect. 5.2).

5. Results and discussion

The goal of our simulations is to show the influence of a protostellar magnetic field on the bursting behavior of MRI- and TI-unstable disks. Therefore, in Sect. 5.1 the bursting behavior and the long-term evolution of such disks is investigated. In Sect. 5.2 we perform long-term runs with different magnetic field strengths $B_\star$ to investigate the effect of magnetic torques on the inner disk dynamics and its consequences for the long-term behavior. Additionally, the effect of different MRI activation temperatures is discussed in Sect. 5.3.

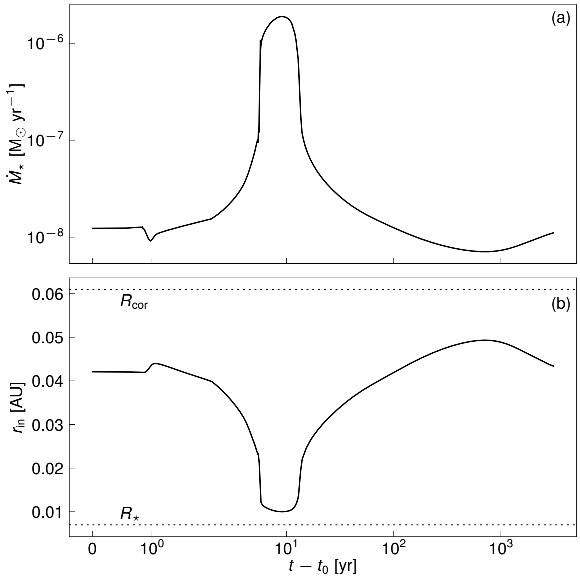

Fig. 6. *a*: accretion rate for a full TI-triggered outburst for our fiducial model `fid` (cf. Table 1). *b*: variation of the inner boundary during the burst is shown in (*a*). Here, t_0 corresponds to the onset of the first burst. The two dashed lines denote the protostellar radius $R_\star$ and the corotation radius $r_{\rm cor}$.

5.1. Episodic accretion and long-term evolution of magnetically truncated low-mass protoplanetary disks

Armitage et al. (2001) and Zhu et al. (2010) argue that a protoplanetary disk cannot sustain a steady mass transport rate in the radial direction from $r \approx 100$ AU to its inner edge at a few stellar radii, because GI in the outer disk feeds too much mass to the inner disk where it piles up. This leads to viscous heating in this region of enhanced density and eventually to the activation of the MRI. Enhanced radial mass transport $\dot{M}$ in the MRI-active disk yields more viscous heating and hence facilitates triggering of the thermal instability (e.g., Bell & Lin 1994).

In Table 1 the parameters for our fiducial model `fid` are stated. $\dot{M}_{\rm init}$ corresponds to the constant mass transport rate throughout the disk, which is obtained for the stationary initial model constructed as described in Sect. 3.5. The protostellar parameters (mass $M_\star$, radius $R_\star$, magnetic dipole field

A&A 655, A110 (2021)

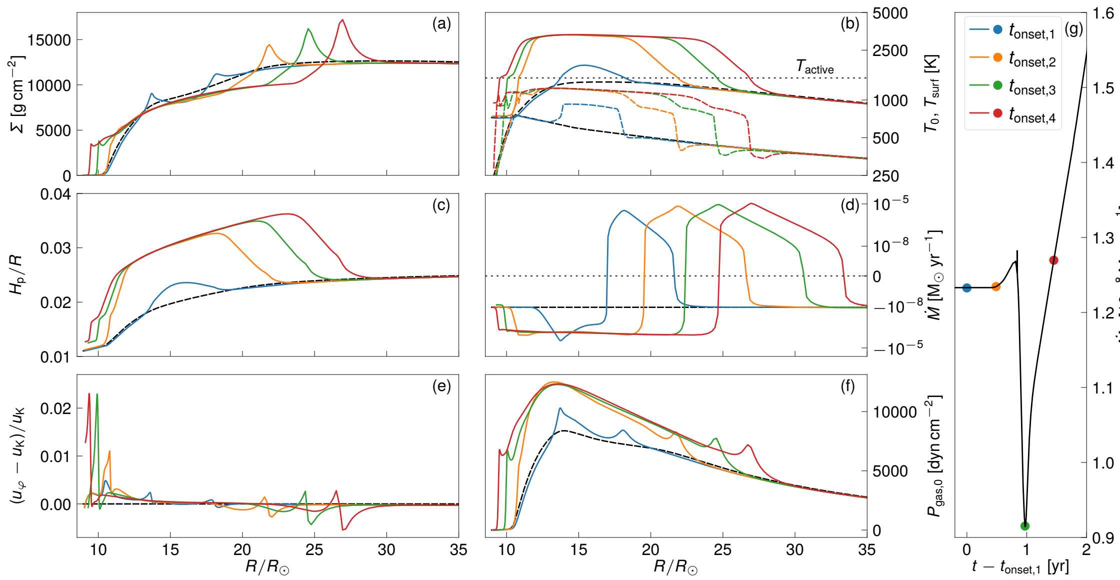

Fig. 7. Various disk quantities for certain times $t_{\rm onset,1}$–$t_{\rm onset,4}$ describing an outburst onset phase. *Panels a–c*: radial surface density structure Σ and the pressure scale-height $H_{\rm p}$ during the onset of an outburst, respectively. *Panel b*: midplane gas temperature T_0 (solid) and the surface temperature $T_{\rm surf}$ (dashed). The dotted line marks the activation temperature $T_{\rm active}$. *Panel d*: radial mass transport rate $\dot{M}$, where the dotted line corresponds to $\dot{M} = 0$. The deviation from a Keplerian accretion disk is shown in *panel e*, whereas *panel f*: gas pressure at the midplane $P_{\rm gas,0}$. Finally, *panel g* maps the various snapshots in time to the stages during the onset of an outburst. The dashed black line in *panels a–f* denote the stationary initial model as described in Sect. 3.5.

strength $B_\star$, and the corotation radius $r_{\rm cor}$), together with the disk parameters (α-viscosity parameter due to MRI $\alpha_{\rm MRI}$, the ratio $\alpha_{\rm MRI}/\alpha_{\rm base}$, and the thermal instability activation temperature $T_{\rm active}$) and the opacity prescription (cf. Fig. 1), determine the initial disk mass $M_{\rm disk,init}$ for the stationary initial model. We choose our parameters such that $M_{\rm disk,init} \approx 0.01\,M_\odot$ to ensure a gravitationally stable disk (see Sects. 2.1 and 2.4). For all simulation runs in Table 1, no external mass reservoir is assumed to resemble the configuration of a late class II star–disk system, and therefore $\dot{M}(r_{\rm out}) = 0$.

The column density Σ, midplane gas temperature $T_{\rm gas}$, scale height $H_{\rm p}$, the radial mass transport rate $\dot{M}$, the relative deviation from the Keplerian velocity $u_{\rm K}$, and the midplane gas pressure $P_{\rm gas,0}$ of our fiducial model `fid` are shown in Fig. 7 during onset of a TI-triggered burst. Zhu et al. (2010) observed short phases during outbursts in their simulations, where the thermal instability could not be sustained (they termed this phenomenon *drop-outs*), whose cause they interpreted to be the lack of radial advection in their simulations. We include radial advection (cf. Sect. 2.1) in our models and do not observe such drop-outs, which confirms their interpretation. Shortly before $t_{\rm onset,1}$, a TI is triggered at $r \approx 15\,R_\odot$, which can be seen by a steep rise in $T_{\rm gas,0}$ (panel b of Fig. 7). Simultaneously, the TI strongly increases local viscosity, to which the disk reacts by redistributing material to both the inner and outer disk annuli (e.g., Bell & Lin 1994). This increases Σ at both neighboring disk annuli above the threshold at which TI is also triggered. Hence, two ionization fronts are starting to travel inwards and outwards, which can be seen most clearly in panels a, b, and e of Fig. 7 for different points in time from $t_{\rm onset,1}$ to $t_{\rm onset,4}$. Both ionization fronts heat up the disk (see Fig. 7b) which leads to an increased scale height $H_{\rm p}$ (Fig. 7c). This in turn yields a region where the disk is shadowed from protostellar irradiation. Our models incorporate geometric shadowing caused by local elevations in $H_{\rm p}$ (cf. Sect. 2.3), which can be seen in Fig. 7b as a drop in surface temperature $T_{\rm surf}$ just behind (from the perspective of the protostar) the outward-traveling ionization front. As soon as the inward-bound wave reaches the rim of the inner disk, heated (and hence more viscous) material can no longer be redistributed further inwards, and the disk starts to transition into the outburst phase. The gas temperature at the inner boundary $T_{\rm gas,0}(r_{\rm in})$ rises very quickly and is accompanied by a sharp increase in viscosity and hence in $\dot{M}_\star$ (cf. panel g of Fig. 7).

The deviation from the diffusion approach investigated in Sect. 4.1 can be seen clearly in panels e and f of Fig. 7. The relative difference of u_φ compared to the Keplerian velocity $u_{\rm K}$ peaks at ~0.02, which is an order of magnitude larger than the predicted $u_\varphi \approx 0.996\,u_{\rm K}$ for a viscous protoplanetary accretion disk (see Armitage 2010). Additionally, the rotational velocity u_φ not only becomes subKeplerian but also superKeplerian (see panel e in Fig. 7). This feature is strongest along the propagating ionization fronts, as there the surface density has localized peaks, which in turn leads to an altered (with respect to a quasiKeplerian accretion disk) viscous net shear on the disk annuli at those radii. The relative influence of gas pressure $P_{\rm gas}$ on a certain annulus compared to the viscous force is shown in Fig. 8. The region at around 10 solar radii in Fig. 8 corresponds to the location of the inward-bound ionization front, whereas the outer ionization front is located at approximately $24\,R_\odot$. The magnetic braking of the inner disk inside $r_{\rm cor}$ leads to an increased radial velocity $u_{\rm r}$ and hence to a drop in Σ towards $r_{\rm in}$, which leads to the pressure force changing sign at around $22\,R_\odot$. Furthermore, it can be seen in Fig. 8 that the gas pressure alters the disk dynamics close to the inner disk radius, which is because that is

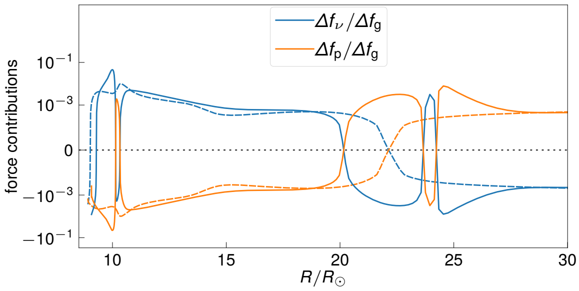

Fig. 8. Net contributions of pressure Δf_p and viscous force Δf_ν on an disk annulus are shown for the inner disk. The forces are in units of the net gravitational force Δf_g at its corresponding radius. The dashed lines outline the various force contributions for the stationary initial model. The dotted horizontal line shall help to visualize where the force contributions change sign.

where the pressure gradient becomes steepest (apart from local disturbances like ionization fronts). The influence of the pressure gradient even exceeds the viscous contributions, which is, once more, an indication that the full set of hydrodynamic equations are required to properly model the inner regions of a disk. The sharp decrease in $\dot{M}_\star$ between $t_{\mathrm{onset},2}$ and $t_{\mathrm{onset},3}$ in Fig. 7 occurs because of the small-scale structure of the inbound wave when it reaches r_{in} (for a thorough analysis of the thermal instability see Bell & Lin 1994).

Figure 9 shows the whole disk during a TI-induced outburst. The outward-bound ionization front as described in detail by Bell & Lin (1994) stalls at $t \approx t_{\mathrm{burst},4}$ at a radius where the swept-up material is no longer capable of increasing Σ sufficiently for the disk annulus to become thermally unstable (cf. b in Fig. 9). The increased accretion rate yields a higher accretion luminosity, which in turn causes a higher temperature at the disk surface and a puffing-up of the irradiated outer disk (panel c of Fig. 9). The detailed effects of the increased scale height, relating to shadowing of the disk behind this bump, will be studied in another paper of this series. The ongoing depletion of the inner disk inside the ionization front due to strongly increased viscosity eventually leads to a drop in gas temperature $T_{\mathrm{gas},0}$. At approximately $t_{\mathrm{burst},3}$, hydrogen is able to recombine again and a cooling wave starts to propagate inwards (radially outer green vertical dashed line and arrow in panel b of Fig. 9). The cooler gas then leads to a drop in optical depth (cf. Fig. 1), which results in termination of the TI. This inward-bound perturbation becomes clearly visible at $t_{\mathrm{burst},4}$ and $t_{\mathrm{burst},5}$ in panels a to c of Fig. 9, where the position and direction of the cooling front is marked with a vertical dashed line and an arrow, respectively. As this wave propagates towards the inner disk radius r_{in}, the lower temperature leads to a decrease in viscosity and hence the outburst enters the decaying phase and the disk inside the ionization front empties on a viscous timescale t_{visc}, which for our model `fid` is $t_{\mathrm{visc}} \lesssim 100$ years in the MRI-active region.

In panel d the influence of the protostellar magnetic field (see also Sect. 5.2) is revealed in the form of a considerably sub-Keplerian rotational velocity u_φ towards the inner radius. This is due the protostellar magnetic torque acting on the disk. As a further consequence, the radial velocity of the disk starts to increase inside the corotation radius r_{cor}. However, before the radial velocity u_r is even close to the free-fall velocity, the protostellar magnetic field dominates the disk dynamics (e.g., Bessolaz et al. 2008) and the accretion flow transitions into accreting funnels. This transition zone at the inner rim leads to a drop in surface density Σ and as a consequence yields a lower gas temperature $T_{\mathrm{gas},0}$. Additionally, because of the decreasing accretion rate $\dot{M}_\star$, the inner radius is moving outwards (cf. panels a to d in Fig. 9), which in combination with the lower temperature leads to an additional cooling wave starting at the inner edge and propagating outwards (color-coded vertical dashed lines and corresponding radially outward-oriented arrows close to the inner rim in panel b of Fig. 9). At $t_{\mathrm{burst},5}$, the two waves have almost met each other (cf. color-coded vertical lines corresponding to $t_{\mathrm{burst},5}$ in panel b of Fig. 9), resulting in the turnoff of the TI almost everywhere in the inner region, eventually marking the end of the outburst. Hence, compared to models without the influence of a stellar magnetic field, an additional cooling wave traveling outwards has an influence on the time needed for the inner disk to become thermally stable again. This because the outer cooling front does not travel inwards until it reaches the inner disk rim but is met by the outward-bound cooling wave earlier. Material is then fed to the inner regions from the outer regions and accumulates until a disk annulus becomes thermally unstable again, therefore completing a burst cycle.

Such burst cycles occur as long as the inner disk can be fed with material from the outer regions and consequently is capable of heating up the inner regions sufficiently through viscous dissipation. In Fig. 10 this repeated episodic accretion can be seen in panel a. This process is repeated 49 times before the disk mass can no longer provide a sufficiently strong accretion flow of gas to heat the inner disk above the MRI activation temperature T_{active} once more. For our fiducial model `fid`, the disk becomes quiescent at $\sim 2.35 \times 10^5$ years and below a disk mass of $\sim 7 \times 10^{-3}\, M_\odot$. Panel b of Fig. 10 shows the variation of the inner radius r_{in} as it reacts to a changing accretion rate. After the bursts have ceased and the disk has become quiescent, the accretion rate decreases, as the disk continually loses mass over its lifetime (cf. panel c of Fig. 10). The constantly decreasing accretion rate also has an impact on the location of the inner radius. The magnetic field is able to disrupt the disk farther out, as $\dot{M}_\star$ becomes weaker. The apparent push of r_{in} outside the initial corotation radius $r_{\mathrm{cor,init}}$ can be explained with a super-Keplerian rotation velocity caused by the positive pressure gradient in the innermost disk in the vicinity of $r_{\mathrm{cor,init}}$ (cf. Fig. 8) and therefore a slight change in r_{cor} towards larger radii.

5.2. Influence of the stellar magnetic field

In Sect. 5.1 we analyze and describe our fiducial model `fid`. It can be clearly seen that a protostellar magnetic field is influencing the disk close to the inner boundary r_{in}. In agreement with Vorobyov et al. (2019), we argue that the inner boundary has an effect on the global disk structure and therefore on the long-term evolution of a protoplanetary disk. We emphasize in Sect. 3.1 that a 1D approach outside of $r \approx 0.5$ AU has certain limitations in describing the disk structure appropriately. However, our focus in this section is to investigate how different magnetic field strengths (see Table 1) are effecting the bursting behavior of the disk. The MRI and TI ignition point lies well below 0.5 AU, which is an essentially axisymmetric region of the disk (e.g., Lesur 2020), and therefore the assumptions of our model are valid approximations. Additionally, we restrict our studies in this work to low-mass disks where no gravitational instabilities are expected to break their axisymmetry.

In Fig. 11 the initial magnetic field strengths for different stationary models (cf. Table 1) are shown. We can determine two effects of the stellar magnetic field. First, the inner

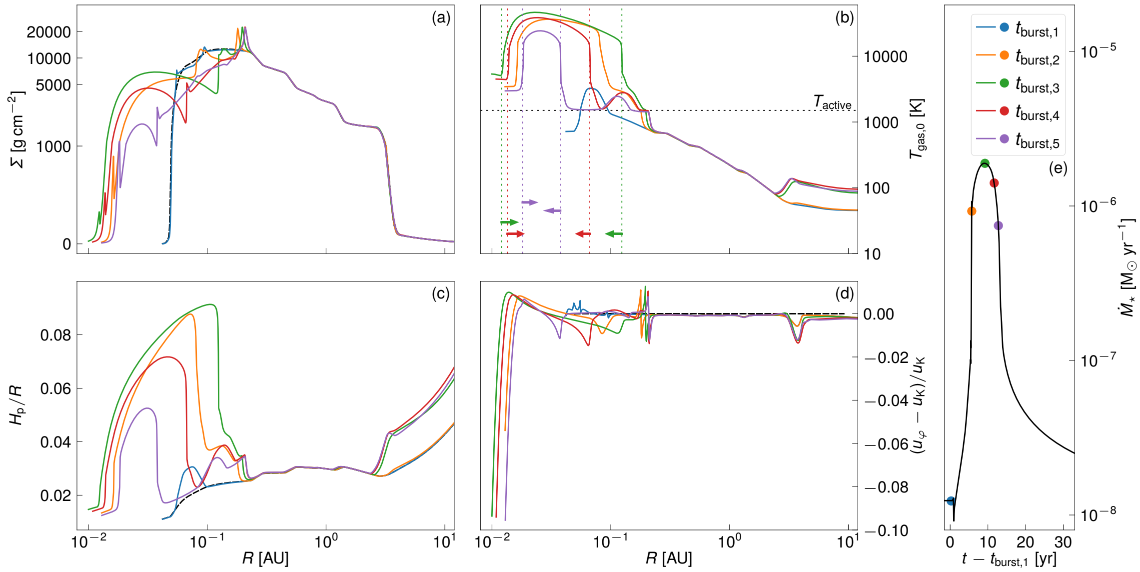

Fig. 9. *Panels a–c*, as well as (*e*), are the same disk properties as in Fig. 7, but for five points in time $t_{burst,1}$ to $t_{burst,5}$ during an outburst. *Panel d*: same quantity as (e) in Fig. 7. The dashed black line in *panels a–d* denote the stationary initial model as described in Sect. 3.5. The radial range in this plot is chosen from r_{in} to 10 AU. The color-coded, dashed vertical lines and corresponding arrows mark the position of the cooling waves and their propagation direction, respectively.

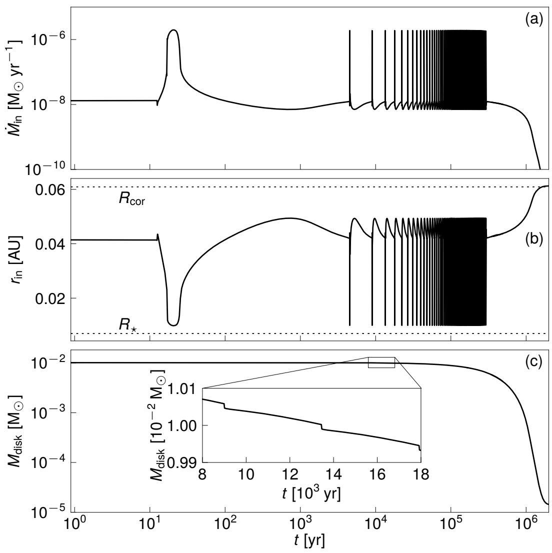

Fig. 10. Long-term evolution for our fiducial model `fid` (see Table 1). *Panels a* and *b*: accretion rate $\dot{M}_{in}$ at the inner boundary and its corresponding movement of the inner radius r_{in}. The evolving total disk mass M_{disk} is presented in *panel c*. The inset in panel c shows the step-like decrease in disk mass M_{disk} caused by outbursts.

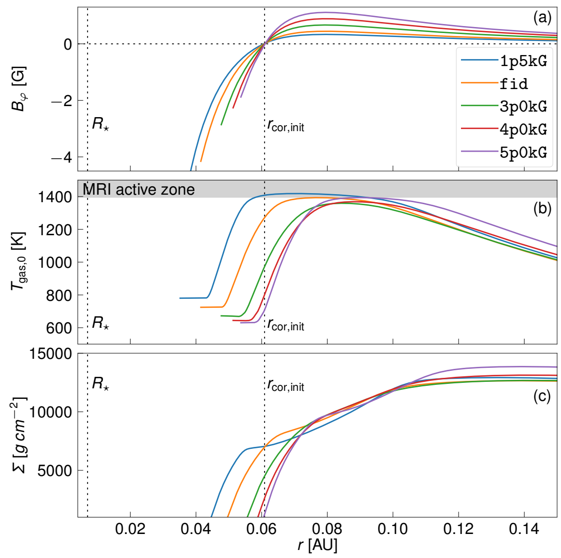

Fig. 11. Comparison of (*a*) the toroidal protostellar magnetic field component B_φ as stated in Eq. (8), (*b*) the midplane gas temperature $T_{gas,0}$, and (*c*) the surface density Σ for the different stationary initial models in Table 1 of varying protostellar magnetic field strengths, ranging from $B_\star$ = 1.5 kG to 5 kG. The MRI active zone starts at little over 1400 K for our choice of T_{active} = 1530 K and T_{width} = 50 K. The vertical dashed lines denote the position of the stellar radius $R_\star$ and the initial corotation radius $r_{cor,init}$.

boundary of the disk is pushed outward for a higher field strength due to the stronger magnetic pressure (see Eq. (47)). Additionally, a stronger field also has a stronger propelling effect on the disk gas just outside of the corotation radius r_{cor} (cf. panel a of Fig. 11). Material in this area starts to get pushed outwards, and the disk starts to pile up material because disk gas is still accreting from the outer disk inwards (see panel c of Fig. 11). This

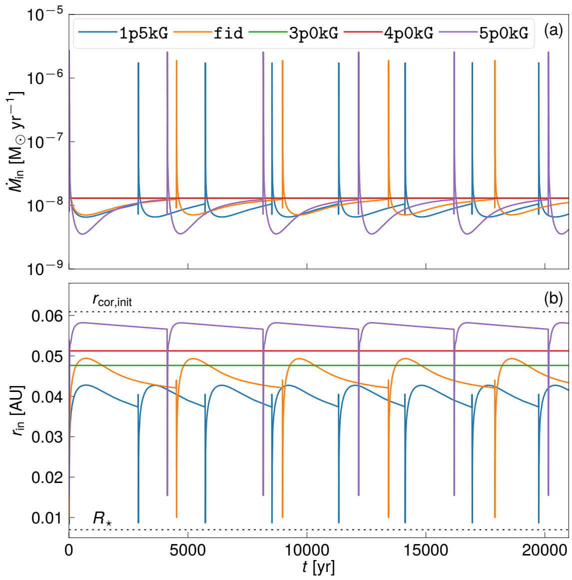

Fig. 12. Comparison of the models in Table 1. *Panel a*: accretion rate $\dot{M}_\star$ and (*b*) the corresponding inner radius $r_{\rm in}$, respectively. The colors correspond to the same models as in Fig. 11. The horizontal dashed lines denote the position of the stellar radius $R_\star$ and the initial corotation radius $r_{\rm cor,init}$.

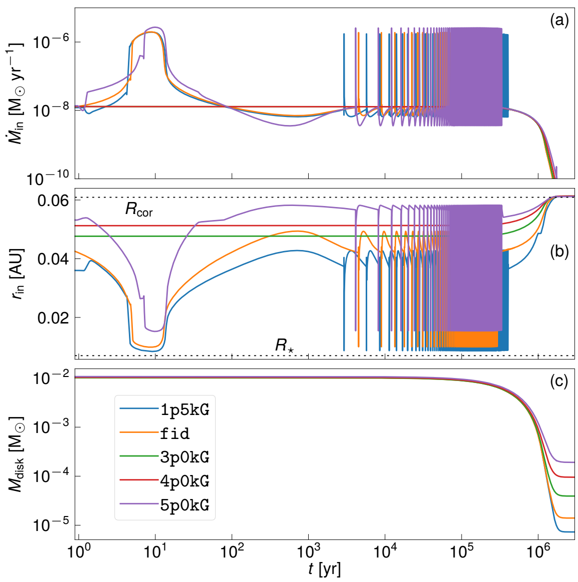

Fig. 13. Same models as in Fig. 12, but for the full disk lifetime. The onset of the first burst of every model has been aligned in time to provide a better comparability regarding burst frequency and burst strength. *Panel b*: the dashed lines denote the initial corotation radius $R_{\rm cor,init}$ and the protostellar radius $R_\star$.

leads to increased viscous heating and therefore to a higher midplane gas temperature $T_{\rm gas,0}$ (see panel b of Fig. 11). If the magnetic field is chosen to be stronger than a certain threshold field strength (the exact value depends on the disk and stellar parameters), then the aforementioned pile-up of material is sufficient to trigger the MRI. For the disk parameters chosen in this work, this limiting value is $B_{\star,\rm up} \approx 4.5$ kG. Consequently, the higher $T_{\rm gas,0}$ is sufficient for deeper disk layers to be become MRI-active, which in turn leads to even higher viscosity and temperature (cf. panel b of Fig. 11). Eventually, this triggers TI at some ignition radius, which then starts an outburst cycle.

Also notable is the effect of a relatively weak magnetic field on the disk. A lower magnetic field strength yields an inner radius $r_{\rm in}$ closer to the protostar. Consequently, the disk is heated up to higher temperatures and the MRI/TI can be triggered. As a result, for all stellar magnetic fields $B_\star$ lower than a lower limit field strength $B_{\star,\rm low}$, a disk also undergoes episodic accretion. For the parameters in Table 1, this lower limit is at $B_{\star,\rm low} \approx 2$ kG, which we use for our fiducial model `fid` (cf. panel b of Fig. 11).

We also conduct long-term runs for all models in Table 1. In Fig. 12, the accretion rate on the star $\dot{M}_\star$ and the movement of the inner radius $r_{\rm in}$ are plotted in panels a and b, respectively. The models `1p5kG` (blue solid) and `fid` (orange solid) become thermally unstable due to the proximity of the inner radius $r_{\rm in}$ to the star, which can be seen in panel b of Fig. 12. The burst frequency (cf. panel a of Fig. 12) depends on how fast the gas temperature $T_{\rm gas,0}$ exceeds the activation temperature $T_{\rm active}$. For disks with stellar magnetic field strengths $B_\star < B_{\star,\rm low}$ the burst frequency increases for weaker magnetic fields $B_\star$, because the weaker the stellar field $B_\star$, the further inwards the disk stretches. This leads to even higher gas temperatures and therefore to a disk prone to TI. Equally importantly, for $B_\star > B_{\star,\rm up}$, the stronger $B_\star$, the more effectively the propelling effect can fling material outwards, and hence the more material piles up outside of $r_{\rm cor}$. The gas temperature then also increases with higher $B_\star$ and TI is triggered faster. Models `1p5kG` and `fid` satisfy the constraint $B_\star < B_{\star,\rm low}$ and `5p0kG` satisfies $B_\star > B_{\star,\rm up}$. For intermediate magnetic fields of $B_{\star,\rm low} < B_\star < B_{\star,\rm up}$, no outbursting behavior develops (models `3p0kG` and `4p0kG`). We note that the actual threshold values for $B_\star$ depend on the choice of stellar and disk parameters and have to be determined anew for every different parameter set (cf. Fig. 16). For weaker fields, the inner disk radius $r_{\rm in}$ is pushed very close to the stellar radius (cf. Eq. (47) and panel b of Fig. 12); in the case of our model `1p5kG`, the inner radius $r_{\rm in} \approx 1.5\,R_\star$.

In Fig. 13 the full disk lifetime is plotted. In panels a and b it can be seen that the transition of the disk into its quiescent state occurs later for models `1p5kG` and `5p0kG`, which is due to their higher maximum temperature $T_{\rm gas,0}$ (compared to `fid`) which can also be seen in panel b of Fig. 11. The physical explanation for the different rest disk masses in panel c of Fig. 13 is that below a certain disk mass threshold, the protostellar field is effectively preventing further accretion onto the protostar (propeller regime) and hence the disk mass stabilizes at a certain value. The strength of the magnetic field then determines the lower disk mass $M_{\rm disk}$, below which further accretion is quenched by B_φ.

Towards the end of the disk lifetime, the disk mass and consequently the accretion rate $\dot{M}_\star$ drop, resulting in $r_{\rm in}$ shifting towards larger radii (cf. Fig. 13 and Eq. (47)). With decreasing $\dot{M}_\star$ the gas pressure $P_{\rm gas}$ eventually exceeds the ram pressure $P_{\rm ram}$ and controls the movement of the inner disk radius $r_{\rm in}$. For all models, this transition occurs inside the corotation radius $r_{\rm cor}$. For a sufficiently strong stellar magnetic field, the propelling effect just outside $r_{\rm cor}$ piles up material (cf. Fig. 11) and increases $P_{\rm gas}$ until it exceeds $P_{\rm ram}$, thus keeping $r_{\rm in}$ inside $r_{\rm cor}$. We want to note here that current 2D simulations of the propelling regime show a more complex behavior (e.g., Ustyugova et al. 2006;

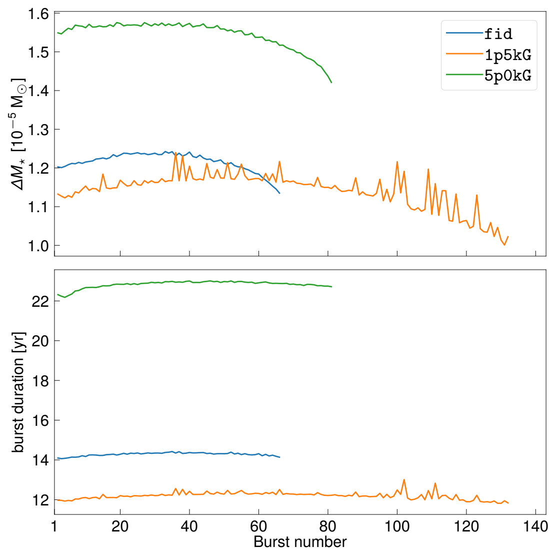

Fig. 14. Time evolution of the outbursting behavior of the disk, shown for all consecutive bursts during disk evolution. *Panel a*: mass accretion onto the protostar during an outburst $\Delta M_\star$, whereas *panel b*: burst duration for a certain burst.

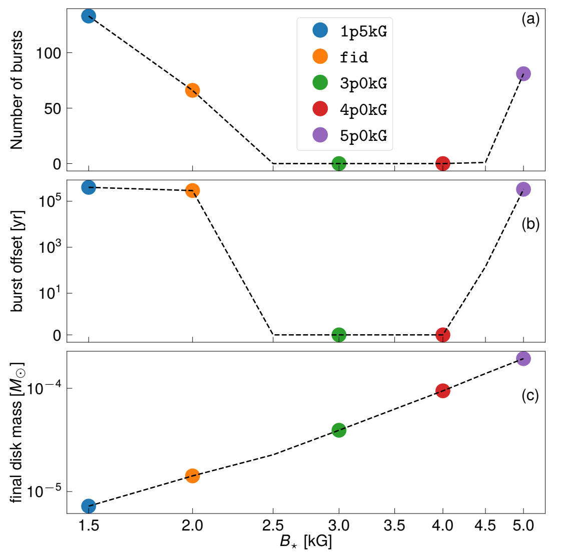

Fig. 15. Comparison of (*a*) the number of bursts, (*b*) the burst offset time of the disk, and (*c*) the final disk mass for all models in Table 1 and additionally for models with $B_\star$ = 2.5 kG, 3.5 kG and 4.5 kG. The color coding is the same as for Fig. 11, whereas the black dashed line linearly connects the data points and has the sole purpose of emphasizing the burst-free region in *panels a* and *b* as well as indicating the power-law for the final mass in (*c*).

Romanova et al. 2009, 2018). A specific part of the piled up matter is accreted onto the star while another is ejected in winds. Inclusion of disk winds in our model, for example, which are shown to play an important role for the inner boundary (e.g., Königl et al. 2011), would reduce pile up of matter (see panel a in Fig. 11) and consequently increase $B_{\star,\mathrm{up}}$. Thus, the results presented here have to be considered as a limiting case.

In addition to the long-term evolution of the disk for different values of the stellar magnetic field, we compare the duration of bursts and the accreted disk mass onto the star $\Delta M_\star$ for each individual outburst (cf. Fig. 14). For a given stellar magnetic field strength, the burst duration as well as $\Delta M_\star$ remain approximately constant until the disk has depleted to a degree where the stellar disk can no longer feed the inner region with sufficient mass to become MRI- or TI-unstable. The small variability of the duration and the accreted mass of consecutive bursts is due to the fact that the ignition radius for the MRI/TI remains effectively unaltered for the disk during its bursting phase, which then yields a very similar maximum radius for the outward-bound ionization front and consequently a similar burst duration and $\Delta M_\star$. Relaxing the assumption of axisymmetry probably adds more variability to the results (e.g., Vorobyov et al. 2020) and shall be reviewed in further studies. However, for an increasing stellar magnetic field strength, the burst duration and $\Delta M_\star$ increase. Because of the stronger magnetic pressure with an increasing stellar magnetic field, the inner disk radius r_{in} as well as the MRI ignition point are pushed outwards (cf. panel b of Fig. 11). Additionally, more mass is piled up directly outside the MRI ignition point (cf. panel c of Fig. 11), which also increases the disk temperature in this region. As a result, the outward-bound ionization front reaches further out, which increases the burst duration and the piled up mass outside the MRI ignition point increases $\Delta M_\star$.

Figure 15 specifically depicts the thermally stable zone for $B_\star$ between roughly 2.5 kG and 4.5 kG. The final disk mass towards the end of a disk's lifetime seems to behave like a power-law (cf. panel c of Fig. 15). A possible explanation for this is that an almost dissolved disk with little mass cannot counteract the propelling forces of the stellar magnetic field and hence cannot accrete onto the star. The stellar field is modeled as a dipole and the resulting centrifugal force would also yield a power law; nevertheless a more thorough analysis is planned in further studies to investigate this behavior in more detail. Panel b of Fig. 15 depicts the point in time where the disk ceases to burst (burst offset), whereas panel a shows the number of bursts for a certain model. Figure 15 indicates that stellar magnetic fields, which are weaker than the lower limit or stronger than the upper limit of $B_\star$, will lead to more bursts, depending on the size of the deviations from those limits.

5.3. Variation of activation temperature and mass transport rate

To test the robustness of the results of Sect. 5.2, we varied the MRI activation temperature T_{active} together with the initial mass transport rate $\dot{M}_{\mathrm{init}}$. For all previous simulations, T_{active} is fixed to 1530 K (see Table 1). A different choice of T_{active} will affect the radius at which the deep layer of the disk becomes MRI-active and TI is triggered. Choosing a lower activation temperature will result in more models becoming thermally unstable. The value range between $B_{\star,\mathrm{low}}$ and $B_{\star,\mathrm{up}}$ becomes smaller. A higher activation temperature T_{active}, on the other hand, will increase this region as there will be fewer models in which T_{gas} can exceed T_{active}. We can reproduce our main results for different values of T_{active} by adapting the mass transport rate $\dot{M}$ throughout the disk. Choosing T_{active} = 1300 K and $\dot{M}_{\mathrm{init}}$ of 0.97 × 10^{-8} $M_\odot$/yr^{-1}, the range of the stellar magnetic field $B_\star$ in which outbursts are suppressed extends from 2.5 to 3.5 kG (see Fig. 16).

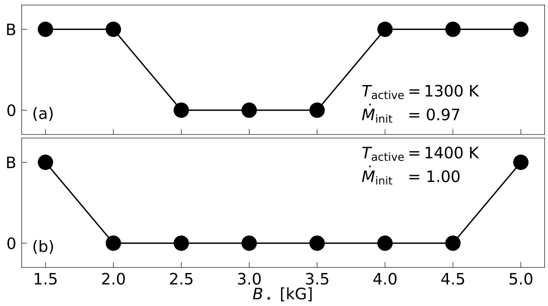

Fig. 16. Bursting behavior depending on the stellar magnetic field $B_\star$ for different $T_{\rm active}$. A distinction is made between models that produce outbursts (B) and models in which outbursts are suppressed (0). $T_{\rm active}$ is set to 1300 K and 1400 K in *panels a* and *b*, respectively. The accretion rate $\dot{M}_{\rm init}$ is given in units of $10^{-8}\ M_\odot/{\rm yr}^{-1}$.

For choosing $T_{\rm active} = 1400$ K and $\dot{M}_{\rm init}$ of $1.0 \times 10^{-8}\ M_\odot/{\rm yr}^{-1}$, outbursts are suppressed between 2.0 and 4.5 kG. The adapted values of $\dot{M}_{\rm init}$, which correspond to the quiescent accretion rate between two outbursts, are all in agreement with Armitage et al. (2001). We would like to emphasize that the exact interpretation of these results requires a more detailed parameter study and is left for future work.

6. Conclusion

In this study we conduct fully implicit 1+1D hydrodynamic simulations of protoplanetary disks with a focus on the inner regions. The TAPIR code (see Ragossnig et al. 2020) is capable of solving the full set of hydrodynamic equations, which enables us to include additional physics, such as for example the effects of local pressure gradients, protostellar magnetic fields, or features in the angular velocity.

Previous studies (e.g., Bell & Lin 1994; Armitage et al. 2001; Zhu et al. 2009a) wherein 1D long-term simulations were also performed used the viscous diffusion equation for the temporal evolution of the disk. We demonstrate in Sect. 4 that this approach shows significant deviations –at least locally close to the star– from a full solution of the hydrodynamic equations. Furthermore, we also adopt a description of the magnetic truncation radius based on the equality of magnetic pressure and ram pressure (see e.g., Hartmann et al. 2016). Complementary to that approach, we incorporate the gas pressure influence in our models, covering $P_{\rm gas} > P_{\rm ram}$.

In the first paper of this series, we study the effect of protostellar magnetic torques on the long-term behavior of protoplanetary disks. These torques slow down or accelerate the disk depending on the radial location compared to the corotation radius $r_{\rm cor}$, and thus necessitate a self-consistent treatment of the momentum equation in the angular direction. Diffusion approaches are not well suited to modeling an inner disk threaded by a stellar magnetic field.

Layered-viscosity models as proposed by Armitage et al. (2001) can, for certain parameters, become thermally unstable and repeatedly experience FU Ori-like episodic accretion events (e.g., Bell & Lin 1994). Interestingly, the burst strength and burst frequency are strongly dependent on the stellar magnetic field strength $B_\star$.

On the one hand, a stronger $B_\star$ corresponds to a larger inner disk radius $r_{\rm in}$, which leads to less radiative heating of the surface of the inner disk and consequently to a cooler disk. On the other hand, a stronger toroidal magnetic field component B_φ also acts as a propeller outside of the corotation radius $r_{\rm cor}$, effectively flinging material outwards. This pushed out disk gas combines with the inward-directed accretion flow, resulting in a larger radially localized surface density Σ. This leads to a higher gas temperature $T_{\rm gas}$, which counteracts the cooling effect of a farther out $r_{\rm in}$. We find that there exists a limit value for $B_\star$, above which a disk gets sufficiently heated to become thermally unstable.

A weaker $B_\star$ leads to a small inner radius $r_{\rm in}$, and therefore the inner disk gets hotter due to the proximity to the protostar. We find that if the protostellar magnetic field $B_\star$ is weaker than a certain upper limit, then the inner disk becomes hot enough to also become thermally unstable.

Summarizing these results, a region of protostellar magnetic field of intermediate strength exists where (for a certain set of disk and star parameters) no bursts occur. Below and above this region the models can become thermally unstable. These results are later reproduced with different value sets of the MRI activation temperature $T_{\rm active}$ and mass transport rate $\dot{M}$. Additionally, the burst strength and burst frequency are also altered by a varying $B_\star$, which changes the duration of the thermally unstable phase of such disks. We find that the burst duration and mass accretion rate caused by a single outburst only vary slightly for consecutive bursts, which is due to the almost constant radial position of the MRI/TI ignition point during the bursting phase of a disk. Moreover, for stronger stellar magnetic fields, the burst duration and accretion mass during an outburst increase because the MRI ignition point gets pushed radially outwards. We conducted long-term simulations to study the influence of the protostellar field and found that disks tend to have more frequent but weaker bursts if $B_\star$ is either far below or far above the aforementioned intermediate zone. Our simulations show that for weaker stellar magnetic fields, the inner disk radius $r_{\rm in}$ is pushed very close to the stellar radius $R_\star$. For even weaker fields or stronger bursts the magnetic field could be squashed to the stellar surface and could therefore suppress the accretion funnels as well as the resulting accretion shock (e.g., Hartmann et al. 2016) and thus provide an explanation for the lack of UV excess in FU Ori-like star–disk systems (e.g., Bell & Lin 1994).

In this work, we show that a detailed model of the inner disk regions is essential for the simulations of protoplanetary disks, especially during episodic outbursts. We agree in this regard with Vorobyov et al. (2019). for example, and are confident that the TAPIR code (Ragossnig et al. 2020) is well suited to representing the inner disk region in global 2D long-term simulations.

6.1. Limitations of this work

While the TAPIR-code is capable of treating the inner disk self-consistently, there are also limitations to this approach. Our 1D model is mainly suited to simulation of the inner disk. This is because in the inner regions, viscous shear becomes stronger and therefore angular perturbations cannot be sustained, even for short times (for a conclusive discussion see e.g., Lesur 2020). Therefore the assumption of axisymmetry is a valid approximation in the inner regions.

Furthermore, because of the assumption of vertical thermal equilibrium, radiative transport in the z-direction is only included approximately. Photoevaporation of the inner disk definitely has an effect on the inner radius of the disk, as well as on the star–disk-interaction as gas is removed, especially from the inner part of the disk. However, these effects will not effect the qualitative statements of this work and will be investigated in upcoming studies. Furthermore, we use a simple dust model with a constant dust-to-gas ratio. The dust is included in the opacity calculation, but the back-reaction onto the gas or dust dynamics is not considered yet. This approximation has only a minor effect on the main findings from this study. However, a more realistic time-dependent dust model would increase the accuracy of our code.

We also neglect some details of the star–disk interaction. In our model, $B_\star$ is prescribed as a dipole field, which is an approximation, especially in the case of very high accretion rates. Nevertheless, for an qualitative study of the effects of magnetic torque on the disk evolution, the details of the field topology are of minor order. Additionally, the transfer of angular momentum from the star to the disk and vice versa has not been modeled in this work, as we focused on the effect of an existing magnetic field on disk evolution. We agree that this effect should be investigated in further studies, because a time-dependent stellar angular velocity also results in the corotation radius r_{cor} moving radially inwards and outwards, which has a potential effect on the outbursting behavior of disks.

6.2. Further work

In upcoming studies of this series, we will study the effects of magnetic fields and stellar radiation on the pressure scale height, which leads to a shadowed disk region, where less stellar radiation can heat the disk surface. Another study will involve a model for the star–disk interaction and the inclusion of higher-order magnetic field moments like quadrupole and octopole contributions to the stellar magnetic field topology. We will use the altered magnetic field structure to study the effect on the outbursting behavior of disks.

Equally interesting is the inclusion of large-scale disk fields. Those fields have been investigated in 1D models (e.g., Guilet & Ogilvie 2012, 2014). The incorporation of such magnetic field models in the TAPIR code enables us to self-consistently solve the inner disk and the disk field topology simultaneously. This further allows estimates of how much mass and angular momentum can be transported away by magneto-centrifugally driven outflows during for example an FU Ori-like outburst. Also important is the inclusion of photo-evaporative winds, especially during an outburst, because this is when the accretion luminosity is highly elevated. The effects of outflows due to photo-evaporation coupling with a large-scale disk magnetic field are equally interesting, as then not only mass is transported away but also angular momentum, which further modifies the disk dynamics.

Acknowledgements. E. I. V. acknowledge support of Ministry of Science and Higher Education of the Russian Federation under the grant 075-15-2020-780 (N13.1902.21.0039; Sect. 6).

References

Alexander, D. R., & Ferguson, J. W. 1994, ApJ, 437, 879
Armitage, P. J. 2010, Astrophysics of Planet Formation (Boulder: University of Colorado)
Armitage, P. J. 2011, ARA&A, 49, 195
Armitage, P. J., Livio, M., & Pringle, J. E. 2001, MNRAS, 324, 705
Audard, M., Ábrahám, P., Dunham, M. M., et al. 2014, Protostars and Planets VI (Tucson: University of Arizona Press), 387
Bae, J., Hartmann, L., Zhu, Z., & Gammie, C. 2013, ApJ, 764, 141
Balbus, S. A., & Hawley, J. F. 1991, ApJ, 376, 214
Bell, K. R., & Lin, D. N. C. 1994, ApJ, 427, 987
Bessolaz, N., Zanni, C., Ferreira, J., Keppens, R., & Bouvier, J. 2008, A&A, 478, 155
Bouvier, J., Alencar, S. H. P., Harries, T. J., Johns-Krull, C. M., & Romanova, M. M. 2007, in Protostars and Planets V, eds. B. Reipurth, D. Jewitt, & K. Keil, 479
Caffau, E., Ludwig, H. G., Steffen, M., Freytag, B., & Bonifacio, P. 2011, Sol. Phys., 268, 255
Contreras Peña, C., Lucas, P. W., Minniti, D., et al. 2017, MNRAS, 465, 3011
Crida, A., Morbidelli, A., & Masset, F. 2007, A&A, 461, 1173
Dorfi, E. 1998, in Computational Methods for Astrophysical Fluid Flow (Berlin, Heidelberg: Springer-Verlag), Saas-Fee Advanced Courses, 27, 263
Dorfi, E., & Drury, L. 1987, J. Comput. Phys., 69, 175
Dorfi, E., Pikall, H., Stökl, A., & Gautschy, A. 2006, Comput. Phys. Commun., 174, 771
Eisner, J. A., & Hillenbrand, L. A. 2011, ApJ, 738, 9
Ferguson, J. W., Alexander, D. R., Allard, F., et al. 2005, ApJ, 623, 585
Flock, M., Fromang, S., Turner, N. J., & Benisty, M. 2016, ApJ, 827, 144
Gammie, C. F. 1996, ApJ, 457, 355
Guilet, J., & Ogilvie, G. I. 2012, MNRAS, 424, 2097
Guilet, J., & Ogilvie, G. I. 2014, MNRAS, 441, 852
Hartmann, L., & Bae, J. 2018, MNRAS, 474, 88
Hartmann, L., & Kenyon, S. J. 1996, ARA&A, 34, 207
Hartmann, L., Herczeg, G., & Calvet, N. 2016, ARA&A, 53, 135
Henning, T., & Stognienko, R. 1996, A&A, 311, 291
Herbig, G. H. 1989, Eur. South. Obs. Conf. Workshop Proc., 33, 233
Herbst, W., Bailer-Jones, C. A. L., & Mundt, R. 2001, ApJ, 554, L197
Hillenbrand, L. A., Contreras Peña, C., Morrell, S., et al. 2018, ApJ, 869, 146
Kadam, K., Vorobyov, E., Regály, Z., Kóspál, Á., & Ábrahám, P. 2019, ApJ, 882, 96
Kadam, K., Vorobyov, E., Regály, Z., Kóspál, Á., & Ábrahám, P. 2020, ApJ, 895, 41
Kluźniak, W., & Rappaport, S. 2007, ApJ, 671, 1990
Königl, A., Romanova, M. M., & Lovelace, R. V. E. 2011, MNRAS, 416, 757
Kóspál, Á., Ábrahám, P., Acosta-Pulido, J. A., et al. 2016, A&A, 596, A52
Kurosawa, R., Romanova, M. M., & Harries, T. J. 2008, MNRAS, 385, 1931
Lesur, G. 2020, Magnetohydrodynamics of Protoplanetary Discs (Cambridge: Cambridge University Press)
Livio, M., & Pringle, J. E. 1992, MNRAS, 259, 23P
Lubow, S. H., Papaloizou, J. C. B., & Pringle, J. E. 1994, MNRAS, 268, 1010
Matt, S. P., Pinzón, G., de la Reza, R., & Greene, T. P. 2010, ApJ, 714, 989
Pollack, J. B., McKay, C. P., & Christofferson, B. M. 1985, Icarus, 64, 471
Pollack, J. B., Hollenbach, D., Beckwith, S., et al. 1994, ApJ, 421, 615
Pringle, J. E. 1981, ARA&A, 19, 137
Ragossnig, F., Dorfi, E. A., Ratschiner, B., et al. 2020, Comput. Phys. Commun., 256, 107437
Rappaport, S. A., Fregeau, J. M., & Spruit, H. 2004, ApJ, 606, 436
Romanova, M., & Kurosawa, R. 2014, in 8th International Conference of Numerical Modeling of Space Plasma Flows (ASTRONUM 2013), eds. N. V. Pogorelov, E. Audit, & G. P. Zank, ASP Conf. Ser., 488, 127
Romanova, M. M., & Owocki, S. P. 2015, Space Sci. Rev., 191, 339
Romanova, M. M., Ustyugova, G. V., Koldoba, A. V., & Lovelace, R. V. E. 2004, ApJ, 610, 920
Romanova, M. M., Ustyugova, G. V., Koldoba, A. V., & Lovelace, R. V. E. 2009, MNRAS, 399, 1802
Romanova, M. M., Blinova, A. A., Ustyugova, G. V., Koldoba, A. V., & Lovelace, R. V. E. 2018, New Astron., 62, 94
Shakura, N., & Sunyaev, R. 1973, A&A, 24, 337
Stoekl, A., & Dorfi, E. 2014, EGU Gen. Assem. Conf. Abstr., 16, 2472
Toomre, A. 1964, ApJ, 139, 1217
Tscharnuter, W. M., & Winkler, K.-H. A. 1979, Comput. Phys. Commun., 18, 171
Ustyugova, G. V., Koldoba, A. V., Romanova, M. M., & Lovelace, R. V. E. 2006, ApJ, 646, 304
van Leer, B. 1977, J. Comput. Phys., 23, 276
Vorobyov, E. I., & Basu, S. 2007, MNRAS, 381, 1009
Vorobyov, E. I., & Pavlyuchenkov, Y. N. 2017, A&A, 606, A5
Vorobyov, E. I., Skliarevskii, A. M., Elbakyan, V. G., et al. 2019, A&A, 627, A154
Vorobyov, E. I., Khaibrakhmanov, S., Basu, S., & Audard, M. 2020, A&A, 644, A74
Zhu, Z., Hartmann, L., Calvet, N., et al. 2007, ApJ, 669, 483
Zhu, Z., Hartmann, L., Calvet, N., et al. 2008, ApJ, 684, 1281
Zhu, Z., Espaillat, C., Hinkle, K., et al. 2009a, ApJ, 694, L64
Zhu, Z., Hartmann, L., Gammie, C., & McKinney, J. C. 2009b, ApJ, 701, 620
Zhu, Z., Hartmann, L., Gammie, C. F., et al. 2010, ApJ, 713, 1134
Zhu, Z., Jiang, Y.-F., & Stone, J. M. 2020, MNRAS, 495, 3494

Appendix A: Implicit time-step

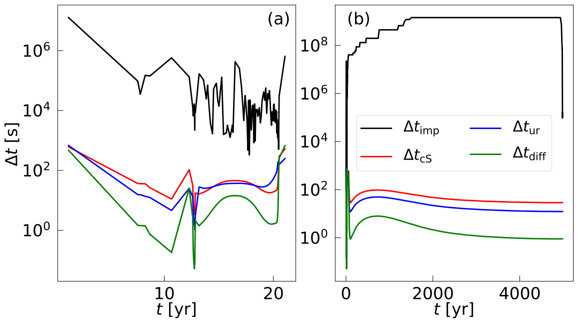

Fig. A.1. Comparison of the implicit time-step $\Delta t_{\rm imp}$ to time-step limitations imposed by the CFL condition with respect to the speed of sound $\Delta t_{\rm cS}$, the radial velocity $\Delta t_{\rm ur}$, and the diffusion $\Delta t_{\rm diff}$ for our fiducial model; (a) during an outburst and (b) during the quiescent phase between two outbursts. The decrease in $\Delta t_{\rm imp}$ at the right side denotes the beginning of the next outburst.

Implicit numerical models are not bound to the CFL condition and can benefit from larger time-steps and consequently shorter simulation times compared to explicit models. To quantify this difference, we compare the maximum possible time-step– $\Delta t \leq \Delta r/u_{\rm i}$ –allowed by the CFL condition; with the radial grid size Δr and a velocity $u_{\rm i}$ with which information propagates. In an accretion disk, there are several velocities that transport information. For this order-of-magnitude approximation, we want to compare the effects of the speed of sound $c_{\rm S}$ with those of the radial velocity $u_{\rm r}$. Additionally, the time-step limitation of diffusion in the disk– $\Delta t \leq \Delta r^2/D$ –is taken into account. Here, D is the diffusion coefficient and is connected to the viscosity ν via the Schmidt number $Sc = \nu/D$. Following Armitage (2011), Sc is of the order of unity and $Sc = 1$ is used. In Fig. A.1, the time-step used in the implicit TAPIR code is compared to the theoretical time-step limitations imposed by the CFL condition for an explicit method. During an outburst, the implicit time-step exceeds the explicit time-step by up to two orders of magnitude and during the quiescent phase, by up to six orders of magnitude. Our model also incorporates an adaptive time-step control, which increases or decreases Δt until the Newton-Raphson iteration (cf. Sect. 3.2) converges towards a solution. This results in shorter time-steps during bursts and longer time-steps in quiet phases, because in the latter case the disk quantities change slowly over time and a solution can still be found for longer time-steps. We can conclude that an explicit model with the same radial resolution would increase the computational time from days to months or even years, which again justifies this implicit approach.

Chapter 7

Paper II - The poloidal large-scale field topology in protoplanetary disks

Title: Protoplanetary disks around magnetized young stars with large-scale magnetic fields I: Steady-state solutions.
Authors: **D. Steiner**, L. Gehrig, M. Güdel
Year: 2025
Journal: Astronomy & Astrophysics
State of publication: Accepted for publication (September 8th 2025)
DOI: (Pending) 10.1051/0004-6361/202554871

Personal Contribution: As first author, the majority of the writing has been done by me. All figures have been done by me. All simulations have been performed by me. A tremendous amount of work was needed to include non-ideal MHD effects and the large-scale field in the simulation. All work related to this has been done by me. The co-authors have provided feedback on the final manuscript and in the form of scientific discussions.

In this publication we have studied the large-scale field topology in Class II protoplanetary disks with a novel approach. Determining of the strength and form of the poloidal field is currently challenging due to large uncertainties in describing magnetic flux transport. We have taken an initial, purely vertical, large-scale magnetic field and allowed it to evolve towards a stationary state. This steady state is reached because magnetic advection and diffusion eventually balance each other in the absence of MHD outflows. While our simulations are axisymmetric 1+D calculations, we have carefully modeled the ionization structure and the vertical velocity profile of the disk. This allows us to determine, if magnetic flux is transported inwards or outwards. Ohmic diffusion and ambipolar diffusion have been taken into account, but the Hall effect has not been considered. The decision to use stationary models for our analysis has enabled us to compare our results to those of other large-scale field models of stationary disks. Our approach also includes the inner disk region self-consistently and takes into account a stellar dipole field. We have found that the large-scale field in the inner disk region is influenced by a stellar dipole, while the large-scale magnetic field topology in the outer disk is governed by the efficiency of ambipolar diffusion. We have also conducted a parameter study, where we have focused on the variation of stellar parameters with the goal of investigating the dependency of the large-scale field topology on stellar parameters. To date, the connection between a star-disk system and a large-scale disk field has not been studied in long-term hydrodynamical simulations.

Astronomy & Astrophysics manuscript no. output
October 13, 2025

Protoplanetary disks around magnetised young stars with large-scale magnetic fields I: Steady-state solutions

D. Steiner[1], L. Gehrig[1], M. Güdel[1]

Department of Astrophysics, University of Vienna, Türkenschanzstrasse 17, A-1180 Vienna

Received 30 March 2025; accepted 8 September 2025

ABSTRACT

Context. Describing the large-scale field topology of protoplanetary disks (PPDs) involves significant difficulties and uncertainties. The transport of the large-scale field inside the disk plays an important role in understanding its evolution.

Aims. We aim to improve our understanding of the dependences that stellar magnetic fields pose on the large-scale field. We focus on the innermost disk region ($\lesssim 0.1$ AU), which is crucial for understanding the long-term disk evolution.

Methods. We present a novel approach combining the evolution of a 1+1D hydrodynamic disk with a large-scale magnetic field consisting of a stellar dipole truncating the disk and a fossil field. The magnetic flux transport includes advection and diffusion due to laminar non-ideal magnetohydrodynamic (MHD) effects, such as Ohmic and ambipolar diffusion. Due to the implicit nature of the numerical method, long-term simulations (of the order of several viscous timescales) are feasible.

Results. The large-scale magnetic field topology in stationary models shows a distinct dependence on specific parameters. The innermost disk region is strongly affected by the stellar rotation period and magnetic field strength. The outer disk regions are affected by the X-ray luminosity and the fossil field. Varying the mass flow through the disk affects the large-scale disk field throughout its radial extent.

Conclusions. The topology of the large-scale disk field is affected by several stellar and disk parameters. This will affect the efficiency of MHD outflows, which depend on the magnetic field topology. Such outflows might originate from the very inner disk region, the dead zone, or the outer disk. In subsequent studies, we will use these models as a starting point for conducting long-term evolution simulations of the disk and large-scale field on scales of $\sim 10^6$ years in order to investigate the combined evolution of the disk, the magnetic field topology, and the resulting MHD outflows.

Key words. protoplanetary disks – accretion, accretion disks – stars: protostars – stars: rotation methods: numerical

1. Introduction

Protoplanetary disks (PPDs) do not evolve in isolation from their environment. Among other parameters, magnetic fields play a crucial role in understanding the evolution of PPDs and can be present in two regions of a disk: (i) strong stellar magnetic fields from the forming protostar, which is most likely partly or fully convective, interacting with the innermost disk, and (ii) large-scale magnetic fields threading the whole disk (e.g. Ohashi et al. 2018; Tang et al. 2023), whose origin is the subject of current research. Either the field is generated inside the disk by some dynamo effect (e.g. Reyes-Ruiz et al. 2004; Brandenburg et al. 1995) or the field is already present during the collapse of the protostellar cloud core (e.g. Dudorov & Khaibrakhmanov 2014). The stellar magnetic field as well as the large-scale disk field strongly influence the dynamics of an evolving PPD on a macroscopic scale (e.g. Ferreira et al. 2006; Bai & Stone 2013; Simon et al. 2013). For instance, angular momentum can be transferred between a protostar and a disk through torques of the stellar field acting on the inner disk parts. The details of such a coupled star-disk system are complex and involve the inclusion of many parameters, for example, the abundance and efficiency of accretion-powered stellar winds (APSW; (Gehrig & Vorobyov 2023)). Additionally, the position of a magnetically truncated inner disk radius (e.g. Hartmann et al. 2016; Steiner et al. 2021) or the launch of magnetocentrifugal winds (MCWs; (Blandford & Payne 1982)) are also dependent on the large-scale field. Apart from the macroscopic influence, the development of the magneto-rotational instability (MRI), which in some disk regions is believed to play a non-negligible role in driving accretion (Balbus & Hawley 1991), relies on the abundance of an initial large-scale seed field. The strength of the large-scale field is also believed to be important for determining the efficiency of MRI in PPDs (e.g. Bai & Stone 2011). One approach to investigate how MRI is altered by a magnetic field is to assume a maximally efficient MRI in a steady-state disk, which then determines the magnetic field strength for every radius in the disk (e.g. Mohanty et al. 2018; Delage et al. 2022).

The dipole field strengths of classical T Tauri stars (CTTS) range between 500 G and 1.5 kG (e.g. Johns-Krull et al. 1999; Johnstone et al. 2014a) and are therefore strong enough to disrupt the disk at a certain radius, the so-called magnetic truncation radius, r_{trunc} (Hartmann et al. 2016). Although the details of magnetospheric accretion remain very complex to investigate (e.g. Romanova et al. 2002), it has been shown by Bessolaz et al. (2008) that under the assumption of a dipolar stellar magnetic field, the disk is magnetically truncated very close to the equipartition of magnetic pressure and thermal gas pressure (for detailed simulations of the inner disk movement during disk evolution, e.g. Steiner et al. 2021). Actual observations of large-scale magnetic fields threading a PPD remain challenging; however, magnetic fields have been detected on virtually every observationally accessible scale, including fields abundant in molecular clouds (e.g. Crutcher & Kemball 2019), which indicate that large-scale magnetic fields are likely to be present in a newly forming protostellar core and the resulting PPD. Recent observations of outflows and jets originating from the disk (e.g. Lee 2020) as well as polarisation mapping of the surroundings of T Tauri stars (e.g. Bertrang et al. 2017; Brauer et al. 2017) further strengthen the assumption of large-scale magnetic fields being abundant in PPDs. Additionally, the observation and high-precision measurement of the Zeeman effect in various emission lines has led to the calculation of an upper limit for some PPDs of the order of ∼ 10 mG for both the poloidal and toroidal fields at $r \approx 40$ AU (e.g. Lankhaar & Teague 2023).

The interaction between the disk and the large-scale field is complex. Early 1+1D studies found that an initially purely vertical fossil field threading a thin disk is not dragged inwards efficiently due to outward-directed diffusion counterbalancing inward-directed magnetic advection very easily (e.g. Lubow et al. 1994). Taking the vertical velocity profile of the disk into account has modified this result such that a large-scale field can also be dragged inwards efficiently in a thin disk due to a larger radial mass transport and higher ionisation near the disk surface. The corresponding magnetic resistivity is then adequately averaged in the vertical direction to represent this enhanced magnetic flux transport Guilet & Ogilvie (2012, 2014). However, the source of resistivity is still a subject of investigation. Earlier studies have used turbulent resistivity to describe the non-ideal effects (e.g. Lubow et al. 1994; Guilet & Ogilvie 2012, 2014), but recent studies strongly indicate that PPDs are laminar almost everywhere but the innermost disk region (e.g. Dudorov & Khaibrakhmanov 2014; Mohanty et al. 2018; Delage et al. 2022). Laminar non-ideal diffusion can be caused by Ohmic diffusion (OD), ambipolar diffusion (AD), or the Hall effect (HE).

Apart from 1+1D models, global long-term evolution models have been conducted, including magnetic fields in 2+1D (e.g. Vorobyov et al. 2020). Such models have to deal with the numerical difficulties of conducting magnetohydrodynamic (MHD) simulations over an extended period of time. In particular, the incorporation of magnetic diffusion poses challenges to the numerical stability of a scheme. Furthermore, such models are limited with respect to the position of the inner disk boundary, since the Courant-Friedrichs-Levy (CFL) condition (Courant et al. 1928) severely limits the time step achievable in a disk simulation inside of ∼ 1 AU. The model of Vorobyov et al. (2020) incorporates large-scale magnetic fields but without considering non-ideal magnetic diffusion due to numerical challenges, which leads to unusually strong magnetic advection and field amplification in their models.

The previous models used to study the influence of a large-scale magnetic field fall short in the following cases: (i) modelling the long-term simulations of a disk and large-scale magnetic field including the inner disk; (ii) modelling the effects of a stellar dipole together with a large-scale field on the inner disk and the topology, especially in the inner disk; (iii) describing the effects of a MCW on the long-term evolution of a PPD. In this work, we aim to investigate the evolution of a large-scale field towards a stationary state for a disk truncated by a stellar dipole. It has been shown that the inner disk treatment is crucial in terms of long-term evolution (e.g. Vorobyov et al. 2019; Steiner et al. 2021; Gehrig et al. 2022). Therefore, a combined treatment of both stellar- and disk components has the potential to alter the disk properties in the inner disk, compared to the common assumption of a torque-free inner disk boundary. A self-consistent evolution of the disk and large-scale magnetic field offers the possibility to study the disk field topology and strength not through assuming maximum efficient MRI (e.g. Mohanty et al. 2018; Delage et al. 2022) but through inward-dragging and amplification of a more physically motivated background fossil field. Furthermore, our simulations are not confined to steady-state models and allowed us to follow the disk field evolution over time. In this work, we introduce our new model and focus on the validation of our method by comparison with current work (e.g. Dudorov & Khaibrakhmanov 2014; Mohanty et al. 2018; Delage et al. 2022). Therefore, we focus on steady-state models. By combining the stellar and disk field components, we can study the effects of various parameters on the large-scale disk field, such as the stellar rotation period, magnetic field strength, X-ray luminosity, and the accretion rate (Sec. 3). These results form the basis for investigating MCWs self-consistently with a hydrodynamic accretion disk in the subsequent studies of this series.

2. Model description

The construction of a long-term evolution simulation of a PPD including a stellar magnetic field and a large-scale magnetic field involves a model describing the hydrodynamic flow of the disk while also covering the temperature structure of the disk and the influence of magnetic fields (cf. Sec. 2.1).

2.1. Basic equations

We use TAPIR for our 1+1D simulations (Ragossnig et al. 2020; Steiner et al. 2021), which solves the hydrodynamic equations using a fully implicit time integration scheme. Hence, the CFL condition does not restrict the timestep.[1] This allowed us to also include the very inner disk in our long-term hydrodynamic simulations, which is necessary to incorporate the torque of the stellar dipole and pressure gradients in our model (Steiner et al. 2021). The vertical disk extent is assumed to be hydrostatic, allowing for a vertical integration of the hydrodynamic equations Eqs. (1) - (3) (analogously to e.g. Vorobyov et al. 2020; Steiner et al. 2021). The effects of a magnetic field, $\boldsymbol{B}$, threading the disk is included by adding the non-ideal induction equation Eq. (4),

$$\frac{\partial \Sigma}{\partial t} + \nabla \cdot (\Sigma \boldsymbol{u}) = 0\,, \tag{1}$$

$$\frac{\partial (\Sigma \boldsymbol{u})}{\partial t} + \nabla \cdot (\Sigma \boldsymbol{u} : \boldsymbol{u}) - \frac{B_z \boldsymbol{B}}{2\pi} + \nabla P_{\rm gas} + \nabla \cdot Q + \Sigma \nabla \psi + H_{\rm p} \nabla \left(\frac{B_z^2}{4\pi}\right) = 0\,, \tag{2}$$

$$\frac{\partial (\Sigma\, e)}{\partial t} + \nabla \cdot (\Sigma\, \boldsymbol{u}\, e) + P_{\rm gas} \nabla \cdot \boldsymbol{u} + Q : \nabla \boldsymbol{u} - 4\pi \Sigma \kappa_{\rm R} \,(J - S) + \dot{E}_{\rm rad} = 0\,, \tag{3}$$

$$\frac{\partial \boldsymbol{B}}{\partial t} - \nabla \times (\boldsymbol{u} \times \boldsymbol{B}) + \nabla \times (\eta_{\rm O} \boldsymbol{J}) - \nabla \times \left(\frac{\eta_{\rm A}}{|\boldsymbol{B}|^2} \boldsymbol{J} \times \boldsymbol{B} \times \boldsymbol{B}\right) = 0\,, \tag{4}$$

where Σ, e, and $\boldsymbol{u} \equiv (u_{\rm r}, u_{\varphi}, 0)^{\rm T}$ denote current density, specific inner energy density and the gas velocity restricted to the planar direction. We used an ideal equation of state for which the gas pressure can be written as $P_{\rm gas} = \Sigma\, e\, (\gamma - 1)$ with an adiabatic coefficient $\gamma = 7/5$ (e.g. Vorobyov et al. 2020) and which allows for the definition of the pressure scale height, $H_{\rm p}$. The

[1] We discuss the timestep-control in our models in Sec. A.

terms including the viscous pressure tensor, Q, describe the viscous torque enabling radial angular momentum transport and the viscous heating in Eq. (2) and Eq. (3), respectively. The disk is heated and cooled by stellar irradiation and radiative cooling through its surface on both sides of the disk, respectively. Additionally, vertical radiative transport is included in the diffusion limit by assuming local thermal equilibrium (LTE) in vertical direction. Heating, cooling and vertical radiative transport are described by the net heating- and cooling rate per unit surface in Eq. (3), $\dot{E}_{\rm rad}$. In our model radiative transport in radial direction is also included approximately in the diffusion limit, which is described by the term $\Sigma\,\kappa_{\rm R}\;(J-S)$, where J and S denote the zeroth moment of the radiation field and the source function, respectively (for a detailed explanation see Ragossnig et al. 2020).

The viscous-α was implemented analogously to Steiner et al. (2021). We adopted the layered-viscosity model of Gammie (1996), which reads as

$$\alpha = \alpha_{\rm base} + \alpha_{\rm surf} + \alpha_{\rm deep}\,, \tag{5}$$

where $\alpha_{\rm base}$, $\alpha_{\rm surf}$, and $\alpha_{\rm deep}$ denote the base viscosity in the dead zone (DZ), the viscosity due to active MRI in the disk's surface layer, and the α-viscosity in the deeper disk layers. The surface layer is defined on each side of the disk with a thickness corresponding to a column density of $\Sigma_0 = 100\,{\rm g\,cm^2}$ (measured from the disk surface inwards). If $\Sigma > \Sigma_0$, non-thermal ionisation cannot penetrate deeper into the disk, and a deep layer with a different viscosity $\alpha_{\rm deep}$ is assumed:

$$\alpha_{\rm surf}(r) = \alpha_{\rm MRI,eff}\left[s_\Sigma\,\frac{\Sigma_0}{\Sigma(r)} + (1-s_\Sigma)\right]\,, \tag{6}$$

$$\alpha_{\rm deep}(r) = \alpha_{\rm MRI,eff}\;s_\Sigma\left(1-\frac{\Sigma_0}{\Sigma(r)}\right)s\,(T_0)\,, \tag{7}$$

$$s_\Sigma = \begin{cases}1 & \forall \quad \Sigma \geq \Sigma_0\\ 0 & \text{otherwise}\end{cases}\,, \tag{8}$$

where $\alpha_{\rm MRI,eff}$ denotes the effective α due to MRI. For all radii $r > r_{\rm DZ,out}$ (where $r_{\rm DZ,out}$ denotes the outer DZ boundary), MRI operates with reduced efficiency due to AD (e.g. Delage et al. 2022). We modelled this effect by applying a reduced $\alpha_{\rm AD} < \alpha_{\rm MRI}$ in the region $r > r_{\rm DZ,out}$ (the values for $\alpha_{\rm MRI}$, $\alpha_{\rm AD}$, and $\alpha_{\rm base}$ used in our reference model are listed in Table 2):

$$\alpha_{\rm MRI,eff} = \begin{cases}\alpha_{\rm MRI} & \forall \quad r < r_{\rm DZ,out}\\ \alpha_{\rm AD} & \forall \quad r \geq r_{\rm DZ,out}\end{cases}\,. \tag{9}$$

The factor $s(T_0)$ determines if the deep layer becomes MRI-active (Steiner et al. 2021, e.g.), which would lead to episodic accretion events (e.g. Steiner et al. 2021; Cecil et al. 2024). In this work the development of episodic accretion is suppressed by setting $s(T_0) = 0$, which is due to the focus on stationary disks in this work (a stationary disk does not have any time-dependent features such as episodic accretion).

The net heating- or cooling rate, $\dot{E}_{\rm rad}$, is written as follows,

$$\dot{E}_{\rm rad} = \Gamma - \Lambda\,, \tag{10}$$

where Γ and Λ describe the heating and cooling rate per unit surface, respectively. The heating rate is a combination of both viscous heating and stellar irradiation on both sides of the disk surface. Viscous heating of the gas happens mostly close to the midplane, where ρ is largest. The corresponding inner energy e is transported vertically up to the disk surface, yielding a temperature, $T_{\rm surf}$, at the disk surface, if LTE and an optically thick disk is assumed ($\tau \gg 1$). With the additional assumption of the source function S being constant over the vertical extent of the disk, $T_{\rm surf}$ can be written as (e.g. Dong et al. 2016; Ragossnig et al. 2020)

$$T_{\rm surf}^4 = \frac{8\,\tau_{\rm P}\,\sigma_{\rm SB}}{1+2\,\tau_{\rm P}+\frac{3}{2}\,\tau_{\rm R}\,\tau_{\rm P}}\left(T_{\rm gas,0}^4 + T_{\rm amb}^4 + \frac{L_\star}{4\,\pi\,r^2}f_{\rm irr}\,\sin\alpha_{\rm irr}\right)\,. \tag{11}$$

Here, $\tau_{\rm R} = \kappa_{\rm R}\,\rho_0\,H_{\rm p} = \kappa_{\rm R}\,\Sigma\,/\,\sqrt{2}$ and $\tau_{\rm P} = \kappa_{\rm P}\,\Sigma\,/\,\sqrt{2}$ describe the Rosseland and Planck mean opacity, respectively. $\kappa_{\rm R}$ has two contributions: (i) a gaseous component $\kappa_{\rm R,gas}$ using the method of Ferguson et al. (2005) with the protostellar abundances of Asplund et al. (2021), and (ii) a dust-dominated component for low temperatures $\kappa_{\rm R,dust}$ ($T_{\rm gas} < 500\,$K). Then $\kappa_{\rm R} = \kappa_{\rm R,gas} + f_{\rm dust}\,\kappa_{\rm R,dust}$, where $f_{\rm dust}$ denotes the gas-to-dust ratio (Pollack et al. 1985). The Planck mean opacity is approximated with $\kappa_{\rm P} = 2.4\,\kappa_{\rm R}$ and is based on Nakamoto & Nakagawa (1994); Hueso & Guillot (2005). The Stefan-Boltzmann constant is denoted as $\sigma_{\rm SB}$, and $T_{\rm amb}$ is the ambient temperature of the interstellar medium (ISM). The parameters $f_{\rm irr}$ and $\alpha_{\rm irr}$ describe which percentage of the stellar irradiation is reflected at the surface and the impact angle of the irradiation at the surface (with respect to the midplane). We note that we did not include the heating of the disk surface due to stellar X-ray irradiation (cf, Güdel 2015, and also Sec. 4.4). Then Γ and Λ can be written as (e.g. Vorobyov et al. 2020)

$$\Gamma = \frac{8\,\tau_{\rm P}\,\sigma_{\rm SB}}{1+2\,\tau_{\rm P}+\frac{3}{2}\,\tau_{\rm R}\,\tau_{\rm P}}\left(\frac{L_\star}{4\,\pi\,r^2}f_{\rm irr}\,\sin\alpha_{\rm irr} + T_{\rm amb}^4\right)\,, \tag{12}$$

$$\Lambda = \frac{8\,\tau_{\rm P}\,\sigma_{\rm SB}}{1+2\,\tau_{\rm P}+\frac{3}{2}\,\tau_{\rm R}\,\tau_{\rm P}}T_{\rm gas,0}^4\,. \tag{13}$$

The stellar magnetic field at the disk surface (which in our case was chosen to be the magnetic surface $z_{\rm B}$, cf. Guilet & Ogilvie 2012, explained in detail in Sec. 2.2) was modeled as a dipole with the components in cylindrical coordinates $\boldsymbol{B}_\star = (B_{{\rm r},\star}, B_{\varphi,\star}, B_{{\rm z},\star})^{\rm T}$ (analogously to Steiner et al. 2021; Gehrig & Vorobyov 2023, but without ignoring the radial component of the dipole):

$$B_{{\rm z},\star}(r,z) = B_\star\,R_\star^3\,\frac{r^2-2\,z^2}{\left(\sqrt{r^2+z^2}\right)^5}\,, \tag{14}$$

$$B_{{\rm r},\star}(r,z) = -B_\star\,R_\star^3\,\frac{3\,r\,z}{\left(\sqrt{r^2+z^2}\right)^5}\,, \tag{15}$$

$$B_{\varphi,\star} \simeq -\alpha_{\rm cor}\,B_{{\rm z},\star}(r,z)\left[1-\left(\frac{\Omega_\star}{\Omega(r)}\right)^{\alpha_{\rm cor}}\right]\,, \tag{16}$$

$$\alpha_{\rm cor} \equiv \begin{cases}+1 & \text{if } r < r_{\rm cor}\\ -1 & \text{if } r > r_{\rm cor}\end{cases}\,, \tag{17}$$

where $B_\star$ denotes the magnetic field strength at the stellar surface and $R_\star$ the stellar radius. $\alpha_{\rm cor}$ is a parameter which ensures that $\max(|{\rm B}_{\varphi,\star}|) \simeq |B_{{\rm z},\star}|$. This occurs very close to the star and at a certain distance outside the corotation radius, $r_{\rm cor}$, and is physically motivated by the assumption that a stronger winding of the dipole would lead to buoyancy and reconnection of $B_{\varphi,\star}$ (e.g. Steiner et al. 2021; Gehrig & Vorobyov 2023).

2.2. Large-scale magnetic disk field

In this study we made the following assumptions about the large-scale disk magnetic field: (i) The magnetic field is formally averaged in azimuthal direction and temporally over the dynamical timescale at a certain radius, which means that the large-scale field in our model is axisymmetric. Additionally, the averaging results in only the macroscopic net field being considered and the microscopic fluctuations, which eventually lead to turbulence and to MRI, being modelled in the usual way using the isotropic α-viscosity (Shakura & Sunyaev 1973) and the turbulent resistivity, η_t (e.g. Guilet & Ogilvie 2012, 2014). (ii) We did not include a toroidal field component, B_φ, in the disk exterior (above the disk surface) in our model to avoid the complexity of starting a MHD wind. Hence, B_φ^s [2] was set to zero by means of a Dirichlet boundary condition (i.e., $B_\varphi^s = 0$; for an in-depth analysis of the possible boundary conditions for B_φ^s cf. Khaibrakhmanov & Dudorov 2022). B_φ^s acts as an outer boundary at the disk surface for a toroidal field inside the disk. This means that B_φ inside the disk can be non-vanishing due to shearing of B_r caused by differential rotation, as long as it is connected to the exterior field at the disk surface (cf. Sec. 2.4 for a more detailed treatment). This causes additional diffusion and therefore contributes to the (vertically averaged) magnetic flux transport velocity, $\bar{\bar{u}}_\psi$ (e.g. Guilet & Ogilvie 2012; Leung & Ogilvie 2019, and Eq. (51) below). (iii) The magnetic field was assumed to be stationary in vertical direction, compared to its slow evolution in radial direction. This is due to the assumption of a geometrically thin disk (i.e., $H_p/r \ll 1$; e.g. Guilet & Ogilvie 2012, for a discussion of the difference between viscous and vertical dynamical timescales in terms of an asymptotic expansion of the basic MHD equations, cf. also Sec. 2.7). (iv) No dynamo effect, which might develop in the disk (e.g. Reyes-Ruiz et al. 2004), was considered in this work. The poloidal, large-scale magnetic field, $\boldsymbol{B} = (B_r, 0, B_z)^T$, can be represented by the magnetic flux ψ,

$$\boldsymbol{B} = \nabla\psi \times \boldsymbol{e}_\varphi\,, \tag{18}$$

where e_φ describes the azimuthal unit vector in cylindrical coordinates (e.g. Guilet & Ogilvie 2014). The induction equation Eq. (4) can then be written as follows (e.g. Ogilvie & Livio 2001),

$$\frac{\partial\psi(r,z)}{\partial t} + \boldsymbol{u}\cdot\nabla\psi(r,z) = \eta(r,z)\,r^2\,\nabla\cdot\left(\frac{1}{r^2}\nabla\psi(r,z)\right), \tag{19}$$

$$\eta(r,z) = \eta_O(r,z) + \eta_A(r,z) + \eta_t(r,z)\,, \tag{20}$$

where η is the combination of all resistivity mechanisms considered in this work, i.e. turbulent resistivity, OD, AD, which are denoted by η_t, η_O, and η_A, respectively. We note that η_A in Eq. (20) only denotes the 'Ohm-like' contribution. AD also has a 'Hall-like' contribution, which was neglected in this work due to a vanishing toroidal field in the disk exterior above the surface. This in turn causes the 'Hall-like' contribution to vanish (e.g. Leung & Ogilvie 2019). Assuming a thin disk allowed $\psi(r,z)$ to be split into a radial contribution, $\psi_0(r)$, and a small contribution, which describes the vertical dependence, $\psi_1(r,z)$, and for which $|\psi_1| \ll |\psi_0|$ holds,

$$\psi(r,z) = \psi_0(r) + \psi_1(r,z)\,, \tag{21}$$

$$B_z = \frac{1}{r}\frac{\partial\psi_0}{\partial r} = B_{z,d} + B_{z,\star}\,, \tag{22}$$

$$B_r = -\frac{1}{r}\frac{\partial\psi_1}{\partial z} = B_{r,d} + B_{r,\star}\,, \tag{23}$$

[2] The superscript "s" means that we take the value of the corresponding physical quantity at the disk surface.

where B_r and B_z denote the combined stellar and large-scale fields in radial and vertical direction, respectively. Our simulations were done in 1+1D; however Eq. (19) is height-dependent and can be evaluated at any z above the midplane, which makes it necessary to average Eq. (19) vertically. Analogously to Ogilvie & Livio (2001); Guilet & Ogilvie (2014), a sensible choice is a conductivity-weighted vertical average up to the magnetic surface, z_B (for the remainder of this work also referenced as disk surface), which is the height above the disk where magnetic and thermal gas pressure are equal (or equivalently, where the plasma beta $\beta(z = z_B) = 1$). In the case of a hydrostatically stratified disk z_B reads as

$$z_B = H_p\sqrt{\ln\left(\frac{2}{\pi}\beta_0\right)}\,, \tag{24}$$

$$\beta_0 \equiv \frac{8\,\pi\,P_{gas}}{B_z^2}\,, \tag{25}$$

where β_0 and z_B describe the plasma beta at the disk midplane and the magnetic surface, respectively. Averaging this way results in $\bar{\bar{\eta}}$ being dominated by vertical disk layers of high conductivity (low resistivity) and takes into account that the magnetic field is transported inwards more effectively in vertical disk layers of high conductivity. Applying the conductivity-weighted vertical averaging to η and the radial gas velocity, u_r, yields

$$\frac{1}{\bar{\bar{\eta}}(r)} \equiv \frac{1}{z_B}\int_0^{z_B}\frac{1}{\eta(r,z)}\mathrm{d}z$$
$$= \frac{1}{z_B}\int_0^{z_B}\frac{1}{\eta_O(r,z) + \eta_A(r,z) + \eta_t(r,z)}\mathrm{d}z\,, \tag{26}$$

$$\bar{\bar{u}}_r(r) \equiv \frac{\bar{\bar{\eta}}(r)}{z_B}\int_0^{z_B}\frac{u_r(r,z)}{\eta(r,z)}\mathrm{d}z\,, \tag{27}$$

where the double-bar notation denotes conductivity-weighted averaged quantities. Integrating Eq. (19) vertically between $[-z_B, z_B]$ and applying Eqs. (22) - (23) as well as using Eqs. (26) - (27), we can rewrite the magnetic flux transport equation Eq. (19) in a height-independent form (strictly following Guilet & Ogilvie 2014),

$$\frac{\partial\psi_0(r)}{\partial t} + r\,\bar{\bar{u}}_\psi\,B_z = 0\,, \tag{28}$$

$$\bar{\bar{u}}_\psi = \bar{\bar{u}}_r + \frac{\bar{\bar{\eta}}}{z_B}\frac{1}{B_z}\left(B_r(r, z = z_B^-) - z_B\frac{\partial B_z}{\partial r}\right), \tag{29}$$

where z_B^- denotes the vertical height at the surface, but approached from inside the disk (analogously z_B^+ denotes the magnetic surface approached from above the disk). This is important for modelling the connection at the disk surface between an external magnetic field and the large-scale field inside the disk Sec. 2.4 (e.g. Guilet & Ogilvie 2014). The vertical averaging performed in Eq. (29) has no description of the vertical dependency of B_r inside the disk, but only its value at the surface $B_r(r, z = z_B^-)$. The determination of this external field is not trivial and is described in Sec. 2.3. Additionally, averaging $\bar{\bar{u}}_r$ and $\bar{\bar{\eta}}$ requires knowing the vertical profiles of $u_r(r,z)$ and $\eta(r,z)$. Assuming $\beta \gg 1$ inside the disk and a constant viscous-α in vertical direction allows us to find an analytic expression for the vertical velocity profiles (e.g. Guilet & Ogilvie 2012; Leung & Ogilvie 2019), which we briefly summarise in Sec. 2.4). For the vertical profile of η we need the ionisation fraction, x_e, which can be caused by thermal ionisation or by various non-thermal ionisation sources such as X-rays and cosmic rays. We discuss all ionisation sources included in our model in Sec. 2.5.

2.3. External magnetic field

The radial magnetic field at the disk surface, $B_{\mathrm{r}}^{\mathrm{s}}$, is connected to the exterior field above and below the disk, which is a superposition of three components: (i) a fossil field, B_∞, formally created by currents at infinity, (ii) the stellar dipole field, $\boldsymbol{B}_\star$, and (iii) the field created by purely toroidal currents (due to our assumption of a poloidal field), J_φ, in the disk. Due to the thin-disk approximation used in our model we only need to describe the radial part of the large-scale field's flux function, ψ_0 (cf. Eq. (28)). The three magnetic flux contributions from the fossil field, stellar dipole, and current density, J_φ, in the disk are denoted by ψ_∞, $\psi_\star$, and ψ_{d}, respectively,

$$\psi_0 = \psi_\infty + \psi_\star + \psi_{\mathrm{d}} \,. \tag{30}$$

The Biot-Savart law was used to find an expression for the large-scale magnetic field and hence for the corresponding magnetic flux, ψ_{d}, of an axisymmetric current distribution, J_φ^{s}, by integrating the field caused by the current loops at every r over the full radial extent of the disk (e.g. Jackson 1999; Ogilvie 1997):

$$\psi_{\mathrm{d}}(r) = \frac{1}{\pi}\int_{r_{\mathrm{in}}}^{r_{\mathrm{out}}} \frac{r\,r'}{r+r'}\left[\frac{(2-k^2)\,K(k) - 2\,E(k)}{k^2}\right] J_\varphi^{\mathrm{s}}(dr')\,dr' \,, \tag{31}$$

$$k^2 = \frac{4\,r\,r'}{(r+r')^2}\,, \tag{32}$$

$$E(k) = \int_0^{\pi/2} (1-k^2\,\sin^2(x))^{1/2}\,dx\,, \tag{33}$$

$$K(k) = \int_0^{\pi/2} (1-k^2\,\sin^2(x))^{-1/2}\,dx\,, \tag{34}$$

where $E(k)$ is the complete elliptic integral of the first kind and $K(k)$ corresponds to the complete elliptic integral of the second kind (e.g. Guilet & Ogilvie 2014). Applying Stokes' theorem to Eq. (18) allows the disk's radial field at the surface, $B_{\mathrm{r,d}}^{\mathrm{s}}$, to be connected with J_φ^{s} at the disk surface (e.g. Ogilvie 1997; Guilet & Ogilvie 2014):

$$B_{\mathrm{r,d}}^{\mathrm{s}}(r) = 2\,J_\varphi^{\mathrm{s}}(r)\,. \tag{35}$$

We note that $B_{\mathrm{r,d}}^{\mathrm{s}}$ describes the radial field corresponding to the currents in the disk only, without any contributions from stellar dipole or fossil field.

The magnetic fluxes ψ_∞ and $\psi_\star$ are calculated as follows,

$$\psi_\infty = \frac{r^2 - R_\star^2}{2} B_\infty\,, \tag{36}$$

$$\psi_{\star,0} = B_\star\,R_\star^3\left(\frac{1}{R_\star} - \frac{1}{r}\right)\,, \tag{37}$$

which both can be readily calculated, since the stellar dipole field, $B_\star$, and the fossil field, B_∞, are both parameters of our model. Since Eq. (28) describes the evolution of ψ_0 at a certain time, we can use Eq. (35) with Eq. (31) to find a relation between ψ_{d} and $B_{\mathrm{r,d}}^{\mathrm{s}}$ and then reorganise Eq. (30) as follows,

$$\psi_{\mathrm{d}} = \psi_0 - \psi_\infty - \psi_\star\,. \tag{38}$$

Finally, for calculating $B_{\mathrm{r,d}}^{\mathrm{s}}$ we interpreted the integral of Eq. (31) as a linear operator, $\mathcal{L}$, which can then be formally inverted to obtain

$$B_{\mathrm{r,d}}^{\mathrm{s}} = \mathcal{L}^{-1}\,\psi_{\mathrm{d}}\,. \tag{39}$$

Numerically, $\mathcal{L}^{-1}$ is represented as a matrix describing the relationship between all discretised values of $B_{\mathrm{r,d}}^{\mathrm{s}}$ and ψ_{d}. Its construction and inversion is non-trivial and numerically expensive and is briefly discussed in App. A.

2.4. Analytical vertical velocity and magnetic field profile

In 1+1D, hydrodynamical models usually employ a density-weighted, vertically averaged radial and rotational velocity, $\bar{u}_{\mathrm{r}}(r)$ and $\bar{u}_\varphi(r)$, respectively, and therefore the actual velocity structure is usually not resolved by assuming a vertically constant velocity $\boldsymbol{u} = (u_{\mathrm{r}}(r), u_\varphi(r), 0)^{\mathrm{T}}$. However, work done by Guilet & Ogilvie (2012); Leung & Ogilvie (2019) indicates that radial magnetic flux transport can significantly deviate from mass transport, if the vertical velocity structure is included. This is due to the two different vertical averaging mechanisms for mass and magnetic flux transport (cf. Sec. 2.2 and Eqs. (26) - (27)). Using that the vertical dynamical timescale is much shorter than the radial diffusion and viscous timescales, the disk structure in vertical direction appears stationary with respect to viscous evolution, and therefore is treated as such (e.g. Guilet & Ogilvie 2012; Dudorov & Khaibrakhmanov 2014; Leung & Ogilvie 2019).

Strictly following the work of Guilet & Ogilvie (2014); Leung & Ogilvie (2019), the disk can be split into two zones vertically: (i) the regions within the magnetic surface, z_{B}, where it is assumed that the magnetic field is passive, i.e. $\beta \gg 1$, and (ii) a magnetically dominated region outside z_{B}, where in the absence of outflows the magnetic field can be modelled as force-free. It follows that in the case of a vertically constant α and with a passive large-scale field, the gas velocity profiles are parabolic in the vertical direction,

$$u_{\mathrm{r}} = u_{\mathrm{r},0}(r) + u_{\mathrm{r},2}(r)\frac{z^2}{H_{\mathrm{p}}^2}\,, \tag{40}$$

$$u_\varphi = u_{\varphi,0}(r) + u_{\varphi,2}(r)\frac{z^2}{H_{\mathrm{p}}^2}\,, \tag{41}$$

where $u_{\mathrm{r},0}$ and $u_{\varphi,0}$ denote the radial and toroidal velocities at the disk midplane, respectively, whereas $u_{\mathrm{r},2}$ and $u_{\varphi,2}$ are functions which describe the vertical dependency of u_{r} and u_φ. After integration of the vertical, stationary disk profile (e.g. Guilet & Ogilvie 2012), $u_{\mathrm{r},2}$ and $u_{\varphi,2}$ take the following form,

$$u_{\mathrm{r},2} = \frac{\alpha\,c_{\mathrm{s}}}{1+4\,\alpha^2}\left(\frac{3\,H_{\mathrm{p}}}{r} - 5\,\frac{\partial H_{\mathrm{p}}}{\partial r}\right)\,, \tag{42}$$

$$u_{\varphi,2} = \frac{c_{\mathrm{s}}}{2}\left(\frac{\partial H_{\mathrm{p}}}{\partial r} - \frac{3\,H_{\mathrm{p}}}{2\,r}\right) + \frac{\alpha^2\,c_{\mathrm{s}}}{1+4\,\alpha^2}\left(\frac{3\,H_{\mathrm{p}}}{r} - 5\,\frac{\partial H_{\mathrm{p}}}{\partial r}\right)\,. \tag{43}$$

We note that, strictly speaking, Eq. (40) and Eq. (41) can only be written as above for a vertically constant α. It was shown that a more realistic vertical profile of α, which is certainly expected in a real-world PPD, has only a minor influence on the large-scale magnetic field in steady-state (e.g. Guilet & Ogilvie 2014). Therefore, the use of those simplified profiles in this work is a viable approximation. However, the diffusion timescale at which the magnetic field evolves may be altered significantly (e.g. Leung & Ogilvie 2019), which makes it necessary to adopt a more realistic vertical velocity profile for future work for cases when the detailed time evolution matters (e.g. the time-dependent long-term disk evolution with an outflow).

The magnetic field profiles $B_{\mathrm{r}}(r,z)$ and $B_\varphi(r,z)$ are dependent on the values of the exterior field components $B_{\mathrm{r}}^{\mathrm{s}}$ and B_φ^{s} at the disk surface. As mentioned above, to avoid the complications of a magnetically induced outflow, no toroidal field at the disk surface was assumed, i.e. $B_\varphi^{\mathrm{s}} = 0$. However, inside the disk ($0 \le z \le z_{\mathrm{B}}$) a toroidal component can develop (e.g. Guilet & Ogilvie 2012). The two-zone model briefly described above has the disadvantage that the intermediate region $\beta \approx 1$ between the passive region $\beta \gg 1$ and the magnetically dominated disk corona $\beta \ll 1$ is infinitesimally small, which leads to a jump between the values of $B_\mathrm{r}(r,z)$ and $B_\varphi(r,z)$ just below $(z = z_\mathrm{B}^-)$ and above $(z = z_\mathrm{B}^+)$ the disk surface,

$$B_\mathrm{r}(z = z_\mathrm{B}^-) = B_\mathrm{r}(z = z_\mathrm{B}^+) + \Delta B_\mathrm{r} \,, \tag{44}$$

$$B_\varphi(z = z_\mathrm{B}^-) = B_\varphi(z = z_\mathrm{B}^+) + \Delta B_\varphi \,, \tag{45}$$

where ΔB_r and ΔB_φ are the jump conditions for the radial and toroidal field, respectively. The boundary conditions for B_r and B_φ and jump conditions are read as follows (e.g. Guilet & Ogilvie 2012, for an in-depth derivation),

$$B_\mathrm{r}(z_\mathrm{B}^+) = B_\mathrm{r}^\mathrm{s} + H_\mathrm{p}\,\frac{\partial B_z}{\partial r} \,, \tag{46}$$

$$\Delta B_\mathrm{r} = -H_\mathrm{p}\,\pi\,\frac{\partial B_\varphi}{\partial z}\bigg|_{z=z_\mathrm{B}^-} \,, \tag{47}$$

$$B_\varphi(z_\mathrm{B}^+) = 0 \,, \tag{48}$$

$$\Delta B_\varphi = 0 \,. \tag{49}$$

We note that the vertical profile of $B_\varphi(r,z)$ is indeed important to obtain the jump condition Eq. (47) for B_r. With Eqs. (46) - (49), the final form of the vertical profiles for B_r and B_φ reads as (Guilet & Ogilvie 2012; Leung & Ogilvie 2019, but using OD, 'Ohm-like' AD, ignoring HE, and including hydrodynamical terms)

$$\begin{aligned} B_\mathrm{r}(r, z < z_\mathrm{B}) = {} & \frac{z}{1 - \pi\,c_\mathrm{s}\,H_\mathrm{p}/(2\,\eta_{z_\mathrm{B}})}\left[\frac{B_\mathrm{r}^\mathrm{s}}{z_\mathrm{B}} + \frac{\partial B_z}{\partial r}\right. \\ & \left. + \left(5 - \frac{3\,\pi\,c_\mathrm{s}\,H_\mathrm{p}}{2\,\eta_{z_\mathrm{B}}}\right)\frac{B_z\,u_{\mathrm{r},2}\,z_\mathrm{B}^2}{H_\mathrm{p}^2\,15\,\eta_{z_\mathrm{B}}} - \frac{4\,B_z\,\pi\,u_{\varphi,2}}{3\,\eta_{z_\mathrm{B}}}\right] \\ & - \frac{B_z\,u_{\mathrm{r},2}\,z^3}{3\,\eta_{z_\mathrm{B}}\,H_\mathrm{p}^2} \,, \end{aligned} \tag{50}$$

$$\begin{aligned} B_\varphi(r, z < z_\mathrm{B}) = {} & \frac{c_\mathrm{s}}{2\,H_\mathrm{p}\,\eta_{z_\mathrm{B}}\,[1 - \pi\,c_\mathrm{s}\,H_\mathrm{p}/(2\,\eta_{z_\mathrm{B}})]}\Bigg[\\ & \frac{1}{2}\left(\frac{B_\mathrm{r}^\mathrm{s}}{z_\mathrm{B}} + \frac{\partial B_z}{\partial r}\right) z\,(z^2 - z_\mathrm{B}^2) \\ & + \frac{B_z\,u_{\mathbf{r},2}\,z(z^2 - z_\mathrm{B}^2)}{120\,\eta_{z_\mathrm{B}}^2\,H_\mathrm{p}^2}\left[z_\mathrm{B}^2\,(3\,c_\mathrm{s}\,H_\mathrm{p}\,\pi - 14\,\eta_{z_\mathrm{B}})\right. \\ & \left. -(z^2\,(6\,c_\mathrm{s}\,H_\mathrm{p}\,\pi - 20\,\eta_{z_\mathrm{B}})\right] \\ & - \frac{2\,B_z\,u_{\varphi,2}\,z\,(z_\mathrm{B}^2 - z^2)}{3\,c_\mathrm{s}\,H_\mathrm{p}\,\eta_{z_\mathrm{B}}}(2\,\eta_{z_\mathrm{B}} - c_\mathrm{s}\,H_\mathrm{p})\Bigg] \,, \end{aligned} \tag{51}$$

where $\eta_{z_\mathrm{B}} = \eta(z = z_\mathrm{B})$. Taking the value of η at $z = z_\mathrm{B}$ for B_r and B_φ is justified both by taking the value of η at the transition zone $(z \approx z_\mathrm{B})$ and by the fact that the marginally stable mode allowing a single bending of the field line in radial direction is localised around the transition zone as well (e.g. Ogilvie & Livio 2001; Guilet & Ogilvie 2012; Leung & Ogilvie 2019, for a thorough analysis of the marginal stability theory). Finally, the magnetic transport velocity can be calculated by evaluating B_r at $z = z_\mathrm{B}^-$ and by using Eq. (29),

$$\begin{aligned} \bar{\bar{u}}_\psi = {} & \bar{\bar{u}}_\mathrm{r} + \frac{\bar{\bar{\eta}}}{B_z}\,\frac{\pi\,c_\mathrm{s}\,H_\mathrm{p}/(2\,\eta_{z_\mathrm{B}})}{1 - \pi\,c_\mathrm{s}\,H_\mathrm{p}/(2\,\eta_{z_\mathrm{B}})}\,\frac{\partial B_z}{\partial r} \\ & + \frac{1}{1 - \pi\,c_\mathrm{s}\,H_\mathrm{p}/(2\,\eta_{z_\mathrm{B}})}\left[\frac{\bar{\bar{\eta}}}{z_\mathrm{B}}\,\frac{B_\mathrm{r}^\mathrm{s}}{B_z}\right. \\ & \left. + \left(5 - \frac{3\,\pi\,c_\mathrm{s}\,H_\mathrm{p}}{2\,\eta_{z_\mathrm{B}}}\right)\frac{z_\mathrm{B}^2}{H_\mathrm{p}^2}\,\frac{u_{\mathrm{r},2}\,\bar{\bar{\eta}}}{15\,\eta_{z_\mathrm{B}}} - \frac{4\,\pi\,u_{\varphi,2}\,\bar{\bar{\eta}}}{3\,\eta_{z_\mathrm{B}}}\right] \\ & - \frac{u_{\mathrm{r},2}\,z_\mathrm{B}^2\,\bar{\bar{\eta}}}{3\,H_\mathrm{p}^2\,\eta_{z_\mathrm{B}}} \,. \end{aligned} \tag{52}$$

We note that $\bar{\bar{\eta}}$ and η_{z_B} are appearing multiple times in Eq. (52), which emphasises again the need for a detailed model of $\eta(r,z)$ (see Sec. 2.5).

For solving Eqs. (1) - (3), the usual density-weighted vertical averages were used for the unknowns Σ, e, and $\boldsymbol{u}$ (e.g. Ragossnig et al. 2020). Therefore, using the vertical velocity profiles Eqs. (40) - (41), $\bar{u}_{\mathrm{r}(\varphi)}$[3] were obtained as follows,

$$\bar{u}_{\mathrm{r}(\varphi)} = \frac{1}{\Sigma}\int_{-\infty}^{\infty} u_{\mathrm{r}(\varphi)}(r,z)\,\rho(r,z)\,dz = u_{\mathrm{r}(\varphi),0} + u_{\mathrm{r}(\varphi),2} \,, \tag{53}$$

Since $u_{\mathrm{r}(\varphi),2}$ can be calculated using Eqs. (42) - (43), the remaining unknowns with respect to $\boldsymbol{u}$ are $u_{\mathrm{r}(\varphi),0}$.

2.5. Non-ideal resistivity model

Magnetic resistivity, $\eta(r,z)$, occurs due to turbulence, in our case denoted by η_t, or laminar, non-ideal diffusion processes such as OD, η_O; AD, η_A; and diffusion due to HE, η_H. However, η_H was not considered in this work. η_t is connected to the turbulence causing the MRI, and therefore to α. The laminar diffusion processes are dependent on the ionisation fraction, x_e, and the vertical temperature structure, $T_\mathrm{gas}(r,z)$, and are discussed in this section.

Turbulent resistivity: The assumption of η_t being caused by the same turbulence as MRI and therefore turbulent viscosity, ν, leads to the expectation that the strengths of η_t and ν are of the same order. This is described by the magnetic Prandtl number, $\mathcal{P}$, which is defined as

$$\mathcal{P} = \frac{\nu}{\eta_\mathrm{t}} \,, \tag{54}$$

where $\mathcal{P}$ is fixed in this work to the value $\mathcal{P} = 1$, which leads to

$$\eta_\mathrm{t} = \nu \,. \tag{55}$$

Laminar resistivity: Both η_O and η_A depend on x_e in the disk,

$$x_\mathrm{e} = \frac{n_\mathrm{e}}{n_\mathrm{tot}} = \frac{n_\mathrm{e}}{n_\mathrm{e} + n_\mathrm{n} + n_\mathrm{i}} \approx \frac{n_\mathrm{e}}{n_\mathrm{n}} \,, \tag{56}$$

where n_tot, n_e, n_n, and n_i denote the total number density, and the number densities of electrons, neutrals, and ions, respectively. By far the most abundant element in PPDs is molecular hydrogen. Therefore, the assumption of $n_{\mathrm{H}_2} \approx n_\mathrm{n} \approx n_\mathrm{tot}$ is valid (e.g.

[3] The index $r(\varphi)$ stands for the radial and toroidal velocity component to abbreviate the otherwise identical formulae.

Mohanty et al. 2018). We note that $\eta_{\rm O}$ is defined as

$$\eta_{\rm O} = \frac{c^2}{4\,\pi\,\sigma_{\rm O}}\,, \tag{57}$$

$$\sigma_{\rm O} \approx \frac{e^2\,n_{\rm e}}{m_{\rm e}\,\langle\sigma v\rangle_{\rm en}} = \frac{e^2\,x_{\rm e}\,n_{\rm tot}}{m_{\rm e}\,\langle\sigma v\rangle_{\rm en}}\,, \tag{58}$$

where $\sigma_{\rm O}$ denotes the Ohmic conductivity and is directly proportional to $x_{\rm e}$ (e.g. Bai & Goodman 2009). The rate coefficient of electron-neutral collisions and electron mass are described by $\langle\sigma v\rangle_{\rm en}$ and $m_{\rm e}$, respectively.

We note that $\eta_{\rm A}$ has an additional dependency on both the magnetic field strength and Σ (e.g. Lesur et al. 2014) and can be written as (again for the assumption of electrons and single-charged ions only)

$$\eta_{\rm A} = \beta_{\rm i}\,\beta_{\rm e}\,\eta_{\rm O}\,, \tag{59}$$

$$\beta_{\rm i(e)} = \frac{e\,B}{m_{\rm i(e)}\,c}\,\frac{1}{\gamma_{\rm i(e)}\,\rho_{\rm n}}\,. \tag{60}$$

Here $\beta_{\rm i(e)}$ denote the Hall parameters (e.g. Mohanty et al. 2018) for single-charged ions (index 'i') and electrons (index 'e'). The variables $m_{\rm i}$, $\rho_{\rm n}$, and $\gamma_{\rm i(e)}$ identify the mean ion mass, density of neutral gas and the drag coefficient for ions or electrons, respectively. With the following definitions of $\gamma_{\rm i(e)}$, $\langle\sigma v\rangle_{\rm en}$, and the rate coefficient of ion-neutral collisions, $\langle\sigma v\rangle_{\rm in}$ (e.g. Wardle 2007; Mohanty et al. 2018),

$$\gamma_{\rm i(e)} = \frac{\langle\sigma v\rangle_{\rm in(en)}}{m_{\rm i(e)} + m_{\rm n}}\,, \tag{61}$$

$$\langle\sigma v\rangle_{\rm in} = 1.6\times10^{-9}\,{\rm cm^3\,s^{-1}}\,, \tag{62}$$

$$\langle\sigma v\rangle_{\rm en} = 10^{-15}\left(\frac{128\,k_{\rm B}\,T_{\rm e}}{9\,\pi\,m_{\rm e}}\right)\,{\rm cm^3\,s^{-1}}\,, \tag{63}$$

the laminar resistivities, $\eta_{\rm O}$ and $\eta_{\rm A}$, can be written as (assuming that the electron temperature $T_{\rm e} = T_{\rm gas}$):

$$\eta_{\rm O}(r,z) \approx 230\,\sqrt{T_{\rm gas}(r,z)}\,\frac{1}{x_{\rm e}(r,z)}\,{\rm cm^2\,s^{-1}}\,, \tag{64}$$

$$\eta_{\rm A}(r,z) \approx 4.95\times10^{-15}\,\frac{|\boldsymbol{B}|^2}{\rho(r,z)^2\,x_{\rm e}(r,z)}\,{\rm cm^2\,s^{-1}}\,. \tag{65}$$

We point out that we have explicitly stated the radial and vertical dependency of $T_{\rm gas}$, $x_{\rm e}$, ρ, $\eta_{\rm O}$, and $\eta_{\rm A}$ to emphasise that it is necessary to model these dependences in a 1+1D model in an approximate way. Gas in a PPD is either ionised thermally (depicted by $x_{\rm e,th}$) or non-thermally ($x_{\rm e,nth}$),

$$x_{\rm e} = x_{\rm e,th} + x_{\rm e,nth}\,. \tag{66}$$

Thermal ionisation: A high gas temperature, $T_{\rm gas}(r,z)$, causes ionising collisions between atoms, which are counteracted by recombination of those same atoms with electrons. This eventually leads to an equilibrium level of ionisation and is described by the Saha equation (e.g. Mohanty et al. 2018), in the following shown for potassium (subscript K)

$$\frac{n_{\rm e}\,n_{\rm +,K}}{n_{\rm 0,K}} = 2.41\times10^{15}\,\sqrt{T_{\rm gas}^3}\,\exp\left(-\frac{5.04\times10^4\,{\rm K}}{T_{\rm gas}}\right)\,{\rm cm^{-3}} \tag{67}$$

$$= \mathcal{S}_{\rm K}(T_{\rm gas})\,{\rm cm^{-3}}\,, \tag{68}$$

where $n_{\rm 0,K}$ and $n_{\rm +,K}$ are the number densities of neutral and ionised potassium, respectively. The function $\mathcal{S}_{\rm K}(T_{\rm gas})$ denotes the right-hand side of Eq. (67) and is dependent on $T_{\rm gas}$ only. Following Mohanty et al. (2018), the thermal ionisation fraction, $x_{\rm e,th}$, can then be written as,

$$x_{\rm e,th} = \frac{-1 + \sqrt{1 + 4\,x_{\rm K}\,(n_{\rm tot}/\mathcal{S}_{\rm K}(T_{\rm gas}))}}{2\,n_{\rm tot}/\mathcal{S}_{\rm K}(T_{\rm gas})}\,, \tag{69}$$

where $x_{\rm K}$ is the ionisation fraction of potassium and is set to $x_{\rm K} = 1.97\times10^{-7}$ (e.g. Mohanty et al. 2018). The formulation of $x_{\rm e,th}$ as in Eq. (69) covers an important edge case: In a stratified disk atmosphere, density significantly drops in the surface layers ($n_{\rm tot} \to 0$) which leads to a high $x_{\rm e}$ (cf. Eq. (56)). In the case of an equilibrium ionisation this eventually leads to $x_{\rm e,th} \approx x_{\rm K}$.

For properly describing thermal ionisation, not only the radial gas temperature profile, but also an approximation in vertical direction $T_{\rm gas}(r,z)$ is needed. At the midplane $\rho(r, z = 0) = \rho_0(r)$ is largest, which leads to effective viscous heating at $z = 0$. The resulting thermal radiation is transported radially and vertically through the disk according to Eq. (3). Additionally, the disk is both heated by stellar radiation on its surface (on both sides) and also cools radiatively across its surface (cf. Eq. (11)). Assuming LTE and using the Eddington approximation, the vertical temperature distribution can be approximated in the optical thick case ($\tau \gg 1$) as (e.g. Hubeny 1990),

$$T_{\rm gas}^4(r,z) = T_{\rm gas,0}^4 - \frac{\tau_{\rm R}^-(r,z)}{\tau_{\rm R}}(T_{\rm gas,0}^4 - T_{\rm surf}^4)\,, \tag{70}$$

where $\tau_{\rm R}^-(r,z) \equiv \kappa_{\rm R}\,\Sigma\,{\rm erf}(z/(\sqrt{2}\,H_{\rm p}))/\sqrt{2\,\pi}$ and $T_{\rm gas,0}$ are the optical depth from the midplane up to the height z and the midplane gas temperature, respectively. With Eq. (70) $x_{\rm e}$ can be calculated in vertical direction (cf. Eq. (69)).

Thermal ionisation is very likely to only be significant in the inner disk ($r \lesssim 0.2$ AU), which has two reasons: (i) viscous heating is more effective in the inner regions with large Σ, as long as the disk is optically thick, and (ii) in regions very close to the star, the disk becomes optically thin and the irradiation from the star suffices for the gas to get thermally ionised, i.e. after heating by absorption.

Non-thermal ionisation: The main sources for non-thermal ionisation are galactic cosmic rays and stellar X-ray as well as FUV radiation. Additionally, radioactive decay (RA) plays a role in some regions close to the disk midplane. The cosmic-ray ionisation rate, $\xi_{\rm CR}$, is adapted from Lesur et al. (2014),

$$\xi_{\rm CR} = 10^{-16}\,\exp\left\{-\frac{\Sigma}{9.6\times10^2\,{\rm g\,cm^{-2}}}\right\}\,{\rm s^{-1}}\,, \tag{71}$$

whereas the X-ray ionisation rate, $\xi_{\rm XR}$, can be modelled according to a fit done by Bai & Goodman (2009); Delage et al. (2022), using an X-ray temperature of $T_{\rm XR} = 3$ keV. X-ray photons can either directly ionise the gas, $\xi_{\rm XR,dir}$, or indirectly ionise it through scattering, $\xi_{\rm XR,sca}$,

$$\xi_{\rm XR,dir} = \frac{L_{\rm XR}}{10^{29}\,{\rm erg\,s^{-1}}}\left(\frac{r}{1\,{\rm AU}}\right)^{-2.2} \tag{72}$$

$$\xi_{\rm XR,dir,0}\left[\exp\left\{-\left(\frac{\Sigma^+}{\Sigma_{\rm XR,dir}}\right)^{0.4}\right\}+\exp\left\{-\left(\frac{\Sigma^-}{\Sigma_{\rm XR,dir}}\right)^{0.4}\right\}\right], \tag{73}$$

$$\xi_{\rm XR,sca} = \frac{L_{\rm XR}}{10^{29}\,{\rm erg\,s^{-1}}}\left(\frac{r}{1\,{\rm AU}}\right)^{-2.2}$$

$$\xi_{\rm XR,sca,0}\left[\exp\left\{-\left(\frac{\Sigma^+}{\Sigma_{\rm XR,sca}}\right)^{0.65}\right\}+\exp\left\{-\left(\frac{\Sigma^-}{\Sigma_{\rm XR,sca}}\right)^{0.65}\right\}\right], \tag{74}$$

where $\Sigma_{\rm XR,dir} = 3.5\times10^{-3}\,{\rm g\,cm^{-2}}$ and $\Sigma_{\rm XR,sca} = 1.64\,{\rm g\,cm^{-2}}$ are the penetration depths for direct and scattered X-ray ionisation (e.g. Delage et al. 2022), respectively. $\Sigma^+ = \int_z^\infty \rho(r,z)\,dz$ and $\Sigma^- = \Sigma - \Sigma^+$ denote the column densities above and below a certain height z, respectively. Additionally, $\xi_{\rm XR,dir,0} = 6\times10^{-12}\,{\rm s^{-1}}$ and $\xi_{\rm XR,sca,0} = 10^{-15}\,{\rm s^{-1}}$ describe the undamped direct and scattered X-ray ionisation, respectively. Finally, a rather simple radioactive decay ionisation rate, $\xi_{\rm RA}$, is adopted according to Lesur et al. (2014), ignoring radial variation and the effects of varying dust-to-gas ratio (e.g. Delage et al. 2022),

$$\xi_{\rm RA} = 10^{-19}\,{\rm s^{-1}}\,. \tag{75}$$

The effects of FUV radiation were neglected in this work, as the penetration depth of FUV is of order $10^{-2}\,{\rm g\,cm^{-2}}$ and yields an ionisation front in the uppermost surface layer of a PPD. Therefore, FUV ionisation becomes significant when modelling MCWs or photoevaporative winds (e.g. Cecil et al. 2024), but is not likely to play an important role in modelling the resistivity for magnetic flux transport of a large-scale, purely poloidal field inside the disk. The total ionisation rate, ξ, was then written as

$$\xi = \xi_{\rm CR} + \xi_{\rm XR,dir} + \xi_{\rm XR,sca} + \xi_{\rm RA}\,. \tag{76}$$

In an equilibrium state, which is necessary in assuming a steady-state in vertical direction, ionisation is balanced by radiative recombination, $\alpha_{\rm r}$, and recombination on dust particles, $\alpha_{\rm d}$, in the following way,

$$(1-x_{\rm e,nth})\,\xi = \alpha_{\rm r}\,x_{\rm e,nth}^2\,n_{\rm tot} + \alpha_{\rm d}\,x_{\rm e,nth}\,n_{\rm tot}\,, \tag{77}$$

where we assumed that the number density of neutrals is very close to the total number density, $n_{\rm n} \approx n_{\rm tot}$, and that the temperature regimes of thermal and non-thermal ionisation are non-overlapping. This is a good approximation, because thermal ionisation becomes dominant above $T_{\rm th,active} \gtrsim 1000\,K$ and has a very narrow transition temperature range. Below $T_{\rm th,active}$ non-thermal ionisation dominates. Hence, the non-thermal ionisation fraction, $x_{\rm e,nth}$, can be calculated separately from $x_{\rm e,th}$ (e.g. Vorobyov et al. 2020). We note that dissociative recombination was not considered in this work due to the fact that radiative and dust recombination yield an upper and lower limit for $x_{\rm e,nth}$, respectively (e.g. Dudorov & Khaibrakhmanov 2014), whereas dissociative recombination leads to an ionisation fraction between those limits.

The radiative recombination rate, $\alpha_{\rm r}$, can be approximated by (e.g. Spitzer 1978; Vorobyov et al. 2020)

$$\alpha_{\rm r} = 2.07\times10^{-11}\,T_{\rm gas}^{-1/2}\,{\rm cm^3\,s^{-1}}\,, \tag{78}$$

Table 1. Dust recombination rate for the dust grain size $a_{\rm d} = 0.1\,\mu$m and different gas temperature regimes.

T [K]	dust recombination rate $\alpha_{\rm d}$ [$\rm cm^3\,s^{-1}$]
< 150	4.5×10^{-17}
150 – 400	linear decrease from 4.5×10^{-17} to 3.0×10^{-18}
400 – 1500	3.0×10^{-18}
1500 – 2000	linear decrease from 3.0×10^{-18} to 0
> 2000	0

whereas for the dust recombination rate, $\alpha_{\rm d}$, we adopt a parametrisation described by Dudorov & Khaibrakhmanov (2014), which is depicted in Table 1 and is valid for a grain size $a_{\rm d} = 0.1\,\mu$m and a dust-to-gas ratio $f_{\rm dust} = 0.01$. Formally $\alpha_{\rm d}$ is defined as

$$\alpha_{\rm d} = X_{\rm g}\,\langle\sigma_{\rm g}\,V_{\rm ig}\rangle\,, \tag{79}$$

where $X_{\rm g}$, $\sigma_{\rm g}$, and $V_{\rm ig}$ denote the number density fraction of dust grains, the grain cross-section, and ion-grain relative velocity (e.g. Dudorov & Khaibrakhmanov 2014). In the case of a fixed $f_{\rm dust}$, the following relations hold,

$$X_{\rm g} = \frac{n_{\rm d}}{n_{\rm tot}} \propto a_{\rm d}^{-3}\,, \tag{80}$$

$$\sigma_{\rm g} \propto a_{\rm d}^2\,, \tag{81}$$

which, according to Eq. (79), leads to the overall scaling of $\alpha_{\rm d}$:

$$\alpha_{\rm d} \propto a_{\rm d}^{-3}\,a_{\rm d}^2 \propto a_{\rm d}^{-1}\,. \tag{82}$$

Therefore a different grain size, $a_{\rm d}$, can be used by taking the values of Table 1 for $a_{\rm d}$ and then by scaling it according to Eq. (82) (e.g. Dudorov & Khaibrakhmanov 2014).

2.6. Solution procedure

Our 1+1D model aims to solve the hydrodynamical equations Eqs. (1) - (3) together with a poloidal large-scale field as described in Eq. (28) (cf. Sec. 2.1 and Sec. 2.2). The vertical structure of the disk is crucial in understanding the radial magnetic flux transport of the large-scale field. Hence, we have provided a description of the vertical velocity profile (analogously to Guilet & Ogilvie 2012; Leung & Ogilvie 2019) (cf. Sec. 2.4) and a model for the vertical ionisation fraction and resistivity (cf. Sec. 2.5. The large-scale field was assumed to be seeded by an external fossil field, which was taken to be force-free (in the absence of outflows) and which served as a boundary at the disk surface for the large-scale field in the disk interior (cf. Sec. 2.3). The vertical velocity and resistivity profiles were vertically averaged to fit into a 1+1D approach. The solving procedure followed the following steps:

1. Calculate the vertical velocity contributions, $u_{\rm r,2}$ and $u_{\varphi,2}$ (see Eqs. (42) - (43)). The radial contributions $u_{\rm r,0}$ and $u_{\varphi,0}$ were solved through the hydrodynamic simulation.
2. Determine the density-weighted vertical averages, $\bar{u}_{\rm r}$ and $\bar{u}_\varphi$ (see Eq. (53)).
3. Obtain $\psi_{\rm d}$ by subtracting the magnetic flux contributions of stellar dipole and external field as in Eq. (38).
4. Calculate $\mathcal{L}$ (cf.Eq. (31) and Eq. (39)) and inversion to obtain $B_{\rm r}^{\rm s}$ (see App. A for details).

5. Determine x_e (see Eq. (66), Eq. (69) and Eq. (77)), the vertical temperature profile (see Eq. (70)) as well as η_O and η_A (see Eq. (64) and Eq. (65), respectively) for all radii at five different heights ($z = 0$, $z = H_p$, $z = H_p + \frac{1}{3}(z_B - H_p)$, $z = H_p + \frac{2}{3}(z_B - H_p)$, and $z = z_B$).
6. Calculate the conductivity-weighted vertically averaged $\bar{\bar{\eta}}(r)$ between $-z_B \leq z \leq z_B$. The necessary integration over $\eta(r, z) = \eta_O(r, z) + \eta_A(r, z)$ is done by piece-wise numerical integration using the values for the heights z calculated in the preceding step (see Eq. (26)).
7. Determine the conductivity-weighted vertically averaged radial velocity $\bar{\bar{u}}_r$ (see Eq. (27)) by using $\bar{\bar{\eta}}$.
8. Determine the magnetic flux transport velocity $\bar{\bar{u}}_\psi$ by using $\bar{\bar{\eta}}$, $\bar{\bar{u}}_r$ and $\eta(r, z = z_B)$ (see Eq. (52)).
9. Finally, solve the hydrodynamical equations Eqs. (1) - (3) and Eq. (28) with TAPIR (e.g Ragossnig et al. 2020).

The most expensive operation (in the context of simulation time) is the inversion of the operator, $\mathcal{L}$. The details of this inversion and the steps taken to maintain adequate performance in solving the MHD equations are explained in Sec. A.

2.7. Validity of our approximations for modelling the vertical disk and magnetic field structure

We used a 1+1D disk model and assumed a geometrically thin disk ($H_p/r \ll 1$), which usually means that the radial and toroidal velocity components, $u_r(r)$ and $u_\varphi(r)$, respectively, are taken to be constant in the vertical direction. However, describing the evolution of a large-scale magnetic field required modelling of magnetic advection and diffusion, which both are strongly dependent on the ionisation degree and velocity structure in vertical direction (e.g. Guilet & Ogilvie 2012; Leung & Ogilvie 2019; Delage et al. 2022, see also Sec. 2.2 and Sec. 2.4). Hence, we discuss the validity of the essential approximations for describing the vertical disk- and large-scale magnetic field structure. The key points are (for a detailed discussion cf. App. B):

– The focus on Class II PPDs justifies the use of the thin-disk approximation.
– A comparison of the viscous timescale, t_{visc}, and the dynamical timescale, t_{dyn}, justifies the use of stationary vertical velocity- and large-scale magnetic field profile (see also Sec. 3.2).
– The assumption of a dominant vertical magnetic field is valid for most of the disk, as long as the large-scale magnetic field remains weak, and the inclination angle does not exceed $i > 30°$. The validity is only questionable in the innermost disk region, where magnetic compression likely plays a role.
– The somewhat arbitrary choice of vertical layers for the calculation of x_e, as well as OD and AD in the vertical direction, is justified through a comparison with a profile with different choices of vertical layers. It can be concluded that our approach with 5 layers is a good compromise between numerical cost and reasonable accuracy.
– For describing the thermally ionised region in the inner disk a vertical temperature profile was used. It is compared to and in good agreement with 2D simulations of the vertical disk structure (e.g. Jankovic et al. 2021).

Not only the validity of our approximations, but also the comparison with former work is important. To this end we compared our reference model with the analytic profiles of Dudorov & Khaibrakhmanov (2014) and found very good agreement with their radial magnetic field profiles (see Fig. 3 in Sec. 3.3). We have also dedicated Sec. 4.1 for comparing our results with the work of various authors. We found that our results are consistent with the models of Mohanty et al. (2018) and Delage et al. (2022). Especially the calculation of the ionisation degree and resistivity profiles are in very good agreement with the work of those authors. The work of Jankovic et al. (2021) also agrees well with our model of the inner disk and the vertical temperature structure and thermally ionised region. The sum of all those comparisons strengthens the confidence that our approximate disk model is capable of reproducing the results from previous studies (e.g. Dudorov & Khaibrakhmanov 2014; Guilet & Ogilvie 2014) but also has the ability to provide additional scientific insights. We nevertheless discuss remaining fundamental limitations of our model methodology in Sec. 4.4. Some of these can be overcome in future work. However, we do not consider them to be of crucial importance in the framework of our present study that focuses on the investigation of the poloidal large-scale magnetic field topology threading a stationary disk.

3. Results

We split our results into three main categories: (i) the evolution of a background fossil field towards a steady state (see Sec. 3.1), (ii) the in-depth study of the solution obtained after the large-scale magnetic field in the disk has become stationary (see Sec. 3.3), and (iii) a parameter study of how the resulting stationary system consisting of a disk, star, and large-scale magnetic field changes for different parameters (see Secs. 3.4 - 4.3).

3.1. Evolution of the large-scale magnetic field towards a stationary state

For validation of the large-scale magnetic field structure obtained in this paper, it is useful to compare it to similar, already available work done on this topic (e.g. Guilet & Ogilvie 2014; Mohanty et al. 2018; Delage et al. 2022), which use a stationary magnetic field topology. A (magneto)hydrodynamic treatment of the large-scale field requires evolving the field and disk sufficiently long to eventually reach a stationary state. This is done with TAPIR in two stages for our reference model (see Table 2):

(i) The first stage consists of evolving the disk with a prescribed stellar field and a prescribed large-scale disk field, analogously to Steiner et al. (2021). The stationary disk is obtained by self-consistently calculating the position of the inner disk boundary, r_{in}, taking into account the accretion rate, $\dot{M}(r_{in})$, and the initial stellar magnetic field strength, $B_{\star,0}$. Additionally, we start with a radially constant, purely vertical, large-scale disk magnetic field, $B_{d,0}(r) = B_\infty$ (see Eq. (36) in Sec. 2.2), threading the disk at time $t = 0$. This field is superimposed with the stellar magnetic field to provide an initial star-disk magnetic field threading the disk, $B_0 = B_{\star,0} + B_{d,0}$ (see Sec. 2.2), and is kept constant during the first stage. This essentially means that only the disk 'feels' the impact of the magnetic field, whereas the magnetic field dragging due to radial mass transport is not considered during this first stage.
(ii) The second stage then relaxes the constraints of a temporally constant large-scale field by allowing for the evolution of the magnetic field from the initial configuration B_0 towards a stationary field topology by interacting with the accretion disk (using the parameters of Table 2). In this phase, the disk and magnetic field are evolving as a coupled system.Starting with

Table 2. Parameters used for the reference model.

Stellar parameters		Disk parameters	
$M_\star$ $[M_\odot]^a$	0.7	$\dot{M}_{\rm init}$ $[M_\odot\,{\rm yr}^{-1}]^e$	$5.0 \cdot 10^{-9}$
$R_\star$ $[R_\odot]^a$	2.096	$\alpha_{\rm MRI}{}^f$	10^{-2}
$L_\star$ $[L_\odot]^a$	1.09	$\alpha_{\rm AD}{}^g$	$5 \cdot 10^{-3}$
$P_\star$ $[{\rm d}]^b$	4.0	$\alpha_{\rm base}{}^h$	10^{-4}
$B_\star$ $[{\rm kG}]^c$	1.0		
$L_{\rm X}$ $[{\rm erg\,s^{-1}}]^d$	10^{30}		
Fossil field parameters			
$\beta_0(r_{\rm out})^i$	10^2		

Notes. [(a)] Stellar parameters $M_\star$, $R_\star$ and $L_\star$ are taken from pre-main sequence (PMS) isochrones created by Baraffe et al. (2015) for a T Tauri star with an age of $t = 1$ Myr.
[(b)] The rotation period $P_\star$ is chosen to lie in the expected range between 1 and 10 days (e.g. Irwin & Bouvier 2009).
[(c)] $B_\star$ for Class II objects is believed to lie between 0.1 kG and 1.0 kG (e.g. Johnstone et al. 2014b).
[(d)] X-ray luminosities of classical T Tauri stars lie between 10^{28} erg s^{-1} and 10^{32} erg s^{-1} (e.g. Preibisch et al. 2005).
[(e)] Accretion rates for classical T Tauri stars lie between 10^{-10} M$_\odot$ yr^{-1} and 10^{-7} M$_\odot$ yr^{-1} (see Vorobyov et al. 2017)
[(f)] Viscosity due to MRI is believed to result in α between 10^{-4} and 10^{-1} (e.g. Zhu et al. 2007; Vorobyov & Basu 2009).
[(g)] AD reduces the effectivity of MRI, which results in a smaller $\alpha_{\rm AD}$ (e.g. Delage et al. 2022).
[(h)] The base viscosity is much lower than the viscosity caused by MRI; hence $\alpha_{\rm base} \ll \alpha_{\rm MRI}$.
[(i)] A plasma beta, $\beta_0(r_{\rm out})$, in our reference model corresponds to $B_\infty \approx 3.8 \cdot 10^{-3}$ G. This is in the range of [10^{-5} G, 10^{-1} G] from studies of the fossil field in protostellar cores (e.g. Crutcher et al. 2004; Masson et al. 2016).

the stationary disk obtained from the first stage, the magnetic field is allowed to advect inward, caused by radial mass transport through the disk. Due to non-ideal MHD effects (in this study turbulent resistivity, OD, and AD are considered, see Sec. 2.5) the magnetic field advection is counteracted by diffusion, which at some point in time balances the inward-directed advection velocity, $u_{\rm adv}$, which then yields a stationary magnetic field.

In Fig. 1, we present the large-scale magnetic field evolution with a focus on the timescales until it reaches its final stationary state. The relevant timescale describing the radial magnetic flux transport is the diffusion timescale, $t_{\rm diff} \equiv r^2/\bar{\bar{\eta}}$. As a reference, we adopt the value of $t_{\rm diff,stat}$, corresponding to the stationary large-scale field, at the outer DZ boundary, $r_{\rm DZ,out}$. In the very inner disk ($r \lesssim 0.1$ AU), the stellar dipole field is dominating the large-scale field, which is represented by a low $\bar{\bar{u}}_\psi$ and a relatively high $\boldsymbol{B}$ in the inner disk for the whole disk evolution. Interestingly, despite a reduced radial mass transport, $\dot{M}$, in the DZ (between the two vertical white dashed lines in Fig. 1), the large-scale field in the DZ is effectively advected inwards[4]. This is due to significant magnetic flux transport in the upper disk layers, which is taken into account in our model by the conductivity-weighted vertical averaged resistivity, $\bar{\bar{\eta}}$ (see Sec. 3.3), and results in a considerably larger $\bar{\bar{u}}_\psi$ compared to $\bar{u}_{\rm r}$ in the DZ. The sharp decrease of $t_{\rm diff,stat}$ in the vicinity $r_{\rm DZ,out}$, together with the inward-directed magnetic field transport, leads to accumulation of magnetic flux, ψ, early on during magnetic field evolution (starting at $t \sim 10^{-1}\, t_{\rm diff,stat}(r_{\rm DZ,out})$). This causes a steep radial gradient in ψ and therefore an increase in $B_{\rm z,d}$ just inside the outer DZ boundary, revealing a locally increased field strength, $|\boldsymbol{B}|$ (cf. colour-coding of Fig. 1, around $r_{\rm DZ,out}$). In the outer disk, the large-scale field is not transported as effectively as in the inner region, which is due to AD being the dominant non-ideal MHD effect over the whole vertical extent in the outer disk. Eventually, this yields a larger $\bar{\bar{\eta}}$ in the outer disk and therefore a smaller $\bar{\bar{u}}_\psi$. For $t \gtrsim 10\, t_{\rm diff,stat}(r_{\rm DZ,out})$ the large-scale field becomes essentially stationary everywhere in the disk. This means that vertically averaged magnetic advection and magnetic diffusion compensate each other, the resulting magnetic flux transport velocity, $\bar{\bar{u}}_\psi = 0$ (see Eq. (29)), and the gray lines in Fig. 1 become vertical.

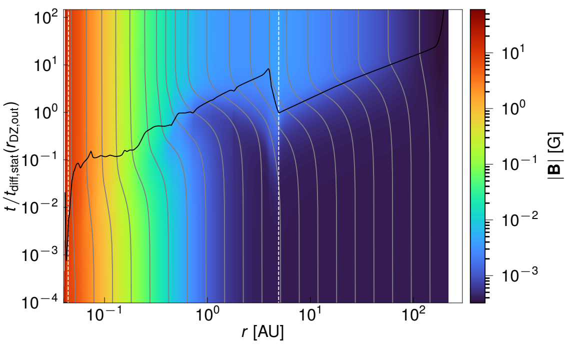

Fig. 1. Time evolution of the magnetic field strength over time (normalised in units of the diffusion timescale of the stationary model at the outer DZ boundary, $t_{\rm diff,stat}(r_{\rm DZ,out})$), where the colour-coding represents the magnetic field strength, $|\boldsymbol{B}|$, at every point in space and time. The gray lines show magnetic flux transport over time, using the effective, vertically averaged magnetic field transport velocity, $\bar{\bar{u}}_\psi$. The dashed white lines denote the inner and outer boundary of the DZ, respectively, whereas the black full line denotes the diffusion timescale, $t_{\rm diff,stat}$, of our stationary model. The inner DZ boundary is located very close to the inner disk rim.

3.2. Remarks on the validity of stationary models

In this work most of our conclusions are drawn from the analysis of stationary PPD models. Since disks are evolving over time, it is important to discuss the validity of using stationary models. In our 1+1D models we use a vertically averaged viscous-α (see Eq. (5), based on the layered viscosity model of Gammie 1996, see also Steiner et al. (2021)), which implies that viscous accretion varies in vertical direction between different layers. A localised perturbation changing $\alpha(r, z)$ at some radius r and some height z would lead to an increased or decreased local density, $\rho(r, z)$, and therefore would cause a deviation from a hydrostatic vertical equilibrium at r. Additionally, the vertically averaged α would change at r, which over time would lead to a bump or gap in $\Sigma(r)$. The development of such gaps or bumps would occur on the local viscous timescale, $t_{\rm visc}$, whereas the return to a local vertical hydrostatic equilibrium would happen on the local dynamical timescale, $t_{\rm dyn}$ (e.g. Delage et al. 2022). Therefore, an approximate stationary model can be understood as a time-

[4] We emphasise that the gray lines in Fig. 1 shall not be confused with field lines, but serve as an indicator, where magnetic flux transport is occurring during field evolution.

averaged disk, where such local perturbations are smoothed out under the assumption that the relaxation to a hydrostatic equilibrium happens much faster than the development of a bump or gap in Σ, or $t_{\rm dyn}(r) \ll t_{\rm visc}(r)$.

Additionally, we have to discuss the validity of a stationary large-scale magnetic field, which can be argued similarly in comparing the timescale of global magnetic field evolution to the timescale at which such perturbations typically occur. It has been argued by Dudorov & Khaibrakhmanov (2014) that the magnetic field in vertical direction also changes on $t_{\rm dyn}$. In contrast, the large-scale magnetic field in radial direction evolves on the local diffusion timescale, $t_{\rm diff}$, which requires $t_{\rm dyn} \ll t_{\rm diff}$ for a valid temporal averaging of local large-scale magnetic field perturbations.

Finally, PPDs typically disperse after ~ 1 – 4 Myrs (e.g. Delage et al. 2022; Ben et al. 2025), which raises the question if such disks live long enough to allow the disk and large-scale magnetic field to evolve towards a stationary state (i.e. steady-state accretion with $\dot{M}$ = const.). This means that we also have to verify that the global evolution timescales of both disk and large-scale magnetic field, $t_{\rm visc}$ and $t_{\rm diff}$, respectively, are shorter or of the order of typical disk lifetimes (e.g. Delage et al. 2022). In

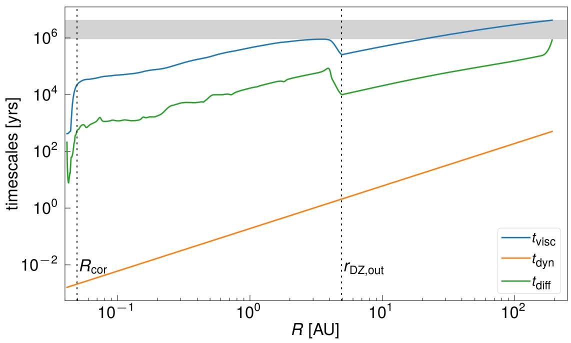

Fig. 2. Timescales of our reference model (cf. Table 2) relevant to the long-term evolution of a PPD and a large-scale magnetic field. The solid blue, orange, and green lines correspond to the viscous timescale, $t_{\rm visc}$; the dynamical timescale, $t_{\rm dyn}$; and the magnetic diffusion timescale, $t_{\rm diff}$, respectively. The vertical, dashed black lines correspond to the corotation radius, $R_{\rm cor}$, and the outer DZ boundary, $r_{\rm DZ,out}$. Finally, the gray area marks the region between 1 Myr and 4 Myrs and depicts the expected lifetime of a PPD.

Fig. 2 we can see that the conditions, $t_{\rm dyn} \ll t_{\rm visc}$ and $t_{\rm dyn} \ll t_{\rm diff}$, are both fulfilled everywhere in the disk, which allowed us temporally average over local perturbations of the vertical disk structure and vertical large-scale magnetic field profile. Furthermore, Fig. 2 shows that $t_{\rm diff}$ and $t_{\rm visc}$ are indeed shorter or of the order of a typical PPD lifetime, which justifies the assumption that the disk is likely to establish (near) steady-state accretion and therefore stationarity over most of its radial extent before it dissolves (e.g. Delage et al. 2022, for a similar argumentation).

3.3. The reference model

In this section, we describe the details of our reference disk model, especially the large-scale disk magnetic field topology. The field is strongly dependent on the resistivity profile, $\bar{\bar{\eta}}(r, z)$, which in turn is dependent on the ionisation fraction, $x_{\rm e}(r, z)$. Therefore, we investigated in more detail the vertical and radial profile of $x_{\rm e}$ and η, which then can be used to construct the conductivity-weighted vertical resistivity average, $\bar{\bar{\eta}}$, counteracting advection.

Large-scale magnetic field profile: We present and analyse the stationary magnetic field structure. As already discussed in Sec. 3.1, the field in the inner disk is dominated by the stellar dipole field (see Eqs. (14) - (16)). Since $B_{\rm z,\star} \propto r^{-3}$, the vertical magnetic field, $B_{\rm z}$, in the inner disk also follows this power law (see (a) in Fig. 3). The field evolution in the outer disk is strongly influenced by AD, which according to an analytical model from (Dudorov & Khaibrakhmanov 2014), should lead to a dependency $B_{\rm z} \propto r^{-5/8}$ in the case of an irradiated disk, which we can verify with our model (see (a) in Fig. 3). Amplification of the fossil field in the outer region is roughly $B_{\rm z}/B_{\rm z}(t = 0) \approx 10$, whereas in the inner disk, due to the dominant stellar field component, almost no amplification is observed. However, the disk field is advected inwards and a radial field component at the disk surface, $B_{\rm r}^{\rm s}$, develops, which leads to an inclination of the large-scale field with respect to the disk normal (see (b) in Fig. 3). The value of 30° shown in (b) of Fig. 3 corresponds to the critical field inclination, for which cold MCWs can be launched (e.g. Ogilvie 1997; Ogilvie & Livio 2001, and Sec. 4.2).

Inside the DZ close to $r_{\rm DZ,out}$, the radial field, $B_{\rm r}^{\rm s}$, decreases significantly compared to its value outside the DZ. This can be explained by comparing the viscous timescale, $t_{\rm visc}$, to $t_{\rm diff,stat}$: If $t_{\rm diff,stat}$ is significantly shorter than $t_{\rm visc}$, then the large-scale field diffuses outwards before any significant inward-directed advection takes place. As a consequence, field lines are only weakly inclined and $B_{\rm r}^{\rm s}$ stays small compared to $B_{\rm z}$ (see zone around $t_{\rm diff,DZ}$ in Fig. 4). Only very close to the inner rim $t_{\rm diff,stat}/t_{\rm visc} \approx 1$, which means that there $B_{\rm r}^{\rm s} \approx B_{\rm z}$ (cf. spike in $B_{\rm r}^{\rm s}$ close to the inner rim in (b) of Fig. 3 and in Fig. 4). This steep increase in $t_{\rm diff,stat}$ close to $r_{\rm in}$ is a result of three effects, which occur in a very narrow radial region close to the inner rim: (i) At the transition from optically thin to optically thick gas a dip in $T_{\rm gas}$ (for details see below paragraph about the temperature profile and (b) of Fig. 6 leads to a reduced $x_{\rm e,th}$ and consequently to a larger $\bar{\bar{\eta}}$, which is equivalent to a shorter $t_{\rm diff,stat}$. (ii) However, just slightly further inwards, the stellar irradiation starts to dominate the disk temperature, which leads to rising $T_{\rm gas}$ (see (b) of Fig. 6) and a steep decrease of $\bar{\bar{\eta}}$ once more (or equivalently to a sharp increase of $t_{\rm diff,stat}$, see Fig. 4) (iii) Closest to $r_{\rm in}$, $\bar{\bar{\eta}}$ rises again (equivalently $t_{\rm diff,stat}$ becomes shorter) slightly towards $r_{\rm in}$ which is due to small Σ and relatively large $|\boldsymbol{B}|$ provided by the stellar dipole field (we recall that $\eta_{\rm A} \propto |\boldsymbol{B}|^2 \rho^{-2}$, also see Eq. (59)).

The magnetic plasma beta at the midplane, β_0, describes the relative importance of the large-scale field in the disk. We start the time evolution with a fossil field, which corresponds to $\beta_0(r = r_{\rm out}) = 10^2$ at the outer disk rim, $r_{\rm out}$. In the AD-dominated outer disk, the model of Dudorov & Khaibrakhmanov (2014) predicts a radial dependency $\beta_0 \propto r^{-3/2}$ in the case of an irradiated, optically thick disk, which our results also reflect (see (c) in Fig. 3).

Resistivity profile: The ionisation fraction profile in radial and vertical direction, $x_{\rm e}(r, z)$, is necessary to calculate the corresponding OD and AD profiles, $\eta_{\rm O}$ and $\eta_{\rm A}$, respectively. Both thermal and non-thermal ionisation are taken into account (see Sec. 2.5) and show that the innermost region ($r \leq 0.044$ AU) is optically thin due to low Σ and the gas temperature, $T_{\rm gas}$, is dominated by stellar irradiation. Hence, the very inner disk has a high $x_{\rm e}$; however, at ~ 0.044 AU, the disk becomes sufficiently dense to turn optically thick for stellar radiation and the primary heat-

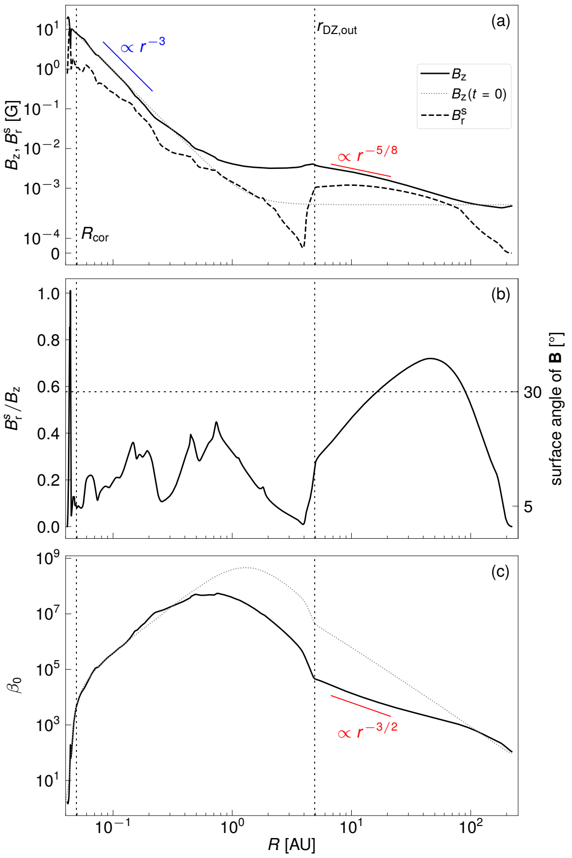

Fig. 3. Poloidal stationary magnetic field profile of our reference model (see Table 2). Panel (a) shows both the vertical and radial magnetic field component at the surface, B_z and B_r^s, respectively. Panel (b) depicts the ratio of B_r^s/B_z, which is a measure for the inclination of the field lines, whereas panel (c) shows the magnetic plasma beta β_0 at the disk midplane. The vertical dashed line correspond to the corotation radius, $R_{\rm cor}$, and $r_{\rm DZ,out}$, respectively. The dotted, gray lines in panels (a) and (c) describe the corresponding values at $t = 0$, whereas the horizontal dotted line in panel (b) denotes a surface angle of 30° with respect to the midplane normal.

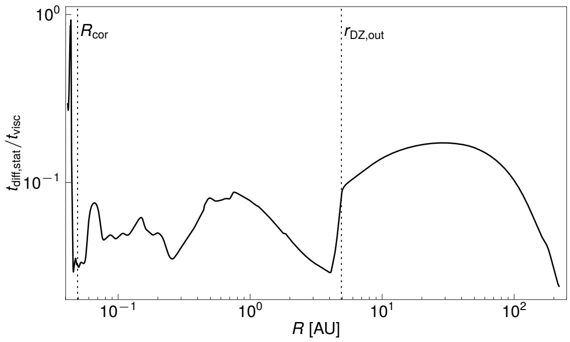

Fig. 4. Comparison of the viscous timescale, $t_{\rm visc}$, and the diffusion timescale, $(t_{\rm diff,stat})$. The vertical dashed lines close to the inner rim and at ∼ 4 AU represent $R_{\rm cor}$ and $r_{\rm DZ,out}$, respectively.

ing process transitions from stellar irradiation to viscous heating. Additionally, the disk has a DZ between $0.06\,\mathrm{AU} \lesssim r \lesssim 5$ AU, where the inner part of the DZ close to the midplane $r \lesssim 0.2$ AU is subject to thermal ionisation due to viscous heating (cf. region of large ionisation in the inner disk region close to the midplane in (a) of Fig. 5). Above $z \approx H_{\rm p}$, thermal ionisation is not effective anymore, since the disk is hydrostatically stratified and ρ above $H_{\rm p}$ becomes very small. Finally, the upper disk is penetrated mainly by X-rays and cosmic rays, yielding an expected significant $x_{\rm e,nth}$ in the surface layer.

Ohmic diffusion, $\eta_{\rm O}$, is only significant inside the DZ, which is also in agreement with predictions made by other authors (e.g. Bai & Stone 2013; Delage et al. 2022). Interestingly, the DZ also spans above (and below) the thermally ionised region in the inner disk, which means that the very weakly ionised gas is shifted to intermediate heights, where thermal ionisation cannot be maintained due to low gas density and non-thermal ionisation sources cannot penetrate deep enough to ionise the gas. The disk surface layer is sufficiently well ionised by non-thermal processes, such that $\eta_{\rm O} \propto x_{\rm e}^{-1}$ is very inefficient in the disk surface (see (b) of Fig. 5)

Ambipolar diffusion, $\eta_{\rm A}$, is effectively quenched in the thermally ionised disk region, which is due to both high gas density, ρ, and large $x_{\rm e}$ (we recall that $\eta_{\rm A} \propto |\boldsymbol{B}|^2 \rho^{-2} x_{\rm e}^{-1}$, see Eq. (65)). Inside the DZ, $\eta_{\rm A}$ is also negligible compared to $\eta_{\rm O}$ due to its strong dependency on ρ. In the surface layer as well as in the outer disk; however, AD becomes the dominant diffusion process. The magnetic field strength, $|\boldsymbol{B}|$, is roughly independent of height, z, and therefore the relative importance of $|\boldsymbol{B}|$ compared to ρ increases with z (see (c) of Fig. 5). The combined resistivity profile $\eta = \eta_{\rm O} + \eta_{\rm A}$ is plotted in panel (d) of Fig. 5. The regions of low η are the thermally ionised disk region, a thin layer at intermediate height z inside the DZ and in the outer disk close to the midplane. Recalling Eq. (26), the vertical averaging process of $\bar{\bar{\eta}}$ favours layers of low η, as in those regions magnetic flux transport, $\bar{u}_\psi$, is more efficient. As explained in Sec. 2.5 it is important for our model to vertically average the resistivity profile, $\bar{\bar{\eta}}$, due to constraint of a 1+1D model. Therefore, we evaluated $(\eta_{\rm O} + \eta_{\rm A})(r, z)$ at five different heights, including at the midplane, the pressure scale height, and the magnetic surface: $z = 0$, $z = H_{\rm p}$, and $z_{\rm B}$, respectively. Additionally, for $\bar{\bar{\eta}}$ to also incorporate the effects of the DZ above the thermally ionised region and of the disk layer of comparatively low resistivity between the DZ and the surface layer, $\bar{\bar{\eta}}$ is evaluated at two additional heights, $z = H_{\rm p} + \frac{1}{3}(z_{\rm B} - H_{\rm p})$ and $z = H_{\rm p} + \frac{2}{3}(z_{\rm B} - H_{\rm p})$ to adequately describe that in different radial sections different vertical layers contribute dominantly to $\bar{\bar{\eta}}$ (see (e) of Fig. 5):

- In the thermally ionised region ($r \lesssim 0.3$ AU), η is dominated by the vertical disk layers close to the disk midplane (the dashed orange line and dash-dotted green line are closest to the blue full line for $r \lesssim 0.3$ AU, see panel (e) of Fig. 5).
- In the region inside the DZ, but further out than the thermally ionised region ($0.3\,\mathrm{AU} \lesssim r \leq r_{\rm DZ,out}$), η is dominated by a region above the vertical extent of the DZ but deep enough below the disk surface for non-thermal radiation not ionising the gas. In this intermediate region, AD is the dominant non-ideal diffusion process (the purple dash-dotted line is very close to the full blue line in this region, see panel (e) of Fig. 5).
- Outside of the DZ ($r \geq r_{\rm DZ,out}$), the disk is dominated by AD, which is least effective close to the disk midplane and

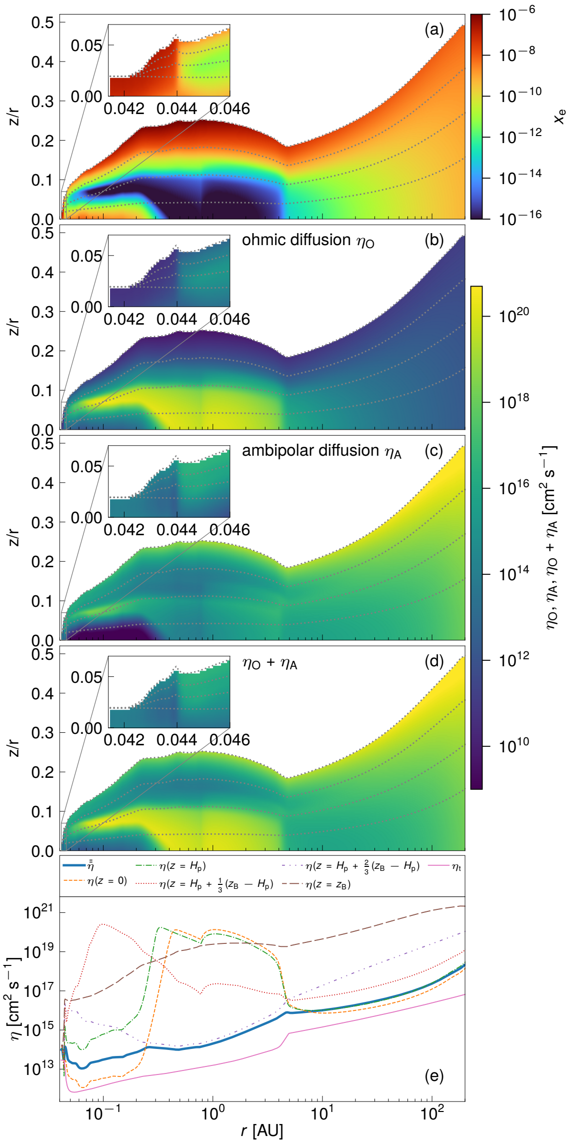

Fig. 5. For better understanding of the regimes of thermal and non-thermal ionisation, the radial and vertical profiles of (a) ionisation fraction, x_e; (b) the contribution of OD, η_O; (c) the contribution of AD, η_A; and (d) the combined resistivity, $\eta(r,z) = \eta_O(r,z) + \eta_A(r,z)$, are plotted for our reference model, which is explained in Sec. 3.1 (cf. Table 2). The dashed gray lines in (a)-(d) correspond to specific heights above the disk midplane ($z = 0$, $z = H_p$, $z = H_p + \frac{1}{3}(z_B - H_p)$, $z = H_p + \frac{2}{3}(z_B - H_p)$, and $z = z_B$). In (e) the combined resistivity is plotted for those specific heights, as well as the resulting vertically averaged resistivity $\bar{\bar{\eta}}$ (thick blue line). For comparison the turbulent resistivity, η_t, corresponding to a Prandtl number of 1 is also plotted, showing that $\eta_t \ll \bar{\bar{\eta}}$ almost everywhere except for the very inner region.

therefore most dominant for calculating the average $\bar{\bar{\eta}}$ (the dashed orange line and dash-dotted green line are very close to the blue full line, see panel (e) of Fig. 5).

For comparison, the turbulent resistivity, η_t, resulting from a magnetic Prandtl number, $\mathcal{P} = 1$, is also included in the vertical average of $\bar{\bar{\eta}}$ and is taken to be vertically constant, which means that η_t is added at every height to $\eta(r,z)$. It has been pointed out by other authors (e.g. Dudorov & Khaibrakhmanov 2014) that η_t is only important in the innermost hot disk with high x_e (cf. the magenta line in panel (e) of Fig. 5).

Temperature profile: The disk temperature profile, $T_{gas}(r)$, is important for determining the thermal gas pressure, P_{gas}, as well as the pressure scale height, H_p, and the magnetic surface, z_B. All of those quantities are important to get the magnetic flux transport and the large-scale magnetic field topology, $(B_r^s(r), 0, B_z(r))^T$. The optically thick regions of the disk are dominated by viscous heating, whereas T_{gas} in the optically thin regions is determined by stellar irradiation and the ambient temperature (for implementation details, see Ragossnig et al. 2020; Steiner et al. 2021).

We highlight one important temperature feature close to the inner edge of the disk, resulting in a distinct dip in the temperature of the disk (see (b) of Fig. 6). At the transition between the optically thick (white) and the optically thin (grey) region, we compare the individual energy contributions. The pressure work rate, $P_{gas}\nabla \cdot \boldsymbol{u}$, has a negative sign, which means that pressure aids the gas to be pushed inwards due to $-\Delta P_{gas} < 0$ in this area. Additionally, the net energy advected by the radial gas flow into a disk annulus just outside R_{cor} is positive, because of the stellar torques acting on the inner disk. However, for $r < R_{cor}$ the stellar dipole brakes the gas and gas starts to fall radially faster towards the star. This leads to $\dot{E}_{adv} < 0$, because more material exits than enters any disk annulus at $r < R_{cor}$ (see (a) of Fig. 6). The combined effect of pressure work and advection at $r \approx R_{cor}$, $P_{gas}\nabla\cdot\boldsymbol{u} + \dot{E}_{adv} < 0$, leads to a net drain of inner energy e from the disk annuli in this area and is equivalent to a lower $T_{gas,0}$. For our reference model, this leads to a drop below $T_{gas,0} < 1500$ K (see (b) of Fig. 6). At this temperature, some dust can still survive (e.g. Ferguson et al. 2005).

3.4. Variation of stellar parameters

In this section we investigate the influence of stellar magnetic field strength, $|\boldsymbol{B}_\star|$, rotation period, $P_\star$, and the X-ray luminosity, L_X, on the large-scale magnetic field topology. All stellar parameters are held constant throughout the magnetic field evolution towards the steady-state solution. The parameter range for $P_\star$ is varied between 4 and 6 days, which is based on observations of young stellar objects in the Orion Nebular Cluster (Herbst et al. 2002). We choose $|\boldsymbol{B}_\star|$ to range from 200 G to 1 kG by referring to the analysis of observed magnetic maps published by Johnstone et al. (2014a). We also study the effects of a varying X-ray luminosity, L_X, by lowering and increasing our reference value of $L_X = 10^{30}$ erg s^{-1} by a factor of 10, which is well within the limits of observations made by Preibisch et al. (2005).

3.4.1. Influence of stellar rotation period:

A longer $P_\star$ yields R_{cor} and r_{in} moving radially outwards (see Gehrig et al. 2022, and all panels of Fig. 7). Different rotation periods, $P_\star$, do not have any significant influence on the disk structure or the magnetic field topology outside of $r \gtrsim 0.3$ AU (see (b), (d) and (f) of Fig. 7). In the inner disk, however, the disk and large-scale magnetic field have a dependency on $P_\star$.

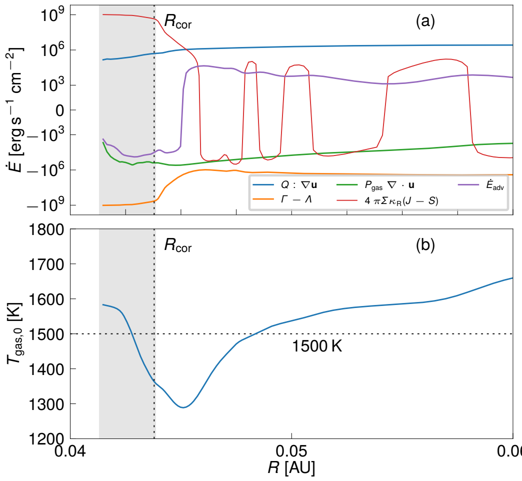

Fig. 6. Panel (a), energy contributions to the overall inner energy budget for every disk annulus at radius r. $Q : \nabla \boldsymbol{u}, \Gamma{-}\Lambda, P_{gas}\, \nabla{\cdot}\boldsymbol{u}, 4\,\pi\,\Sigma\,\kappa_R(J{-}S)$, and $\dot{E}_{adv}$, denote energy rates per unit volume due to viscous heating, heating or cooling over the surface, work done by gas pressure per unit time, radial radiation flux, and net inner energy advection, respectively (see Eq. (3)). Panel (b), plot of the midplane gas temperature, $T_{gas,0}$. The vertical dashed line in all panels denotes the corotation radius, R_{cor}, and the gray area marks the optically thin region in the inner disk.

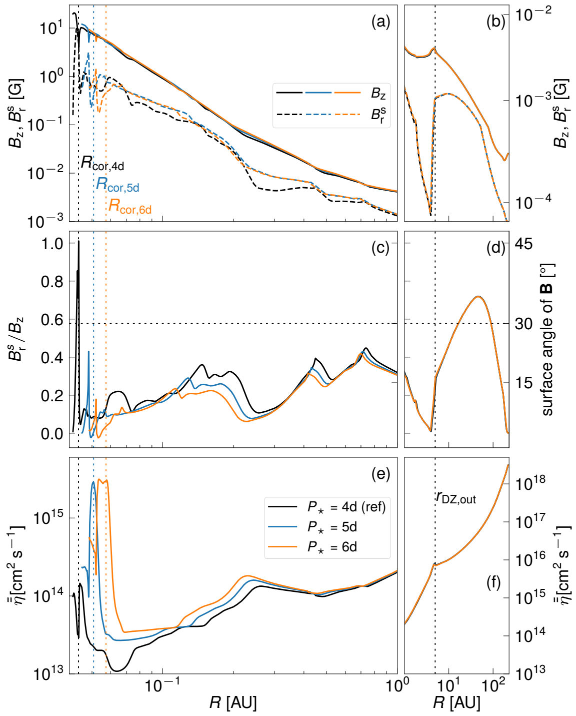

Fig. 7. Comparison of the magnetic field topology between our reference model ($P_\star = 4$ days, black) and two stars with $P_\star = 5$ days (blue) and $P_\star = 6$ days (orange). The vertical dashed lines mark the positions of R_{cor} and are colour-coded accordingly. Panels (a) and (b) show the vertical and radial magnetic field profiles in the inner and outer disk, respectively. Panels (c) and (d) depict the conductivity-weighted, vertically averaged resistivity $\bar{\bar{\eta}}$, whereas panels (e) and (f) describe the ratio B_r^s/B_z. The scale on the right-hand side of (c) and (d) denotes the angle of the magnetic field lines to the midplane normal, which corresponds to $\tan^{-1}(B_r^s/B_z)$. The dashed horizontal line marks a surface angle of 30°, which is an indicator for efficient MHD winds (see text).

The stellar magnetic field just outside R_{cor} accelerates the disk gas, therefore counteracting viscous accretion, which is usually referred as 'propeller effect' (e.g. Steiner et al. 2021). This leads to accumulation of mass in the area outside R_{cor} in the disk region $R_{cor} \leq r \lesssim 0.3$ AU. A higher Σ diminishes $x_{e,nth}$ and therefore increases $\eta(r, z)$ in the disk layers at intermediate heights. However, those intermediate-height disk layers are essentially defining $\bar{\bar{\eta}}$ in the disk for $R_{cor} \leq r \lesssim 0.3$ AU (see (e) of Fig. 5); hence $\bar{\bar{\eta}}$ is increased in this region (see (e) of Fig. 7). Close to R_{cor}, we observe that $\bar{\bar{\eta}}$ increases significantly more for slow rotating stars. This is due to lower $T_{gas,0}$ for larger r, leading to a lower x_e and therefore to a larger $\bar{\bar{\eta}}$. In panel (b), we can then see the expected result that a larger $\bar{\bar{\eta}}$ causes less inclined field lines. For $r < R_{cor}$ the narrow and steep increase of B_r^s/B_z (see Sec. 3.3) becomes less pronounced for larger $P_\star$ (see (c) of Fig. 7). This is because not only R_{cor} but also the optically thin region close to r_{in} shifts towards larger radii. There, the disk is colder (compared to faster rotating stars), which results in less effective thermal ionisation and a less pronounced dip of η in the innermost disk region.

3.4.2. Influence of stellar magnetic field strength:

Different stellar magnetic field strengths, $|\boldsymbol{B}_\star|$, do not alter the large-scale field topology in the outer disk for $r \gtrsim 1$ AU (see (b), (d), and (f) of Fig. 8). The inner radius, r_{in}, moves closer to the star for weaker stellar dipole fields (Steiner et al. 2021, and Fig. 8), and hence the disk close to r_{in} becomes hotter. This means that for weaker $|\boldsymbol{B}_\star|$, even in the region of the dip in $T_{gas,0}$ (see Sec. 3.3), the gas stays hot enough for efficient thermal ionisation and leads to a less distinct spike in B_r^s/B_z for weaker dipole fields (see (c) of Fig. 8). The magnetic field is also altered inside the DZ, which is caused by a different mechanism as in the very inner disk. A larger $|\boldsymbol{B}_\star|$ also leads to a larger large-scale field strength, B_d, in the radial range 0.1 AU $\lesssim r \lesssim 1$ AU (see (a) of Fig. 8). In this region, AD, η_A, dominantly contributes to $\bar{\bar{\eta}}$ (Sec. 3.3). Since $\eta_A \propto B^2$, a small value of $B_\star$ results in a smaller resistivity and the large-scale field is dragged inwards more efficiently. Consequently, the surface angle increases (see (b) and (c) of Fig. 8). This effect is even amplified by the fact that a weaker field provides less resistance against bending, causing the difference between different stellar magnetic field strengths to be even more significant.

3.4.3. Influence of stellar X-ray luminosity:

The stellar X-ray luminosity, L_X, is directly proportional to the non-thermal X-ray ionisation, both direct ionisation Eq. (73) and through scattering Eq. (74). Therefore, it is expected that an increase of L_X causes a higher non-thermal ionisation fraction, $x_{e,nth}$, in the upper disk layers, thus leading to a reduced vertically averaged resistivity, $\bar{\bar{\eta}}$. This is indeed the case for our models (see Fig. 9); however in the inner disk region $r \lesssim 0.15$ AU the dominant ionisation mechanism is thermal ionisation, which explains the lack of variation in this disk region (see Fig. 9).

A lower $\bar{\bar{\eta}}$ means a more effective coupling of the large-scale field to the disk, which leads to more magnetic flux transport to-

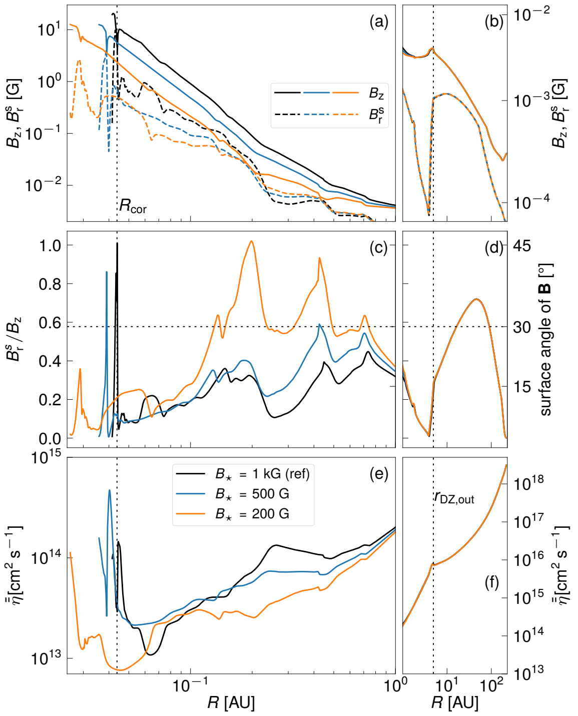

Fig. 8. Same as Fig. 7 but for different values of $|\boldsymbol{B}_\star|$. The stellar field strengths, $|\boldsymbol{B}_\star|$, of 1 kG, 500 G, and 200 G respectively correspond to the black, blue, and orange lines.

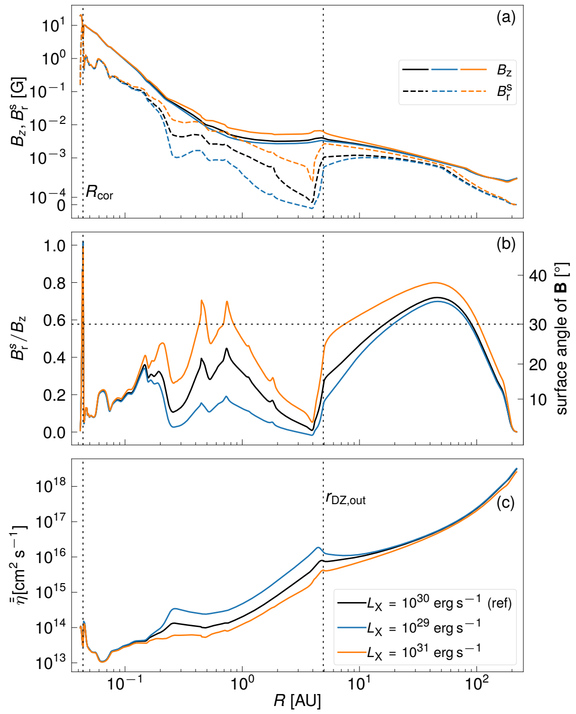

Fig. 9. Same as in Fig. 7 but for different stellar X-ray luminosities, L_X, reaching from 10^{29} erg s^{-1} to 10^{31} erg s^{-1}.

wards the star and therefore a stronger large-scale disk field (see (a) in Fig. 9), which in turn increases η_A and so lessens the effect of a stronger L_X to a certain degree, but remains of minor significance compared to the effect of increased $x_{e,nth}$. More effective magnetic field dragging also results in a stronger radial large-scale field component, B_r^s, as well as a larger ratio B_r^s/B_z, which corresponds to a larger surface angle of the resulting field (see (b) and (c) of Fig. 9). Contrary to the variation of $P_\star$ and $B_\star$, also the magnetic field in the outer parts of the disk is influenced by a varying L_X. This is also expected, as the dominant ionisation process in the outer disk is non-thermal ionisation. In summary, the effects of L_X on the large-scale field topology lead to a stronger large-scale field for larger values of L_X and additionally allow for a significantly stronger inclined large-scale field for all radii $r \gtrsim 0.2$ AU.

3.5. Influence of the mass transport rate

We investigate how the variation of $\dot{M}$ influences the magnetic field in the disk. In the picture of a steady-state disk and the viscous α description, the mass transport rate through the disk defines the surface density profile. A higher $\dot{M}$ results in a larger DZ, which extends further outwards due to a larger Σ and therefore to lower non-thermal ionisation in the layers below the disk surface (e.g. Steiner et al. 2021; Delage et al. 2022). The outer boundary of the disk, r_{out}, is defined by the condition of $\Sigma = 1\,\mathrm{g\,cm^{-2}}$ (Vorobyov et al. 2020) and hence also shifts towards larger radii for a more massive disk.

Having a more massive and larger disk, we expect the large-scale magnetic field to react in the outer disk in the following way: A larger disk can drag (and amplify) the fossil field inwards from further out. Hence, for a given r in the outer disk (sufficiently far away from the outer disk boundary to rule out any boundary effects), the large-scale field is expected to be slightly stronger. (ii) A lower x_e due to a larger Σ, and therefore a reduced $x_{e,nth}$, results in less magnetic flux transport and leads to a less inclined field. We can confirm both of those expectations with our results (see $r \sim 10$ AU in (b) and (d) of Fig. 10) The increased field inclination in the DZ for a more massive disk can be explained in the following way: A more massive disk is more extended in the vertical direction (larger H_p), which means that the vertical disk layers contributing most to magnetic flux transport are at larger z. As stated in Sec. 2, in our model $u_r \propto z^2$ (cf. Eq. (40)) and for the vertical average $\bar{\bar{u}}_r$ the disk layers of low resistivity are given more weight (cf. Eq. (27)). This means that for a more massive disk, magnetic flux transport is faster in the layers above the dead zone, which results in a larger inclined large-scale field (cf. (d) of Fig. 10).

In the inner disk, r_{in} also shifts towards smaller radii for a larger $\dot{M}$ due to increased ram pressure (for details cf. Steiner et al. 2021, cf. also (a), (c) and (e) of Fig. 10). Our model with $\dot{M} = 10^{-9}\,\mathrm{M_\odot\,yr^{-1}}$ shows a large increase in $\bar{\bar{\eta}}$ (compared to the other models with higher $\dot{M}$) at the transition from an optically thick to an optically thin disk (cf. Sec. 3.3 and panel (b) of Fig. 6), because the disk is colder, both due to less viscous heating and its larger radial distance from the star. The strong diffusion of B_r^s in this region is superimposed with the radial contribution of $B_{r,\star}^s$ (cf. Eq. (15) results in B_r^s changing sign in a very narrow region. The spike in B_r^s/B_z is not visible for a disk with low $\dot{M}$, because the disk is truncated before $T_{\mathrm{gas},0}$ rises high enough to decrease $\bar{\bar{\eta}}$ sufficiently (cf. (e) of Fig. 10. In contrast, for larger disk masses the dip in $T_{\mathrm{gas},0}$ is less distinct due to its proximity to the star, which also results in a less pronounced spike in inclination compared to our reference model (cf. (c) of Fig. 10).

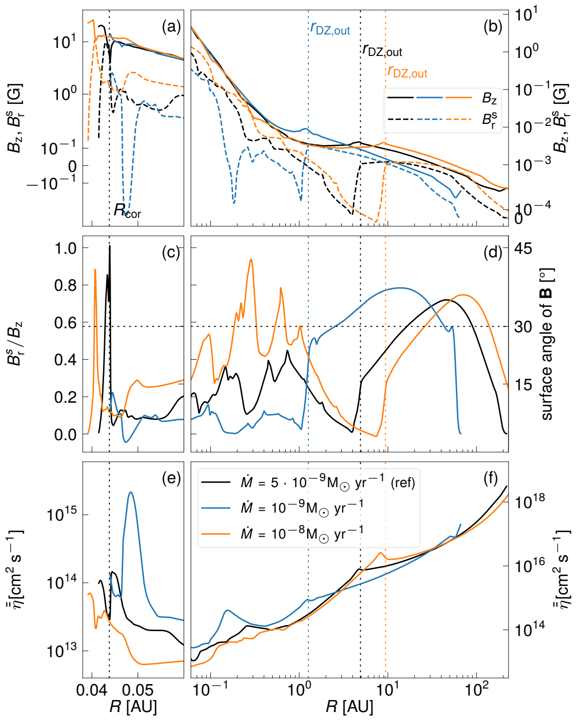

Fig. 10. Same as in Fig. 7 but for different $\dot{M}$. The colour-coded vertical dashed lines correspond to the outer dead zone boundaries, $r_{\mathrm{DZ,out}}$, of the respective disk model.

4. Discussion

In this paper we have presented long-term, hydrodynamic simulations of a PPD with a large-scale magnetic field until the disk and large-scale magnetic field become stationary. This allowed us to iterate further on the work done by other authors (e.g. Lubow et al. 1994; Guilet & Ogilvie 2014), who have evolved a large-scale field threading a simplified, stationary disk, but whose models lack the inclusion of laminar, non-ideal effects, which in our case are limited to OD and AD. Additionally, due to the implicit time integration scheme of TAPIR, we are able to include the very inner disk region and therefore include the impact of a stellar dipole both on the inner disk and on the large-scale field by using the hydrodynamic disk evolution model of e.g. Steiner et al. (2021); Gehrig et al. (2022).

Our results show that the large-scale field develops on the magnetic diffusion timescale, which differs between the DZ and the region further outwards, causing a distinction between the field inside and outside the DZ. Furthermore, the large-scale field is significantly bent in the very inner disk and in the outer disk (outside the DZ), but not in the dead zone close to the outer dead zone rim, which is in agreement with simulations carried out by other authors (e.g. Bai & Stone 2013; Zhu & Stone 2018). Additionally, we show that varying stellar parameters such as stellar magnetic field strength, $|\boldsymbol{B}_\star|$; X-ray luminosity, L_X; and stellar rotation period $P_\star$ can influence the large-scale magnetic field topology by altering the large-scale field strength and inclination. Our study also reveals which parameters influence the large-scale field in the very inner disk, the DZ, or the outer regions of the disk.

4.1. Comparison with recent studies

Our approach is novel in that it is able to evolve a PPD, including the very inner disk, threaded by a large-scale field magnetohydrodynamically up to the point where the model becomes stationary without imposing any external stationarity constraint on it. Comparing our model to recent studies using other methods to determine the large-scale field structure in a PPD is therefore important to provide additional justification for our approach.

Dudorov & Khaibrakhmanov (2014) use a standard, geometrically thin, α-viscosity accretion disk of Shakura & Sunyaev (1973) to describe the disk and also include stellar irradiation as an additional heating source apart from viscous heating. A significant difference compared to our model is that they neglect radial magnetic flux transport, which makes the calculation of the external magnetic field solution at each time step unnecessary (e.g. Ogilvie 1997; Guilet & Ogilvie 2014) and a constant fossil field description suffices. By contrast, our model incorporates a changing external field due to radial dragging, which also influences the vertical profile of B_r inside the disk (e.g. Guilet & Ogilvie 2012; Leung & Ogilvie 2019) and therefore leads to changes in the magnetic field profiles compared to Dudorov & Khaibrakhmanov (2014). The radial profiles of B_z and B_r^s compare qualitatively well with our results. Moreover, the dependency of dust grain size and L_X agrees well with our findings; however, in the very inner disk there are differences: (i) The disk of Dudorov & Khaibrakhmanov (2014) is everywhere optically thick, which is not the case close to the inner boundary for a more realistic inner disk boundary, which leads to a different temperature profile close to the inner rim and hence influences x_e as well as η. (ii) No stellar dipole has been modelled in their work, which would alter the disk structure around the corotation radius (Steiner et al. 2021) and also influences the large-scale disk field close to the inner rim. Notably, we obtain less inclined field lines than Dudorov & Khaibrakhmanov (2014) in the inner disk, which is a combined effect of an optically thin inner disk and a more realistic inner boundary. Additionally, we don't include a toroidal field component, B_φ^s, in the disk exterior above and below the disk, as this would add the complexity of launching magnetically induced outflows. Dudorov & Khaibrakhmanov (2014) include B_φ^s, but do not consider outflows in their model.

We also compared our results to both Mohanty et al. (2018) and Delage et al. (2022), as the authors of both papers use an alternative approach to determine the large-scale magnetic field structure. The primary focus of those studies is to determine the effect of the magnetic field strength and non-ideal MHD effects on the α-viscosity and therefore on the disk structure. Nevertheless, the determination of the ionisation fraction, x_e, is implemented analogously: Mohanty et al. (2018) use thermal ionisation in the inner disk, whereas non-thermal ionisation in our models is analogous to Delage et al. (2022). In both papers, a standard diffusion disk model is used to describe a stationary disk, which especially in the inner disk leads to differences between the disk structure in Mohanty et al. (2018) and our model.

A diffusion approach cannot take into account any pressure gradients occurring in the inner disk and is not able to account for the effect of a stellar dipole (cf. Steiner et al. 2021). Therefore, the Σ-profile in our disk differs from the model in Mohanty et al. (2018). Moreover, they used a constant opacity $\kappa_\mathrm{R} = 10\,\mathrm{cm}^2\,\mathrm{g}^{-1}$, which is different from κ_R in our models, as we obtained a small dusty ring just outside the optically thin region closest to the inner disk rim for most of our models. This opacity feature, together with the ionised, strongly heated innermost disk, leads in our simulations to a large inclination of the large-scale disk field very close to the star. However, Mohanty et al. (2018) uses an α-viscosity, which is dependent on the magnetic field strength. This results in $\alpha \approx 0.1$ in the very inner disk and is a factor 10 higher than our adopted value of $\alpha_\mathrm{MRI} = 0.01$ (cf. Table 2). Therefore, the disk structure in the inner disk is accreting more effectively, which yields a less steep increase in Σ for larger r and a DZ inner boundary further outwards. The most notable difference in both Mohanty et al. (2018) and Delage et al. (2022) with respect to the determination of the large-scale field strength in the disk is their use of an iterative approach: To obtain a stationary disk the condition $\dot{M}$ = const. has to be fulfilled. The α-viscosity at every radius determines $\dot{M}$ and is dependent on the large-scale field strength (root-mean-square (r.m.s.) field, cf. Sano et al. 2004) under the assumption of a maximally efficient MRI. Then, iteratively, a disk structure can be obtained with $\dot{M}$ = const. and a corresponding α and magnetic field. This approach cannot account for an external fossil field or a stellar dipole field threading the inner disk, since the field is solely determined by the condition of maximally efficient MRI. There is no evidence that MRI determines the large-scale field strength and not vice versa (also mentioned and discussed by Delage et al. 2022). The results for the radial profile of $|\boldsymbol{B}|$ in Delage et al. (2022) differ from our results especially in the DZ, where their magnetic field strength follows a power-law over the whole disk, contrary to our results, where a DZ has a clear impact on the radial profiles of B_z and B_r^s.

4.2. Implications of large-scale field inclination

The inclination angle of the large-scale field lines is a crucial parameter in determining the existence and strength of magnetocentrifugally accelerated outflows (e.g. Ogilvie & Livio 1998; Campbell & G. 1999; Ogilvie & Livio 2001)). We adopt the simple wind model of Ogilvie & Livio (1998) for a rough estimate of the wind mass loss, $\dot{M}_\mathrm{wind}$, which we could expect for a MCW launching from the disk surface. In accordance with our two-zone model of Guilet & Ogilvie (2012), the large-scale field is assumed to be force-free above the disk, which results in rigidly rotating field lines up to the Alfvénic surface (the surface above the disk where the wind velocity surpasses the Alfvén-velocity),

$$B_\mathrm{r}(z > z_\mathrm{B}) = B_\mathrm{z}\,\tan(i)\,, \tag{83}$$

where i denotes the inclination angle at the disk surface with respect to the midplane normal. We note that we only assume the Alfvénic surface to be located somewhere above the sonic surface and make no effort to determine its actual position in this work. In theory, the Alfvén point along a field line determines how much angular momentum can be transported by the wind, whereas the sonic point determines the mass of the wind flow. Hence, for an estimate of the wind mass, we use that it has to pass through the sonic point at height z_sonic and assume that $z_\mathrm{B} < z_\mathrm{sonic} \ll r$. The last assumption is needed for the approximation of a rigid field line. Then the MCW mass loss, $\dot{M}_\mathrm{wind}$, is determined through (for a much more comprehensive explanation, cf. Ogilvie & Livio 1998, 2001)

$$\Omega_1^\mathrm{s} \equiv \frac{u_\varphi(z = z_\mathrm{B})}{r} - \Omega_\mathrm{K}\,, \tag{84}$$

$$\Delta\Phi \equiv \frac{\Omega_\mathrm{K}\,z_\mathrm{B} - 2\,\Omega_1^\mathrm{s}\,r\,\tan(i)}{2(3\,\tan^2(i) - 1)}\,, \tag{85}$$

$$\dot{M}_\mathrm{wind} = \rho(z = z_\mathrm{B})\,c_\mathrm{s}\,\cos(i)\exp\left(\frac{-\Delta\Phi}{c_\mathrm{s}^2} - \frac{1}{2}\right)\,. \tag{86}$$

Here, ΔΦ denotes the effective centrifugal potential and Ω_1^s the deviation from Keplerian rotation, Ω_K, at the disk surface. We further assume that the MCW is launched at $z = z_\mathrm{B}$. The resulting $\dot{M}_\mathrm{wind}$ for our reference model is shown in Fig. 11 and reveals that the most favourable regions for a MCW are very close to the inner disk boundary, r_in, and in the outer, AD-dominated disk for $r > r_\mathrm{DZ,out}$. These regions of increased $\dot{M}_\mathrm{wind}$ have also

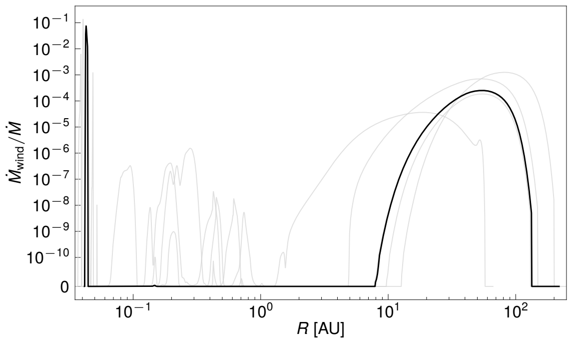

Fig. 11. Magnetocentrifugal winds mass loss, $\dot{M}_\mathrm{wind}$, according to Eq. (86) for our reference model (black). All other models discussed in this paper are shown as light grey lines to further illustrate the two dominant wind regimes in the innermost disk and in the outer disk.

been obtained through simulations performed by other authors (e.g. Armitage 2011; Suzuki et al. 2016; Lesur 2021) and observations (Güdel et al. 2018). Nevertheless, we stress the point that this analysis of MCW mass loss is preliminary and serves the purpose of showing that purely magnetocentrifugally driven winds are possible in disks for realistic α-values and fossil field strengths. We interpret these results as a promising starting point for upcoming simulations, including the effects of MHD outflows. A realistic disk model with MHD outflows has to include the effects of angular momentum loss from the wind, which would lead to increased mass transport and magnetic flux transport, and most likely would lead to the opening of a gap (see Armitage 2011). Additionally, some models suggest an inverted Σ-profile in the case of effective winds (e.g. Suzuki et al. 2016), which further confirms that winds need to be included in our MHD disk evolution model as a next step.

4.3. Variation of the fossil field

The fossil field strength, B_∞, in PPDs is a topic of active studies (e.g. Crutcher et al. 2004; Masson et al. 2016; Tsukamoto et al. 2023) and lies in the range of [10^{-5} G, 10^{-1} G]. Especially the upper end of this range is intriguing with respect to disk evolution, since such strong magnetic fields can potentially influence disk evolution. Also, with respect to magnetic field evolution in disks, stronger fields are expected to behave differently.

A stronger field causes a larger effective resistivity, especially in the outer disk, since there AD is dominant (recall that $\eta_A \propto |\boldsymbol{B}|^2$, cf. Eq. (65)).

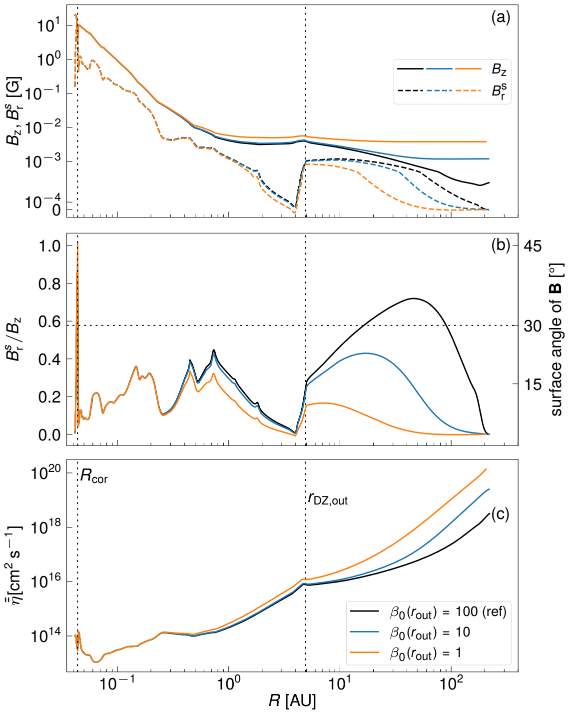

Fig. 12. Stationary magnetic field topology for different initial fossil field strengths. The reference model uses a fossil field with $\beta_0 = 10^2$ (black) and is compared to two models with a stronger initial field ($\beta_0 = 10$ (blue) and $\beta_0 = 1$ (orange)). The panels are the same as in Fig. 8. The vertical dashed lines correspond to R_{cor} and $r_{DZ,out}$.

An increased $\bar{\bar{\eta}}$ then causes less effective magnetic flux transport and a less inclined field geometry in the outer disk (cf. (b) of Fig. 12). Interestingly, the field strength for the two models with $\beta_0(r_{out}) = 10$ and $\beta_0(r_{out}) = 100$ is almost indistinguishable for all $r \lesssim r_{DZ,out}$. The model with $\beta_0(r_{out}) = 1$ yields a larger B_z until the stellar dipole dominates the large-scale field strength. Summarising the results shows that a stronger fossil field, B_∞, leads to a less inclined outer disk field, but has no effect on the inner magnetic field topology due to the dominance of the stellar dipole field.

We emphasise that these results should be taken with a grain of salt, since a basic assumption of our large-scale field model is the two-zone model of Guilet & Ogilvie (2012); Leung & Ogilvie (2019), which assumes a passive magnetic field in the disk ($\beta_0 \gg 1$), which is clearly not the case in our model with $\beta_0(r_{out}) = 1$ (see Sec. 2.4). A large-scale field with $\beta_0 \leq 1$ would influence the vertical disk structure (e.g. Ogilvie 1997) and therefore should be taken as a rough estimate of the outer magnetic field structure.

4.4. Model limitations

In this work we conducted long-term MHD simulations of the whole disk while including the very inner disk region $r < 0.1$ AU, a stellar dipole field, and a large-scale disk field. Covering sufficient time to allow the disk and large-scale field to become stationary, while simultaneously including the inner disk, made it necessary to make various simplifications and assumptions:

– We used a 1+1D model to conduct our simulations. Hence, the disk and the large-scale field were assumed to be axisymmetric. This constrained us to treat some intrinsically 3D natured phenomena in a simplified way. One example is the inner boundary: The disk is magnetically disrupted by the stellar magnetic field at a certain radius close to the star and is accreted along magnetic funnels (e.g. Romanova et al. 2004). However, such funnels are highly non-axisymmetric, and we therefore used the results of Bessolaz et al. (2008) to construct a physically motivated inner boundary (see Steiner et al. 2021). The disk in the vertical direction is assumed to be hydrostatic, and the disk gas temperature is assumed constant for the hydrodynamic evolution of the disk; however, for the approximation of the ionisation fraction, a temperature profile is used to obtain a better model of the vertical ionisation profile. This is slightly inconsistent, but is not believed to change our results, as the temperature for the hydrodynamic evolution would be included as a density-weighted vertical average and hence would be very close to the midplane value of T_{gas} (cf. Sec. 2.5).
– In this work, we focused on studying the poloidal magnetic field structure and did not include toroidal fields. Although we considered the effects of toroidal fields inside the disk, the toroidal field in the disk exterior was assumed to vanish. However, the large-scale field very likely winds up corresponding to a disk field B_φ^s component in the disk exterior above the disk surface. This, in turn, would imply some outflow coupling to the large-scale field. The launching mechanism could be purely magnetocentrifugal, purely thermal (photo-evaporation), or a combination of both mechanisms (e.g. Lesur 2021). The addition of magnetically and thermally induced outflows and their effects on the long-term disk evolution are the focus of subsequent studies using this model, as it is not constrained to steady-state solutions. This work focused on the effects of a stellar dipole and stellar rotation on the large-scale field topology, while the disk was self-consistently simulated.
– We did not include FUV radiation in our model, which is expected to strongly ionise the upper atmosphere (e.g. Rab et al. 2017) and can be important in the study of magnetic field evolution, as the large-scale field is radially transported in the disk surface layer in large parts of the disk. Additionally, an ionised upper atmosphere is important for the study of magnetically induced outflows and should be included in upcoming papers aiming to investigate disk evolution, including MCWs.
– We did not include the effects of EUV heating of the thin, upper disk atmosphere due to secondary processes following the ionisation of the gas. As proposed by Glassgold et al. (2004, 2012); Güdel (2015), up to 50% of the energy deposited in the upper atmosphere is used to heat the gas. For future work, including photoevaporative winds and magnetically driven outflows, these effects should be taken into consideration.
– The Hall effect is not included in our studies; however, it is the dominant non-ideal, laminar diffusion process in a large radial range of PPDs (e.g. Wardle 2007; Bai & Stone 2017; Leung & Ogilvie 2019). The HE is linked to magnetically induced outflows (e.g. Leung & Ogilvie 2019), which strongly

indicates that this effect should be integrated in an upcoming model including magnetised winds. Nevertheless, the treatment of the HE keeps being challenging due to its anisotropic character, which only allows for an approximate treatment in a 1+1D disk model.

- Dust is treated in our model very simply. The dust-to-gas ratio is assumed to be constant radially and in time, which is very unlikely to ever occur in a realistic disk. Recent work shows that dust can accumulate in rings, which influences the vertical temperature equilibrium and can trigger FU Ori-like outbursts, if those rings occur in the inner disk (e.g. Testi et al. 2014; Vorobyov et al. 2020, 2022). Additionally, we did not include any dust evolution model, ignoring coagulation, fragmentation, or settling of dust grains, which can lead to different ionisation fractions for different dust grain sizes (e.g. Dudorov & Khaibrakhmanov 2014; Delage et al. 2022).

5. Summary and conclusion

In this study, we have extended the 1+1D disk evolution model of Ragossnig et al. (2020); Steiner et al. (2021) with a large-scale magnetic field evolution model (cf. Sec. 2.2). An implicit time integration scheme allowed us to self-consistently include the very inner disk while performing long-term (of the order of the disk viscous timescale) simulations. Including a large-scale field makes it necessary to carefully model the ionisation in the disk both in radial and vertical direction in order to be able to determine the magnetic resistivity in the disk (cf. Sec. 2.5). In our model, we included non-ideal MHD effects, for example, OD and AD. The scientific objectives of this work were twofold. First was to determine the large-scale field topology in a steady-state disk truncated by a stellar dipole. The transition towards a stationary field yielded the following conclusions:

- Using the conductivity-weighted averaging for the radial magnetic transport velocity, $\bar{\bar{u}}_\psi$, and resistivity, $\bar{\bar{\eta}}$, proposed by Guilet & Ogilvie (2012), we were able to include the effects of the vertical disk profile and did not have to ignore magnetic advection at the disk surface (or layers at intermediate heights) in the framework of a 1+1D simulation.
- Similar to the results of Guilet & Ogilvie (2014); Dudorov & Khaibrakhmanov (2014), the field is advected inwards effectively in the outer disk and in the inner MRI-active disk. The inclination of the large-scale field lines in the outer DZ is reduced, whereas in the inner DZ, magnetic flux transport in the layers above the DZ leads to a non-negligible inclination.
- The vertical large-scale field component, B_z, in the inner disk is dominated by the stellar dipole field, whereas the radial field, B_r^s, depends on the detailed ionisation structure in the disk.
- The large-scale field inclination in the outer disk is dominated by AD. We managed to reproduce the same power-law dependences for B_z and β_0 as, for example, Dudorov & Khaibrakhmanov (2014), which indicates the validity of our approach.
- The self-consistent hydrodynamical treatment of a magnetically truncated, irradiated disk shows that the radial profiles of Σ, $\boldsymbol{u}$, and T_{gas} also lead to a complex large-scale field structure in the inner disk. This is a unique property of our model, as we are not limited by small time steps in the inner disk, and hence long-term simulations of the large-scale field (even though they are conducted with the goal of constructing a stationary model) have not been covered yet (e.g. Dudorov & Khaibrakhmanov 2014; Mohanty et al. 2018; Delage et al. 2022).

The second scientific objective was to perform a parameter study to investigate how stellar and disk parameters influence the large-scale field topology, namely, $P_\star$, $B_\star$, L_X, and $\dot{M}$, and the strength of the fossil field. We found that different stellar parameters influence the large-scale magnetic field topology in different disk regions :

- The stellar dipole strength, $|\boldsymbol{B}_\star|$, influences the large-scale field in the inner disk ($r < 1$ AU) in two ways. First, a weaker dipole field results in disk truncation closer to the star (e.g. Hartmann et al. 2016), where the disk is hotter and therefore has a larger ionisation level. Second, a stronger $|\boldsymbol{B}_\star|$ also increases AD in the region dominated by the dipole and therefore results in a large-scale field with less inclined field lines.
- A fast or slow rotating star with the rotation period, $P_\star$, also affects the large-scale field by R_{cor} being closer to or further away from the star. It only affects the inner disk, $r < 0.3$ AU, in that a slower rotating star (larger $P_\star$) leads to a less distinct increase of the field inclination very close to the star.
- The large-scale field in the DZ and the outer disk is strongly dependent on the X-ray luminosity. A larger L_X results in a larger ionisation fraction at the disk surface above the DZ and in the outer disk surface layers. In those disk layers, the large-scale field is advected radially inwards most effectively in those disk regions.
- Changing $\dot{M}$ changes the disk structure and therefore also alters the large-scale field topology. In summary, a larger $\dot{M}$ results in a larger inclined field in the dead zone and in r_{in} shifting towards smaller radii, which in turn leads to a pronounced spike in field inclination very close to the star.

This study shows that a large-scale field threading a disk is also dependent on stellar parameters and has non-negligible inclined field lines. Therefore, the next step in this planned series of papers will be to include a wind model dependent on the large-scale field topology and the disk structure. Our simulation framework, TAPIR (e.g. Ragossnig et al. 2020), has an implicit time integration scheme. Therefore, we can conduct long-term simulations covering the whole disk lifetime while including the inner disk, the interaction with a stellar dipole, a large-scale field, and a wind model. This will help answer the question of how disks evolve under the influence of magnetically induced winds in combination with viscous accretion. It will also further allow us to provide estimates on the mass loss and angular momentum loss rates that such winds would produce. An exciting scientific question is whether MCWs lead to an unstable configuration in the disk, as a strongly inclined field triggers a strong MCW, which then removes angular momentum and further increases the inclination. In such a scenario, multiple gaps could be opened in the disk. Equally interesting is the interaction of photoevaporative flows with a large-scale field and the reaction of the large-scale field to high accretion rates during an accretion outburst.

Acknowledgements. We thank the referee for the constructive feedback that helped to improve and clarify the manuscript.

References

Armitage, P. J. 2011, Annual Review of Astronomy and Astrophysics, 49, 195
Armitage, P. J., Livio, M., & Pringle, J. E. 2001, MNRAS, 324, 705
Asplund, M., Amarsi, A. M., & Grevesse, N. 2021, A&A, 653, A141
Bai, X.-N. & Goodman, J. 2009, ApJ, 701, 737
Bai, X.-N. & Stone, J. M. 2011, in AAS/Division for Extreme Solar Systems Abstracts, Vol. 2, AAS/Division for Extreme Solar Systems Abstracts, 36.03

Bai, X.-N. & Stone, J. M. 2013, Astrophys. Journal, Vol. 769, Issue 1, Artic. id. 76, 21 pp. (2013)., 769 [arXiv:1301.0318]
Bai, X.-N. & Stone, J. M. 2017, ApJ, 836, 46
Balbus, S. A. & Hawley, J. F. 1991, ApJ, 376, 214
Baraffe, I., Homeier, D., Allard, F., & Chabrier, G. 2015, A&A, 577, A42
Bell, K. R. & Lin, D. N. C. 1994, ApJ, 427, 987
Ben, G. M., Jose, J., & Hernández, J. 2025, MNRAS, 541, 2246
Bertrang, G. H. M., Flock, M., & Wolf, S. 2017, MNRAS, 464, L61
Bessolaz, N., Zanni, C., Ferreira, J., Keppens, R., & Bouvier, J. 2008, A&A, 478, 155
Blandford, R. D. & Payne, D. G. 1982, MNRAS, 199, 883
Brandenburg, A., Nordlund, A., Stein, R. F., & Torkelsson, U. 1995, ApJ, 446, 741
Brauer, R., Wolf, S., & Flock, M. 2017, A&A, 607, A104
Campbell, C. G. & G., C. 1999, Mon. Not. R. Astron. Soc., 310, 1175
Cecil, M., Gehrig, L., & Steiner, D. 2024, A&A, 687, A136
Courant, R., Friedrichs, K., & Lewy, H. 1928, Math. Ann., 100, 32
Crutcher, R. M. & Kemball, A. J. 2019, Frontiers in Astronomy and Space Sciences, 6, 66
Crutcher, R. M., Nutter, D. J., Ward-Thompson, D., & Kirk, J. M. 2004, ApJ, 600, 279
Delage, T. N., Okuzumi, S., Flock, M., Pinilla, P., & Dzyurkevich, N. 2022, A&A, 658, A97
Dong, R., Vorobyov, E., Pavlyuchenkov, Y., Chiang, E., & Liu, H. B. 2016, ApJ, 823, 141
Dorfi, E. & Drury, L. 1987, J. Comput. Phys., 69, 175
Dudorov, A. E. & Khaibrakhmanov, S. A. 2014, Ap&SS, 352, 103
Ferguson, J. W., Alexander, D. R., Allard, F., et al. 2005, ApJ, 623, 585
Ferreira, J., Dougados, C., & Cabrit, S. 2006, A&A, 453, 785
Gammie, C. F. 1996, ApJ, 457, 355
Gehrig, L., Steiner, D., Vorobyov, E. I., & Güdel, M. 2022, A&A, 667, A46
Gehrig, L. & Vorobyov, E. I. 2023, A&A, 673, A54
Glassgold, A. E., Galli, D., & Padovani, M. 2012, ApJ, 756, 157
Glassgold, A. E., Najita, J., & Igea, J. 2004, ApJ, 615, 972
Güdel, M. 2015, in European Physical Journal Web of Conferences, Vol. 102, European Physical Journal Web of Conferences, 00015
Güdel, M., Eibensteiner, C., Dionatos, O., et al. 2018, A&A, 620, L1
Guilet, J. & Ogilvie, G. I. 2012, Mon. Not. R. Astron. Soc. Vol. 424, Issue 3, pp. 2097-2117., 424, 2097
Guilet, J. & Ogilvie, G. I. 2014, Mon. Not. R. Astron. Soc. Vol. 441, Issue 1, p.852-868, 441, 852
Hartmann, L., Herczeg, G., & Calvet, N. 2016, Annual Review of Astronomy and Astrophysics, 54, 135
Herbst, W., Bailer-Jones, C. A. L., Mundt, R., Meisenheimer, K., & Wackermann, R. 2002, A&A, 396, 513
Hubeny, I. 1990, ApJ, 351, 632
Hueso, R. & Guillot, T. 2005, A&A, 442, 703
Irwin, J. & Bouvier, J. 2009, in IAU Symposium, Vol. 258, The Ages of Stars, ed. Mamajek, E. E., Soderblom, D. R., & Wyse, R. F. G., 363–374
Jackson, J. D. 1999, Classical electrodynamics, 3rd edn. (New York, NY: Wiley)
Jankovic, M. R., Owen, J. E., Mohanty, S., & Tan, J. C. 2021, MNRAS, 504, 280
Johns-Krull, C. M., Valenti, J. A., & Koresko, C. 1999, ApJ, 516, 900
Johnstone, C. P., Jardine, M., Gregory, S. G., Donati, J. F., & Hussain, G. 2014a, MNRAS, 437, 3202
Johnstone, C. P., Jardine, M., Gregory, S. G., Donati, J. F., & Hussain, G. 2014b, MNRAS, 437, 3202
Khaibrakhmanov, S. A. & Dudorov, A. E. 2022, Astronomy Reports, 66, 872
Lankhaar, B. & Teague, R. 2023, A&A, 678, A17
Lee, C.-F. 2020, A&A Rev., 28, 1
Lesur, G., Flock, M., Ercolano, B., et al. 2023, in Astronomical Society of the Pacific Conference Series, Vol. 534, Protostars and Planets VII, ed. Inutsuka, S., Aikawa, Y., Muto, T., Tomida, K., & Tamura, M., 465
Lesur, G., Kunz, M. W., & Fromang, S. 2014, AAP, 566, A56
Lesur, G. R. J. 2021, A&A, 650, A35
Leung, P. K. C. & Ogilvie, G. I. 2019, MNRAS, 487, 5155
LeVeque, R. J., Mihalas, D., Dorfi, E. A., & Müller, E. 1997, Astrophysics of Planet Formation (Saas-Fee Advanced Course 27. Lecture Notes 1997 Swiss Society for Astrophysics and Astronomy)
Lubow, S. H., Papaloizou, J. C. B., & Pringle, J. E. 1994, MNRAS, 268, 1010
Masson, J., Chabrier, G., Hennebelle, P., Vaytet, N., & Commerçon, B. 2016, A&A, 587, A32
Mohanty, S., Jankovic, M. R., Tan, J. C., & Owen, J. E. 2018, ApJ, 861, 144
Nakamoto, T. & Nakagawa, Y. 1994, ApJ, 421, 640
Ogilvie, G. I. 1997, Mon. Not. R. Astron. Soc., 288, 63
Ogilvie, G. I. & Livio, M. 1998, ApJ, 499, 329
Ogilvie, G. I. & Livio, M. 2001, ApJ, 553, 158
Ohashi, S., Kataoka, A., Nagai, H., et al. 2018, ApJ, 864, 81
Pollack, J. B., McKay, C. P., & Christofferson, B. M. 1985, Icarus, 64, 471
Preibisch, T., Kim, Y.-C., Favata, F., et al. 2005, ApJS, 160, 401
Rab, C., Güdel, M., Padovani, M., et al. 2017, A&A, 603, A96
Ragossnig, F., Dorfi, E. A., Ratschiner, B., et al. 2020, Computer Physics Communications, 256, 107437
Ragossnig, F., Dorfi, E. A., Ratschiner, B., et al. 2019, 1+1D implicit disk computations, 3rd edn. (Computer Physics and Communications)
Reyes-Ruiz, M., Pérez-Tijerina, E., & Sánchez-Salcedo, F. J. 2004, in Revista Mexicana de Astronomia y Astrofisica, vol. 27, Vol. 22, Revista Mexicana de Astronomia y Astrofisica Conference Series, ed. Garcia-Segura, G., Tenorio-Tagle, G., Franco, J., & Yorke, H. W., 113–116
Romanova, M. M., Ustyugova, G. V., Koldoba, A. V., & Lovelace, R. V. E. 2002, ApJ, 578, 420
Romanova, M. M., Ustyugova, G. V., Koldoba, A. V., & Lovelace, R. V. E. 2004, ApJ, 610, 920
Sano, T., Inutsuka, S.-i., Turner, N. J., & Stone, J. M. 2004, ApJ, 605, 321
Shakura, N. I. & Sunyaev, R. A. 1973, A&A, 24, 337
Simon, J. B., Bai, X.-N., Armitage, P. J., Stone, J. M., & Beckwith, K. 2013, ApJ, 775, 73
Spitzer, L. 1978, Physical processes in the interstellar medium (Wiley-Interscience)
Steiner, D., Gehrig, L., Ratschiner, B., et al. 2021, A&A, 655, A110
Suzuki, T. K., Ogihara, M., Morbidelli, A., Crida, A., & Guillot, T. 2016, A&A, 596, A74
Tang, Y.-W., Dutrey, A., Koch, P. M., et al. 2023, ApJ, 947, L5
Testi, L., Birnstiel, T., Ricci, L., et al. 2014, in Protostars and Planets VI, ed. Beuther, H., Klessen, R. S., Dullemond, C. P., & Henning, T., 339
Tsukamoto, Y., Maury, A., Commercon, B., et al. 2023, in Astronomical Society of the Pacific Conference Series, Vol. 534, Protostars and Planets VII, ed. Inutsuka, S., Aikawa, Y., Muto, T., Tomida, K., & Tamura, M., 317
Vorobyov, E. I. & Basu, S. 2009, MNRAS, 393, 822
Vorobyov, E. I., Elbakyan, V., Hosokawa, T., et al. 2017, A&A, 605, A77
Vorobyov, E. I., Khaibrakhmanov, S., Basu, S., & Audard, M. 2020, A&A, 644, A74
Vorobyov, E. I., Skliarevskii, A. M., Elbakyan, V. G., et al. 2019, A&A, 627, A154
Vorobyov, E. I., Skliarevskii, A. M., Molyarova, T., et al. 2022, A&A, 658, A191
Wardle, M. 2007, Ap&SS, 311, 35
Zhu, Z., Hartmann, L., Calvet, N., et al. 2007, ApJ, 669, 483
Zhu, Z. & Stone, J. M. 2018, ApJ, 857, 34

Appendix A: Numerical details

A fully implicit time integration requires an initial model to start with, and its basics are explained in Steiner et al. (2021). As explained in detail in Ragossnig et al. (2020), the hydrodynamical equations can be represented by local interactions and the resulting Jacobian can be efficiently inverted. The addition of a large-scale magnetic field adds a long-range acting component, which cannot be represented by a localised set of variables anymore and therefore is unsuitable for adding as a fully implicit component.

The timestep, Δt, in our model is not restricted by the CFL-condition (see also Dorfi & Drury 1987; Ragossnig et al. 2019; Steiner et al. 2021). Thus, an evolution from an initial model towards a steady state solution can be achieved over $\sim t_{\rm visc}$ using the full set of hydrodynamic equations. However, very large timesteps can result in an unphysical "damping" of processes occurring on smaller timescales. To avoid this issue, we start with a small timestep (100 seconds) and perform a Newton-Raphson iteration for obtaining a new solution (LeVeque et al. 1997; Ragossnig et al. 2020). After a successful iteration, the timestep is adapted by applying the following criteria:

- The number of iterations, $n_{\rm it}$, needed to obtain a new solution determines if the new timestep is increased or decreased.

The timestep control is implemented in the following way for the determination of a new timestep, $\Delta t^{\rm (new)}$:

$$\Delta t^{\rm (new)} = \begin{cases} 1.5\,\Delta t^{\rm (old)} & \text{if} \quad n_{\rm it} = 1 \\ 1.2\,\Delta t^{\rm (old)} & \text{if} \quad n_{\rm it} = 2 \\ 1.0\,\Delta t^{\rm (old)} & \text{if} \quad n_{\rm it} = 3 \\ 0.8\,\Delta t^{\rm (old)} & \text{if} \quad n_{\rm it} = 4 \\ 0.5\,\Delta t^{\rm (old)} & \text{otherwise} \end{cases} , \tag{A.1}$$

This implementation of an adaptive timestep control allows TAPIR to react to perturbations occurring during disk evolution: If a perturbation causes the solution to differ much between two timesteps, more iterations are needed to find a new solution, and the timestep is reduced for the next iteration. It is also possible that the Newton-Raphson iteration does not converge anymore for a chosen timestep, which also leads to the maximum timestep reduction. As the solution approaches a stationary state, the variation between two iterations becomes small, and the timestep increases towards large values. In theory, the values of Δt have no upper limit for a true stationary solution. We assume our solution to be stationary when we have reached 10 times $t_{\rm visc}(r_{\rm out})$.

However, we double-checked every simulation run by taking the final stationary model and restarting the simulation with the initial small timestep of $\Delta t = 100$ seconds. If there is no variation during the second simulation between the initial and final model, we can rule out that a very large Δt towards the end of a simulation run would dampen any perturbations. This is the case for all models presented in this work.

The external large-scale fossil field connects the field inside the disk to the force-free field in the vacuum above and below the disk and therefore acts as non-local dependency all over the disk. The relation between the toroidal currents and the corresponding flux function of the disk field at the midplane, $\psi_{\rm d}$, is described in Eq. (31) and is calculated at every grid point (index i) in the following way,

$$\psi_{\rm d}(r) = \int_{r_{\rm in}}^{r_{\rm out}} \mathcal{L}(r, r')\, B_{\rm r}^{\rm s}(r')\, dr' \ , \tag{A.2}$$

which can be discretised in the following way (e.g. Guilet & Ogilvie 2014),

$$\psi_{\rm d}(r_{\rm i}) \approx \sum_{\rm j=1}^{\rm n} L_{\rm ij}\, B_{\rm r}^{\rm s}(r_{\rm j}) \ , \tag{A.3}$$

where we have used Eq. (35) to connect $B_{\rm r}^{\rm s}$ to the currents in the disk, $J_{\varphi}^{\rm s}$. The summation maximum n is the number of numerical cells (the radial grid size), whereas $L_{\rm ij}$ represents the linear operator, $\mathcal{L}$ (cf. Sec. 2.2), in cylindrical coordinates and is defined as,

$$L_{\rm ij} \equiv \frac{2}{\pi} \int_{r_{\rm j-1/2}}^{r_{\rm j+1/2}} \frac{r_{\rm i}\, r'}{r_{\rm i} + r'} \left[\frac{(2 - k^2)\, K(k) - 2\, E(k)}{k^2} \right] dr' \ . \tag{A.4}$$

The radial grid points $r_{\rm j\pm1/2}$ represent radii in between two neighbouring grid points (e.g. Guilet & Ogilvie 2014). The integral is calculated for every grid cell using a Romberg integrator for sufficient accuracy. Then $L_{\rm ij}$ is inverted to yield $B_{\rm r}^{\rm s}$ at every grid point, $r_{\rm i}$,

$$B_{\rm r}^{\rm s}(r_{\rm i}) \approx \sum_{\rm j=1}^{\rm n} L_{\rm ij}^{-1}\, \psi_{\rm d}(r_{\rm j}) \ , \tag{A.5}$$

A narrow bandwidth is required for the Jacobian of our implicit integration scheme for efficient inversion, which requires a local formulation of the hydrodynamical equations (e.g. Ragossnig et al. 2020). Since Eq. (A.5) yields a global dependency at every grid point, the following approximation can be made,

$$B_{\rm r}^{\rm s}(r_{\rm i}) \approx \sum_{\rm j=i-l}^{\rm i+u} L_{\rm ij}^{-1}\, \psi_{\rm d}(r_{\rm j}) + \sum_{\rm j=1}^{\rm i-l-1} L_{\rm ij}^{-1}\, \psi_{\rm d}(r_{\rm j}^{\rm A}) + \sum_{\rm j=i+u+1}^{\rm n} L_{\rm ij}^{-1}\, \psi_{\rm d}(r_{\rm j}^{\rm A}) \ , \tag{A.6}$$

where 'l' and 'u' are indices below and above the grid index 'i', respectively, and correspond to l = u = 2 in our work. Furthermore, $r_{\rm j}^{\rm A}$ is the grid point at position 'j' at the old time step, which means that $B_{\rm r}^{\rm s}$ is calculated semi-implicitly, in contrast to the full-implicit treatment of all other hydrodynamical quantities. This way the localised narrow-banded Jacobian can be maintained at the cost of an explicit part. Additionally, since we use an adaptive grid in TAPIR to adapt the inner rim as well as to achieve better numerical accuracy in regions of steep gradients, $L_{\rm ij}$ would need to be calculated and inverted at each time step anew. This would result in greatly increased numerical cost in obtaining a solution of the system of equations at a new time step. Since $L_{\rm ij}$ is a property of the numerical grid only, and the grid is varied slowly by means of the grid equation (Ragossnig et al. 2020), the deviation of the grid between two time steps remains small. Therefore, it is a viable approximation to invert $L_{\rm ij}$ not at every time step but only after a certain maximum threshold grid deviation is exceeded with respect to the last grid configuration used for inversion:

$$\gamma_{\rm inv} = \max \left(\frac{|r_{\rm i}(t_{\rm inv,new}) - r_{\rm i}(t_{\rm inv,old})|}{t_{\rm inv,new} - t_{\rm inv,old}} \right) , \tag{A.7}$$

where $\gamma_{\rm inv}$, $r_{\rm i}(t_{\rm inv,new(old)})$, and $t_{\rm inv,new(old)}$ are the threshold grid deviation triggering the inversion of $L_{\rm ij}$, the numerical grid, and the time at the new (old) inversion time, respectively. The determination of $\gamma_{\rm inv}$ is complex and dependent on the actual time step because of the explicit component in Eq. (A.5), which introduces numerical instabilities above a certain time step. It is therefore necessary to calibrate $\gamma_{\rm inv}$ for every calculation and time step in order to obtain stable solutions.

Appendix B: Validation of the model describing the vertical disk structure

Thin disk approximation: In this work we focus on Class II star-disk systems, i.e. we assume that a potential envelope has already accreted onto the disk and the central star. This means that the disk geometry of a disk without an envelope is much thinner in vertical direction. We therefore can assume that even with an outer flared disk, a Class II disk maintains an approximate geometrically thin structure, which justifies our assumption and is furthermore also used by many other publications (e.g. Bell & Lin 1994; Lubow et al. 1994; Armitage et al. 2001; Mohanty et al. 2018; Delage et al. 2022; Lesur et al. 2023).

Assumption of a stationary vertical velocity- and magnetic field profile : Perturbations of the vertical structure relax on the dynamical timescale, $t_{\rm dyn}$. This is true for perturbations of both the large-scale magnetic field and the disk structure in vertical direction (e.g. Guilet & Ogilvie 2012). As $t_{\rm dyn}$ is much shorter than the viscous timescale, $t_{\rm visc}$, and the magnetic diffusion timescale, $t_{\rm diff}$, which are the respective timescales at which the disk and the large-scale magnetic field evolve radially, the assumption of stationarity for the vertical disk profile is justified (cf. timescales in Fig. 2 of Sec. 3.2).

Assumption of a dominant vertical magnetic field component: A basic assumption for deriving the vertical velocity and large-scale magnetic field profile is a dominant vertical field component, B_z (in comparison to B_r^s and B_φ^s, cf. Guilet & Ogilvie 2012; Leung & Ogilvie 2019). This restriction is due to the fact that an analytic vertical profile can only be obtained if magnetic compression is negligible. However, Guilet & Ogilvie (2012) argue after comparison with numerical simulations of the vertical structure of a strongly magnetised disk, that in the absence of magnetically induced outflows the approximation remains well reasonable as long as: (i) the inclination angle does not exceed $i \approx 30°$ and (ii) the magnetic field is sufficiently weak ($\beta_0 \gtrsim 10^2$). A stronger, large-scale magnetic field would lead to magnetic compression and therefore to a changed vertical disk structure, whereas a large inclination angle would very likely cause MCWs (cf. Sec. 4.2 for an estimate and discussion of including MCWs). Both conditions are almost everywhere fulfilled in our simulations, except a very narrow region in the innermost disk and for a region in the AD-dominated region outside of the DZ. However, the main topic of this work is to expand on former studies of the poloidal large-scale magnetic field structure (e.g. Dudorov & Khaibrakhmanov 2014; Guilet & Ogilvie 2012; Mohanty et al. 2018; Delage et al. 2022) by including a self-consistent MHD disk model and a stellar dipole. Magnetic compression would likely play a role in the innermost disk region. This effect will be included in future studies. We therefore stress the point that the validity of the used vertical disk profile is limited in the innermost disk region (cf. Sec. 4.4 for a comprehensive list of our model limitations).

Choice of vertical layers for calculating the ionisation degree and the magnetic resistivity: Our 1+1D model self-consistently solves the MHD disk equations Eqs. (1) - (4) only in the radial direction. For being able to obtain an estimate of the vertical disk structure at every radius r, we calculate the ionisation degree, x_e, as well as OD and AD at the midplane and four different heights z (cf. fifth step in Sec. 2.6 and Sec. 3.3). The choices for the heights of the five layers are justified as follows:

- $z = 0$: The disk midplane is important to capture the impact of a thermally ionised region in the inner disk on magnetic resistivity. It further proves to be the dominant region of magnetic advection in the AD-dominated outer disk (cf. Fig. 5).
- $z = H_p$: At this height, the disk is not likely to be able to maintain thermal ionisation in the inner disk through viscous heating due to a low gas density at $z = H_p$ (Jankovic et al. 2021). Non-thermal ionisation becomes increasingly important in the layers above for $z > H_p$.
- $z = z_B$: The magnetic surface serves as the boundary layer between a passive large-scale magnetic field inside the disk and a force-free magnetically dominated disk exterior (e.g. Guilet & Ogilvie 2012, 2014). The disk surface in our models is located at this height, which is subject to non-thermal ionisation over most of the PPD's radial extent.
- $z = H_p + \frac{1}{3}(z_B - H_p)$ and $z = H_p + \frac{2}{3}(z_B - H_p)$: Those two layers are evenly positioned in vertical direction between $z = H_p$ and $z = z_B$ and are necessary to capture the effects of a MRI-active layer above the DZ. This layer is located just above the DZ but below the disk surface, which is due to two competing physical processes: (i) Non-thermal ionisation decreases resistivity and allows MRI to operate, and (ii) AD increases at larger z, because the gas density strongly decreases while the large-scale magnetic field maintains its strength (e.g. Delage et al. 2022). This leads to an intermediate region where magnetic advection is highly effective despite being in the radial region of the DZ. Because our 1+1D model cannot calculate this MRI layer self-consistently and therefore its exact location (i.e. its height z) at some time, t, is unknown, we chose to include two additional layers to capture the essentials of this MRI-active layer.

For validating if this choice of layers is suited reasonably well to capture the essential physics needed to model magnetic advection and diffusion of a large-scale magnetic field, we have varied the amount of intermediate layers used to calculate both x_e and the resistivities, η_O and η_A (cf. Fig. B.1). More layers lead to

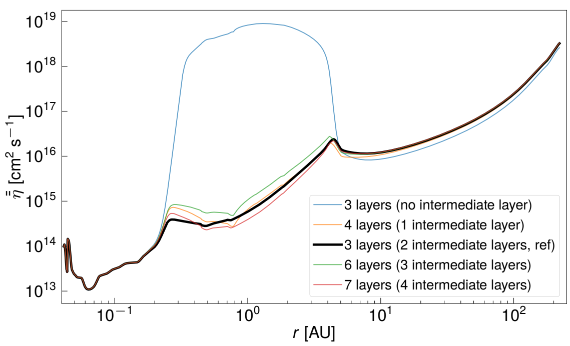

Fig. B.1. Profiles of the vertically conductivity-averaged resistivity, $\bar{\bar{\eta}}$, if calculated with a varying number of vertical layers. The three layers at $z = 0$, $z = H_p$, and $z = z_B$ are always included, whereas the number of intermediate layers between $z = H_p$ and $z = z_B$ is varied. The layers are distributed evenly in the vertical direction between H_p and z_B.

a more accurate description of the vertical disk structure. However, more layers lead to a vastly more complicated time integration scheme (an implicit time integration scheme requires calculating a Jacobian encapsulating all dependences at every grid point) and to a potentially slower convergence of the Newton-Raphson iteration when finding a new solution (see LeVeque et al. 1997; Ragossnig et al. 2020, for an overview of the implicit time integration used in TAPIR). It can be seen in Fig. B.1 that our approach with five layers (i.e. two intermediate layers between H_p and z_B) captures the MRI-active layer well while maintaining a manageable complexity in calculating the aforementioned Jacobian. We note that an approach without any intermediate layer is unsuited for describing magnetic advection in a MRI-active layer above the DZ: the corresponding profile for $\bar{\bar{\eta}}$ vastly overestimates the resulting effective resistivity in the DZ by only taking the values inside the DZ and at the AD-dominated disk surface into account (cf. blue curve in Fig. B.1). We further point out that intermediate layers are only altering the radial $\bar{\bar{\eta}}$-profile in the DZ, while in the inner disk and in the outer disk outside the DZ the number of intermediate layers does not change $\bar{\bar{\eta}}$ significantly. In the inner disk, this is due to the domination of thermal ionisation close to the midplane, which then dominantly contributes to a conductivity-weighted $\bar{\bar{\eta}}$. In the AD-dominated outer disk AD becomes increasingly important with increasing height z, which means that magnetic advection dominantly happens close to the disk midplane.

Vertical temperature profile: Our hydrodynamical equations Eqs. (1) - (4) are formulated in using an isothermal vertical disk structure. Recent studies by e.g. Jankovic et al. (2021) show that the vertical temperature structure in the inner disk is highly dependent on viscous heating and therefore is also dependent on the vertical density structure, but should also be dependent on heating via non-thermal ionisation, making upper layers hotter than the midplane. Hence, the calculation of the ionisation degree by taking the midplane gas temperature, $T_\mathrm{gas,0}$, and using it as the vertically isothermal gas temperature at every height z would vastly overestimate the vertical extent of the thermally ionised disk region. We therefore used a physically motivated vertical gas temperature profile (see Eq. (70), for the physical background, see e.g. Hubeny 1990). The thermally ionised region in our models agrees reasonably well in both the radial and vertical extent with the vertically self-consistent 2D models of Jankovic et al. (2021) and are therefore valid to describe the thermally ionised region. With regard to the discrepancy between the use of an isothermal vertical disk for hydrodynamical simulations while applying a vertical temperature profile for calculating the thermal ionisation degree, we argue as follows: The vertical disk structure (apart from the magnetic field) is described in a 1+1D simulation by density-weighted variables (e.g. Σ, P_gas). Therefore, the disk region around the midplane dominantly contributes to describing the vertical disk structure, which justifies using $T_\mathrm{gas,0}$ as the temperature of an isothermal vertical disk when performing hydrodynamical simulations.

Part IV

Summary, Conclusions and Outlook

Chapter 8

Summary and Conclusions

The structure and evolution of magnetic fields in PPDs depend on many physical and chemical processes. These processes involve the radial and vertical disk structure, i.e., its density, temperature, ionization degree and chemical composition. Further complexity arises from the fact that large-scale magnetic fields are not only dependent on the disk but are also shaping it. First, MRI is strongly dependent on the field strength, which in turbulent disk regions is still the best theory to explain angular momentum transport and accretion. Secondly, the majority of the disk is not turbulent and therefore non-ideal MHD effects have to be taken into account in evolutionary models of large-scale fields, which are (in part) dependent on the field strength itself. Finally, large-scale magnetic fields can also accelerate material up to speeds sufficient to drive an outflow from the disk. Such an outflow removes mass and angular momentum from the disk, thereby altering its long-term evolution. Another important magnetic field component in disks, which is equally important in the context of the long-term disk evolution, is the stellar magnetic field. The stellar field is typically strong in T Tauri stars and can also be regarded as a large-scale magnetic field component, given that it acts on a macroscopic scale and removes angular momentum from the innermost disk region. As mentioned earlier, the evolution of a PPD and topology of the large-scale field depend on the inner disk and, consequently, on the stellar magnetic field. Hence, long-term evolution models of PPDs should not be considered isolated from either the stellar or the large-scale field. Instead, the focus should be on a combined simulation of the star-disk-large-scale-field system.

This brief preceding review of the dependencies between stellar field, disk, and large-scale magnetic field emphasizes the connection between the two main fields of interest in this thesis: (i) The importance of the inner disk region and inner disk boundary in the context of long-term disk evolution, and (ii) the structure of a large-scale magnetic field in PPDs that are magnetically truncated by a stellar field.

In Paper I we studied the impact of a stellar dipole on Class II PPDs. Our objective was to analyze the long-term evolution of an episodically accreting disk truncated by a stellar dipole. For this reason, we developed a 1+1D long-term hydrodynamic simulation capable of including the innermost disk while maintaining the ability to perform long-term evolution simulations. Due to the tremendous efforts toward developing a hydrodynamic simulation with a fully implicit time-integration scheme, we verified it by comparing it to other simpler methods. We discovered that, especially in the inner disk, the commonly used diffusion model for describing the evolution of the surface density is insufficient in capturing the essential physics. In particular, deviations from Keplerian rotation due to pressure gradients and magnetic torques from a stellar dipole are non-negligible in the inner disk. We then proceeded with long-term simulations of disks with episodic accretion and resolved in detail the physical processes leading to those accretion outbursts. Our simulations revealed that during periods of high accretion, the inner disk boundary is pushed inwards, almost reaching the stellar surface. A parameter study varying the stellar magnetic field strength revealed that for stellar dipoles of intermediate strength (the actual values depend on the disk parameters as well as other stellar parameters) episodic accretion can be suppressed. This is due to two different scenarios: (i) In the case of a relatively weak dipole, the inner disk radius moves towards the star. As a result, the inner disk gets heated up, leading to the triggering of episodic outbursts; (ii) in contrast, a very strong stellar field leads to a more pronounced propeller effect for gas beyond the corotation radius. This results in as buildup of gas just outside the corotation radius, leading to more efficient viscous heating and, ultimately, triggering episodic accretion. Between those two extremes a range of stellar dipole magnetic field strengths exist, for which neither stellar irradiation nor viscous heating are sufficient to heat the disk enough to activate MRI in deeper disk layers.

Our scientific objective of Paper II was to gain insight into the large-scale magnetic field topology of Class II disks. Given that disks of this type are laminar over most of their radial and vertical extent, we had to extend our hydrodynamic disk simulation with a description of non-linear MHD effects (in our case Ohmic and ambipolar diffusion) and to include a model describing the ionization degree in the disk. We included thermal ionization and non-thermal ionization due to X-ray stellar radiation, cosmic rays and radioactive decay inside the disk. Most of the magnetic flux transport occurs in the MRI-active surface layers of a disk, which we approximated in terms of a conductivity-weighted vertical average of the magnetic flux transport velocity. We also included a stellar dipole, which both interacts with the innermost disk and acts as an external magnetic field component in addition to the fossil field. To date, work related to the large-scale field topology in disks has been using one of the following three approaches: (i) A global long-term simulation of the large-scale field in a simple, prescribed and stationary disk model; (ii) using a local approximation, in which the radial advection of a field is neglected in favor of the vertical disk profile; (iii) the assumption of a maximally efficient MRI, providing an upper constraint of the large-scale field strength. Our numerical method is capable of covering a sufficient time period ($\sim 10^7 - 10^8$ years) to allow the disk and large-scale field to become truly stationary. Our MHD 1+1D simulations are not limited to local models or a prescribed disk. Instead they can calculate the stationary large-scale field of a magnetically truncated disk self-consistently. The decision of evolving our models to a steady state allowed us to compare our approach against existing work in this scientific field. Our simulations indicate that the large-scale field in the inner disk is dominated by the stellar component. Our results confirm the findings of other studies, i.e., that in the outer disk the large-scale field topology is determined by ambipolar diffusion. In the innermost disk, a narrow region exists, within which the large-scale field has largely inclined field lines. Almost all simulations show this result, caused by complex disk dynamics due to strong stellar irradiation and the magnetic torques from the stellar dipole field. We conducted a parameter study by varying stellar parameters. Summarizing the results of this parameter study show that the large-scale field of a PPD strongly depends on the properties of the star. The large-scale field topology can be directly influenced by a variation of the stellar parameters. Examples include a modified ionization degree due to a variation of the stellar X-ray flux, or a change in AD, caused by a variation of the stellar magnetic field strength. Additionally, the large-scale field topology may be indirectly modified, resulting from a change in the overall disk structure by altering the innermost disk region.

Overall, this thesis demonstrates that the long-term evolution of the disk and the large-scale field are connected, and that a self-consistent treatment of the inner disk is essential when conducting long-term disk simulations. A stellar dipole field alters the dynamics of the innermost disk, thereby interacting with the large-scale field in the inner disk. This, in turn, indirectly influences the long-term evolution of the entire disk and large-scale field.

Chapter 9

Outlook

One of the most important physical processes in PPDs is the transport of angular momentum, either radially outwards or vertically away from the disk by outflows. Class II disks are nowadays commonly considered to be laminar over most of their radial extent. Consequently, MRI is unlikely to be the primary angular momentum transport mechanism driving radial inward-directed mass transport. Angular momentum loss due to magnetically coupled winds provides a promising alternative. Therefore, the subsequent step in our research will be to incorporate magneto-thermal outflows in our model. This has to be done in an approximate way, as the detailed form of the field above the disk cannot be determined in the context of a 1+1D MHD disk model. The Hall effect must be taken into account in the context of outflows coupling to a large-scale magnetic field (see e.g. Lesur, 2021; Leung and Ogilvie, 2019). We are then able to conduct long-term evolution simulations of laminar Class II PPDs over their full extent with outflows. This allows us to study the effects of a wind on the disk dynamics. In the outer disk photoevaporative winds can occur (see e.g. Cecil et al., 2024). These outflows are in part ionized and therefore also couple to a large-scale magnetic field. As a result, these magneto-thermal outflow exert a torque on the disk, probably even facilitating the opening of gaps in the outer disk. It is crucial to include outflows emerging from the innermost disk, as those winds are modifying the star-disk connection. Not only the disk is influenced by the stellar field, but also the star itself spins either up or down, depending on the disk dynamics and winds in the innermost disk regions (see e.g. Gehrig et al., 2022; Gehrig and Vorobyov, 2023). Connected to outflows from PPDs is the question about the lifetime of a disk and how such disks are dissolved. The answer to these questions could provide crucial insights into planet formation, as gaps and lifetime constraints play an important role in planet formation models.

The work presented in this thesis has been carried out using a 1+1D disk simulation, which is suitable for the study of geometrically thin disks (e.g., Class II). Disks in earlier stages are geometrically thicker, therefore extending our studies to those disks requires the development of a 2D MHD simulation capable of performing long-term simulations while including the inner disk. Regarding large-scale magnetic fields, this would enable us to resolve the magnetic field structure both in the disk interior and exterior. Magnetically induced outflows could be calculated self-consistently, which would provide a more reliable estimate of the disk lifetime. Finally, long-term MHD simulations of the inner disk still pose a challenge for most numerical codes due to severe timestep limitations. A numerical code capable of simulating the inner disk over extended periods of time could therefore act as an inner boundary for more sophisticated 2D- or 3D-MHD disk simulations (see e.g. Vorobyov et al., 2019).

References

Anderson, E., Bai, Z., Bischof, C., Blackford, S., Demmel, J., Dongarra, J., Du Croz, J., Greenbaum, A., Hammarling, S., McKenney, A., and Sorensen, D. (1999). *LAPACK Users' Guide*. Society for Industrial and Applied Mathematics, Philadelphia, PA, third edition.

Andrews, S. M. (2020). Observations of Protoplanetary Disk Structures. *ARA&A*, 58:483–528.

Andrews, S. M., Terrell, M., Tripathi, A., Ansdell, M., Williams, J. P., and Wilner, D. J. (2018). Scaling Relations Associated with Millimeter Continuum Sizes in Protoplanetary Disks. *ApJ*, 865(2):157.

Armitage, P., Kley, W., Audard, M., Meyer, M. R., and Alibert, Y. (2019). From Protoplanetary Disks to Planet Formation. Saas-Fee Advanced Course.

Armitage, P. J. (2011). Dynamics of protoplanetary disks. *Annual Review of Astronomy and Astrophysics*, 49(1):195–236.

Armitage, P. J. (2018). *A Brief Overview of Planet Formation*, pages 2185–2203. Springer International Publishing, Cham.

Armitage, P. J. (2020). *Astrophysics of planet formation, Second Edition*.

Armitage, P. J., Livio, M., and Pringle, J. E. (2001). Episodic accretion in magnetically layered protoplanetary discs. *MNRAS*, 324:705–711.

Aspin, C., Reipurth, B., Herczeg, G. J., and Capak, P. (2010). The 2008 Extreme Outburst of the Young Eruptive Variable Star EX Lupi. *ApJ*, 719(1):L50–L55.

Audard, M., Ábrahám, P., Dunham, M. M., Green, J. D., Grosso, N., Hamaguchi, K., Kastner, J. H., Kóspál, Á., Lodato, G., Romanova, M. M., Skinner, S. L., Vorobyov, E. I., and Zhu, Z. (2014). Episodic Accretion in Young Stars. *Protostars and Planets VI*, pages 387–410.

Bae, J., Hartmann, L., Zhu, Z., and Gammie, C. (2013). Variable Accretion Outbursts in Protostellar Evolution. *ApJ*, 764:141.

Bai, X.-N. and Stone, J. M. (2011). Effect of Ambipolar Diffusion on the Nonlinear Evolution of Magnetorotational Instability in Weakly Ionized Disks. *ApJ*, 736(2):144.

Bai, X.-N. and Stone, J. M. (2013). Wind-driven Accretion in Protoplanetary Disks. I: Suppression of the Magnetorotational Instability and Launching of the Magnetocentrifugal Wind. *Astrophys. Journal, Vol. 769, Issue 1, Artic. id. 76, 21 pp. (2013).*, 769.

Bai, X.-N. and Stone, J. M. (2017). Hall Effect-Mediated Magnetic Flux Transport in

Protoplanetary Disks. *ApJ*, 836(1):46.

Bai, X.-N. and Xue-Ning (2014). Hall-effect Controlled Gas Dynamics in Protoplanetary Disks: I. Wind Solutions at the Inner Disk. *Astrophys. Journal, Vol. 791, Issue 2, Artic. id. 137, 22 pp. (2014).*, 791.

Bai, X.-N., Ye, J., Goodman, J., and Yuan, F. (2015). Magneto-thermal Disk Wind from Protoplanetary Disks. *Astrophys. Journal, Vol. 818, Issue 2, Artic. id. 152, 20 pp. (2016).*, 818.

Bai, X.-N., Ye, J., Goodman, J., and Yuan, F. (2016). Magneto-thermal Disk Winds from Protoplanetary Disks. *ApJ*, 818(2):152.

Balbus, S. A. and Hawley, J. F. (1991). A powerful local shear instability in weakly magnetized disks. I - Linear analysis. II - Nonlinear evolution. *Astrophys. J.*, 376:214.

Balbus, S. A. and Hawley, J. F. (1991). A powerful local shear instability in weakly magnetized disks. I - Linear analysis. II - Nonlinear evolution. *ApJ*, 376:214–233.

Balbus, S. A. and Hawley, J. F. (1998). Instability, turbulence, and enhanced transport in accretion disks. *Rev. Mod. Phys.*, 70(1):1–53.

Banzatti, A., Pontoppidan, K. M., Bruderer, S., Muzerolle, J., and Meyer, M. R. (2015). Depletion of Molecular Gas by an Accretion Outburst in a Protoplanetary Disk. *ApJ*, 798(1):L16.

Barranco, J. A. and Marcus, P. S. (2005). Three-dimensional Vortices in Stratified Protoplanetary Disks. *ApJ*, 623(2):1157–1170.

Bell, K. R. and Lin, D. N. C. (1994). Using FU Orionis outbursts to constrain self-regulated protostellar disk models. *ApJ*, 427:987–1004.

Bergin, E. A., Cleeves, L. I., Gorti, U., Zhang, K., Blake, G. A., Green, J. D., Andrews, S. M., Evans, Neal J., I., Henning, T., Öberg, K., Pontoppidan, K., Qi, C., Salyk, C., and van Dishoeck, E. F. (2013). An old disk still capable of forming a planetary system. *Nature*, 493(7434):644–646.

Bertrang, G. H. M., Flock, M., and Wolf, S. (2017). Magnetic fields in protoplanetary discs: from MHD simulations to ALMA observations. *MNRAS*, 464(1):L61–L64.

Bessolaz, N., Zanni, C., Ferreira, J., Keppens, R., and Bouvier, J. (2008). Accretion funnels onto weakly magnetized young stars. *A&A*, 478(1):155–162.

Birnstiel, T., Dullemond, C. P., Zhu, Z., Andrews, S. M., Bai, X.-N., Wilner, D. J., Carpenter, J. M., Huang, J., Isella, A., Benisty, M., Pérez, L. M., and Zhang, S. (2018). The Disk Substructures at High Angular Resolution Project (DSHARP). V. Interpreting ALMA Maps of Protoplanetary Disks in Terms of a Dust Model. *ApJ*, 869(2):L45.

Blandford, R. D. and Payne, D. G. (1982). Hydromagnetic flows from accretion disks and the production of radio jets. *MNRAS*, 199:883–903.

Blinova, A. A., Romanova, M. M., and Lovelace, R. V. E. (2016). Boundary between stable and unstable regimes of accretion. Ordered and chaotic unstable regimes. *MNRAS*, 459(3):2354–2369.

Campbell, C. G. and G., C. (1999). Launching of accretion disc winds along dynamo-generated magnetic fields. *Mon. Not. R. Astron. Soc.*, 310(4):1175–1184.

Cecil, M., Gehrig, L., and Steiner, D. (2024). Time-dependent, long-term hydrodynamic simulations of the inner protoplanetary disk. III. The influence of photoevaporation. *A&A*, 687:A136.

Chen, H., Myers, P. C., Ladd, E. F., and Wood, D. O. S. (1995). Bolometric Temperature and Young Stars in the Taurus and Ophiuchus Complexes. *ApJ*, 445:377.

Ching, T.-C., Lai, S.-P., Zhang, Q., Yang, L., Girart, J. M., and Rao, R. (2016). Helical Magnetic Fields in the NGC 1333 IRAS 4A Protostellar Outflows. *ApJ*, 819(2):159.

Cleeves, L. I., Adams, F. C., Bergin, E. A., and Visser, R. (2013). Radionuclide Ionization in Protoplanetary Disks: Calculations of Decay Product Radiative Transfer. *ApJ*, 777(1):28.

Courant, R., Friedrichs, K., and Lewy, H. (1928). Über die partiellen Differenzengleichungen der mathematischen Physik. *Math. Ann.*, 100:32–74.

Cui, C. and Bai, X.-N. (2021). Global three-dimensional simulations of outer protoplanetary discs with ambipolar diffusion. *MNRAS*, 507(1):1106–1126.

D'Alessio, P., Cantö, J., Calvet, N., and Lizano, S. (1998). Accretion Disks around Young Objects. I. The Detailed Vertical Structure. *ApJ*, 500(1):411–427.

D'Angelo, C. R. and Spruit, H. C. (2010). Episodic accretion on to strongly magnetic stars. *MNRAS*, 406(2):1208–1219.

Delage, T. N., Okuzumi, S., Flock, M., Pinilla, P., and Dzyurkevich, N. (2022). Steady-state accretion in magnetized protoplanetary disks. *A&A*, 658:A97.

Donati, J. F., Gaidos, E., Moutou, C., Cristofari, P. I., Arnold, L., Barber, M. G., and Mann, A. W. (2025). Mass, Gas, and Gauss around a T Tauri Star with SPIRou. *arXiv e-prints*, page arXiv:2505.10564.

Donati, J. F., Jardine, M. M., Gregory, S. G., Petit, P., Bouvier, J., Dougados, C., Ménard, F., Collier Cameron, A., Harries, T. J., Jeffers, S. V., and Paletou, F. (2007). Magnetic fields and accretion flows on the classical T Tauri star V2129 Oph. *MNRAS*, 380(4):1297–1312.

Donati, J.-F., Kouach, D., Lacombe, M., Baratchart, S., Doyon, R., Delfosse, X., Artigau, É., Moutou, C., Hébrard, G., Bouchy, F., Bouvier, J., Alencar, S., Saddlemyer, L., Parès, L., Rabou, P., Micheau, Y., Dolon, F., Barrick, G., Hernandez, O., Wang, S. Y., Reshetov, V., Striebig, N., Challita, Z., Carmona, A., Tibault, S., Martioli, E., Figueira, P., Boisse, I., and Pepe, F. (2018). *SPIRou: A NIR Spectropolarimeter/High-Precision Velocimeter for the CFHT*, page 107.

Donati, J. F., Kouach, D., Moutou, C., Doyon, R., Delfosse, X., Artigau, E., Baratchart, S., Lacombe, M., Barrick, G., Hébrard, G., Bouchy, F., Saddlemyer, L., Parès, L., Rabou, P., Micheau, Y., Dolon, F., Reshetov, V., Challita, Z., Carmona, A., Striebig, N., Thibault, S., Martioli, E., Cook, N., Fouqué, P., Vermeulen, T., Wang, S. Y., Arnold, L., Pepe, F., Boisse, I., Figueira, P., Bouvier, J., Ray, T. P., Feugeade, C., Morin, J., Alencar, S., Hobson, M., Castilho, B., Udry, S., Santos, N. C., Hernandez, O., Benedict, T., Vallée, P., Gallou, G., Dupieux, M., Larrieu, M., Perruchot, S., Sottile, R., Moreau, F., Usher, C., Baril, M., Wildi, F., Chazelas, B., Malo, L., Bonfils, X., Loop, D., Kerley, D., Wevers, I., Dunn, J., Pazder, J., Macdonald, S., Dubois, B., Carrié, E., Valentin, H., Henault, F., Yan, C. H., and Steinmetz, T. (2020). SPIRou: NIR velocimetry and spectropolarimetry at the CFHT. *MNRAS*, 498(4):5684–5703.

Donati, J. F., Skelly, M. B., Bouvier, J., Jardine, M. M., Gregory, S. G., Morin, J., Hussain, G. A. J., Dougados, C., Ménard, F., and Unruh, Y. (2010). Complex magnetic topology and strong differential rotation on the low-mass T Tauri star V2247 Oph. *MNRAS*, 402(3):1426–1436.

Dong, R., Najita, J. R., and Brittain, S. (2018). Spiral Arms in Disks: Planets or Gravitational Instability? *ApJ*, 862(2):103.

Dong, R., Vorobyov, E., Pavlyuchenkov, Y., Chiang, E., and Liu, H. B. (2016). Signatures of Gravitational Instability in Resolved Images of Protostellar Disks. *ApJ*, 823(2):141.

Dudorov, A. E. and Khaibrakhmanov, S. A. (2014). Fossil magnetic field of accretion disks of young stars. *Ap&SS*, 352(1):103–121.

Dullemond, C. P., Isella, A., Andrews, S. M., Skobleva, I., and Dzyurkevich, N. (2020). Midplane temperature and outer edge of the protoplanetary disk around HD 163296. *A&A*, 633:A137.

Dullemond, C. P. and Monnier, J. D. (2010). The Inner Regions of Protoplanetary Disks. *ARA&A*, 48:205–239.

Ercolano, B. and Pascucci, I. (2017). The dispersal of planet-forming discs: theory confronts observations. *Royal Society Open Science*, 4(4):170114.

Feigelson, E. D. and Montmerle, T. (1999). High-Energy Processes in Young Stellar Objects. *ARA&A*, 37:363–408.

Ferguson, J. W., Alexander, D. R., Allard, F., Barman, T., Bodnarik, J. G., Hauschildt, P. H., Heffner-Wong, A., and Tamanai, A. (2005). Low-Temperature Opacities. *ApJ*, 623(1):585–596.

Ferreira, J., Dougados, C., and Cabrit, S. (2006). Which jet launching mechanism(s) in T Tauri stars? *A&A*, 453(3):785–796.

Fukagawa, M., Tamura, M., Itoh, Y., Oasa, Y., Kudo, T., Hayashi, S. S., Kato, E., Ootsubo, T., Itoh, Y., Shibai, H., and Hayashi, M. (2010). Subaru Near-Infrared Imaging of Herbig

Ae Stars. *PASJ*, 62:347.

Gammie, C. F. (1996). Layered Accretion in T Tauri Disks. *ApJ*, 457:355.

Gehrig, L., Steiner, D., Vorobyov, E. I., and Güdel, M. (2022). Time-dependent, long-term hydrodynamic simulations of the inner protoplanetary disk. II. The importance of stellar rotation. *A&A*, 667:A46.

Gehrig, L. and Vorobyov, E. I. (2023). What governs the spin distribution of very young ¡ 1 Myr low-mass stars. *A&A*, 673:A54.

Goldreich, P. and Kylafis, N. D. (1981). On mapping the magnetic field direction in molecular clouds by polarization measurements. *ApJ*, 243:L75–L78.

Greene, T. P., Wilking, B. A., Andre, P., Young, E. T., and Lada, C. J. (1994). Further Mid-Infrared Study of the rho Ophiuchi Cloud Young Stellar Population: Luminosities and Masses of Pre–Main-Sequence Stars. *ApJ*, 434:614.

Gregory, S. G., Matt, S. P., Donati, J. F., and Jardine, M. (2008). The non-dipolar magnetic fields of accreting T Tauri stars. *MNRAS*, 389(4):1839–1850.

Gressel, O., Turner, N. J., Nelson, R. P., and McNally, C. P. (2015). Global Simulations of Protoplanetary Disks With Ohmic Resistivity and Ambipolar Diffusion. *ApJ*, 801(2):84.

Guilet, J. and Ogilvie, G. I. (2012). Transport of magnetic flux and the vertical structure of accretion discs: I. Uniform diffusion coefficients. *Mon. Not. R. Astron. Soc. Vol. 424, Issue 3, pp. 2097-2117.*, 424:2097–2117.

Guilet, J. and Ogilvie, G. I. (2014). Global evolution of the magnetic field in a thin disc and its consequences for protoplanetary systems. *Mon. Not. R. Astron. Soc. Vol. 441, Issue 1, p.852-868*, 441:852–868.

Harrison, R. E., Looney, L. W., Stephens, I. W., Li, Z.-Y., Teague, R., Crutcher, R. M., Yang, H., Cox, E. G., Fernández-López, M., and Shinnaga, H. (2021). ALMA CN Zeeman Observations of AS 209: Limits on Magnetic Field Strength and Magnetically Driven Accretion Rate. *ApJ*, 908(2):141.

Harrison, R. E., Looney, L. W., Stephens, I. W., Li, Z.-Y., Yang, H., Kataoka, A., Harris, R. J., Kwon, W., Muto, T., and Momose, M. (2019). Dust Polarization in Four Protoplanetary Disks at 3 mm: Further Evidence of Multiple Origins. *ApJ*, 877(1):L2.

Hartmann, L., Herczeg, G., and Calvet, N. (2016). Accretion onto pre-main-sequence stars. *Annual Review of Astronomy and Astrophysics*, 54(1):135–180.

Hendler, N., Pascucci, I., Pinilla, P., Tazzari, M., Carpenter, J., Malhotra, R., and Testi, L. (2020). The Evolution of Dust Disk Sizes from a Homogeneous Analysis of 1-10 Myr old Stars. *ApJ*, 895(2):126.

Herbig, G. H. (1977). Eruptive phenomena in early stellar evolution. *ApJ*, 217:693–715.

Herbst, W., Herbst, D. K., Grossman, E. J., and Weinstein, D. (1994). Catalogue of UBVRI Photometry of T Tauri Stars and Analysis of the Causes of Their Variability. *AJ*, 108:1906.

Jackson, J. D. (1999). *Classical electrodynamics*. Wiley, New York, NY, 3rd ed. edition.

Jankovic, M. R., Owen, J. E., Mohanty, S., and Tan, J. C. (2021). MRI-active inner regions of protoplanetary discs. I. A detailed model of disc structure. *MNRAS*, 504(1):280–299.

Johnstone, C. P., Jardine, M., Gregory, S. G., Donati, J. F., and Hussain, G. (2014). Classical T Tauri stars: magnetic fields, coronae and star-disc interactions. *MNRAS*, 437(4):3202–3220.

Kadam, K., Vorobyov, E., Regály, Z., Kóspál, Á., and Ábrahám, P. (2020). Outbursts in Global Protoplanetary Disk Simulations. *ApJ*, 895(1):41.

Kataoka, A., Muto, T., Momose, M., Tsukagoshi, T., Fukagawa, M., Shibai, H., Hanawa, T., Murakawa, K., and Dullemond, C. P. (2015). Millimeter-wave Polarization of Protoplanetary Disks due to Dust Scattering. *ApJ*, 809(1):78.

Kataoka, A., Okuzumi, S., and Tazaki, R. (2019). Millimeter-wave Polarization Due to Grain Alignment by the Gas Flow in Protoplanetary Disks. *ApJ*, 874(1):L6.

Khaibrakhmanov, S. A. (2024). Magnetic fields of protoplanetary disks. *Astronomical and Astrophysical Transactions*, 34(2):139–162.

Klein, B., Donati, J.-F., Hébrard, É. M., Zaire, B., Folsom, C. P., Morin, J., Delfosse, X., and Bonfils, X. (2021). The large-scale magnetic field of Proxima Centauri near activity maximum. *MNRAS*, 500(2):1844–1850.

Konigl, A. and Pudritz, R. E. (2000). Disk Winds and the Accretion-Outflow Connection. In Mannings, V., Boss, A. P., and Russell, S. S., editors, *Protostars and Planets IV*, page 759.

Kóspál, Á., Ábrahám, P., Acosta-Pulido, J. A., Dunham, M. M., García-Álvarez, D., Hogerheijde, M. R., Kun, M., Moór, A., Farkas, A., Hajdu, G., Hodosán, G., Kovács, T., Kriskovics, L., Marton, G., Molnár, L., Pál, A., Sárneczky, K., Sódor, Á., Szakáts, R., Szalai, T., Szegedi-Elek, E., Szing, A., Tóth, I., Vida, K., and Vinkó, J. (2016). Multiwavelength study of the low-luminosity outbursting young star HBC 722. *A&A*, 596:A52.

Kounkel, M., Hartmann, L., Loinard, L., Ortiz-León, G. N., Mioduszewski, A. J., Rodríguez, L. F., Dzib, S. A., Torres, R. M., Pech, G., Galli, P. A. B., Rivera, J. L., Boden, A. F., Evans, Neal J., I., Briceño, C., and Tobin, J. J. (2017). The Gould's Belt Distances Survey (GOBELINS) II. Distances and Structure toward the Orion Molecular Clouds. *ApJ*, 834(2):142.

Kurosawa, R. and Romanova, M. (2013). Possible Observable Signatures of Classical T Tauri Stars Accreting in an Unstable Regime. In *Protostars and Planets VI Posters*.

Lada, C. J. and Wilking, B. A. (1984). The nature of the embedded population in the rho Ophiuchi dark cloud : mid-infrared observations. *ApJ*, 287:610–621.

Ladd, E. F., Adams, F. C., Casey, S., Davidson, J. A., Fuller, G. A., Harper, D. A., Myers, P. C., and Padman, R. (1991). Far-Infrared and Submillimeter Wavelength Observations of Star-forming Dense Cores. II. Images. *ApJ*, 382:555.

Lankhaar, B. and Teague, R. (2023). Three-dimensional magnetic field imaging of protoplanetary disks using Zeeman broadening and linear polarization observations. *A&A*, 678:A17.

Lazarian, A. and Hoang, T. (2007). Radiative torques: analytical model and basic properties. *MNRAS*, 378(3):910–946.

Lesur, G., Ercolano, B., Flock, M., Lin, M. K., Yang, C. C., Barranco, J. A., Benitez-Llambay, P., Goodman, J., Johansen, A., Klahr, H., Laibe, G., Lyra, W., Marcus, P., Nelson, R. P., Squire, J., Simon, J. B., Turner, N., Umurhan, O. M., and Youdin, A. N. (2022). Hydro-, magnetohydro-, and dust-gas dynamics of protoplanetary disks.

Lesur, G. R. J. (2021). Systematic description of wind-driven protoplanetary discs. *A&A*, 650:A35.

Leung, P. K. C. and Ogilvie, G. I. (2019). Local semi-analytic models of magnetic flux transport in protoplanetary discs. *MNRAS*, 487(4):5155–5174.

LeVeque, R. J., Mihalas, D., Dorfi, E. A., and Müller, E. (1997). *Astrophysics of Planet Formation*. Saas-Fee Advanced Course 27. Lecture Notes 1997 Swiss Society for Astrophysics and Astronomy.

Lin, D. N. C. and Pringle, J. E. (1987). A viscosity prescription for a self-gravitating accretion disc. *MNRAS*, 225:607–613.

Lubow, S. H., Papaloizou, J. C. B., and Pringle, J. E. (1994). On the stability of magnetic wind-driven accretion discs. *Mon. Not. R. Astron. Soc.*, 268(4):1010–1014.

Lubow, S. H., Papaloizou, J. C. B., and Pringle, J. E. (1994). On the Stability of Magnetic Wind-Driven Accretion Discs. *MNRAS*, 268:1010.

Masson, J., Chabrier, G., Hennebelle, P., Vaytet, N., and Commerçon, B. (2016). Ambipolar diffusion in low-mass star formation. I. General comparison with the ideal magnetohydrodynamic case. *A&A*, 587:A32.

Mauxion, J., Lesur, G., and Maret, S. (2024). Modeling the secular evolution of embedded protoplanetary disks. *A&A*, 686:A253.

Mazzei, R., Cleeves, L. I., and Li, Z.-Y. (2020). Untangling Magnetic Complexity in Protoplanetary Disks with the Zeeman Effect. *ApJ*, 903(1):20.

Mestel, L. (1965). Problems of Star Formation - I. *qjras*, 6:161.

Mihalas, D. and Mihalas, B. (1984). *Foundations of radiation hydrodynamics*.

Mihalas, D. and Winkler, K.-H. A. (1986). *Radiation Hydrodynamics in Stars and Compact Objects*, volume 255.

Mohanty, S., Jankovic, M. R., Tan, J. C., and Owen, J. E. (2018). Inside-out Planet Formation.

V. Structure of the Inner Disk as Implied by the MRI. *ApJ*, 861(2):144.

Moss, D. and Shukurov, A. (2004). Accretion disc dynamos opened up by external magnetic fields. *A&A*, 413:403–414.

Myers, P. C. and Ladd, E. F. (1993). Bolometric Temperatures of Young Stellar Objects. *ApJ*, 413:L47.

Ogilvie, G. I. (1997). The equilibrium of a differentially rotating disc containing a poloidal magnetic field. *Mon. Not. R. Astron. Soc.*, 288(1):63–77.

Ogilvie, G. I. and Livio, M. (2001). Launching of Jets and the Vertical Structure of Accretion Disks. *ApJ*, 553(1):158–173.

Owen, J. E. (2016). The Origin and Evolution of Transition Discs: Successes, Problems, and Open Questions. *PASA*, 33:e005.

Piessens, R., de Doncker-Kapenga, E., and Ueberhuber, C. W. (1983). *Quadpack. A subroutine package for automatic integration*.

Pudritz, R. E. (1981). Dynamo Action in Turbulent Accretion Discs around Black Holes - Part Two - the Mean Magnetic Field. *MNRAS*, 195:897.

Rab, C., Baldovin-Saavedra, C., Dionatos, O., Vorobyov, E., and Güdel, M. (2016). The Gas Disk: Evolution and Chemistry. *Space Sci. Rev.*, 205(1-4):3–40.

Ragossnig, F., Dorfi, E. A., Ratschiner, B., Gehrig, L., Steiner, D., Stökl, A., and Johnstone, C. P. (2020). 1+1D implicit disk computations. *Computer Physics Communications*, 256:107437.

Romanova, M. and Kurosawa, R. (2014). *Simulations of Accretion onto Magnetized Stars: Results of 3D MHD Simulations and 3D Radiative Transfer*, volume 488 of *Astronomical Society of the Pacific Conference Series*, page 127.

Romanova, M. M., Blinova, A. A., Ustyugova, G. V., Koldoba, A. V., and Lovelace, R. V. E. (2018). Properties of strong and weak propellers from MHD simulations. *New A*, 62:94–114.

Romanova, M. M., Ustyugova, G. V., Koldoba, A. V., and Lovelace, R. V. E. (2011). MRI-driven accretion on to magnetized stars: axisymmetric MHD simulations. *MNRAS*, 416(1):416–438.

Sarafidou, E., Gressel, O., and Ercolano, B. (2025). Global Hall-magnetohydrodynamic simulations of transition disks. *A&A*, 696:A19.

Schib, O., Mordasini, C., Wenger, N., Marleau, G. D., and Helled, R. (2021). The influence of infall on the properties of protoplanetary discs. Statistics of masses, sizes, lifetimes, and fragmentation. *A&A*, 645:A43.

Segura-Cox, D. M., Looney, L. W., Stephens, I. W., Fernández-López, M., Kwon, W., Tobin, J. J., Li, Z.-Y., and Crutcher, R. (2015). The Magnetic Field in the Class 0 Protostellar Disk of L1527. *ApJ*, 798(1):L2.

Shakura, N. I. and Sunyaev, R. A. (1973). Black holes in binary systems. Observational appearance. *A&A*, 24:337–355.

Simon, J. B., Bai, X.-N., Armitage, P. J., Stone, J. M., and Beckwith, K. (2013). Turbulence in the Outer Regions of Protoplanetary Disks. II. Strong Accretion Driven by a Vertical Magnetic Field. *ApJ*, 775(1):73.

Spitzer, L. (1978). *Physical processes in the interstellar medium.*

Spruit, H. C. (1996). Magnetohydrodynamic winds and jets from accretion disks.

Stasevic, S., Milli, J., Mazoyer, J., Lagrange, A. M., Bonnefoy, M., Faramaz-Gorka, V., Ménard, F., Boccaletti, A., Choquet, E., Shuai, L., Olofsson, J., Chomez, A., Ren, B., Rubini, P., Desgrange, C., Gratton, R., Chauvin, G., Vigan, A., and Matthews, E. (2023). An inner warp discovered in the disk around HD 110058 using VLT/SPHERE and HST/STIS. *A&A*, 678:A8.

Steiner, D., Gehrig, L., Ratschiner, B., Ragossnig, F., Vorobyov, E. I., Güdel, M., and Dorfi, E. A. (2021). Time-dependent, long-term hydrodynamic simulations of the inner protoplanetary disk - i. the importance of stellar magnetic torques. *A&A*, 655:A110.

Stephens, I. W., Looney, L. W., Kwon, W., Fernández-López, M., Hughes, A. M., Mundy, L. G., Crutcher, R. M., Li, Z.-Y., and Rao, R. (2014). Spatially resolved magnetic field structure in the disk of a T Tauri star. *Nature*, 514(7524):597–599.

Stepinski, T. F. and Levy, E. H. (1991). Dynamo Magnetic Field Modes in Thin Astrophysical Disks: an Adiabatic Computational Approximation. *ApJ*, 379:343.

Suzuki, T. K., Ogihara, M., Morbidelli, A., Crida, A., and Guillot, T. (2016). Evolution of protoplanetary discs with magnetically driven disc winds. *A&A*, 596:A74.

Tazzari, M., Testi, L., Natta, A., Ansdell, M., Carpenter, J., Guidi, G., Hogerheijde, M., Manara, C. F., Miotello, A., van der Marel, N., van Dishoeck, E. F., and Williams, J. P. (2017). Physical properties of dusty protoplanetary disks in Lupus: evidence for viscous evolution? *A&A*, 606:A88.

Terebey, S., Shu, F. H., and Cassen, P. (1984). The collapse of the cores of slowly rotating isothermal clouds. *ApJ*, 286:529–551.

Toomre, A. (1964). On the gravitational stability of a disk of stars. *ApJ*, 139:1217–1238.

Torres, R. M., Loinard, L., Mioduszewski, A. J., Boden, A. F., Franco-Hernández, R., Vlemmings, W. H. T., and Rodríguez, L. F. (2012). VLBA Determination of the Distance to nearby Star-forming Regions. V. Dynamical Mass, Distance, and Radio Structure of V773 Tau A. *ApJ*, 747(1):18.

Tripathi, A., Andrews, S. M., Birnstiel, T., and Wilner, D. J. (2017). A millimeter Continuum Size-Luminosity Relationship for Protoplanetary Disks. *ApJ*, 845(1):44.

Umebayashi, T. and Nakano, T. (1981). Fluxes of Energetic Particles and the Ionization Rate in Protostars and the Primitive Solar Nebula. In Hasegawa, H., Oya, H., and Shimizu, M., editors, *14th ISAS Lunar and Planetary Symposium*, page 293.

van Leer, B. (1974). Towards the Ultimate Conservation Difference Scheme. II. Monotonicity and Conservation Combined in a Second-Order Scheme. *Journal of Computational Physics*, 14:361–370.

Vlemmings, W. H. T., Lankhaar, B., Cazzoletti, P., Ceccobello, C., Dall'Olio, D., van Dishoeck, E. F., Facchini, S., Humphreys, E. M. L., Persson, M. V., Testi, L., and Williams, J. P. (2019). Stringent limits on the magnetic field strength in the disc of TW Hya. ALMA observations of CN polarisation. *A&A*, 624:L7.

Vorobyov, E. I. (2010). Embedded Protostellar Disks Around (Sub-)Solar Protostars. I. Disk Structure and Evolution. *ApJ*, 723(2):1294–1307.

Vorobyov, E. I. and Basu, S. (2007). Self-regulated gravitational accretion in protostellar discs. *Monthly Notices of the Royal Astronomical Society*, 381(3):1009–1017.

Vorobyov, E. I., Khaibrakhmanov, S., Basu, S., and Audard, M. (2020). Accretion bursts in magnetized gas-dust protoplanetary disks. *A&A*, 644:A74.

Vorobyov, E. I. and Pavlyuchenkov, Y. N. (2017). Improving the thin-disk models of circumstellar disk evolution. The 2+1-dimensional model. *AAP*, 606:A5.

Vorobyov, E. I., Skliarevskii, A. M., Elbakyan, V. G., Pavlyuchenkov, Y., Akimkin, V., and Guedel, M. (2019). Gravitoviscous protoplanetary disks with a dust component. I. The importance of the inner sub-au region. *A&A*, 627:A154.

Wardle, M. (2007). Magnetic fields in protoplanetary disks. *Ap&SS*, 311(1-3):35–45.

Williams, J. P. and Cieza, L. A. (2011). Protoplanetary Disks and Their Evolution. *ARA&A*, 49(1):67–117.

Williams, J. P. and McPartland, C. (2016). Measuring Protoplanetary Disk Gas Surface Density Profiles with ALMA. *ApJ*, 830(1):32.

Xu, W. and Kunz, M. W. (2021). Formation and evolution of protostellar accretion discs - II. From 3D simulation to a simple semi-analytic model of Class 0/I discs. *MNRAS*, 508(2):2142–2168.

Zaire, B., Donati, J. F., Alencar, S. P., Bouvier, J., Moutou, C., Bellotti, S., Carmona, A., Petit, P., Kóspál, Á., Shang, H., Grankin, K., Manara, C., Alecian, E., Gregory, S. P., Fouqué, P., and the SLS consortium (2024). Magnetic field, magnetospheric accretion, and candidate planet of the young star GM Aurigae observed with SPIRou. *MNRAS*, 533(3):2893–2915.

Zhang, K., Bergin, E. A., Schwarz, K., Krijt, S., and Ciesla, F. (2019). Systematic Variations of CO Gas Abundance with Radius in Gas-rich Protoplanetary Disks. *ApJ*, 883(1):98.

Zhu, Z., Espaillat, C., Hinkle, K., Hernandez, J., Hartmann, L., and Calvet, N. (2009). The Differential Rotation of FU Ori. *ApJ*, 694:L64–L68.

Zhu, Z., Hartmann, L., Gammie, C. F., Book, L. G., Simon, J. B., and Engelhard, E. (2010).

Long-term Evolution of Protostellar and Protoplanetary Disks. I. Outbursts. *ApJ*, 713:1134–1142.

Zhu, Z., Stone, J. M., and Calvet, N. (2024). A global 3D simulation of magnetospheric accretion - I. Magnetically disrupted discs and surface accretion. *MNRAS*, 528(2):2883–2911.

Zusammenfassung

Die Erforschung von protoplanetaren Scheiben, welche einen jungen Stern umgeben, kann uns helfen die Entstehung unseres eigenen Sonnensystems zu verstehen. Junge Sterne haben sehr starke Magnetfelder, welche mit der sie umgebenden Scheibe interagieren, und so das Akkretionsverhalten dieser Scheiben beeinflussen. Im ersten Teil dieser Dissertation haben wir deshalb das Langzeitverhalten von Scheiben studiert, für den Fall dass ein stellares Magnetfeld mit der Scheibe interagiert. Zu diesem Zweck verwenden wir TAPIR (The Adaptive Implicit RHD Code), einen 1+1D Hydrodynamik-Code mit einem impliziten Zeitintegrationsschema, um auch die innerste Scheibenregion über ihre gesamte Lebensdauer zu simulieren. Die gesamte Scheibe wird selbstkonsistent simuliert, wobei auch der innere Rand der Scheibe dynamisch berechnet wird als der Radius, an welchem das stellare Feld ausreicht um die Scheibe in sogenannte magnetische Trichter aufzubrechen. Langzeitberechnungen haben gezeigt, dass die innerste Scheibe selbstkonsistent mitgerechnet werden sollte, da ansonsten das Drehmoment des stellaren Dipols sowie starke Druckgradienten nicht mitberücksichtigt werden können. Zusätzlich wurde gezeigt, dass die Magnetfeldstärke des stellaren Dipols starken Einfluss darauf nimmt, ob die Scheibe episodisch akkretiert, und falls ja, die Magnetfeldstärke die Frequenz und Häufigkeit dieser Ereignisse beeinflusst.

Neben stellaren Magnetfeldern haben auch großskalige Magnetfelder in der Scheibe Einfluss auf die zeitliche Entwicklung von protoplanetaren Scheiben. Die Topologie solcher Felder ist entscheidend dafür, ob und mit welcher Stärke magneto-zentrifugal und/oder magneto-thermisch beschleunigte Winde auftreten. Um die poloidale Struktur dieser großskaligen Magnetfelder zu untersuchen, haben wir TAPIR um eine Beschreibung dieser großskaligen Magnetfelder und um ein Modell zur Beschreibung von nicht-idealen MHD-Effekten erweitert. Die Simulationen haben gezeigt, dass das stellare Magnetfeld die Evolution und Topologie in der inneren Scheibe dominiert, und das das großskalige Magnetfeld die Topologie in der äußeren Scheibe bestimmt. Außerdem hat eine Parameterstudie die Erkenntnis gezeigt, dass stellare Parameter wie Rotationsperiode, stellare Magnetfeldstärke und Stärke der stellaren Röntgenstrahlung, die Topologie des großskaligen Magnetfelds überall in der Scheibe überall beeinflussen kann.

Zukünftig werden wir ein Windmodell zu TAPIR hinzufügen und das gekoppelte System von Stern, Scheibe und Winden simulieren über die gesamte Lebensdauer einer Scheibe. Dies wird uns einerseits ermöglichen, die Stern-Scheiben-Kopplung noch besser zu modellieren und andererseits erlauben, das erste Mal den Einfluss von verschiedenen Magnetfeldparametern auf die Lebensdauer einer Scheibe zu studieren.

Part V

Appendices

Acknowledgements / Danksagung

It's finally done. Writing this thesis felt a lot like driving down a very bumpy road, with the occasional landslide thrown in. That's why having people around who can support you, guide you, and help you find your way again when you're lost, is so important.

This project has been a part of my life for over a decade, and throughout that time, it has shaped me more than anything else. I started my studies as a somewhat overconfident student, and now, looking back, I realize how humbling the journey has been. It taught me that working together with smart, passionate, and brilliant people in the scientific community is the best way to bring out the best in all of us (and certainly in me). So, my heartfelt thanks go to everyone I've had the pleasure of meeting and working with during these years. You made this journey possible.

Now, I want to take a moment to thank a few people who were truly instrumental in shaping this work. My interest in theoretical astrophysics first sparked way back when I took those undergraduate courses taught by Ernst Dorfi. I was genuinely thrilled when he welcomed me into his group; first as a Master's student, and later for my Ph.D. Ernst was one of those bright minds I mentioned earlier, and over the years, he also became a dear friend.

My Ph.D. topic was quite a challenge, but Ernst always had another idea, another angle to try, whenever I ran into a problem. His creativity and optimism kept me going more times than I can count. That's why it was such a heavy blow when Ernst passed away a few years ago - I lost not just a mentor, but a friend. I can't thank him in person anymore, but I want you, dear reader, to know this: it was Ernst who gave me the initial push, the belief, and the guidance that made this Ph.D. project possible in the first place.

I'd also like to say a big thank you to Manuel Güdel, who kindly took on the role of my supervisor after Ernst's untimely death. By then, I was already working full-time outside of academia, and organizing regular meetings had become much more difficult. Therefore, I'm especially thankful to Manuel for his flexibility and patience. He met with me regularly after work to go through my progress and the problems that came up along the way. He also took the time and effort to really dig into my Ph.D. topic, which I deeply respect and do not take for granted.

During most of my time as a Ph.D. student, I had the pleasure of working closely with the other members of Ernst's group. We were a bunch of funny, interesting, and wildly different people sharing the same passion for astrophysics. I can't even begin to count the hours spent discussing some weird astrophysical problem with Florian, only to realize in the end that we didn't even disagree: we just had two different perspectives. These discussions were very valuable to me, because they pushed me to rethink problems and improve my own arguments. So thank you, Flo, for regularly approaching science from different angles. Thank you, Bernhard, for being your wonderfully original self, and for all the scientific chats, whether over coffee or a beer. And to Ines, Michael, Arijane, and Thomas: thank you. Without you, this group wouldn't have been what it was: a place to work, learn, and have fun.

The last unmentioned member of this group, Lukas, deserves a few lines of his own. In the later years of my Ph.D., Lukas started his own doctorate, and we ended up working closely together on many research projects. Alongside Manuel, he became a key person I could turn to for discussing all kinds of scientific and numerical challenges. Collaborating with Lukas, and having him as a kind of sparring partner, played a big role in helping me finally bring this thesis to completion.

Because of how long it took me to finish this project, my wife Anna has never known me *not* being a Ph.D. student. That also means she's been there for all the struggles and frustrations that came with it. She's had to deal with my mood swings and moments of doubt - and what can I say? She still sticks with me. Especially during the final, stressful period of finishing this thesis, she shielded me from every distraction she could, which is no easy task. For all that, for her patience, and for always knowing whether to comfort me or to kick my ass, I can simply say: I love you. Without you, I wouldn't be writing these last lines.

Last, but definitely not least, I want to thank my family. Thank you to my mother, who always encouraged me to follow my dreams and do whatever made me happy. She welcomed me home when I needed it, and she has always been there to listen to all my thoughts - and still is. I also want to thank my sister. She's not a scientist and doesn't share my fascination for physics or astronomy, but she was there when I needed help, and that's what matters most. Family is important: without that home base, I couldn't have pulled this off.

Finally, after more than a decade working on this project, let me end with one thing that hasn't changed: I'm still not fed up with astrophysics, and I'll keep doing research for sure! And the reason this passion is still alive is because of each and every one of you. Thanks to all of you for helping me reach the end of this long and winding road.

Reprint permissions

Astronomy and Astrophysics
Editor in Chief: T. Forveille

merging
Annales d'Astrophysique
Arkiv for Astronomi
Bulletin of the Astronomical Institutes of the Netherlands
Bulletin Astronomique
Journal des Observateurs
Zeitschrift fur Astrophysik
Bulletin of the Astronomical Institutes of Czechoslovakia

T. Forveille
Astronomy & Astrophysics
Observatoire de Paris
61, avenue de l'Observatoire
75014 Paris, France

Tel.: 33 0(1) 43 29 05 41
Fax: 33 0(1) 43 29 05 57
e-mail: aanda.paris@obspm.fr
Web: http://www.aanda.org

Paris, 19 Sept. 2025

Reprint Permission

Material:
Article by Steiner et al. 2021, A&A, 655, A110
Fig. 1 in Masson et al. 2016, A&A, 582, A32

To be used in:
PhD thesis entitled "Large-scale magnetic fields in protoplanetary disks", University of Vienna

Permission granted to:
Daniel Steiner
daniel.steiner@univie.ac.at

I hold copyright on the material referred to above, and hereby grant permission for its use as requested herewith.

The article should be reproduced as a whole in a coherent fashion fully consistent with the version published in A&A.

Credit should be given as follows:
Credit: Author, A&A, vol, page, year, reproduced with permission © ESO.

Thierry Forveille
A&A Editor-in-Chief

Sponsored by Argentina, Armenia, Austria, Belgium, Bulgaria, Chile, Croatia, Czech Republic, Denmark, Estonia, Finland, France, Germany, Greece, Hungary, Italy, Lithuania, Netherlands, Norway, Poland, Portugal, Slovak Republic, Spain, Sweden, and Switzerland.
Produced and distributed by EDP Sciences for ESO.

PARTIES:

1. **Cambridge University Press** (Licensor); and
2. **Daniel Steiner** (Licensee).

Thank you for your recent permission request. Some permission requests for use of material published by the Licensor, such as this one, are now being facilitated by PLSclear.

Set out in this licence cover sheet (the **Licence Cover Sheet**) are the principal terms under which Licensor has agreed to license certain Licensed Material (as defined below) to Licensee. The terms in this Licence Cover Sheet are subject to the attached General Terms and Conditions, which together with this Licence Cover Sheet constitute the licence agreement (the **Licence**) between Licensor and Licensee as regards the Licensed Material. The terms set out in this Licence Cover Sheet take precedence over any conflicting provision in the General Terms and Conditions.

Free Of Charge Licence Terms

Licence Date:	17/09/2025
PLSclear Ref No:	109687

The Licensor

Company name:	Cambridge University Press
Address:	University Printing House Shaftesbury Road Cambridge CB2 8BS GB

The Licensee

Licensee Contact Name:	Daniel Steiner
Licensee Address:	Hafinger Weg 33/5 Sankt Pölten 3100 Austria

Licensed Material

title:	Astrophysics of Planet Formation
ISBN:	10.1017/9781108344227
publisher:	Cambridge University Press
Issue Date	16.09.2025

Are you requesting permission to reuse the cover of the publication?	No
Article Title	Astrophysics of Planet Formation
Article URL	https://doi.org/10.1017/9781108344227
Figure number & title	Figure 2.3 Geometry for calculation of the radial temperature profile of a razor- thin protoplanetary disk
Page numbers	62
Are you the author of the content that you are requesting to reuse?	No
Is the content you are requesting available through an Open Access Licence?	No
Additional Information	I intend to use the Figure in my PhD thesis. I want to briefly explain heating and cooling processes in protoplanetary disks, and this figure helps to explain radiative heating. I also got permission from the author Phil Armitage to use the figure.
Will you be changing or editing the image?	No

For Use In Licensee's Publication(s)

usage type	Book, Journal, Magazine or Academic Paper-Thesis or Dissertation
Will your dissertation be placed in an online repository?	Yes
Author	Daniel Steiner
Estimated publication date	18.12.2025
Language	English
Title of dissertation/thesis	Large-scale magnetic fields in protoplanetary disks
University or institution	University of Viena
Unlimited circulation?	No

Rights Granted

Exclusivity:	Non-Exclusive
Format:	Thesis or Dissertation
Language:	English
Territory:	World
Duration:	Lifetime of Licensee's Edition
Maximum Circulation:	5

GENERAL TERMS AND CONDITIONS

1. <u>Definitions and Interpretation</u>

1.1 Capitalised words and expressions in these General Terms and Conditions have the meanings given to them in the Licence Cover Sheet.

1.2 In this Licence any references (express or implied) to statutes or provisions are references to those statutes or provisions as amended or re-enacted from time to time. The term including will be construed as illustrative, without limiting the sense or scope of the words preceding it. A reference to in writing or written includes faxes and email. The singular includes the plural and vice versa.

2. <u>Grant of Rights</u>

2.1 The Licensor grants to Licensee the non-exclusive right to use the Licensed Material as specified in the Licence Cover Sheet.

2.2 The rights licensed to Licensee under this Licence do not include the right to use any third party copyright material incorporated in the Licensed Material. Licensee should check the Licensed Material carefully and seek permission for the use of any such third party copyright material from the relevant copyright owner(s).

2.3 Unless otherwise stated in the Licence Cover Sheet, the Licensed Material may be:

2.3.1 subjected to minor editing, including for the purposes of creating alternative formats to provide access for a beneficiary person (provided that any such editing does not amount to derogatory treatment); and/or

2.3.2 used for incidental promotional use (such as online retail providers' search facilities).

2.4 Save as expressly permitted in this Licence or as otherwise permitted by law, no use or modification of the Licensed Material may be made by Licensee without Licensor's prior written permission.

3. <u>Copyright Notice and Acknowledgement</u>

3.1 Licensee must ensure that the following notices and acknowledgements are reproduced prominently alongside each reproduction by Licensee of the Licensed Material:

3.1.1 the title and author of the Licensed Material;

3.1.2 the copyright notice included in the Licensed Material; and

3.1.3 the statement "Reproduced with permission of The Licensor through PLSclear."

4. <u>Reversion of Rights</u>

4.1 The rights licensed to Licensee under this Licence will terminate immediately and automatically upon the earliest of the following events to occur:

4.1.1 the Licensed Material not being used by Licensee within 18 months of the Licence Date;

4.1.2 expiry of the Licence Duration; or

4.1.3 the Maximum Circulation being reached.

5. Miscellaneous

5.1 By using the Licensed Material, Licensee will be deemed to have accepted all the terms and conditions contained in this Licence.

5.2 This Licence contains the entire understanding and agreement of the parties relating to its subject matter and supersedes in all respects any previous or other existing arrangements, agreements or understandings between the parties whether oral or written in relation to its subject matter.

5.3 Licensee may not assign this Licence or any of its rights or obligations hereunder to any third party without Licensor's prior written consent.

5.4 This Licence is governed by and shall be construed in accordance with the laws of England and Wales and the parties hereby irrevocably submit to the non-exclusive jurisdiction of the Courts of England and Wales as regards any claim, dispute or matter arising under or in relation to this Licence.

Marketplace

Order Date	16-Sep-2025	**Type of Use**	Republish in a thesis/dissertation
Order License ID	1651905-1	**Publisher**	ANNUAL REVIEWS
ISSN	1545-4282	**Portion**	Chart/graph/table/figure

LICENSED CONTENT

Publication Title	Annual review of astronomy and astrophysics	**Publication Type**	e-Journal
		Start Page	483
Article Title	Observations of Protoplanetary Disk Structures	**End Page**	528
		Issue	1
		Volume	58
Date	01/01/1963	**URL**	http://books.google.com/books?id=7HuuAAAAIAAJ
Language	English		
Country	United States of America		
Rightsholder	Annual Reviews, Inc.		

REQUEST DETAILS

Portion Type	Chart/graph/table/figure	**Distribution**	Worldwide
Number of Charts / Graphs / Tables / Figures Requested	2	**Translation**	Original language of publication
		Copies for the Disabled?	No
Format (select all that apply)	Print, Electronic	**Minor Editing Privileges?**	No
		Incidental Promotional Use?	No
Who Will Republish the Content?	Academic institution	**Currency**	EUR
Duration of Use	Life of current edition		
Lifetime Unit Quantity	Up to 499		
Rights Requested	Main product		

NEW WORK DETAILS

Title	Large-scale magnetic fields in protoplanetary disks	**Institution Name**	University of Vienna
		Expected Presentation Date	2025-12-18
Instructor Name	Daniel Steiner		

ADDITIONAL DETAILS

Order Reference Number	N/A	**The Requesting Person / Organization to Appear on the License**	Daniel Steiner

REQUESTED CONTENT DETAILS

Title, Description or Numeric Reference of the Portion(s)	Figure 2, Figure 4	**Title of the Article / Chapter the Portion Is From**	Observations of Protoplanetary Disk Structures
Editor of Portion(s)	Andrews, Sean M.	**Author of Portion(s)**	Andrews, Sean M.
Volume / Edition	58	**Issue, if Republishing an Article From a Serial**	1
Page or Page Range of Portion	483-528	**Publication Date of Portion**	2020-08-18

RIGHTSHOLDER TERMS AND CONDITIONS

If any part of the material to be used (for example, figures and tables) has appeared in our publication with credit or acknowledgement to another source, permission must also be sought from that source. If such permission is not obtained then that material may not be included in your publication/copies. Suitable acknowledgement to the source must be made, either as a footnote or in a reference list at the end of your publication.
Annual Reviews publishes Open Access Articles in both its Open Access journals and within its subscription titles, which may allow for certain types of reuse without permission. Before proceeding, please refer to the article's copyright line to determine whether the content you wish to use is Open Access. For Open Access content, please refer to the license terms for the work which you wish to reuse. Any reuse not included in the license terms will require permission. In all instances, full and appropriate attribution to the original source must be given. Further, permission does not cover any third party copyrighted material which may appear in the Annual Reviews work requested, and additional permission from the rights holder of such material may be required. If any part of the material to be used (for example, figures and tables) has appeared in our publication with credit or acknowledgement to another source, permission must also be sought from that source. If such permission is not obtained then that material may not be included in your publication/copies. Suitable acknowledgement to the source must be made, either as a footnote or in a reference list at the end of your publication. Please contact Annual Reviews with any questions.

Marketplace Permissions General Terms and Conditions

The following terms and conditions ("General Terms"), together with any applicable Publisher Terms and Conditions, govern User's use of Works pursuant to the Licenses granted by Copyright Clearance Center, Inc. ("CCC") on behalf of the applicable Rightsholders of such Works through CCC's applicable Marketplace transactional licensing services (each, a "Service").

1) **Definitions.** For purposes of these General Terms, the following definitions apply:

"License" is the licensed use the User obtains via the Marketplace platform in a particular licensing transaction, as set forth in the Order Confirmation.

"Order Confirmation" is the confirmation CCC provides to the User at the conclusion of each Marketplace transaction. "Order Confirmation Terms" are additional terms set forth on specific Order Confirmations not set forth in the General Terms that can include terms applicable to a particular CCC transactional licensing service and/or any Rightsholder-specific terms.

"Rightsholder(s)" are the holders of copyright rights in the Works for which a User obtains licenses via the Marketplace platform, which are displayed on specific Order Confirmations.

"Terms" means the terms and conditions set forth in these General Terms and any additional Order Confirmation Terms collectively.

"User" or "you" is the person or entity making the use granted under the relevant License. Where the person accepting the Terms on behalf of a User is a freelancer or other third party who the User authorized to accept the General Terms on the User's behalf, such person shall be deemed jointly a User for purposes of such Terms.

"Work(s)" are the copyright protected works described in relevant Order Confirmations.

2) **Description of Service.** CCC's Marketplace enables Users to obtain Licenses to use one or more Works in accordance with all relevant Terms. CCC grants Licenses as an agent on behalf of the copyright rightsholder identified in the relevant Order Confirmation.

3) **Applicability of Terms.** The Terms govern User's use of Works in connection with the relevant License. In the event of any conflict between General Terms and Order Confirmation Terms, the latter shall govern. User acknowledges that Rightsholders have complete discretion whether to grant any permission, and whether to place any limitations on any grant, and that CCC has no right to supersede or to modify any such discretionary act by a Rightsholder.

4) **Representations; Acceptance.** By using the Service, User represents and warrants that User has been duly authorized by the User to accept, and hereby does accept, all Terms.

5) **Scope of License; Limitations and Obligations.** All Works and all rights therein, including copyright rights, remain the sole and exclusive property of the Rightsholder. The License provides only those rights expressly set forth in the terms and conveys no other rights in any Works

6) **General Payment Terms.** User may pay at time of checkout by credit card or choose to be invoiced. If the User chooses to be invoiced, the User shall: (i) remit payments in the manner identified on specific invoices, (ii) unless otherwise specifically stated in an Order Confirmation or separate written agreement, Users shall remit payments upon receipt of the relevant invoice from CCC, either by delivery or notification of availability of the invoice via the Marketplace platform, and (iii) if the User does not pay the invoice within 30 days of receipt, the User may incur a service charge of 1.5% per month or the maximum rate allowed by applicable law, whichever is less. While User may exercise the rights in the License immediately upon receiving the Order Confirmation, the License is automatically revoked and is null and void, as if it had never been issued, if CCC does not receive complete payment on a timely basis.

7) **General Limits on Use.** Unless otherwise provided in the Order Confirmation, any grant of rights to User (i) involves only the rights set forth in the Terms and does not include subsequent or additional uses, (ii) is non-exclusive and non-transferable, and (iii) is subject to any and all limitations and restrictions (such as, but not limited to, limitations on duration of use or circulation) included in the Terms. Upon completion of the licensed use as set forth in the Order Confirmation, User shall either secure a new permission for further use of the Work(s) or immediately cease any new use of the Work(s) and shall render inaccessible (such as by deleting or by removing or severing links or other locators) any further copies of the Work. User may only make alterations to the Work if and as expressly set forth in the Order Confirmation. No Work may be used in any way that is unlawful, including without limitation if such use would violate applicable sanctions laws or regulations, would be defamatory, violate the rights of third parties (including such third parties' rights of copyright, privacy, publicity, or other tangible or intangible property), or is otherwise illegal, sexually explicit, or obscene. In addition, User may not conjoin a Work with any other material that may result in damage to the reputation of the Rightsholder. Any unlawful use will render any licenses hereunder null and void. User agrees to inform CCC if it becomes aware of any infringement of any rights in a Work and to cooperate with any reasonable request of CCC or the Rightsholder in connection therewith.

8) **Third Party Materials.** In the event that the material for which a License is sought includes third party materials (such as photographs, illustrations, graphs, inserts and similar materials) that are identified in such material as having been used by permission (or a similar indicator), User is responsible for identifying, and seeking separate licenses (under this Service, if available, or otherwise) for any of such third party materials; without a separate license, User may not use such third party materials via the License.

9) **Copyright Notice.** Use of proper copyright notice for a Work is required as a condition of any License granted under the Service. Unless otherwise provided in the Order Confirmation, a proper copyright notice will read substantially as follows: "Used with permission of [Rightsholder's name], from [Work's title, author, volume, edition number and year of copyright]; permission conveyed through Copyright Clearance Center, Inc." Such notice must be provided in a reasonably legible font size and must be placed either on a cover page or in another location that any person, upon gaining access to the material which is the subject of a permission, shall see, or in the case of republication Licenses, immediately adjacent to the Work as used (for example, as part of a by-line or footnote) or in the place where substantially all other credits or notices for the new work containing the republished Work are located. Failure to include the required notice results in loss to the Rightsholder and CCC, and the User shall be liable to pay liquidated damages for each such failure equal to twice the use fee specified in the Order Confirmation, in addition to the use fee itself and any other fees and charges specified.

10) **Indemnity.** User hereby indemnifies and agrees to defend the Rightsholder and CCC, and their respective employees and directors, against all claims, liability, damages, costs, and expenses, including legal fees and expenses, arising out of any use of a Work beyond the scope of the rights granted herein and in the Order Confirmation, or any use of a Work which has been altered in any unauthorized way by User, including claims of defamation or infringement of rights of copyright, publicity, privacy, or other tangible or intangible property.

11) **Limitation of Liability.** UNDER NO CIRCUMSTANCES WILL CCC OR THE RIGHTSHOLDER BE LIABLE FOR ANY DIRECT, INDIRECT, CONSEQUENTIAL, OR INCIDENTAL DAMAGES (INCLUDING WITHOUT LIMITATION DAMAGES FOR LOSS OF BUSINESS PROFITS OR INFORMATION, OR FOR BUSINESS INTERRUPTION) ARISING OUT OF THE USE OR INABILITY TO USE A WORK, EVEN IF ONE OR BOTH OF THEM HAS BEEN ADVISED OF THE POSSIBILITY OF SUCH DAMAGES. In any event, the total liability of the Rightsholder and CCC (including their respective employees and directors) shall not exceed the total amount actually paid by User for the relevant License. User assumes full liability for the actions and omissions of its principals, employees, agents, affiliates, successors, and assigns.

12) **Limited Warranties.** THE WORK(S) AND RIGHT(S) ARE PROVIDED "AS IS." CCC HAS THE RIGHT TO GRANT TO USER THE RIGHTS GRANTED IN THE ORDER CONFIRMATION DOCUMENT. CCC AND THE RIGHTSHOLDER DISCLAIM ALL OTHER WARRANTIES RELATING TO THE WORK(S) AND RIGHT(S), EITHER EXPRESS OR IMPLIED, INCLUDING WITHOUT LIMITATION

IMPLIED WARRANTIES OF MERCHANTABILITY OR FITNESS FOR A PARTICULAR PURPOSE. ADDITIONAL RIGHTS MAY BE REQUIRED TO USE ILLUSTRATIONS, GRAPHS, PHOTOGRAPHS, ABSTRACTS, INSERTS, OR OTHER PORTIONS OF THE WORK (AS OPPOSED TO THE ENTIRE WORK) IN A MANNER CONTEMPLATED BY USER; USER UNDERSTANDS AND AGREES THAT NEITHER CCC NOR THE RIGHTSHOLDER MAY HAVE SUCH ADDITIONAL RIGHTS TO GRANT.

13) **Effect of Breach.** Any failure by User to pay any amount when due, or any use by User of a Work beyond the scope of the License set forth in the Order Confirmation and/or the Terms, shall be a material breach of such License. Any breach not cured within 10 days of written notice thereof shall result in immediate termination of such License without further notice. Any unauthorized (but licensable) use of a Work that is terminated immediately upon notice thereof may be liquidated by payment of the Rightsholder's ordinary license price therefor; any unauthorized (and unlicensable) use that is not terminated immediately for any reason (including, for example, because materials containing the Work cannot reasonably be recalled) will be subject to all remedies available at law or in equity, but in no event to a payment of less than three times the Rightsholder's ordinary license price for the most closely analogous licensable use plus Rightsholder's and/or CCC's costs and expenses incurred in collecting such payment.

14) **Additional Terms for Specific Products and Services.** If a User is making one of the uses described in this Section 14, the additional terms and conditions apply:

a) ***Print Uses of Academic Course Content and Materials (photocopies for academic coursepacks or classroom handouts).*** For photocopies for academic coursepacks or classroom handouts the following additional terms apply:

i) The copies and anthologies created under this License may be made and assembled by faculty members individually or at their request by on-campus bookstores or copy centers, or by off-campus copy shops and other similar entities.

ii) No License granted shall in any way: (i) include any right by User to create a substantively non-identical copy of the Work or to edit or in any other way modify the Work (except by means of deleting material immediately preceding or following the entire portion of the Work copied) (ii) permit "publishing ventures" where any particular anthology would be systematically marketed at multiple institutions.

iii) Subject to any Publisher Terms (and notwithstanding any apparent contradiction in the Order Confirmation arising from data provided by User), any use authorized under the academic pay-per-use service is limited as follows:

A) any License granted shall apply to only one class (bearing a unique identifier as assigned by the institution, and thereby including all sections or other subparts of the class) at one institution;

B) use is limited to not more than 25% of the text of a book or of the items in a published collection of essays, poems or articles;

C) use is limited to no more than the greater of (a) 25% of the text of an issue of a journal or other periodical or (b) two articles from such an issue;

D) no User may sell or distribute any particular anthology, whether photocopied or electronic, at more than one institution of learning;

E) in the case of a photocopy permission, no materials may be entered into electronic memory by User except in order to produce an identical copy of a Work before or during the academic term (or analogous period) as to which any particular permission is granted. In the event that User shall choose to retain materials that are the subject of a photocopy permission in electronic memory for purposes of producing identical copies more than one day after such retention (but still within the scope of any permission granted), User must notify CCC of such fact in the applicable permission request and such retention shall constitute one copy actually sold for purposes of calculating permission fees due; and

F) any permission granted shall expire at the end of the class. No permission granted shall in any way include any right by User to create a substantively non-identical copy of the Work or to edit or in any other way modify the Work (except by means of deleting material immediately preceding or following the entire portion of the Work copied).

iv) Books and Records; Right to Audit. As to each permission granted under the academic pay-per-use Service, User shall maintain for at least four full calendar years books and records sufficient for CCC to determine the numbers of copies made by User under such permission. CCC and any representatives it may designate shall have the right to audit such books and records at any time during User's ordinary business hours, upon two days' prior notice. If any such audit shall determine that User shall have underpaid for, or underreported, any photocopies sold or by three percent (3%) or more, then User shall bear all the costs of any such audit; otherwise, CCC shall bear the costs of any such audit. Any amount determined by such audit to have been underpaid by User shall immediately be paid to CCC by User, together with interest thereon at the rate of 10% per annum from the date such amount was originally due. The provisions of this paragraph shall survive the termination of this License for any reason.

b) ***Digital Pay-Per-Uses of Academic Course Content and Materials (e-coursepacks, electronic reserves, learning management systems, academic institution intranets).*** For uses in e-coursepacks, posts in electronic reserves, posts in learning management systems, or posts on academic institution intranets, the following additional terms apply:

i) The pay-per-uses subject to this Section 14(b) include:

A) **Posting e-reserves, course management systems, e-coursepacks for text-based content,** which grants authorizations to import requested material in electronic format, and allows electronic access to this material to members of a designated college or university class, under the direction of an instructor designated by the college or university, accessible only under appropriate electronic controls (e.g., password);

B) **Posting e-reserves, course management systems, e-coursepacks for material consisting of photographs or other still images not embedded in text,** which grants not only the authorizations described in Section 14(b)(i)(A) above, but also the following authorization: to include the requested material in course materials for use consistent with Section 14(b)(i)(A) above, including any necessary resizing, reformatting or modification of the resolution of such requested material (provided that such modification does not alter the underlying editorial content or meaning of the requested material, and provided that the resulting modified content is used solely within the scope of, and in a manner consistent with, the particular authorization described in the Order Confirmation and the Terms), but not including any other form of manipulation, alteration or editing of the requested material;

C) **Posting e-reserves, course management systems, e-coursepacks or other academic distribution for audiovisual content,** which grants not only the authorizations described in Section 14(b)(i)(A) above, but also the following authorizations: (i) to include the requested material in course materials for use consistent with Section 14(b)(i)(A) above; (ii) to display and perform the requested material to such members of such class in the physical classroom or remotely by means of streaming media or other video formats; and (iii) to “clip” or reformat the requested material for purposes of time or content management or ease of delivery, provided that such “clipping” or reformatting does not alter the underlying editorial content or meaning of the requested material and that the resulting material is used solely within the scope of, and in a manner consistent with, the particular authorization described in the Order Confirmation and the Terms. Unless expressly set forth in the relevant Order Conformation, the License does not authorize any other form of manipulation, alteration or editing of the requested material.

ii) Unless expressly set forth in the relevant Order Confirmation, no License granted shall in any way: (i) include any right by User to create a substantively non-identical copy of the Work or to edit or in any other way modify the Work (except by means of deleting material immediately preceding or following the entire portion of the Work copied or, in the case of Works subject to Sections 14(b)(1)(B) or (C) above, as described in such Sections) (ii) permit “publishing ventures” where any particular course materials would be systematically marketed at multiple institutions.

iii) Subject to any further limitations determined in the Rightsholder Terms (and notwithstanding any apparent contradiction in the Order Confirmation arising from data provided by User), any use authorized under the electronic course content pay-per-use service is limited as follows:

A) any License granted shall apply to only one class (bearing a unique identifier as assigned by the institution, and thereby including all sections or other subparts of the class) at one institution;

B) use is limited to not more than 25% of the text of a book or of the items in a published collection of essays, poems or articles;

C) use is limited to not more than the greater of (a) 25% of the text of an issue of a journal or other periodical or (b) two articles from such an issue;

D) no User may sell or distribute any particular materials, whether photocopied or electronic, at more than one institution of learning;

E) electronic access to material which is the subject of an electronic-use permission must be limited by means of electronic password, student identification or other control permitting access solely to students and instructors in the class;

F) User must ensure (through use of an electronic cover page or other appropriate means) that any person, upon gaining electronic access to the material, which is the subject of a permission, shall see:

- a proper copyright notice, identifying the Rightsholder in whose name CCC has granted permission,

- a statement to the effect that such copy was made pursuant to permission,
- a statement identifying the class to which the material applies and notifying the reader that the material has been made available electronically solely for use in the class, and
- a statement to the effect that the material may not be further distributed to any person outside the class, whether by copying or by transmission and whether electronically or in paper form, and User must also ensure that such cover page or other means will print out in the event that the person accessing the material chooses to print out the material or any part thereof.

G) any permission granted shall expire at the end of the class and, absent some other form of authorization, User is thereupon required to delete the applicable material from any electronic storage or to block electronic access to the applicable material.

iv) Uses of separate portions of a Work, even if they are to be included in the same course material or the same university or college class, require separate permissions under the electronic course content pay-per-use Service. Unless otherwise provided in the Order Confirmation, any grant of rights to User is limited to use completed no later than the end of the academic term (or analogous period) as to which any particular permission is granted.

v) Books and Records; Right to Audit. As to each permission granted under the electronic course content Service, User shall maintain for at least four full calendar years books and records sufficient for CCC to determine the numbers of copies made by User under such permission. CCC and any representatives it may designate shall have the right to audit such books and records at any time during User's ordinary business hours, upon two days' prior notice. If any such audit shall determine that User shall have underpaid for, or underreported, any electronic copies used by three percent (3%) or more, then User shall bear all the costs of any such audit; otherwise, CCC shall bear the costs of any such audit. Any amount determined by such audit to have been underpaid by User shall immediately be paid to CCC by User, together with interest thereon at the rate of 10% per annum from the date such amount was originally due. The provisions of this paragraph shall survive the termination of this license for any reason.

c) ***Pay-Per-Use Permissions for Certain Reproductions (Academic photocopies for library reserves and interlibrary loan reporting) (Non-academic internal/external business uses and commercial document delivery).*** The License expressly excludes the uses listed in Section (c)(i)-(v) below (which must be subject to separate license from the applicable Rightsholder) for: academic photocopies for library reserves and interlibrary loan reporting; and non-academic internal/external business uses and commercial document delivery.

i) electronic storage of any reproduction (whether in plain-text, PDF, or any other format) other than on a transitory basis;

ii) the input of Works or reproductions thereof into any computerized database;

iii) reproduction of an entire Work (cover-to-cover copying) except where the Work is a single article;

iv) reproduction for resale to anyone other than a specific customer of User;

v) republication in any different form. Please obtain authorizations for these uses through other CCC services or directly from the rightsholder.

Any license granted is further limited as set forth in any restrictions included in the Order Confirmation and/or in these Terms.

d) ***Electronic Reproductions in Online Environments (Non-Academic-email, intranet, internet and extranet).*** For "electronic reproductions", which generally includes e-mail use (including instant messaging or other electronic transmission to a defined group of recipients) or posting on an intranet, extranet or Intranet site (including any display or performance incidental thereto), the following additional terms apply:

i) Unless otherwise set forth in the Order Confirmation, the License is limited to use completed within 30 days for any use on the Internet, 60 days for any use on an intranet or extranet and one year for any other use, all as measured from the "republication date" as identified in the Order Confirmation, if any, and otherwise from the date of the Order Confirmation.

ii) User may not make or permit any alterations to the Work, unless expressly set forth in the Order Confirmation (after request by User and approval by Rightsholder); provided, however, that a Work consisting of photographs or other still images not embedded in text may, if necessary, be resized, reformatted or have its resolution modified without additional express permission, and a Work consisting of audiovisual content may, if necessary, be "clipped" or reformatted for purposes of time or content management or ease of delivery (provided that any such resizing, reformatting, resolution modification or "clipping" does not alter the underlying editorial content or meaning of the Work used, and that the resulting material is used solely within the scope of, and in a manner consistent with, the particular License described in the Order Confirmation and the Terms.

15) **Miscellaneous.**

a) User acknowledges that CCC may, from time to time, make changes or additions to the Service or to the Terms, and that Rightsholder may make changes or additions to the Rightsholder Terms. Such updated Terms will replace the prior terms and conditions in the order workflow and shall be effective as to any subsequent Licenses but shall not apply to Licenses already granted and paid for under a prior set of terms.

b) Use of User-related information collected through the Service is governed by CCC's privacy policy, available online at www.copyright.com/about/privacy-policy/.

c) The License is personal to User. Therefore, User may not assign or transfer to any other person (whether a natural person or an organization of any kind) the License or any rights granted thereunder; provided, however, that, where applicable, User may assign such License in its entirety on written notice to CCC in the event of a transfer of all or substantially all of User's rights in any new material which includes the Work(s) licensed under this Service.

d) No amendment or waiver of any Terms is binding unless set forth in writing and signed by the appropriate parties, including, where applicable, the Rightsholder. The Rightsholder and CCC hereby object to any terms contained in any writing prepared by or on behalf of the User or its principals, employees, agents or affiliates and purporting to govern or otherwise relate to the License described in the Order Confirmation, which terms are in any way inconsistent with any Terms set forth in the Order Confirmation, and/or in CCC's standard operating procedures, whether such writing is prepared prior to, simultaneously with or subsequent to the Order Confirmation, and whether such writing appears on a copy of the Order Confirmation or in a separate instrument.

e) The License described in the Order Confirmation shall be governed by and construed under the law of the State of New York, USA, without regard to the principles thereof of conflicts of law. Any case, controversy, suit, action, or proceeding arising out of, in connection with, or related to such License shall be brought, at CCC's sole discretion, in any federal or state court located in the County of New York, State of New York, USA, or in any federal or state court whose geographical jurisdiction covers the location of the Rightsholder set forth in the Order Confirmation. The parties expressly submit to the personal jurisdiction and venue of each such federal or state court.

Last updated October 2022

CCC Marketplace

This is a License Agreement between Daniel Steiner ("User") and Copyright Clearance Center, Inc. ("CCC") on behalf of the Rightsholder identified in the order details below. The license consists of the order details, the Marketplace Permissions General Terms and Conditions below, and any Rightsholder Terms and Conditions which are included below.

All payments must be made in full to CCC in accordance with the Marketplace Permissions General Terms and Conditions below.

Order Date	15-Sep-2025	**Type of Use**	Republish in a thesis/dissertation
Order License ID	1651704-1	**Publisher**	ANNUAL REVIEWS
ISSN	1545-4282	**Portion**	Chart/graph/table/figure

LICENSED CONTENT

Publication Title	Annual review of astronomy and astrophysics	**Publication Type**	e-Journal
Article Title	Protoplanetary Disks and Their Evolution	**Start Page**	67
Date	01/01/1963	**End Page**	117
Language	English	**Issue**	1
Country	United States of America	**Volume**	49
Rightsholder	Annual Reviews, Inc.	**URL**	http://books.google.com/books?id=7HuuAAAAIAAJ

REQUEST DETAILS

Portion Type	Chart/graph/table/figure	**Distribution**	Worldwide
Number of Charts / Graphs / Tables / Figures Requested	2	**Translation**	Original language of publication
Format (select all that apply)	Print, Electronic	**Copies for the Disabled?**	No
Who Will Republish the Content?	Academic institution	**Minor Editing Privileges?**	No
Duration of Use	Life of current edition	**Incidental Promotional Use?**	No
Lifetime Unit Quantity	Up to 499	**Currency**	EUR
Rights Requested	Main product		

NEW WORK DETAILS

Title	Large-scale magnetic fields in protoplanetary disks	**Institution Name**	University of Vienna
Instructor Name	Daniel Steiner	**Expected Presentation Date**	2025-12-18

ADDITIONAL DETAILS

Order Reference Number	N/A	**The Requesting Person / Organization to Appear on the License**	Daniel Steiner

REQUESTED CONTENT DETAILS

Title, Description or Numeric Reference of the Portion(s)	Figure 2 and Figure 3	**Title of the Article / Chapter the Portion Is From**	Protoplanetary Disks and Their Evolution
Editor of Portion(s)	Williams, Jonathan P.; Cieza, Lucas A.	**Author of Portion(s)**	Williams, Jonathan P.; Cieza, Lucas A.
Volume / Edition	49	**Issue, if Republishing an Article From a Serial**	1
Page or Page Range of Portion	67-117	**Publication Date of Portion**	2011-09-22

RIGHTSHOLDER TERMS AND CONDITIONS

If any part of the material to be used (for example, figures and tables) has appeared in our publication with credit or acknowledgement to another source, permission must also be sought from that source. If such permission is not obtained then that material may not be included in your publication/copies. Suitable acknowledgement to the source must be made, either as a footnote or in a reference list at the end of your publication.
Annual Reviews publishes Open Access Articles in both its Open Access journals and within its subscription titles, which may allow for certain types of reuse without permission. Before proceeding, please refer to the article's copyright line to determine whether the content you wish to use is Open Access. For Open Access content, please refer to the license terms for the work which you wish to reuse. Any reuse not included in the license terms will require permission. In all instances, full and appropriate attribution to the original source must be given. Further, permission does not cover any third party copyrighted material which may appear in the Annual Reviews work requested, and additional permission from the rights holder of such material may be required. If any part of the material to be used (for example, figures and tables) has appeared in our publication with credit or acknowledgement to another source, permission must also be sought from that source. If such permission is not obtained then that material may not be included in your publication/copies. Suitable acknowledgement to the source must be made, either as a footnote or in a reference list at the end of your publication. Please contact Annual Reviews with any questions.

Marketplace Permissions General Terms and Conditions

The following terms and conditions ("General Terms"), together with any applicable Publisher Terms and Conditions, govern User's use of Works pursuant to the Licenses granted by Copyright Clearance Center, Inc. ("CCC") on behalf of the applicable Rightsholders of such Works through CCC's applicable Marketplace transactional licensing services (each, a "Service").

1) **Definitions.** For purposes of these General Terms, the following definitions apply:

"License" is the licensed use the User obtains via the Marketplace platform in a particular licensing transaction, as set forth in the Order Confirmation.

"Order Confirmation" is the confirmation CCC provides to the User at the conclusion of each Marketplace transaction. "Order Confirmation Terms" are additional terms set forth on specific Order Confirmations not set forth in the General Terms that can include terms applicable to a particular CCC transactional licensing service and/or any Rightsholder-specific terms.

"Rightsholder(s)" are the holders of copyright rights in the Works for which a User obtains licenses via the Marketplace platform, which are displayed on specific Order Confirmations.

"Terms" means the terms and conditions set forth in these General Terms and any additional Order Confirmation Terms collectively.

"User" or "you" is the person or entity making the use granted under the relevant License. Where the person accepting the Terms on behalf of a User is a freelancer or other third party who the User authorized to accept the General Terms on the User's behalf, such person shall be deemed jointly a User for purposes of such Terms.

"Work(s)" are the copyright protected works described in relevant Order Confirmations.

2) **Description of Service.** CCC's Marketplace enables Users to obtain Licenses to use one or more Works in accordance with all relevant Terms. CCC grants Licenses as an agent on behalf of the copyright rightsholder identified in the relevant Order Confirmation.

3) **Applicability of Terms.** The Terms govern User's use of Works in connection with the relevant License. In the event of any conflict between General Terms and Order Confirmation Terms, the latter shall govern. User acknowledges that Rightsholders have complete discretion whether to grant any permission, and whether to place any limitations on any grant, and that CCC has no right to supersede or to modify any such discretionary act by a Rightsholder.

4) **Representations; Acceptance.** By using the Service, User represents and warrants that User has been duly authorized by the User to accept, and hereby does accept, all Terms.

5) **Scope of License; Limitations and Obligations.** All Works and all rights therein, including copyright rights, remain the sole and exclusive property of the Rightsholder. The License provides only those rights expressly set forth in the terms and conveys no other rights in any Works

6) **General Payment Terms.** User may pay at time of checkout by credit card or choose to be invoiced. If the User chooses to be invoiced, the User shall: (i) remit payments in the manner identified on specific invoices, (ii) unless otherwise specifically stated in an Order Confirmation or separate written agreement, Users shall remit payments upon receipt of the relevant invoice from CCC, either by delivery or notification of availability of the invoice via the Marketplace platform, and (iii) if the User does not pay the invoice within 30 days of receipt, the User may incur a service charge of 1.5% per month or the maximum rate allowed by applicable law, whichever is less. While User may exercise the rights in the License immediately upon receiving the Order Confirmation, the License is automatically revoked and is null and void, as if it had never been issued, if CCC does not receive complete payment on a timely basis.

7) **General Limits on Use.** Unless otherwise provided in the Order Confirmation, any grant of rights to User (i) involves only the rights set forth in the Terms and does not include subsequent or additional uses, (ii) is non-exclusive and non-transferable, and (iii) is subject to any and all limitations and restrictions (such as, but not limited to, limitations on duration of use or circulation) included in the Terms. Upon completion of the licensed use as set forth in the Order Confirmation, User shall either secure a new permission for further use of the Work(s) or immediately cease any new use of the Work(s) and shall render inaccessible (such as by deleting or by removing or severing links or other locators) any further copies of the Work. User may only make alterations to the Work if and as expressly set forth in the Order Confirmation. No Work may be used in any way that is unlawful, including without limitation if such use would violate applicable sanctions laws or regulations, would be defamatory, violate the rights of third parties (including such third parties' rights of copyright, privacy, publicity, or other tangible or intangible property), or is otherwise illegal, sexually explicit, or obscene. In addition, User may not conjoin a Work with any other material that may result in damage to the reputation of the Rightsholder. Any unlawful use will render any licenses hereunder null and void. User agrees to inform CCC if it becomes aware of any infringement of any rights in a Work and to cooperate with any reasonable request of CCC or the Rightsholder in connection therewith.

8) **Third Party Materials.** In the event that the material for which a License is sought includes third party materials (such as photographs, illustrations, graphs, inserts and similar materials) that are identified in such material as having been used by permission (or a similar indicator), User is responsible for identifying, and seeking separate licenses (under this Service, if available, or otherwise) for any of such third party materials; without a separate license, User may not use such third party materials via the License.

9) **Copyright Notice.** Use of proper copyright notice for a Work is required as a condition of any License granted under the Service. Unless otherwise provided in the Order Confirmation, a proper copyright notice will read substantially as follows: "Used with permission of [Rightsholder's name], from [Work's title, author, volume, edition number and year of copyright]; permission conveyed through Copyright Clearance Center, Inc." Such notice must be provided in a reasonably legible font size and must be placed either on a cover page or in another location that any person, upon gaining access to the material which is the subject of a permission, shall see, or in the case of republication Licenses, immediately adjacent to the Work as used (for example, as part of a by-line or footnote) or in the place where substantially all other credits or notices for the new work containing the republished Work are located. Failure to include the required notice results in loss to the Rightsholder and CCC, and the User shall be liable to pay liquidated damages for each such failure equal to twice the use fee specified in the Order Confirmation, in addition to the use fee itself and any other fees and charges specified.

10) **Indemnity.** User hereby indemnifies and agrees to defend the Rightsholder and CCC, and their respective employees and directors, against all claims, liability, damages, costs, and expenses, including legal fees and expenses, arising out of any use of a Work beyond the scope of the rights granted herein and in the Order Confirmation, or any use of a Work which has been altered in any unauthorized way by User, including claims of defamation or infringement of rights of copyright, publicity, privacy, or other tangible or intangible property.

11) **Limitation of Liability.** UNDER NO CIRCUMSTANCES WILL CCC OR THE RIGHTSHOLDER BE LIABLE FOR ANY DIRECT, INDIRECT, CONSEQUENTIAL, OR INCIDENTAL DAMAGES (INCLUDING WITHOUT LIMITATION DAMAGES FOR LOSS OF BUSINESS PROFITS OR INFORMATION, OR FOR BUSINESS INTERRUPTION) ARISING OUT OF THE USE OR INABILITY TO USE A WORK, EVEN IF ONE OR BOTH OF THEM HAS BEEN ADVISED OF THE POSSIBILITY OF SUCH DAMAGES. In any event, the total liability of the Rightsholder and CCC (including their respective employees and directors) shall not exceed the total amount actually paid by User for the relevant License. User assumes full liability for the actions and omissions of its principals, employees, agents, affiliates, successors, and assigns.

12) **Limited Warranties.** THE WORK(S) AND RIGHT(S) ARE PROVIDED "AS IS." CCC HAS THE RIGHT TO GRANT TO USER THE RIGHTS GRANTED IN THE ORDER CONFIRMATION DOCUMENT. CCC AND THE RIGHTSHOLDER DISCLAIM ALL OTHER WARRANTIES RELATING TO THE WORK(S) AND RIGHT(S), EITHER EXPRESS OR IMPLIED, INCLUDING WITHOUT LIMITATION

IMPLIED WARRANTIES OF MERCHANTABILITY OR FITNESS FOR A PARTICULAR PURPOSE. ADDITIONAL RIGHTS MAY BE REQUIRED TO USE ILLUSTRATIONS, GRAPHS, PHOTOGRAPHS, ABSTRACTS, INSERTS, OR OTHER PORTIONS OF THE WORK (AS OPPOSED TO THE ENTIRE WORK) IN A MANNER CONTEMPLATED BY USER; USER UNDERSTANDS AND AGREES THAT NEITHER CCC NOR THE RIGHTSHOLDER MAY HAVE SUCH ADDITIONAL RIGHTS TO GRANT.

13) **Effect of Breach.** Any failure by User to pay any amount when due, or any use by User of a Work beyond the scope of the License set forth in the Order Confirmation and/or the Terms, shall be a material breach of such License. Any breach not cured within 10 days of written notice thereof shall result in immediate termination of such License without further notice. Any unauthorized (but licensable) use of a Work that is terminated immediately upon notice thereof may be liquidated by payment of the Rightsholder's ordinary license price therefor; any unauthorized (and unlicensable) use that is not terminated immediately for any reason (including, for example, because materials containing the Work cannot reasonably be recalled) will be subject to all remedies available at law or in equity, but in no event to a payment of less than three times the Rightsholder's ordinary license price for the most closely analogous licensable use plus Rightsholder's and/or CCC's costs and expenses incurred in collecting such payment.

14) **Additional Terms for Specific Products and Services.** If a User is making one of the uses described in this Section 14, the additional terms and conditions apply:

a) ***Print Uses of Academic Course Content and Materials (photocopies for academic coursepacks or classroom handouts).*** For photocopies for academic coursepacks or classroom handouts the following additional terms apply:

i) The copies and anthologies created under this License may be made and assembled by faculty members individually or at their request by on-campus bookstores or copy centers, or by off-campus copy shops and other similar entities.

ii) No License granted shall in any way: (i) include any right by User to create a substantively non-identical copy of the Work or to edit or in any other way modify the Work (except by means of deleting material immediately preceding or following the entire portion of the Work copied) (ii) permit "publishing ventures" where any particular anthology would be systematically marketed at multiple institutions.

iii) Subject to any Publisher Terms (and notwithstanding any apparent contradiction in the Order Confirmation arising from data provided by User), any use authorized under the academic pay-per-use service is limited as follows:

A) any License granted shall apply to only one class (bearing a unique identifier as assigned by the institution, and thereby including all sections or other subparts of the class) at one institution;

B) use is limited to not more than 25% of the text of a book or of the items in a published collection of essays, poems or articles;

C) use is limited to no more than the greater of (a) 25% of the text of an issue of a journal or other periodical or (b) two articles from such an issue;

D) no User may sell or distribute any particular anthology, whether photocopied or electronic, at more than one institution of learning;

E) in the case of a photocopy permission, no materials may be entered into electronic memory by User except in order to produce an identical copy of a Work before or during the academic term (or analogous period) as to which any particular permission is granted. In the event that User shall choose to retain materials that are the subject of a photocopy permission in electronic memory for purposes of producing identical copies more than one day after such retention (but still within the scope of any permission granted), User must notify CCC of such fact in the applicable permission request and such retention shall constitute one copy actually sold for purposes of calculating permission fees due; and

F) any permission granted shall expire at the end of the class. No permission granted shall in any way include any right by User to create a substantively non-identical copy of the Work or to edit or in any other way modify the Work (except by means of deleting material immediately preceding or following the entire portion of the Work copied).

iv) Books and Records; Right to Audit. As to each permission granted under the academic pay-per-use Service, User shall maintain for at least four full calendar years books and records sufficient for CCC to determine the numbers of copies made by User under such permission. CCC and any representatives it may designate shall have the right to audit such books and records at any time during User's ordinary business hours, upon two days' prior notice. If any such audit shall determine that User shall have underpaid for, or underreported, any photocopies sold or by three percent (3%) or more, then User shall bear all the costs of any such audit; otherwise, CCC shall bear the costs of any such audit. Any amount determined by such audit to have been underpaid by User shall immediately be paid to CCC by User, together with interest thereon at the rate of 10% per annum from the date such amount was originally due. The provisions of this paragraph shall survive the termination of this License for any reason.

b) ***Digital Pay-Per-Uses of Academic Course Content and Materials (e-coursepacks, electronic reserves, learning management systems, academic institution intranets).*** For uses in e-coursepacks, posts in electronic reserves, posts in learning management systems, or posts on academic institution intranets, the following additional terms apply:

i) The pay-per-uses subject to this Section 14(b) include:

A) **Posting e-reserves, course management systems, e-coursepacks for text-based content,** which grants authorizations to import requested material in electronic format, and allows electronic access to this material to members of a designated college or university class, under the direction of an instructor designated by the college or university, accessible only under appropriate electronic controls (e.g., password);

B) **Posting e-reserves, course management systems, e-coursepacks for material consisting of photographs or other still images not embedded in text,** which grants not only the authorizations described in Section 14(b)(i)(A) above, but also the following authorization: to include the requested material in course materials for use consistent with Section 14(b)(i)(A) above, including any necessary resizing, reformatting or modification of the resolution of such requested material (provided that such modification does not alter the underlying editorial content or meaning of the requested material, and provided that the resulting modified content is used solely within the scope of, and in a manner consistent with, the particular authorization described in the Order Confirmation and the Terms), but not including any other form of manipulation, alteration or editing of the requested material;

C) **Posting e-reserves, course management systems, e-coursepacks or other academic distribution for audiovisual content,** which grants not only the authorizations described in Section 14(b)(i)(A) above, but also the following authorizations: (i) to include the requested material in course materials for use consistent with Section 14(b)(i)(A) above; (ii) to display and perform the requested material to such members of such class in the physical classroom or remotely by means of streaming media or other video formats; and (iii) to "clip" or reformat the requested material for purposes of time or content management or ease of delivery, provided that such "clipping" or reformatting does not alter the underlying editorial content or meaning of the requested material and that the resulting material is used solely within the scope of, and in a manner consistent with, the particular authorization described in the Order Confirmation and the Terms. Unless expressly set forth in the relevant Order Conformation, the License does not authorize any other form of manipulation, alteration or editing of the requested material.

ii) Unless expressly set forth in the relevant Order Confirmation, no License granted shall in any way: (i) include any right by User to create a substantively non-identical copy of the Work or to edit or in any other way modify the Work (except by means of deleting material immediately preceding or following the entire portion of the Work copied or, in the case of Works subject to Sections 14(b)(1)(B) or (C) above, as described in such Sections) (ii) permit "publishing ventures" where any particular course materials would be systematically marketed at multiple institutions.

iii) Subject to any further limitations determined in the Rightsholder Terms (and notwithstanding any apparent contradiction in the Order Confirmation arising from data provided by User), any use authorized under the electronic course content pay-per-use service is limited as follows:

A) any License granted shall apply to only one class (bearing a unique identifier as assigned by the institution, and thereby including all sections or other subparts of the class) at one institution;

B) use is limited to not more than 25% of the text of a book or of the items in a published collection of essays, poems or articles;

C) use is limited to not more than the greater of (a) 25% of the text of an issue of a journal or other periodical or (b) two articles from such an issue;

D) no User may sell or distribute any particular materials, whether photocopied or electronic, at more than one institution of learning;

E) electronic access to material which is the subject of an electronic-use permission must be limited by means of electronic password, student identification or other control permitting access solely to students and instructors in the class;

F) User must ensure (through use of an electronic cover page or other appropriate means) that any person, upon gaining electronic access to the material, which is the subject of a permission, shall see:

- a proper copyright notice, identifying the Rightsholder in whose name CCC has granted permission,

- a statement to the effect that such copy was made pursuant to permission,
- a statement identifying the class to which the material applies and notifying the reader that the material has been made available electronically solely for use in the class, and
- a statement to the effect that the material may not be further distributed to any person outside the class, whether by copying or by transmission and whether electronically or in paper form, and User must also ensure that such cover page or other means will print out in the event that the person accessing the material chooses to print out the material or any part thereof.

G) any permission granted shall expire at the end of the class and, absent some other form of authorization, User is thereupon required to delete the applicable material from any electronic storage or to block electronic access to the applicable material.

iv) Uses of separate portions of a Work, even if they are to be included in the same course material or the same university or college class, require separate permissions under the electronic course content pay-per-use Service. Unless otherwise provided in the Order Confirmation, any grant of rights to User is limited to use completed no later than the end of the academic term (or analogous period) as to which any particular permission is granted.

v) Books and Records; Right to Audit. As to each permission granted under the electronic course content Service, User shall maintain for at least four full calendar years books and records sufficient for CCC to determine the numbers of copies made by User under such permission. CCC and any representatives it may designate shall have the right to audit such books and records at any time during User’s ordinary business hours, upon two days’ prior notice. If any such audit shall determine that User shall have underpaid for, or underreported, any electronic copies used by three percent (3%) or more, then User shall bear all the costs of any such audit; otherwise, CCC shall bear the costs of any such audit. Any amount determined by such audit to have been underpaid by User shall immediately be paid to CCC by User, together with interest thereon at the rate of 10% per annum from the date such amount was originally due. The provisions of this paragraph shall survive the termination of this license for any reason.

c) ***Pay-Per-Use Permissions for Certain Reproductions (Academic photocopies for library reserves and interlibrary loan reporting) (Non-academic internal/external business uses and commercial document delivery).*** The License expressly excludes the uses listed in Section (c)(i)-(v) below (which must be subject to separate license from the applicable Rightsholder) for: academic photocopies for library reserves and interlibrary loan reporting; and non-academic internal/external business uses and commercial document delivery.

i) electronic storage of any reproduction (whether in plain-text, PDF, or any other format) other than on a transitory basis;

ii) the input of Works or reproductions thereof into any computerized database;

iii) reproduction of an entire Work (cover-to-cover copying) except where the Work is a single article;

iv) reproduction for resale to anyone other than a specific customer of User;

v) republication in any different form. Please obtain authorizations for these uses through other CCC services or directly from the rightsholder.

Any license granted is further limited as set forth in any restrictions included in the Order Confirmation and/or in these Terms.

d) ***Electronic Reproductions in Online Environments (Non-Academic-email, intranet, internet and extranet).*** For “electronic reproductions”, which generally includes e-mail use (including instant messaging or other electronic transmission to a defined group of recipients) or posting on an intranet, extranet or Intranet site (including any display or performance incidental thereto), the following additional terms apply:

i) Unless otherwise set forth in the Order Confirmation, the License is limited to use completed within 30 days for any use on the Internet, 60 days for any use on an intranet or extranet and one year for any other use, all as measured from the “republication date” as identified in the Order Confirmation, if any, and otherwise from the date of the Order Confirmation.

ii) User may not make or permit any alterations to the Work, unless expressly set forth in the Order Confirmation (after request by User and approval by Rightsholder); provided, however, that a Work consisting of photographs or other still images not embedded in text may, if necessary, be resized, reformatted or have its resolution modified without additional express permission, and a Work consisting of audiovisual content may, if necessary, be “clipped” or reformatted for purposes of time or content management or ease of delivery (provided that any such resizing, reformatting, resolution modification or “clipping” does not alter the underlying editorial content or meaning of the Work used, and that the resulting material is used solely within the scope of, and in a manner consistent with, the particular License described in the Order Confirmation and the Terms.

15) **Miscellaneous.**

a) User acknowledges that CCC may, from time to time, make changes or additions to the Service or to the Terms, and that Rightsholder may make changes or additions to the Rightsholder Terms. Such updated Terms will replace the prior terms and conditions in the order workflow and shall be effective as to any subsequent Licenses but shall not apply to Licenses already granted and paid for under a prior set of terms.

b) Use of User-related information collected through the Service is governed by CCC's privacy policy, available online at www.copyright.com/about/privacy-policy/.

c) The License is personal to User. Therefore, User may not assign or transfer to any other person (whether a natural person or an organization of any kind) the License or any rights granted thereunder; provided, however, that, where applicable, User may assign such License in its entirety on written notice to CCC in the event of a transfer of all or substantially all of User's rights in any new material which includes the Work(s) licensed under this Service.

d) No amendment or waiver of any Terms is binding unless set forth in writing and signed by the appropriate parties, including, where applicable, the Rightsholder. The Rightsholder and CCC hereby object to any terms contained in any writing prepared by or on behalf of the User or its principals, employees, agents or affiliates and purporting to govern or otherwise relate to the License described in the Order Confirmation, which terms are in any way inconsistent with any Terms set forth in the Order Confirmation, and/or in CCC's standard operating procedures, whether such writing is prepared prior to, simultaneously with or subsequent to the Order Confirmation, and whether such writing appears on a copy of the Order Confirmation or in a separate instrument.

e) The License described in the Order Confirmation shall be governed by and construed under the law of the State of New York, USA, without regard to the principles thereof of conflicts of law. Any case, controversy, suit, action, or proceeding arising out of, in connection with, or related to such License shall be brought, at CCC's sole discretion, in any federal or state court located in the County of New York, State of New York, USA, or in any federal or state court whose geographical jurisdiction covers the location of the Rightsholder set forth in the Order Confirmation. The parties expressly submit to the personal jurisdiction and venue of each such federal or state court.

Last updated October 2022

ELSEVIER LICENSE
TERMS AND CONDITIONS

Sep 24, 2025

This Agreement between Daniel Steiner ("You") and Elsevier ("Elsevier") consists of your license details and the terms and conditions provided by Elsevier and Copyright Clearance Center.

License Number	6110680493449
License date	Sep 16, 2025
Licensed Content Publisher	Elsevier
Licensed Content Publication	New Astronomy
Licensed Content Title	Properties of strong and weak propellers from MHD simulations
Licensed Content Author	M.M. Romanova,A.A. Blinova,G.V. Ustyugova,A.V. Koldoba,R.V.E. Lovelace
Licensed Content Date	Jul 1, 2018
Licensed Content Volume	62
Licensed Content Issue	n/a
Licensed Content Pages	21
Start Page	94
End Page	114
Type of Use	reuse in a thesis/dissertation
Portion	figures/tables/illustrations
Number of figures/tables/illustrations	1
Format	both print and electronic
Are you the author of this Elsevier article?	No
Will you be translating?	No
Title of new work	Large-scale magnetic fields in protoplanetary disks
Institution name	University of Vienna
Expected presentation date	Dec 2025
Portions	Figure 2
The Requesting Person / Organization to Appear on the License	Daniel Steiner
Requestor Location	Mr. Daniel Steiner Hafinger Weg 33 Top 5 Sankt Pölten, Lower Austria 3100 Austria
Publisher Tax ID	GB 494 6272 12
Total	**0.00 EUR**
Terms and Conditions	

INTRODUCTION

1. The publisher for this copyrighted material is Elsevier. By clicking "accept" in connection with completing this licensing transaction, you agree that the following terms and conditions apply to this transaction (along with the Billing and Payment terms and conditions established by Copyright Clearance Center, Inc. ("CCC"), at the time that you opened your RightsLink account and that are available at any time at https://myaccount.copyright.com).

GENERAL TERMS

2. Elsevier hereby grants you permission to reproduce the aforementioned material subject to the terms and conditions indicated.

3. Acknowledgement: If any part of the material to be used (for example, figures) has appeared in our publication with credit or acknowledgement to another source, permission must also be sought from that source. If such permission is not obtained then that material may not be included in your publication/copies. Suitable acknowledgement to the source must be made, either as a footnote or in a reference list at the end of your publication, as follows:
"Reprinted from Publication title, Vol /edition number, Author(s), Title of article / title of chapter, Pages No., Copyright (Year), with permission from Elsevier [OR APPLICABLE SOCIETY COPYRIGHT OWNER]." Also Lancet special credit - "Reprinted from The Lancet, Vol. number, Author(s), Title of article, Pages No., Copyright (Year), with permission from Elsevier."
4. Reproduction of this material is confined to the purpose and/or media for which permission is hereby given. The material may not be reproduced or used in any other way, including use in combination with an artificial intelligence tool (including to train an algorithm, test, process, analyse, generate output and/or develop any form of artificial intelligence tool), or to create any derivative work and/or service (including resulting from the use of artificial intelligence tools).
5. Altering/Modifying Material: Not Permitted. However figures and illustrations may be altered/adapted minimally to serve your work. Any other abbreviations, additions, deletions and/or any other alterations shall be made only with prior written authorization of Elsevier Ltd. (Please contact Elsevier's permissions helpdesk here). No modifications can be made to any Lancet figures/tables and they must be reproduced in full.
6. If the permission fee for the requested use of our material is waived in this instance, please be advised that your future requests for Elsevier materials may attract a fee.
7. Reservation of Rights: Publisher reserves all rights not specifically granted in the combination of (i) the license details provided by you and accepted in the course of this licensing transaction, (ii) these terms and conditions and (iii) CCC's Billing and Payment terms and conditions.
8. License Contingent Upon Payment: While you may exercise the rights licensed immediately upon issuance of the license at the end of the licensing process for the transaction, provided that you have disclosed complete and accurate details of your proposed use, no license is finally effective unless and until full payment is received from you (either by publisher or by CCC) as provided in CCC's Billing and Payment terms and conditions. If full payment is not received on a timely basis, then any license preliminarily granted shall be deemed automatically revoked and shall be void as if never granted. Further, in the event that you breach any of these terms and conditions or any of CCC's Billing and Payment terms and conditions, the license is automatically revoked and shall be void as if never granted. Use of materials as described in a revoked license, as well as any use of the materials beyond the scope of an unrevoked license, may constitute copyright infringement and publisher reserves the right to take any and all action to protect its copyright in the materials.
9. Warranties: Publisher makes no representations or warranties with respect to the licensed material.
10. Indemnity: You hereby indemnify and agree to hold harmless publisher and CCC, and their respective officers, directors, employees and agents, from and against any and all claims arising out of your use of the licensed material other than as specifically authorized pursuant to this license.
11. No Transfer of License: This license is personal to you and may not be sublicensed, assigned, or transferred by you to any other person without publisher's written permission.
12. No Amendment Except in Writing: This license may not be amended except in a writing signed by both parties (or, in the case of publisher, by CCC on publisher's behalf).
13. Objection to Contrary Terms: Publisher hereby objects to any terms contained in any purchase order, acknowledgment, check endorsement or other writing prepared by you, which terms are inconsistent with these terms and conditions or CCC's Billing and Payment terms and conditions. These terms and conditions, together with CCC's Billing and Payment terms and conditions (which are incorporated herein), comprise the entire agreement between you and publisher (and CCC) concerning this licensing transaction. In the event of any conflict between your obligations established by these terms and conditions and those established by CCC's Billing and Payment terms and conditions, these terms and conditions shall control.
14. Revocation: Elsevier or Copyright Clearance Center may deny the permissions described in this License at their sole discretion, for any reason or no reason, with a full refund payable to you. Notice of such denial will be made using the contact information provided by you. Failure to receive such notice will not alter or invalidate the denial. In no event will Elsevier or Copyright Clearance Center be responsible or liable for any costs, expenses or damage incurred by you as a result of a denial of your permission request, other than a refund of the amount(s) paid by you to Elsevier and/or Copyright Clearance Center for denied permissions.

LIMITED LICENSE

The following terms and conditions apply only to specific license types:
15. **Translation**: This permission is granted for non-exclusive world **English** rights only unless your license was granted for translation rights. If you licensed translation rights you may only translate this content into the languages you requested. A professional translator must perform all translations and reproduce the content word for word preserving the integrity of the article.
16. **Posting licensed content on any Website**: The following terms and conditions apply as follows: Licensing material from an Elsevier journal: All content posted to the web site must maintain the copyright information line on the bottom of each image; A hyper-text must be included to the Homepage of the journal from which you are licensing at http://www.sciencedirect.com/science/journal/xxxxx or the Elsevier homepage for books at http://www.elsevier.com; Central Storage: This license does not include permission for a scanned version of the material to be stored in a central repository such as that provided by Heron/XanEdu.
Licensing material from an Elsevier book: A hyper-text link must be included to the Elsevier homepage at http://www.elsevier.com . All content posted to the web site must maintain the copyright information line on the bottom of each image.

Posting licensed content on Electronic reserve: In addition to the above the following clauses are applicable: The web site must be password-protected and made available only to bona fide students registered on a relevant course. This permission is granted for 1 year only. You may obtain a new license for future website posting.
17. **For journal authors:** the following clauses are applicable in addition to the above:
Preprints:
A preprint is an author's own write-up of research results and analysis, it has not been peer-reviewed, nor has it had any other value added to it by a publisher (such as formatting, copyright, technical enhancement etc.).
Authors can share their preprints anywhere at any time. Preprints should not be added to or enhanced in any way in order to appear more like, or to substitute for, the final versions of articles however authors can update their preprints on arXiv or RePEc with their Accepted Author Manuscript (see below).
If accepted for publication, we encourage authors to link from the preprint to their formal publication via its DOI. Millions of researchers have access to the formal publications on ScienceDirect, and so links will help users to find, access, cite and use the best available version. Please note that Cell Press, The Lancet and some society-owned have different preprint policies. Information on these policies is available on the journal homepage.
Accepted Author Manuscripts: An accepted author manuscript is the manuscript of an article that has been accepted for publication and which typically includes author-incorporated changes suggested during submission, peer review and editor-author communications.
Authors can share their accepted author manuscript:

- immediately
    - via their non-commercial person homepage or blog
    - by updating a preprint in arXiv or RePEc with the accepted manuscript
    - via their research institute or institutional repository for internal institutional uses or as part of an invitation-only research collaboration work-group
    - directly by providing copies to their students or to research collaborators for their personal use
    - for private scholarly sharing as part of an invitation-only work group on commercial sites with which Elsevier has an agreement
- After the embargo period
    - via non-commercial hosting platforms such as their institutional repository
    - via commercial sites with which Elsevier has an agreement

In all cases accepted manuscripts should:

- link to the formal publication via its DOI
- bear a CC-BY-NC-ND license - this is easy to do
- if aggregated with other manuscripts, for example in a repository or other site, be shared in alignment with our hosting policy not be added to or enhanced in any way to appear more like, or to substitute for, the published journal article.

Published journal article (JPA): A published journal article (PJA) is the definitive final record of published research that appears or will appear in the journal and embodies all value-adding publishing activities including peer review co-ordination, copy-editing, formatting, (if relevant) pagination and online enrichment.
Policies for sharing publishing journal articles differ for subscription and gold open access articles:
Subscription Articles: If you are an author, please share a link to your article rather than the full-text. Millions of researchers have access to the formal publications on ScienceDirect, and so links will help your users to find, access, cite, and use the best available version.
Theses and dissertations which contain embedded PJAs as part of the formal submission can be posted publicly by the awarding institution with DOI links back to the formal publications on ScienceDirect.
If you are affiliated with a library that subscribes to ScienceDirect you have additional private sharing rights for others' research accessed under that agreement. This includes use for classroom teaching and internal training at the institution (including use in course packs and courseware programs), and inclusion of the article for grant funding purposes.
Gold Open Access Articles: May be shared according to the author-selected end-user license and should contain a CrossMark logo, the end user license, and a DOI link to the formal publication on ScienceDirect.
Please refer to Elsevier's posting policy for further information.
18. **For book authors** the following clauses are applicable in addition to the above: Authors are permitted to place a brief summary of their work online only. You are not allowed to download and post the published electronic version of your chapter, nor may you scan the printed edition to create an electronic version. **Posting to a repository:** Authors are permitted to post a summary of their chapter only in their institution's repository.
19. **Thesis/Dissertation**: If your license is for use in a thesis/dissertation your thesis may be submitted to your institution in either print or electronic form. Should your thesis be published commercially, please reapply for permission. These requirements include permission for the Library and Archives of Canada to supply single copies, on demand, of the complete thesis and include permission for Proquest/UMI to supply single copies, on demand, of the complete thesis. Should your thesis be published commercially, please reapply for permission. Theses and dissertations which contain embedded PJAs as part of the formal submission can be posted publicly by the awarding institution with DOI links back to the formal publications on ScienceDirect.

SPRINGER NATURE LICENSE TERMS AND CONDITIONS

Sep 24, 2025

This Agreement between Daniel Steiner ("You") and Springer Nature ("Springer Nature") consists of your license details and the terms and conditions provided by Springer Nature and Copyright Clearance Center.

License Number	6110620794380
License date	Sep 16, 2025
Licensed Content Publisher	Springer Nature
Licensed Content Publication	Springer eBook
Licensed Content Title	A Brief Overview of Planet Formation
Licensed Content Author	Philip J. Armitage
Licensed Content Date	Jan 1, 2018
Type of Use	Thesis/Dissertation
Requestor type	academic/university or research institute
Format	print and electronic
Portion	figures/tables/illustrations
Number of figures/tables/illustrations	1
Will you be translating?	no
Circulation/distribution	1 - 29
Author of this Springer Nature content	no
Title of new work	Large-scale magnetic fields in protoplanetary disks
Institution name	University of Vienna
Expected presentation date	Dec 2025
Portions	Figure 1
The Requesting Person / Organization to Appear on the License	Daniel Steiner
Requestor Location	Mr. Daniel Steiner Hafinger Weg 33 Top 5 Sankt Pölten, Lower Austria 3100 Austria
Billing Type	Invoice
Billing Address	Daniel Steiner Hafinger Weg 33 Top 5 Sankt Pölten, Austria 3100
Total	**0.00 EUR**

Terms and Conditions

Springer Nature Customer Service Centre GmbH Terms and Conditions

The following terms and conditions ("Terms and Conditions") together with the terms specified in your [RightsLink] constitute the License ("License") between you as Licensee and Springer Nature Customer Service Centre GmbH as Licensor. By clicking 'accept' and completing the transaction for your use of the material ("Licensed Material"), you confirm your acceptance of and obligation to be bound by these Terms and Conditions.

1. Grant and Scope of License

1. 1. The Licensor grants you a personal, non-exclusive, non-transferable, non-sublicensable, revocable, world-wide License to reproduce, distribute, communicate to the public, make available, broadcast, electronically transmit or create derivative works using the Licensed Material for the purpose(s) specified in your RightsLink Licence Details only. Licenses are granted for the specific use requested in the order and for no other use, subject to these Terms and Conditions. You acknowledge and agree that the rights granted to you under this License do not include the right to modify, edit, translate, include in collective works, or create derivative works of the Licensed Material in whole or in part unless expressly stated in your RightsLink Licence Details. You may use the Licensed Material only as permitted under this Agreement and will not reproduce, distribute, display, perform, or otherwise use or exploit any Licensed Material in any way, in whole or in part, except as expressly permitted by this License.

1. 2. You may only use the Licensed Content in the manner and to the extent permitted by these Terms and Conditions, by your RightsLink Licence Details and by any applicable laws.

1. 3. A separate license may be required for any additional use of the Licensed Material, e.g. where a license has been purchased for print use only, separate permission must be obtained for electronic re-use. Similarly, a License is only valid in the language selected and does not apply for editions in other languages unless additional translation rights have been granted separately in the License.

1. 4. Any content within the Licensed Material that is owned by third parties is expressly excluded from the License.

1. 5. Rights for additional reuses such as custom editions, computer/mobile applications, film or TV reuses and/or any other derivative rights requests require additional permission and may be subject to an additional fee. Please apply to journalpermissions@springernature.com or bookpermissions@springernature.com for these rights.

2. Reservation of Rights

Licensor reserves all rights not expressly granted to you under this License. You acknowledge and agree that nothing in this License limits or restricts Licensor's rights in or use of the Licensed Material in any way. Neither this License, nor any act, omission, or statement by Licensor or you, conveys any ownership right to you in any Licensed Material, or to any element or portion thereof. As between Licensor and you, Licensor owns and retains all right, title, and interest in and to the Licensed Material subject to the license granted in Section 1.1. Your permission to use the Licensed Material is expressly conditioned on you not impairing Licensor's or the applicable copyright owner's rights in the Licensed Material in any way.

3. Restrictions on use

3. 1. Minor editing privileges are allowed for adaptations for stylistic purposes or formatting purposes provided such alterations do not alter the original meaning or intention of the Licensed Material and the new figure(s) are still accurate and representative of the Licensed Material. Any other changes including but not limited to, cropping, adapting, and/or omitting material that affect the meaning, intention or moral rights of the author(s) are strictly prohibited.

3. 2. You must not use any Licensed Material as part of any design or trademark.

3. 3. Licensed Material may be used in Open Access Publications (OAP), but any such reuse must include a clear acknowledgment of this permission visible at the same time as the figures/tables/illustration or abstract and which must indicate that the Licensed Material is not part of the governing OA license but has been reproduced with permission. This may be indicated according to any standard referencing system but must include at a minimum 'Book/Journal title, Author, Journal Name (if applicable), Volume (if applicable), Publisher, Year, reproduced with permission from SNCSC'.

4. STM Permission Guidelines

4. 1. An alternative scope of license may apply to signatories of the STM Permissions Guidelines ("STM PG") as amended from time to time and made available at https://www.stm-assoc.org/intellectual-property/permissions/permissions-guidelines/.

4. 2. For content reuse requests that qualify for permission under the STM PG, and which may be updated from time to time, the STM PG supersede the terms and conditions contained in this License.

4. 3. If a License has been granted under the STM PG, but the STM PG no longer apply at the time of publication, further permission must be sought from the Rightsholder. Contact journalpermissions@springernature.com or

bookpermissions@springernature.com for these rights.

5. Duration of License

5. 1. Unless otherwise indicated on your License, a License is valid from the date of purchase ("License Date") until the end of the relevant period in the below table:

Reuse in a medical communications project	Reuse up to distribution or time period indicated in License
Reuse in a dissertation/thesis	Lifetime of thesis
Reuse in a journal/magazine	Lifetime of journal/magazine
Reuse in a book/textbook	Lifetime of edition
Reuse on a website	1 year unless otherwise specified in the License. If you wish to reuse the content on your website for longer than 1 year, please make this clear in the 'additional information' field and the License will include a 'Special Term' to reflect your duration choice.
Reuse in a presentation/slide kit/poster	Lifetime of presentation/slide kit/poster. Note: publication whether electronic or in print of presentation/slide kit/poster may require further permission.
Reuse in conference proceedings	Lifetime of conference proceedings
Reuse in an annual report	Lifetime of annual report
Reuse in training/CME materials	Reuse up to distribution or time period indicated in License
Reuse in newsmedia	Lifetime of newsmedia
Reuse in coursepack/classroom materials	Reuse up to distribution and/or time period indicated in license

6. Acknowledgement

6. 1. The Licensor's permission must be acknowledged next to the Licensed Material in print. In electronic form, this acknowledgement must be visible at the same time as the figures/tables/illustrations or abstract and must be hyperlinked to the journal/book's homepage.

6. 2. Acknowledgement may be provided according to any standard referencing system and at a minimum should include "Author, Article/Book Title, Journal name/Book imprint, volume, page number, year, Springer Nature".

7. Reuse in a dissertation or thesis

7. 1. Where 'reuse in a dissertation/thesis' has been selected, the following terms apply: Print rights of the Version of Record are provided for; electronic rights for use only on institutional repository as defined by the Sherpa guideline (www.sherpa.ac.uk/romeo/) and only up to what is required by the awarding institution.

7. 2. For theses published under an ISBN or ISSN, separate permission is required. Please contact journalpermissions@springernature.com or bookpermissions@springernature.com for these rights.

7. 3. Authors must properly cite the published manuscript in their thesis according to current citation standards and include the following acknowledgement: '*Reproduced with permission from Springer Nature'*.

8. License Fee

You must pay the fee set forth in the License Agreement (the "License Fees"). All amounts payable by you under this License are exclusive of any sales, use, withholding, value added or similar taxes, government fees or levies or other assessments. Collection and/or remittance of such taxes to the relevant tax authority shall be the responsibility of the party who has the legal obligation to do so.

9. Warranty

9. 1. The Licensor warrants that it has, to the best of its knowledge, the rights to license reuse of the Licensed Material. **You are solely responsible for ensuring that the material you wish to license is original to the**

Licensor and does not carry the copyright of another entity or third party (as credited in the published version). If the credit line on any part of the Licensed Material indicates that it was reprinted or adapted with permission from another source, then you should seek additional permission from that source to reuse the material.

9. 2. EXCEPT FOR THE EXPRESS WARRANTY STATED HEREIN AND TO THE EXTENT PERMITTED BY APPLICABLE LAW, LICENSOR PROVIDES THE LICENSED MATERIAL "AS IS" AND MAKES NO OTHER REPRESENTATION OR WARRANTY. LICENSOR EXPRESSLY DISCLAIMS ANY LIABILITY FOR ANY CLAIM ARISING FROM OR OUT OF THE CONTENT, INCLUDING BUT NOT LIMITED TO ANY ERRORS, INACCURACIES, OMISSIONS, OR DEFECTS CONTAINED THEREIN, AND ANY IMPLIED OR EXPRESS WARRANTY AS TO MERCHANTABILITY OR FITNESS FOR A PARTICULAR PURPOSE. IN NO EVENT SHALL LICENSOR BE LIABLE TO YOU OR ANY OTHER PARTY OR ANY OTHER PERSON OR FOR ANY SPECIAL, CONSEQUENTIAL, INCIDENTAL, INDIRECT, PUNITIVE, OR EXEMPLARY DAMAGES, HOWEVER CAUSED, ARISING OUT OF OR IN CONNECTION WITH THE DOWNLOADING, VIEWING OR USE OF THE LICENSED MATERIAL REGARDLESS OF THE FORM OF ACTION, WHETHER FOR BREACH OF CONTRACT, BREACH OF WARRANTY, TORT, NEGLIGENCE, INFRINGEMENT OR OTHERWISE (INCLUDING, WITHOUT LIMITATION, DAMAGES BASED ON LOSS OF PROFITS, DATA, FILES, USE, BUSINESS OPPORTUNITY OR CLAIMS OF THIRD PARTIES), AND WHETHER OR NOT THE PARTY HAS BEEN ADVISED OF THE POSSIBILITY OF SUCH DAMAGES. THIS LIMITATION APPLIES NOTWITHSTANDING ANY FAILURE OF ESSENTIAL PURPOSE OF ANY LIMITED REMEDY PROVIDED HEREIN.

10. Termination and Cancellation

10. 1. The License and all rights granted hereunder will continue until the end of the applicable period shown in Clause 5.1 above. Thereafter, this license will be terminated and all rights granted hereunder will cease.

10. 2. Licensor reserves the right to terminate the License in the event that payment is not received in full or if you breach the terms of this License.

11. General

11. 1. The License and the rights and obligations of the parties hereto shall be construed, interpreted and determined in accordance with the laws of the Federal Republic of Germany without reference to the stipulations of the CISG (United Nations Convention on Contracts for the International Sale of Goods) or to Germany's choice-of-law principle.

11. 2. The parties acknowledge and agree that any controversies and disputes arising out of this License shall be decided exclusively by the courts of or having jurisdiction for Heidelberg, Germany, as far as legally permissible.

11. 3. This License is solely for Licensor's and Licensee's benefit. It is not for the benefit of any other person or entity.

Questions? For questions on Copyright Clearance Center accounts or website issues please contact springernaturesupport@copyright.com or +1-855-239-3415 (toll free in the US) or +1-978-646-2777. For questions on Springer Nature licensing please visit https://www.springernature.com/gp/partners/rights-permissions-third-party-distribution

Other Conditions:

Version 1.5 - June 2025

Questions? E-mail us at customercare@copyright.com.

License